



HAL
open science

Contribution to the development of a fuel cell management system

Milad Bahrami

► **To cite this version:**

Milad Bahrami. Contribution to the development of a fuel cell management system. Engineering Sciences [physics]. Université de Lorraine, 2020. English. NNT : 2020LORR0025 . tel-02881219

HAL Id: tel-02881219

<https://hal.univ-lorraine.fr/tel-02881219>

Submitted on 25 Jun 2020

HAL is a multi-disciplinary open access archive for the deposit and dissemination of scientific research documents, whether they are published or not. The documents may come from teaching and research institutions in France or abroad, or from public or private research centers.

L'archive ouverte pluridisciplinaire **HAL**, est destinée au dépôt et à la diffusion de documents scientifiques de niveau recherche, publiés ou non, émanant des établissements d'enseignement et de recherche français ou étrangers, des laboratoires publics ou privés.



AVERTISSEMENT

Ce document est le fruit d'un long travail approuvé par le jury de soutenance et mis à disposition de l'ensemble de la communauté universitaire élargie.

Il est soumis à la propriété intellectuelle de l'auteur. Ceci implique une obligation de citation et de référencement lors de l'utilisation de ce document.

D'autre part, toute contrefaçon, plagiat, reproduction illicite encourt une poursuite pénale.

Contact : ddoc-theses-contact@univ-lorraine.fr

LIENS

Code de la Propriété Intellectuelle. articles L 122. 4

Code de la Propriété Intellectuelle. articles L 335.2- L 335.10

http://www.cfcopies.com/V2/leg/leg_droi.php

<http://www.culture.gouv.fr/culture/infos-pratiques/droits/protection.htm>

UNIVERSITÉ DE LORRAINE

École Doctorale "Sciences et Ingénierie des Molécules, des Produits, des Procédés, et de l'Énergie"
Département de Formation Doctorale "Energie et mécanique"

THÈSE

présentée à

L'UNIVERSITÉ DE LORRAINE

En vue de l'obtention du

DOCTORAT DE L'UNIVERSITÉ DE LORRAINE

Spécialité: Energie et mécanique

par

Milad Bahrami

Contribution to the development of a fuel cell management system

Soutenue publiquement le 27 mai 2020 devant le jury composé de:

Président	Seddik Bacha	Professeur - Université Grenoble Alpes
Rapporteurs	Marie-Cecile Pera	Professeur - Université de Franche-Comté
	Christophe Turpin	Directeur de Recherche - Laboratoire LAPLACE
Examineurs	Serge Pierfederici	Professeur - Université de Lorraine
	Gaël Maranzana	Professeur - Université de Lorraine
Invité	Jean-Philippe Martin	Maître de conférences - Université de Lorraine
	Arnaud Morin	Ingénieur de recherche HDR- CEA

Thèse préparée au Laboratoire d'Énergies, Mécanique Théorique et Appliquée

Site de l'ENSEM - EA N° 4366

Acknowledgments

The work presented in this thesis was carried out at the Laboratoire d’Energie et de Mécanique Théorique et Appliquée (LEMETA) at the University of Lorraine.

Firstly, I would like to express my deep and sincere gratitude to my supervisors Prof. Gael Maranzana and Prof. Serge Pierfederici for the continuous support of my Ph.D. study and related research, for their patience, motivation, and immense knowledge. Their guidance helped me in all the time of research and writing of this thesis. I could not have imagined having better advisors and mentors for my Ph.D. study. It was a great privilege and honor to work and study under their guidance.

Besides my supervisors, I would like to thank the rest of my thesis committee: Prof. Seddik Bacha, Prof. Marie-Cecile Pera, Prof. Christophe Turpin, DR. Arnaud Morin, Prof. Jean-Philippe Martin for their insightful comments and encouragement, but also for the hard question that incited me to widen my research from various perspectives.

My sincere thanks also go to Prof. Pascal Boulet, Prof. Farid Meibody-Tabar, Prof. Fabrice Lemoine, and Dr. Mathieu Weber, who provided me an opportunity to join their team, and who gave access to the laboratory and research facilities. Without their precious support, it would not be possible to conduct this research.

I thank my fellow lab mates for stimulating discussions, for the sleepless nights we were working together, and for all the fun we have had in the last four years. In particular, I am grateful to Prof. Majid Zandi and Prof. Roghayeh Gavagsaz Ghoachani for helping me to follow my dreams.

Last but not least, I am extremely grateful to my parents for their love, prayers, caring, and sacrifices for educating and preparing me for my future. I am very much thankful to my wife for her love, understanding, prayers, and continuing support to complete this research work. I am extending my heartfelt thanks to my sister and my brother in law for their supports and prayers. Besides, I express my thanks to my father in law, mother in law, and sister in law for their support and valuable prayers.

I also thank my friends (too many to list here but you know who you are!) for providing support and friendship that I needed.

Contents

- General Introduction (Preamble) 1
- Chapter 1 Thesis Context – Presentation of the studied Fuel cell management systems 3
 - 1.1. Introduction 3
 - 1.1.1. Problem statement 4
 - 1.1.2. Methodology 4
 - 1.2. Polymer Electrolyte Membrane Fuel Cell 4
 - 1.3. Degradation 6
 - 1.3.1. Operational conditions 6
 - 1.3.2. Degradation phenomena of FC components 8
 - 1.3.3. Degradation and snowball effects 9
 - 1.4. Durability study 13
 - 1.4.1. Non-model based methods 14
 - 1.4.2. Model-based methods 16
 - 1.4.3. Durability enhancement tool 20
 - 1.5. Conclusions 24
- Chapter 2 Polymer Electrolyte Membrane Fuel cell 26
 - 2.1. Introduction 26
 - 2.2. Heat transfer model 30
 - 2.3. Mass transfer 32
 - 2.3.1. Oxygen transfer 32
 - 2.3.2. Water transfer 35
 - 2.4. Charge transfer 51
 - 2.5. Hydrogen starvation detection 52
 - 2.6. Simulation Results 55
 - 2.6.1. Simulation of one cell 55
 - 2.6.2. Stack simulation 62
 - 2.7. Conclusions 72
- Chapter 3 Power electronics Structure 73
 - 3.1. Introduction 73
 - 3.2. Proposed power electronics structure 75
 - 3.2.1. Operation Modes 75
 - 3.2.2. Design consideration 79
 - 3.3. Control Method 86
 - 3.3.1. Equalizer controller 86

3.3.2.	DC bus voltage regulator	87
3.3.3.	SC voltage controller	91
3.4.	Simulation results.....	92
3.5.	Experimental results.....	96
3.6.	Stability analysis	101
3.7.	Conclusions.....	105
Chapter 4	Management system.....	106
4.1.	Introduction.....	106
4.2.	Proposed management system	106
4.3.	Simulation results.....	113
4.4.	Energy management system.....	137
4.5.	Conclusions.....	141
	General conclusions	142
	Appendix A.....	144
	Bibliography	150

List of Figures

Figure 1-1. Schematic diagram of a PEMFC.....	5
Figure 1-2. Serial connection of cells inside a stack.....	9
Figure 1-3. Heterogeneity between the distributions of gas flows.	10
Figure 1-4. Drying instability and its consequence snowball effects.	10
Figure 1-5. Heterogeneity of the hydrogen gas flow and/or heterogeneity of the cooling fluid at anode side channel.....	11
Figure 1-6. Flooding instability and its consequence snowball effect.....	11
Figure 1-7. Propagation of the instability.....	12
Figure 1-8. Stoichiometry evolution of hydrogen and air as a function of the temperature gradient for boundary conditions of the imposed pressure drop. $\Delta P_{\text{anode}}=12\text{mbar}$. $\Delta P_{\text{cathode}}=47\text{mbar}$. $I=0.5\text{A/cm}^2$. $T_{dp}(\text{anode})=50^\circ\text{C}$. $T_{dp}(\text{cathode})=50^\circ\text{C}$	13
Figure 1-9. PEMFC diagnosis methods.....	14
Figure 1-10. Multi stack topologies: a) Series b) Parallel c) Cascade d) Series-parallel.....	20
Figure 1-11. Cascade topology with different injected power by cell groups.....	21
Figure 1-12. Different types of equalizers.....	22
Figure 1-13. Proposed structure to improve the durability of a stack.....	25
Figure 2-1. Air stoichiometry and pressure drop on the cathode side as a function of time for a single cell as described in [117]. Current density is equal to 0.5A/cm^2 , $T=65^\circ\text{C}$. $P_{\text{out}}=\text{atmospheric pressure}$	28
Figure 2-2. Distribution of the produced water flow between the anode and cathode compartments for two different thermal configurations: a) The same temperature of the plates. b) A temperature gradient of 5°C with a warmer anode (the negative water flux at the anode (blue curve) means that the inlet water vapor that comes from the H_2 humidifier is even drained towards the cathode) [19].....	29
Figure 2-3. Heat transfer model in a cell. The coupling with the cooling fluid and the neighbor cells is achieved thanks to thermal resistances. The thermal inertia of the MEA and plates are considered. Regarding a very low Biot number (R_{GDL}^{th}/R_m^{th}), the MEA is assumed isothermal. Three thermal sources are considered.....	31
Figure 2-4. Oxygen transfer model in the perpendicular direction to the MEA. Because of its very short time constant ($F>50\text{Hz}$), the oxygen storage in the GDL or electrode is not described.....	34
Figure 2-5. Electrical equivalent circuit of the water transfer model in the direction perpendicular to the membrane. Three different water storages are considered in the MEA and channels.....	35
Figure 2-6. Pressure drop at the cathode side as a function of time following a current step and considering an applied air flow rate. The saturation of liquid water is initially zero. Eight current densities $S_{\text{air}}=2$ $S_{\text{H}_2}=1$. $T_{\text{anode}}=67.5^\circ\text{C}$. $T_{\text{cathode}}=62.5^\circ\text{C}$. $HR_{\text{anode}}=0\%$. $HR_{\text{cathode}}\sim 100\%$ (measured as a function of time).....	41
Figure 2-7. Imbibing experiment: the current is generated at $t=175\text{s}$. The stochastic variations following by the regular increase of the pressure drop (no liquid flow) is a sign of the two-phase flow.....	42
Figure 2-8. Relative permeability of the gas as a function of the saturation for the 48 experiments. All the experimental results are superimposed until the start of the two-phase flow.....	43
Figure 2-9. Logarithm of the liquid water flow rate (mol/s) divided by the pressure drop (mbar) as a function of the logarithm of the average saturation in steady-state, for three current densities. Each measurement point 'o' is the average of 10 measurements made under the same	

conditions and the error bar corresponds to the standard deviation. The non-superimposable results lead to a deduction that the liquid relative permeability depends on an additional parameter. Indeed, the airflow produces a constraint on the liquid that changes its relative permeability.....	45
Figure 2-10. Response to a current step of 0.67 A/cm^2 . The cathode compartment is initially dry ($S_c=0$). $T_{dp}=60^\circ\text{C}$. $T_c=62.5^\circ\text{C}$. $T_a=67.5^\circ\text{C}$. At time $t=0$ the average current density increases from 0 to 0.67 A/cm^2 . a) applied pressure drop on the cathode side. b) Simulation result of liquid water saturation in the cathode channel. c) Air stoichiometry as a function of time. This simulation has been performed using the accurate liquid relative permeability corresponding to the current density (red curve in Figure 2-9).....	50
Figure 2-11. Electrical equivalent circuit of the charge transfer model.	51
Figure 2-12. Block diagram of the reduced-order transient PEMFC model.....	54
Figure 2-13. Stack simulation (The cells are under the same pressure drop and they are thermally connected.).....	54
Figure 2-14. Applied current density and inlet/outlet pressure drop.	57
Figure 2-15. Simulation result of the voltage of the cell and cathode potential.	58
Figure 2-16. I-V characteristic simulation of a single cell. A higher saturation level inside the channels leads to a lower airflow during the decreasing the current. As a result, a negligible voltage difference exists between the increasing and decreasing current densities.	58
Figure 2-17. Simulation results of the stoichiometry, temperatures, and water flow-rates in the anode and cathode sides.	60
Figure 2-18. Simulation results of the water vapor relative humidity and concentration, liquid water saturation in the channels, and water content.	61
Figure 2-19. Simulation results of the total water flow-rates and membrane to channel water flow-rates.....	61
Figure 2-20. Simulation results of the oxygen concentration 62	62
Figure 2-21. Block diagram of a stack model consisting of 5 cells..... 63	63
Figure 2-22. Simulation results of the cell temperatures when the cooling fluid temperatures of the third cell increased from 60°C to 75°C at 500 s and decreased to its nominal value of 60°C at 3500 s. A constant current of 30A passing through the cells (The air and hydrogen pressure drops are applied). 64	64
Figure 2-23. Simulation results of the dry gas flow rates and saturation level inside the channels when the cooling fluid temperatures of the third cell increased from 60°C to 75°C at 500 s and decreased to its nominal value of 60°C at 3500 s. A constant current of 30A passing through the cells (The air and hydrogen pressure drops are applied). 65	65
Figure 2-24. Simulation results of the stoichiometry of hydrogen and oxygen, membrane water content, and the cell voltages when the cooling fluid temperatures of the third cell increased from 60°C to 75°C at 500 s and decreased to its nominal value of 60°C at 3500 s. A constant current of 30A passing through the cells (The air and hydrogen pressure drops are applied). 65	65
Figure 2-25. Simulation results of the stack voltage and applied current densities when the cooling fluid temperatures of the third cell increased from 60°C to 75°C at 500 s and decreased to its nominal value of 60°C at 3500 s. A constant current of 30A passing through the cells (The air and hydrogen pressure drops are applied). 66	66
Figure 2-26. Simulation results of the cell temperatures when the exchange current density of the third cell decreased from its nominal value to 10^{-6} times of it at 500 s. A constant current of 10 A passes through the cells (The air and hydrogen pressure drops are applied). 67	67
Figure 2-27. Simulation results of the dry gas flow rates and the saturation level inside the channels when the exchange current density of the third cell decreased from its nominal value to 10^{-6} times of it at 500 s. A constant current of 10 A passes through the cells (The air and hydrogen pressure drops are applied)..... 68	68

Figure 2-28. Simulation results of the cell voltages, membrane water content, and the stoichiometry of hydrogen and oxygen when the exchange current density of the third cell decreased from its nominal value to 10^{-6} times of it at 500 s. A constant current of 10 A passes through the cells (The air and hydrogen pressure drops are applied). The gas flow rates are highly sensitive to temperature gradients in these very low-pressure drops (low current density).	68
Figure 2-29. Simulation results of the stack voltage and applied current densities when the exchange current density of the third cell decreased from its nominal value to 10^{-6} times of it at 500 s. A constant current of 30A passing through the cells (The air and hydrogen pressure drops are applied).	69
Figure 2-30. Simulation results of the cell temperatures when the exchange current density of the third cell decreased from its nominal value to 10^{-6} times of it at 500 s. A constant current of 10 A passes through the cells of the non-insulated stack (The air and hydrogen pressure drops are applied). The initial temperature gradient inside the end cells can be noticed.	70
Figure 2-31. Simulation results of the dry gas flow rates and the saturation level inside the channels when the exchange current density of the third cell decreased from its nominal value to 10^{-6} times of it at 500 s. A constant current of 10 A passes through the cells of the non-insulated stack (The air and hydrogen pressure drops are applied).	71
Figure 2-32. Simulation results of the cell voltages, membrane water content, and the stoichiometry of hydrogen and oxygen when the exchange current density of the third cell decreased from its nominal value to 10^{-6} times of it at 500 s. A constant current of 10 A passes through the cells of the non-insulated stack (The air and hydrogen pressure drops are applied). This very low hydrogen stoichiometry of the first cell is a consequence of the thermal coupling with the clamping plate.	71
Figure 2-33. Simulation results of the stack voltage and applied current densities when the exchange current density of the third cell decreased from its nominal value to 10^{-6} times of it at 500 s. A constant current of 10 A passes through the cells of the non-insulated stack (The air and hydrogen pressure drops are applied).	72
Figure 3-1. Proposed power electronics architecture to realize the fuel cell management system.	73
Figure 3-2. Theoretical waveforms in the steady-state of the proposed equalizer whereas: a) V_{c1} is the lowest voltage between all capacitors b) $V_{c1} \setminus V_{c2}$ is the lowest voltage between the odd\even numbered capacitors.	78
Figure 3-3. Different operation modes of the proposed equalizer. (a) Mode 1: $t_0 < t < t_1$. (b) Mode 2: $t_1 < t < t_2$. (c) Mode3: $t_2 < t < t_3$. (d) Mode 4: $t_3 < t < t_4$.	79
Figure 3-4. The amount of transferred power through the transformer of the proposed equalizer in steady state: (a) Changes in the amount of leakage inductance, when the duty cycle of H-bridge inverter is equal to 0.4 and the first group, injects no power. (b) Changes in the amount of supplied power by the faulted cell and changes in the duty cycle.	83
Figure 3-5. Impact of the leakage inductance on the maximum of leakage current in transient conditions.	85
Figure 3-6. Influence of the leakage inductance on a) the maximum of leakage current b) the maximum of the diode current in steady-state.	85
Figure 3-7. Schematic diagram of the control method used to determine the duty cycle (d) of the H-bridge inverter.	86
Figure 3-8. Schematic diagram of the voltage controller.	88
Figure 3-9. Proposed anti-windup control scheme.	89
Figure 3-10. Maximum step load to calculate the minimum value of the capacitors.	91

Figure 3-11. DC bus voltage drop when load power is changed from -400 W to 400 W, the capacitance of the boost converter output capacitors is 4.7 mF and the SC voltage is equal to half of its nominal voltage (24).	91
Figure 3-12. Schematic diagram of the SC voltage controller.....	92
Figure 3-13. Simulation results of voltage and current waveforms on the primary side of the transformer for d=0.4.	93
Figure 3-14. Simulation results of the Output capacitor voltages in closed-loop when the first group of cells injects no power.	93
Figure 3-15. Simulation results of the voltage changes of the boost converters output capacitors connected to the cells in closed-loop when P_1 is increased from 63W to 100W and the other groups of cells inject the nominal power.	94
Figure 3-16. The dc bus voltage in closed-loop when the first cell power is increased from 63W to 100W and the other groups of cells inject the nominal power.	95
Figure 3-17. 1 Simulation results of the voltage changes of the boost converters output capacitors connected to the cells in closed-loop when P1 is changed from 63W to 100W, P2 is set to 100W, and the other groups of the cells inject the nominal power.	95
Figure 3-18. The dc bus voltage in closed-loop when the first cell power is changed from 63W to 100W, the injected power of the second cell is set to 100W, and the other groups of the cells inject the nominal power.	95
Figure 3-19. Test bench of the proposed system.	96
Figure 3-20. Experimental waveforms of the current and voltage on the primary side of the transformer when first and second fuel cells inject the half of nominal power and duty cycle of H-bridge inverter is equal to 0.4.....	97
Figure 3-21. Experimental results of the Output capacitor voltages when the first group of cells injects no power.	97
Figure 3-22. Voltage changes of the boost converters output capacitors connected to the cells in closed-loop when P_1 is increased from 63W to 100W, and P_2 is set to the nominal power: a) Experimental results b) Simulation results of the average model.	99
Figure 3-23. Voltage changes of the boost converters output capacitors in closed-loop when P_1 is changed from 63W to 100W, and P_2 is set to 100W: a) Experimental results b) Simulation results of the average model.	99
Figure 3-24. Experimental results of the proposed equalizer during the flooding condition of the first cell. (a) Output capacitor voltages. (b) Voltage and current on the primary side of the transformer and current of the first cell.	100
Figure 3-25. Experimental results of the proposed equalizer during the drying condition of the first cell. (a) Output capacitor voltages. (b) Voltage and current on the primary side of the transformer.	100
Figure 3-26. Steady-state voltage changes of the boost converters' output capacitor connected to fuel cells in closed-loop by changing the injected power of the first group of cells while the other groups inject the nominal power of 126 W.	102
Figure 3-27. Eigenvalues of the closed-loop system by changing the injected power of the first group of cells while the other groups inject the nominal power of 126 W.	102
Figure 3-28. Steady-State voltage changes of the boost converters' output capacitor connected to fuel cells in closed-loop by changing the injected power of the first group of cells while the second group of cells injects 50 W and the other groups inject the nominal power of 126 W.	103
Figure 3-29. Dominant eigenvalues of the closed-loop system by changing the injected power of the first group of cells while the second group of cells injects 50 W and the other groups inject the nominal power of 126 W.	103

Figure 3-30. Dominant eigenvalues of the closed-loop system by changing the capacitance value of the first capacitor when the power of the first group of cells is equal to zero W and the other groups inject the nominal power of 126 W.....	104
Figure 3-31. Dominant eigenvalues of the closed-loop system by changing the coupling coefficient when the power of the first group of cells is equal to zero W and the other groups inject the nominal power of 126 W.....	105
Figure 4-1. Block diagram of the proposed management strategy.....	107
Figure 4-2. Block diagram of the FLC.....	107
Figure 4-3. Fuzzification.....	108
Figure 4-4. Applying the fuzzy operator.....	108
Figure 4-5. Implication method.....	109
Figure 4-6. Aggregation method.....	110
Figure 4-7. Block diagram of the FCMS strategy.....	111
Figure 4-8. Block diagram of the second part of the FC management.....	112
Figure 4-9. Schematic diagram of the SC voltage controller that is used for the management system simulation purposes.....	113
Figure 4-10. Membership functions: inputs (St_{H_2} , St_{O_2} , and λ_m) and output (ΔP_e).....	114
Figure 4-11. Simulation results of the cell temperatures when the cooling fluid temperatures of the first group increased at 1000 s and when a constant current of 30A passing through the cells (The air and hydrogen pressure drops are applied).....	116
Figure 4-12. Simulation results of the dry gas flow rates and the saturation level inside the channels when the cooling fluid temperatures of the first group increased at 1000 s and when a constant current of 30A passing through the cells (The air and hydrogen pressure drops are applied).....	117
Figure 4-13. Simulation results of FLC inputs and the cell voltages when the cooling fluid temperatures of the first group increased at 1000 s and when a constant current of 30A passing through the cells (The air and hydrogen pressure drops are applied).	117
Figure 4-14. Simulation results of the normalized value of FLC inputs when the cooling fluid temperatures of the first group increased at 1000 s and when a constant current of 30A passing through the cells (The air and hydrogen pressure drops are applied).	118
Figure 4-15. Simulation results of the normalized value of FLC inputs and the reference power that should be injected by the cell groups when the cooling fluid temperatures of the first group increased at 1000 s and when the FCMS controls the injected power of cells groups (The air and hydrogen pressure drops are applied).....	119
Figure 4-16. Simulation results of the FLC inputs and the single-cell voltages when the cooling fluid temperatures of the first group increased at 1000 s and when the FCMS controls the injected power of cells groups (The air and hydrogen pressure drops are applied).....	119
Figure 4-17. Simulation results of the cell temperatures when the cooling fluid temperatures of the first group increased at 1000 s and when the FCMS controls the injected power of cell groups (The air and hydrogen pressure drops are applied).	120
Figure 4-18. Simulation results of the saturation inside the channels and dry gas flow rates when the cooling fluid temperatures of the first group increased at 1000 s and when the FCMS controls the injected power of cell groups (The air and hydrogen pressure drops are applied).	121
Figure 4-19. Simulation results of the SC voltage, the reference of total power, and the total power injected by cell groups when the cooling fluid temperatures of the first group increased at 1000 s and when the FCMS controls the injected power of cell groups (The air and hydrogen pressure drops are applied).....	121
Figure 4-20. Simulation results of the stack voltage and the injected current by cell groups when the cooling fluid temperatures of the first group increased at 1000 s and when the FCMS	

controls the injected power of cell groups (The air and hydrogen pressure drops are applied).	122
Figure 4-21. Simulation results of the cell temperatures when the cathode side cooling fluid temperature of the first group increased at 1000 s and when a constant current of 30A passing through the cells (The air and hydrogen pressure drops are applied).	123
Figure 4-22. Simulation results of the saturation inside the channels and dry gas flow rates when the cathode side cooling fluid temperature of the first group increased at 1000 s and when a constant current of 30A passing through the cells (The air and hydrogen pressure drops are applied).	124
Figure 4-23. Simulation results of FLC inputs and the cell voltages when the cathode side cooling fluid temperature of the first group increased at 1000 s and when a constant current of 30A passing through the cells (The air and hydrogen pressure drops are applied).	124
Figure 4-24. Simulation results of the normalized value of FLC inputs when the cathode side cooling fluid temperature of the first group increased at 1000 s and when a constant current of 30A passing through the cells (The air and hydrogen pressure drops are applied).	125
Figure 4-25. Simulation results of the normalized value of FLC inputs and the reference power that must be injected by the cell groups when the cathode side cooling fluid temperature of the first group increased at 1000 s and when the FCMS controls the injected power of cells groups (The air and hydrogen pressure drops are applied).	126
Figure 4-26. Simulation results of FLC inputs and the cell voltages when the cathode side cooling fluid temperature of the first group increased at 1000 s and when the FCMS controls the injected power of cells groups (The air and hydrogen pressure drops are applied).	126
Figure 4-27. Simulation results of the cell temperatures when the cathode side cooling fluid temperature of the first group increased at 1000 s and when the FCMS controls the injected power of cells groups (The air and hydrogen pressure drops are applied).	127
Figure 4-28. Simulation results of the dry gas flow rate and saturation inside the channels when the cathode side cooling fluid temperature of the first group increased at 1000 s and when the FCMS controls the injected power of cells groups (The air and hydrogen pressure drops are applied).	127
Figure 4-29. Simulation results of the SC voltage, the reference of total power and the total power injected by cell groups when the cathode side cooling fluid temperature of the first group increased at 1000 s and when the FCMS controls the injected power of cells groups (The air and hydrogen pressure drops are applied).	128
Figure 4-30. Simulation results of the stack voltage and the injected current by cell groups when the cathode side cooling fluid temperature of the first group increased at 1000 s and when the FCMS controls the injected power of cells groups (The air and hydrogen pressure drops are applied).	129
Figure 4-31. Simulation results of the normalized value of the FLC inputs and the reference power that should be injected by the cell groups when the cooling fluid temperatures of the first group increased from 60 °C to 75 °C at 1000 s and decreased to its nominal value of 60 °C at 4000 s (The air and hydrogen pressure drops are applied).	130
Figure 4-32. Simulation results of the FLC inputs and the cell voltages when the cooling fluid temperatures of the first group increased from 60 °C to 75 °C at 1000 s and decreased to 60 °C its nominal value at 4000s (The air and hydrogen pressure drops are applied).	131
Figure 4-33. Simulation results of the cell temperatures when the cooling fluid temperatures of the first group increased from 60 °C to 75 °C at 1000 s and decreased to 60 °C its nominal value at 4000s (The air and hydrogen pressure drops are applied).	132
Figure 4-34. Simulation results of the saturation level inside the channels and dry gas flow rates when the cooling fluid temperatures of the first group increased from 60 °C to 75 °C at	

1000 s and decreased to 60 °C its nominal value at 4000s (The air and hydrogen pressure drops are applied).....	132
Figure 4-35. Simulation results of the SC voltage, the reference of total power and the total power injected by cell groups when the cooling fluid temperatures of the first group increased from 60 °C to 75 °C at 1000 s and decreased to 60 °C its nominal value at 4000s (The air and hydrogen pressure drops are applied).....	133
Figure 4-36. Simulation results of the stack voltage and the injected current by cell groups when the cooling fluid temperatures of the first group increased from 60 °C to 75 °C at 1000 s and decreased to 60 °C its nominal value at 4000s (The air and hydrogen pressure drops are applied).....	133
Figure 4-37. Simulation results of the normalized value of FLC inputs and the reference power that must be injected by the cell groups when the cathode side cooling fluid temperature of the first group increased from 60 °C to 65 °C at 1000 s and decreased to its nominal value of 60 °C at 4000 s (The air and hydrogen pressure drops are applied).....	134
Figure 4-38. Simulation results of FLC inputs and the cell voltages when the cathode side cooling fluid temperature of the first group increased from 60 °C to 65 °C at 1000 s and decreased to its nominal value of 60 °C at 4000 s (The air and hydrogen pressure drops are applied).....	135
Figure 4-39. Simulation results of the cell temperatures when the cathode side cooling fluid temperature of the first group increased from 60 °C to 65 °C at 1000 s and decreased to its nominal value of 60 °C at 4000 s (The air and hydrogen pressure drops are applied).....	136
Figure 4-40. Simulation results of the dry gas flow rate and saturation inside the channels when the cathode side cooling fluid temperature of the first group increased from 60 °C to 65 °C at 1000 s and decreased to its nominal value of 60 °C at 4000 s (The air and hydrogen pressure drops are applied).....	136
Figure 4-41. Simulation results of the SC voltage, the reference of total power and the total power injected by cell groups when the cathode side cooling fluid temperature of the first group increased from 60 °C to 65 °C at 1000 s and decreased to its nominal value of 60 °C at 4000 s (The air and hydrogen pressure drops are applied).	137
Figure 4-42. Simulation results of the stack voltage and the injected current by cell groups when the cathode side cooling fluid temperature of the first group increased from 60 °C to 65 °C at 1000 s and decreased to its nominal value of 60 °C at 4000 s (The air and hydrogen pressure drops are applied).....	137
Figure 4-43. Experimental result of the energy management system when the cell groups are in the normal condition and overload occurs: a) Injected power and load power variations. b) Zoom on powers. c) DC link and SC voltage changes. d) zoom on part c.	138
Figure 4-44. Experimental result of the energy management system when the cell groups are in the normal condition except the first group (drying condition) and overload occurs. a) Injected power and load power variations. b) Zoom on the power. c) DC link and SC voltage changes. d) Output capacitor voltage changes.	139
Figure 4-45. Experimental result of the energy management system when the cell groups are in the normal condition except the first group (flooding condition) and an overload occurred. a) Injected power and load power variations. b) Zoom on the part a. c) DC link and SC voltage changes. d) Output capacitor voltage changes.	140

List of Tables

Table 2.1. Parameters of the model for simulations	55
Table 3.1. The parameters of the proposed system.....	84
Table 3.2. Parameters of the used devices in the test bench.....	96
Table 3.3. Theory and experimental capacitor voltages (V) comparison	98
Table 4.1. Rule base of the fuzzy logic controller	115
Table 4.2. Control parameters.....	115
Table 4.3. Model parameters for the flooding simulation.....	123
Table 4.4. Inputs of the FLC and reference of powers in the steady-state during the drying condition of the first group.....	131
Table 4.5. Inputs of the FLC and reference of powers in the steady-state during the flooding condition of the first group.....	135

General Introduction (Preamble)

International Energy Agency (IEA) reported that global energy demand grew by 2.3% from 2017 and reached 14 gigatons of oil equivalent in 2018, the fastest pace in a decade, leading to 1.7% of growth in energy-related CO₂ emissions (37.1 billion tons). The demand for electricity grew faster than for all other energy sources with an increase of 4%. The share of electricity in global energy consumption reached 20% in 2018.

The renewable energy-based electricity and heat generation can respond to this growing demand while limiting air pollution. Although the share of renewable energy sources in meeting new energy demand keeps growing, the rates of improvement are far below those required to meet the objectives of the Paris Agreement on climate change to reduce the total CO₂ emission.

The essential challenge in using renewable energy sources is the intermittency of their resources. Therefore, new ways to store electricity is inevitable. Hydrogen as an energy carrier can deal with this issue. Hydrogen gas cannot be found in nature but it can be produced by using the excess energy of renewable energy sources. A Polymer Electrolyte Membrane Fuel Cell (PEMFC) as a device that can directly convert hydrogen energy to electricity is an important part of this solution. The cost and durability are the major challenges to enable the diffusion of this technology in the mass market.

The short lifespan of a fuel cell is partly originated from the low voltage of one cell. Many cells must be connected in series in a stack to improve the overall efficiency of the system by increasing the output voltage. Since the same load current passes through the cells in series connection, the lifespan of a stack depends on each cell inside it. Remarkable that the electrochemical behavior of a cell can be managed by modifying its current. Thus, a special management system can improve the durability of the system. The main objective of this thesis is to develop such a management system.

This Ph.D. has been led in “Laboratoire d’Energies, Mécanique Théorique et Appliquée” (LEMTA) laboratory, part of the University of Lorraine, Nancy, France. This project aims to develop a management system, which allows optimizing the reliability and life of PEMFCs in the frame of a multi-vectors microgrid. This management system must diagnose or detect the instability of cells inside a stack and change their operating conditions according to their instability to cure them and improve their functionality. As a result, the durability of PEMFCs can be improved using such a management system. In other words, this management system can control the operating condition of cells in such a way that the electrochemical instabilities can be avoided to improve the lifetime of a stack.

A stack, which allows modifying the current of any number of cells inside it, and a power electronics structure that allows controlling the power flow of different cells are the essential infrastructures to develop a Fuel Cell Management System (FCMS). A new patent of the LEMTA dealing with the PEMFC structure obviates the first requirement. A specific power electronics structure is developed in this thesis. This power electronics structure takes into account the impact of the electrical stress on each cell or a group of cells to guarantee better

aging of the electrochemical system. Although the proposed structure is used to develop an FCMS in this thesis, other applications are conceivable for it or parts of it.

An FCMS should detect the instability of cells and change their reference power based on the detected instabilities. Therefore, a diagnostic method is also developed in this thesis. Given the capability of a mathematical model to express the phenomena of a fuel cell, in this thesis the conditions of a cell are examined based on a model. Developing a comprehensive model, which can detect most of fuel cell instabilities and can model a cell in its stack environment, is another objective of this thesis. This model must also be as simple as possible that can be simulated in real-time. In summary, the FCMS modifies the reference power of the cell groups according to the detected instabilities by the proposed model. The reference power of the cell groups is imposed by the power electronics structure while respecting the load profile.

Before a general conclusion and listing conceivable perspectives, this thesis is presented in four chapters as follows:

- Chapter 1 provides the context and bibliography. The problem statement is given in this chapter. The different diagnostic methods in the literature are compared and the best method is chosen. The various types of power electronics architecture in the literature are also discussed in this chapter. This chapter ends with a description of the proposed power electronics structure.
- A mathematical model of the PEMFC is presented in Chapter 2. This model is a combination of the heat transfer model, mass transfer model, and charge transfer model. Each model is explained and formulated in this chapter. The simulation results are provided at the end of this chapter.
- Chapter 3 describes the power electronics architecture to realize the FCMS. A dynamical average model is provided for the proposed system and the stability analysis is performed. The simulation and experimental results are provided in this chapter to validate the system.

The management strategy is explained in detail in Chapter 4. The simulation results are provided in two different conditions. These simulation results validate the effectiveness of the proposed strategy. Finally, the functionality of the system is experimentally validated in three different conditions.

Chapter 1

Thesis Context – Presentation of the studied Fuel cell management systems

1.1. Introduction

Based on the energy and environmental crisis in the world, the approach is toward using renewable and clean energy. The most important issue of renewable energies is the intermittency of the resources [1], [2]. Hydrogen as an energy carrier can cope with this problem. Low-cost hydrogen can be generated by using the excess energy generation of renewable energy sources and it can be stored in tanks or caves. This gas can be directly converted to electricity by a Fuel Cell (FC) when the grid needs more energy. Polymer Electrolyte Membrane Fuel Cells (PEMFC) are FCs whose technological maturity is the most advanced especially for embedded applications. The normal voltage of one cell is near 0.7 V. Therefore, several cells are connected in series inside of one stack to increase the output voltage. The basic disadvantage of such connections is the lifetime dependency of the stack on each cell lifetime. The other disadvantage of this connection is the probability of the propagation of a fault from one cell to the adjacent ones because of thermal coupling. The cell management can cope with these problems.

Four main barriers against the FC systems penetration in the market are Electrical efficiency, reliability, durability, and cost [3]. Currently, the performance of Polymer Electrolyte Membrane FCs (PEMFC), in terms of power density (4 kW / L) and efficiency, is sufficient to allow large-scale deployment of the technology [4]–[6]. On the other hand, sustainability and cost are two points that need to be improved [7]. To improve the durability, it is possible to develop new materials more resistant but also to better control the operating conditions to avoid the instabilities that lead to irreversible damages [8]. Indeed, a special management system like the battery management systems can cope with the instabilities of the cells inside a stack. In this thesis, the second manner in durability improvement is the principal effort.

This Ph.D. has been led by “Laboratoire d’Energie et de Mécanique Théorique et Appliquée” (LEMTA) laboratory, part of the University of Lorraine, Nancy, France. The main aim of this project is to develop an FC Management System (FCMS) to increase the reliability and durability of FCs. A specific interface converter will enrich a new patent of LEMTA dealing with the FC structure.

Developing such a management system needs a stack, which allows modifying the current of any number of cells inside the stack, and a power electronics structure that allows controlling the power flow of different cells. A new patent obviates the first requirement and allows access to the current of any cells [9]. Due to the low voltage of a cell or a small group of cells, the high

voltage conversion ratio converter like isolated converters is vital but efficiency is the basic challenge [10]–[12].

1.1.1. Problem statement

As mentioned before, one of the most challenging obstacles in wide use of the PEMFCs is their lifetime. The lifespan of the fuel cell can be improved by using better materials. However, it is still possible to increase the lifespan through an electrical interface even in a system with improved materials. In this regard, there have been some efforts in literature, but the fuel cell has been viewed as a stack and closed system in most cases. The electrochemical instabilities of cells can be controlled by managing the cells separately. Furthermore, fault propagation can be prevented by separately controlling the cells. However, handling the low voltage and high current is the main challenge of the power electronics structure. The faults should be detected in the first place to take action against them. A mathematical model can be used to detect multiple faults due to its direct link with the fuel cell phenomena. A comprehensive model that covers all the phenomena of fuel cells is essential for this purpose. This model must also be able to run in real-time. Finally, the management system should make decisions based on the model data and implement it through the power electronics structure.

1.1.2. Methodology

A quantitative method was used based on three principles of bibliography, simulation, and experiments. After reviewing the references on any subject, the proposed system or model was simulated using MATLAB tool. Once the simulation approved the theoretical assumptions, a test bench was developed to obtain the experimental results. Some parameters of the fuel cell model were identified by the result of the experiments. The curve fitting to the experimental results was the main tool for identifying the model parameters. The experimental results were also used to improve and validate the proposed systems and models. For instance, the behavior of the proposed power electronics structure was compared with the experimental results to validate the proposed model of the power electronics structure. Hence, the first chapter is dedicated to the first step of the proposed methodology (bibliography).

This chapter gives a brief state of the art of FCMSs. The reason behind the proposed system is also explained in this chapter. Notable that the literature review is much more completed through the following chapters.

The rest of this chapter is organized as follows: The PEMFC is briefly explained in section 1.2. The degradation phenomena in a PEMFC and different cell instabilities are summarized in section 1.3. The different ways of detecting the faulty cells in the literature and how to cure them are explained in section 1.4. Conclusions are presented in section 1.5.

1.2. Polymer Electrolyte Membrane Fuel Cell

An FC is an electrochemical device that directly converts the chemical energy of the fuel to electricity through an electro-chemical reaction. As shown in Figure 1-1, this device consists of two electrodes (anode and cathode), two bipolar plates and gas diffusion layers, and an electrolyte. One type of FCs is Polymer Electrolyte Membrane -also called Proton Exchange Membrane- (PEM). The electrolyte of the PEMFC is a polymer membrane that can let the protons to transfer. This membrane is dielectric (electrons cannot cross through it) and allows only hydrogen ions (H^+) and water to pass through it. Gas diffusion layers and bipolar plates allow the diffusion of both hydrogen and oxygen [13].

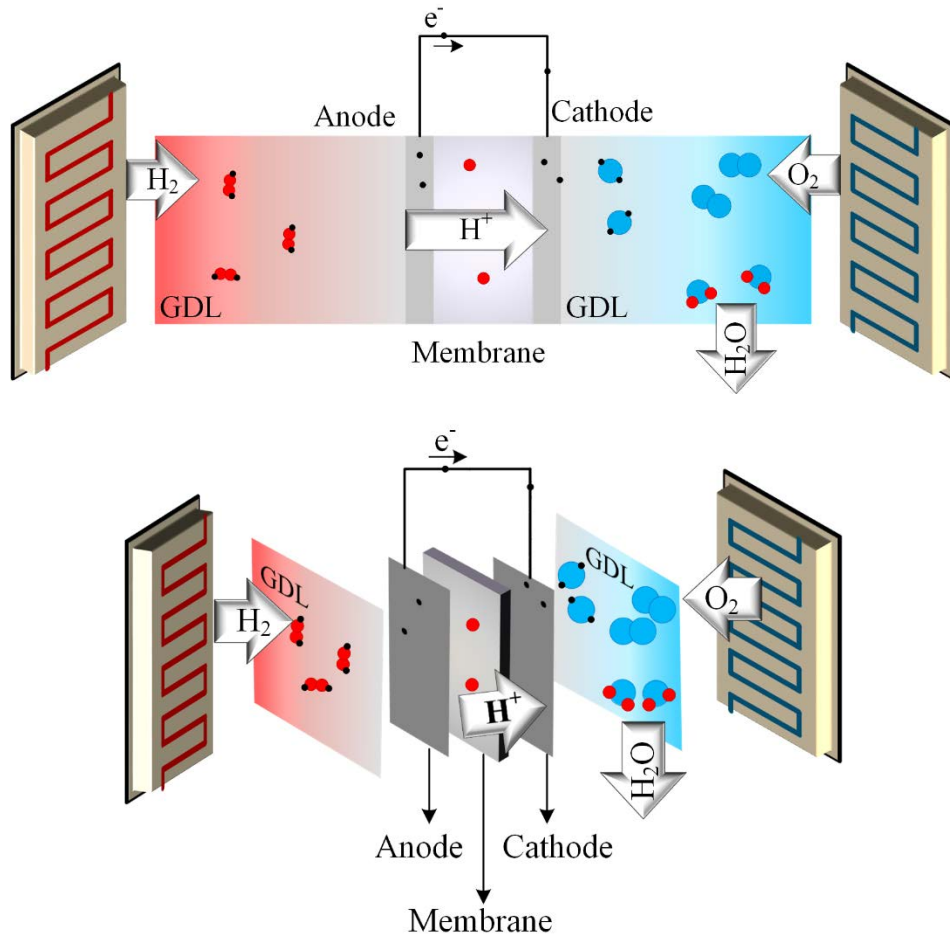


Figure 1-1. Schematic diagram of a PEMFC.

A PEMFC requires a costly amount of platinum as a catalyst in its electrodes (0.3 gPt/kW). The membrane is sandwiched between two electrodes. The platinum catalyst nanoparticles supported on carbon are dispersed in the electrodes. This set is called the Membrane Electrode Assembly (MEA). Hydrogen is split into protons and electrons at the anode side. Platinum catalyzes this reaction. Hydrogen ions can pass through the membrane but electrons travel from the external circuit. Electrons moving through the external circuit means electricity generation. This reaction is called Hydrogen Oxidation Reaction (HOR) and it is as follows:



A flow of pure oxygen or air is delivered to the cathode side where oxygen molecules react with electrons that arrive from external circuits and hydrogen ions that pass through the membrane. The product of this reaction is water. Heat is produced as a by-product. The following reaction is called the Oxygen Reduction Reaction (ORR):



The overall reaction in the PEMFC is as follows:



As seen in this reaction, two molecules of hydrogen react with one molecule of oxygen to produce two molecules of water [14] and four electrons. The reactions inside the FC including HOR, ORR, carbon corrosion, and the water electrolysis are derived by the electrode potential [15].

1.3. Degradation

The Basic challenge in using FCs is the low voltage of one cell. As a result, many of these cells are connected in series to increase the output voltage. This structure is named Stack. The whole system's lifetime depends on each cell inside it. The voltage of one particular cell in a stack may decrease because of specific aging or local malfunctioning such as drying. As a result, more heat is generated in this cell leading to an increase in its temperature and thus an additional voltage loss. This snowball effect can lead to the failure of the cell. Therefore, the whole system's lifetime has been reduced by the effect of this cell. The whole system life can be increased by the fault detection and fault compensation. The durability of PEMFC has a key role in the acceptance of it as a feasible power source. Many factors affect FC performance, such as FC assembly and design, impurities or poisoning, degradation of materials and components, and operational conditions [16]. Water management, thermal management, gas transport, and operating cycles are the main operational conditions that should be controlled [17].

1.3.1. Operational conditions

1.3.1.1. Water management

Water management is a very important factor for PEMFC's lifetime. The excess of water, which is called flooding, blocks the gas diffusion layer pores. Therefore, the reactants are prevented to reach the catalysts and this leads to gas starvation, a drop in cell voltage, and possible irreversible degradations. This excess of water can accelerate other degradations such as corrosion. Inadequate amount of water decreases the proton conductivity of the membrane and ionomer in the electrodes, so that increases the ionic resistance and ohmic losses. If the membrane is exposed to dry conditions for a long time or to moisture cycling, it becomes breakable. In this condition, cracks and fissure may appear on the surface of the membrane, and gas may leak through the membrane. All of these conditions accelerate membrane degradation [18].

1.3.1.2. Thermal management

The operating temperature of FC is about 60-80 °C. Although the high temperatures can enhance the electrochemical reaction kinetic and proton conduction in the membrane, the water vapor pressure is increased in these conditions leading to a low oxygen pressure that is detrimental to oxygen mass transfer. Besides, thermal management is highly coupled with water management. For example, when the two plates –anode and cathode- are not at the same temperature, the produced water goes to the colder one [19], [20]. This coupling means that bad thermal management can lead to fuel starvation.

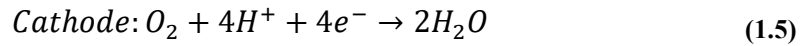
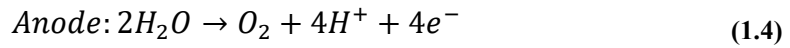
The sub-zero temperatures can freeze the water and damage the cell components. If the water is not removed from the cathode side while the cell is running at sub-zero temperature, water will freeze. Frozen water can prevent the reactants to reach a catalyst. Therefore, a voltage drop occurs. Frequent freezing and melting of water on the membrane surface can scratch the catalyst layer [17].

1.3.1.3. Mass flow management

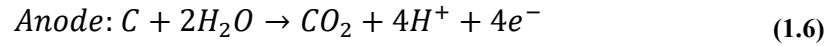
Two types of gas starvation are considered here:

1. Gas (H_2 or O_2) is lacking from a local point of view because the electrode is locally flooded or saturated with another gas. In this case, the potential of the cell is still positive because a small part of the cell is concerned. Anyway, it can be difficult to diagnose. When it happens at the anode (hydrogen starvation), oxygen can cross the membrane and make locally the potential to rise. The potential of the cathode just on the other side of the membrane can reach 1.6V [21]–[25] leading to carbon corrosion and platinum dissolution. On the other hand, oxygen starvation at the cathode is associated with voltage instabilities but is not necessarily detrimental for the FC lifetime.

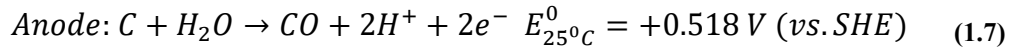
2. The second type of starvation is when gas is lacking so much that sub-stoichiometric conditions are reached. In that case, the voltage of the cell is reversed. The cell is consuming power instead of producing it. When it happens at the cathode (oxygen starvation), H_2 evolution replaces oxygen reduction and no serious electro-chemical damages are expected thanks to the low potential. However, hydrogen peroxide can be produced and degrade the membrane. When it happens at the anode (hydrogen starvation), it does not degrade the cathode as the preceding case because the cell voltage is negative, but the anode whose potential increases until water electrolysis and carbon corrosion becomes possible ($E_{25^{\circ}C}^0 = +1.23 V$ (vs. SHE)). Indeed, the electrolysis of water prepares the protons and electrons for maintaining the current. The water electrolysis at the anode side and cathode side are as follows [15], [26]:



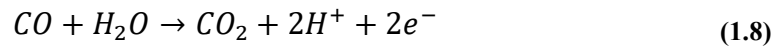
The oxidation reaction of the carbon in the anode catalyst (Pt/C) can also provide the protons to support the load current. This reaction is possible for the potentials above 0.207 V vs. SHE. This reactions is as follows [15], [26]:



The oxidation of carbon to carbon monoxide can also happen under high potential as follows [15], [26]:



However, the oxidation of carbon monoxide to carbon dioxide can be possible under the potential of $E_{25^{\circ}C}^0 = -0.103 V$ (vs. SHE) that is not important while the fuel starvation. This reaction is as follows [26]:



These reactions can reduce the carbon content in the catalyst layer even reduce the carbon content in the backing layer with time. As the carbon is corroded, the noble metal nanoparticles are aggregated into larger particles or they diffuse to the membrane in ionic form. Without these nanoparticles inside the catalyst layer, the FC fails to continue its proper performance [26].

1.3.1.4. Operating cycles

In transportation applications, the operating conditions change frequently. Therefore, the FCs have to work under different operating cycles. In the different cycles of operations, the current of FC is changed and this leads to change the FC potential. The anode potential stays close to the reversible hydrogen potential in FC by pure hydrogen supply. As a result, the cathode potential has to change in different operating cycles. Cathode potential variation has a big influence on the electrode materials such as the degree of oxide coverage of both platinum and

carbon and hydrophobicity of the surface. These potential variations lead notably to a dissolution of the platinum nanoparticles.

If the FC is stopped for a long time, oxygen will cross over to anode side. If FC is started in this condition, the fuel starvation will occur at the start-up time.

Anodic and cathodic pressure drops are low when the power generated by the FC is small. In this condition, the flow of gases is not evenly distributed among the different cells and fuel starvation events are prone to occur [17].

1.3.2. Degradation phenomena of FC components

FC components degradation can be divided into three categories: mechanical, chemical, and thermal degradations. In practice, these three modes of degradation are coupled. Mechanical degradation is caused by the pressure difference between the hydrogen and oxygen, and by stresses that occur due to non-uniform clamping pressure at the channel-rib scale and moisture cycling. Chemical degradation is related to different components of the cell: variation in hydrophobicity of the gas diffusion layer, corrosion of bipolar plates, catalyst poisoning, and polymer decomposition. This category of degradation has many consequences such as a decrease in conductivity, loss of catalyst activity, weakening of the membrane, etc. Excessive temperature and insufficient gas humidity caused thermal degradation. The mechanical and thermal degradation usually can be considered as an irreversible degradation. The degradation of material during the time is also irreversible and cannot be avoided [17] but reduced thanks to adapted system management.

1.3.2.1. Bipolar plates

Bipolar plates provide the flow fields for incoming reactants and outgoing products. Three degradation mechanisms occur in these components: corrosion, the formation of a resistive surface layer, and fractures or deformation of it. The corrosion affects the catalyst layer and the membrane durability due to multivalent cations production. The resistive surface layer formation increases the ohmic resistance [27].

1.3.2.2. Gas diffusion layer (GDL)

GDL is made of a Microporous Layer (MPL) and a Gas Diffusion Backing (GDB). GDL allows the reactants to reach the catalyst layer near the membrane with mixed vapor water. The hydrophobicity of the MPL prevents flooding of the electrode by liquid water coming from the channels or the GDB. The degradation of this component leads to an increase in electrical resistivity and decrease the protection against liquid water [27].

1.3.2.3. Electrodes

The nanoparticle of platinum, the carbon black as the support of these nanoparticles, and ionomer form the porous electrodes. This component of the FC allows the reactants to reach platinum and protons and electrons to transport. According to three parts of the electrodes, four main degradation phenomena can be considered: carbon support oxidation, catalyst dissolution, ionomer attack, and degradation of the topology constituted by the assembly of these three ingredients (loss of porosity). These degradations lead to a decrease in the active area. Platinum dissolution in ionomer, platinum agglomeration, oxide formation on the carbon surface, reactive species generation causing the membrane degradation, and adsorption of contaminants

are the main of these phenomena. The dissolution, oxidation, and agglomeration of platinum mainly concern the cathode for standard operating conditions [27].

1.3.2.4. Membrane

The ionic hydrophilic portions allow the protons to transport through it. The membranes are ionomers such as Nafion. The ionic conductivity of the membrane is increased until a limit due to the increase of the membrane humidity. The membrane allows the protons to pass through it and separate the fuel and oxygen. The lifetime of PEMFC strongly depends on the lifetime of its membrane. The degradation of the membrane is generally of thermal or chemical origin but is accelerated by the mechanical constraints. The chemical degradation refers to the decomposition of the membrane due to the attack of radical species on the membrane. The mechanical degradation refers to the membrane fracture caused by mechanical constraints due to clamping pressure and moisture cycling. The short-circuiting is an electrical current that directly passes through the membrane due to over-compression of the cell [27].

1.3.3. Degradation and snowball effects

As shown in Figure 1-2, the cells inside a stack are connected in series while the reactants and cooling fluid are fed in parallel. Therefore, the same load current passes through the cells. Two basic types of instability may occur (drying and flooding instabilities).

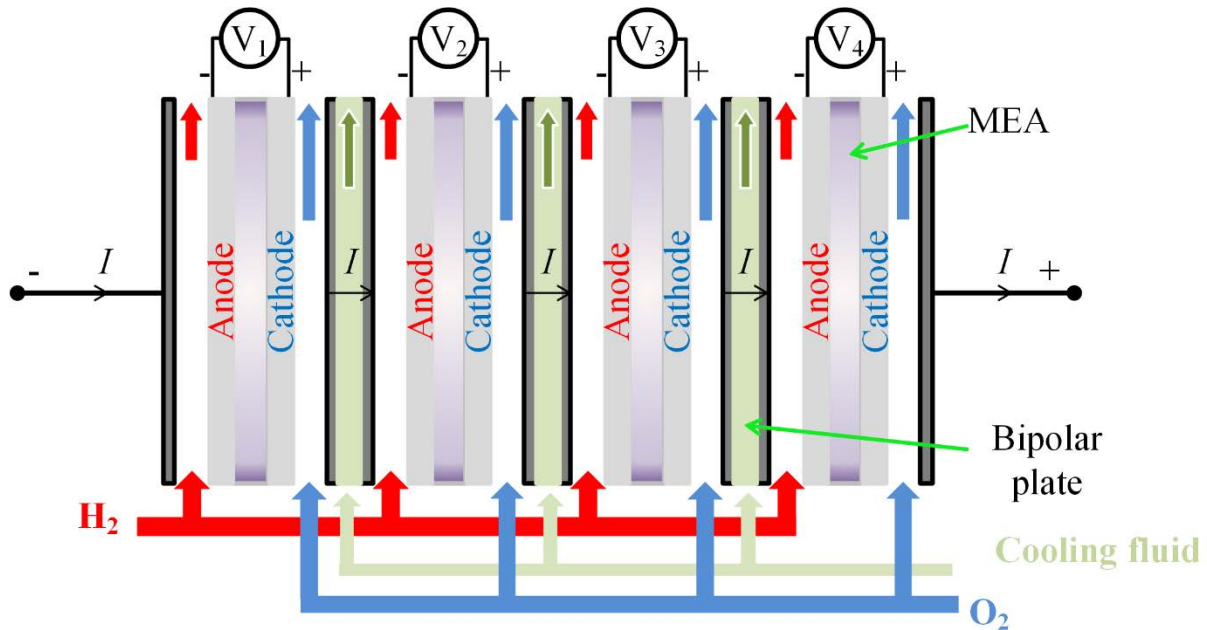


Figure 1-2. Serial connection of cells inside a stack.

1.3.3.1. Drying instability

Due to the manufacturing process of a stack, some heterogeneities are expected over the lifetime of the stack. Heterogeneity in the flow of cooling fluid is one of these heterogeneities that can have an irreversible impact on the membrane. For instance, if one of the cells cannot be cooled down due to the heterogeneity of the cooling fluid between the cells, its temperature starts to increase. As a result, its membrane begins to dry out and it will be more resistive. If the current of this cell cannot be changed, the voltage of this cell drops, and more heat is dissipated by this cell. More heat generation means an increase in cell temperature. This increase in temperature makes the membrane even dryer and thus more resistive. This

phenomenon like a snowball effect can continue until the membrane is completely dried. Once the membrane is completely dried, it can lead to membrane rupture. Due to the lack of uniformity in construction conditions of cells inside a stack and the manufacturing process of a stack, the degradation level of cells inside a stack is not the same. This heterogeneity between the degradation level of cells leads to the under potentials of some cells. If the current of these cells cannot be changed, more heat is generated by more degraded cells. A snowball effect as same as mentioned for the heterogeneity in the flow of cooling fluid can occur in this case. As seen in Figure 1-3, another heterogeneity, which is considered due to the lack of uniformity in construction conditions, is the heterogeneity between the distributions of gas flows. Once the flow of one of the gases or both of them in one cell is higher than other cells, more water is evacuated in the form of vapor. As a result, the amount of liquid water is decreased. The lower amount of liquid water in the channels leads to an increase in the flow of the gas in the corresponding channel. This is another snowball effect. Notable that the increase in the flow of gases can also make the membrane dryer. This consequence is a connection between this snowball effect and the previously mentioned one. These snowball effects are shown in Figure 1-4 to prepare a better view.

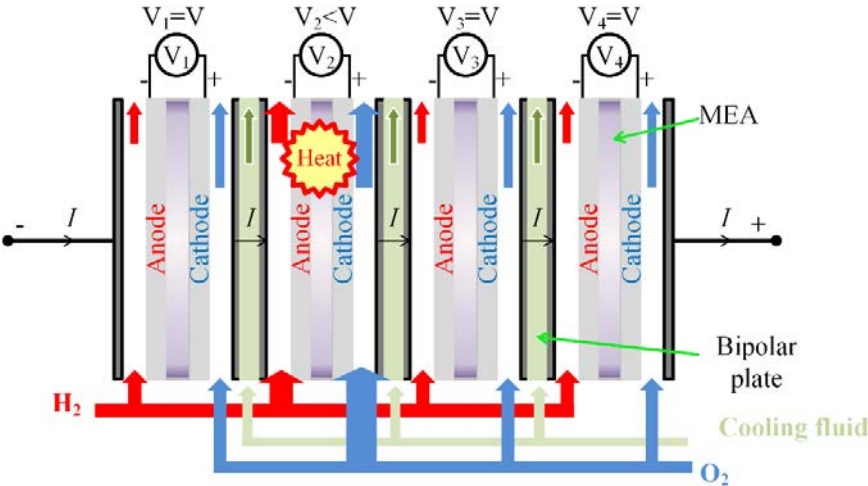


Figure 1-3. Heterogeneity between the distributions of gas flows.

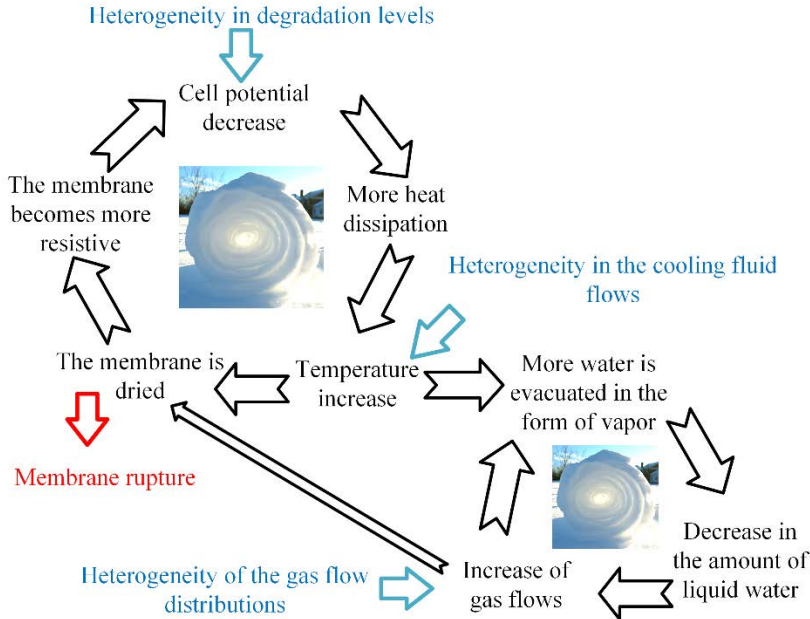


Figure 1-4. Drying instability and its consequence snowball effects.

1.3.3.2. Flooding instability

The heterogeneity between the distributions of gas flows especially at the anode side channel can have another consequence. As seen in Figure 1-5, if more droplets of water appear in the anode side channel of a particular cell, the corresponding hydrogen flow rate becomes slower, and less water vapor is consequently evacuated, leading to the more liquid water production. More water in liquid form inside the channel makes the flow of gas lower. This snowball effect is demonstrated in Figure 1-6. As seen in this figure, another way to initiate this loop is the heterogeneity in the cooling fluid flows. For instance, if the anode side channel of a cell cools down more than other channels, the equilibrium vapor pressure of water is reduced and as a result, the water droplets can be formed in the channel that makes the flow of gas lower. The presence of water in the liquid form on the anode side can have destructive and irreversible effects. The fuel starvation and electrode degradation are the most destructive consequences of the flooding.

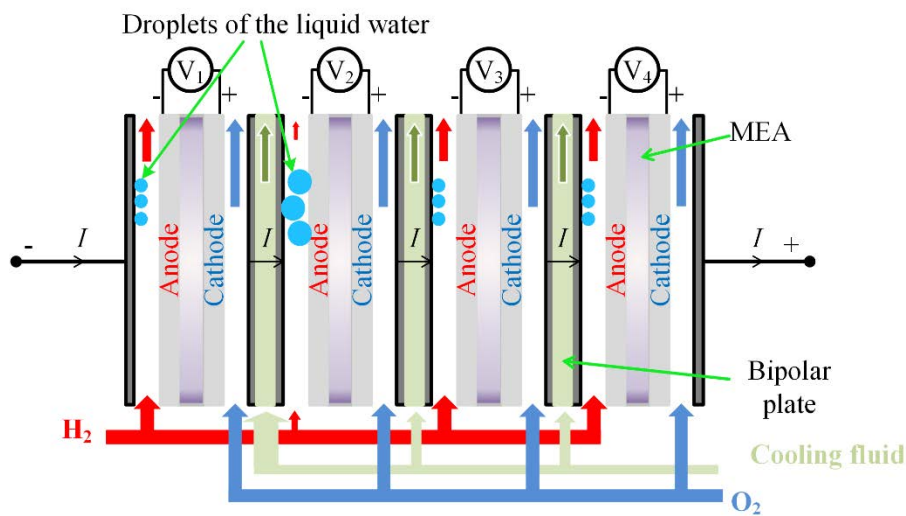


Figure 1-5. Heterogeneity of the hydrogen gas flow and/or heterogeneity of the cooling fluid at anode side channel.

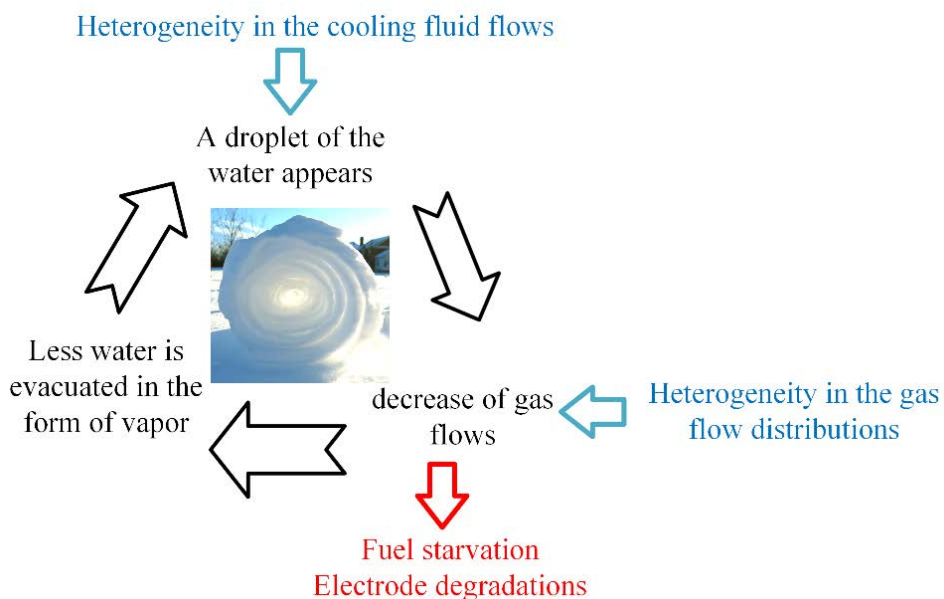


Figure 1-6. Flooding instability and its consequence snowball effect.

1.3.3.3. Propagation of cell degradation

The cells inside a stack are thermally coupled. Therefore, the over-temperature of one cell can influence the adjacent cells. This coupling is schematically depicted in Figure 1-7. As seen in this figure, the second cell has a problem and its temperature has increased. Because of coupling, the anode temperature of the third cell and the cathode temperature of the first cell increase. Thus, a temperature gradient between the anode and cathode appears for the first and third cells. Under this condition, as the produced water is evacuated at the colder side, water droplets are produced where the temperature is lower [20], [28]. Therefore, the water droplets appear on the anode side of the previous cell (the first cell) and the cathode side of the next cell (the third cell). In this condition, the hydrogen starvation and the Oxygen starvation are quietly possible for the previous cell and the next cell respectively. Once the temperature of the adjacent cell has increased because of gas starvation, these cells themselves can propagate this problem to their adjacent cells. Hence, a faulty cell can influence the whole stack and an FC management system can deal with such faults and in the worst condition, electrically separate the faulty cells.

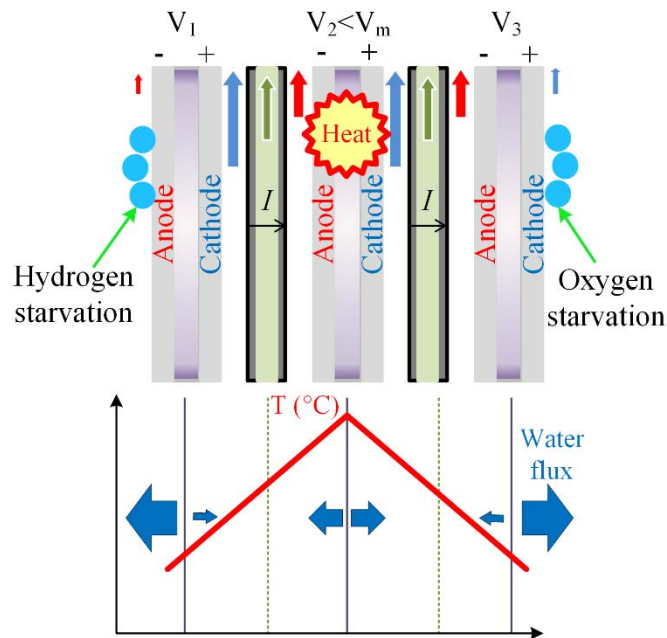


Figure 1-7. Propagation of the instability.

To validate this mechanism qualitatively, an experiment is performed on a single cell by imposing a temperature gradient between the anode and cathode. In this experiment, the gas pressures are applied using a pressure controller, not the flow rates. Figure 1-8 shows the experimental time evolution of the flow rates of hydrogen at the anode and air at the cathode as a function of the temperature gradient direction. The electrical performance of the cell is stable when the temperature of the anode and cathode plates are identical (blue lines). The average stoichiometry of hydrogen and air is 1.5 and 2.2 respectively.

It should be noted that the temperature gradient with a colder anode could cause a fuel starvation phenomenon in this case. The hydrogen flow rate can become equal to the flow rate consumed by the reaction when the anode is colder (red lines). As a result, a voltage drop in the cell potential appears and local fuel starvation near the anode output can occur. This temperature gradient leads to a decrease in the saturation level in the cathode channel. As a result, the air stoichiometry is increased. Regardless of the local fuel starvation, this higher value of air stoichiometry means an improvement in electrical performance due to higher oxygen concentration. Three singularities are observed on the air stoichiometry. The air

stoichiometry significantly decreases when the cell potential is dropped to 0V during the fuel starvation period. This can be explained by the massive flow of hydrogen through the cathode compartment with very low potential ($V < 0.12V \rightarrow$ reduction of protons to hydrogen/hydrogen evolution). This hydrogen reacts directly with the oxygen and causes a sudden production of water which increases the saturation on the cathode side.

Hydrogen stoichiometry increases strongly up to 2.2 (compared to 1.5 without a temperature gradient) when the temperature gradient is reversed (yellow lines). Air stoichiometry becomes very irregular and there are some minor instabilities on the cell potential, but nothing critical.

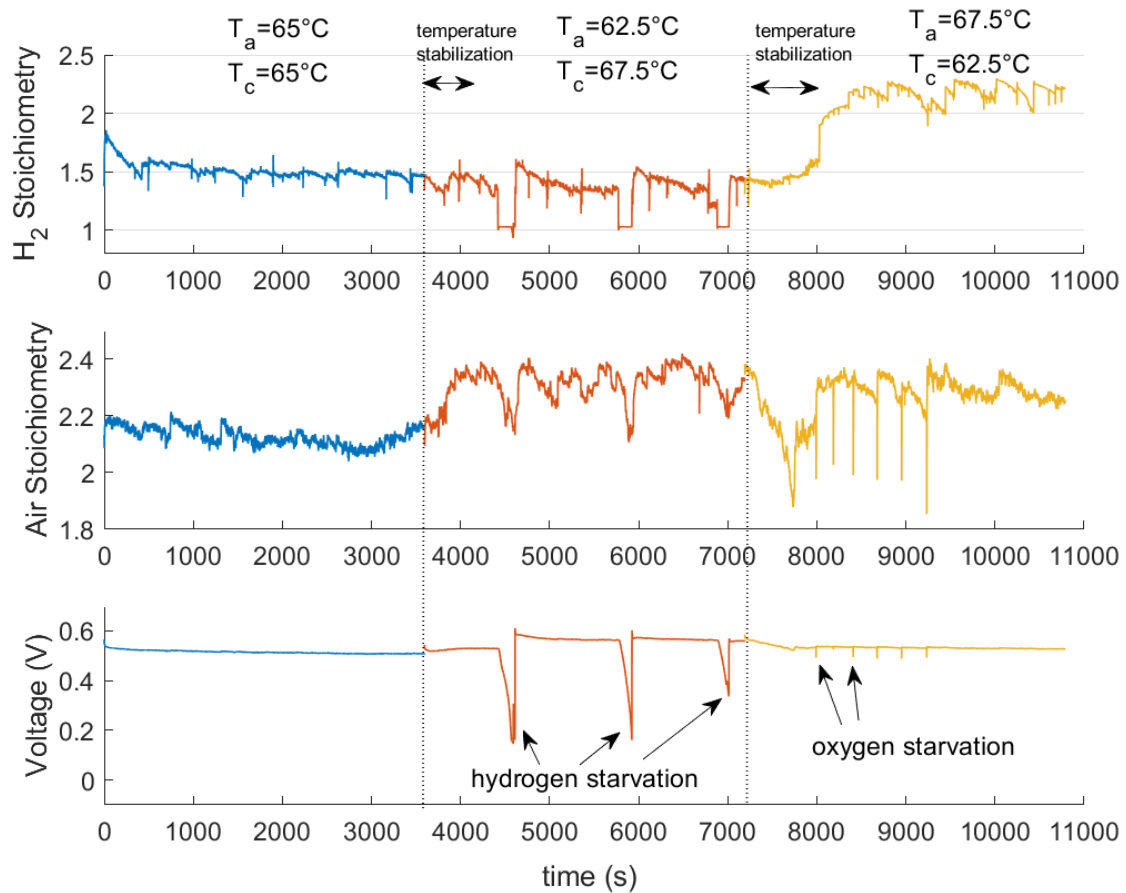


Figure 1-8. Stoichiometry evolution of hydrogen and air as a function of the temperature gradient for boundary conditions of the imposed pressure drop. $\Delta P_{anode}=12\text{mbar}$. $\Delta P_{cathode}=47\text{mbar}$. $I=0.5\text{A}/\text{cm}^2$. $T_{dp}(\text{anode})=50^\circ\text{C}$. $T_{dp}(\text{cathode})=50^\circ\text{C}$.

This experiment illustrates the effect of thermal coupling between cells in a stack and the importance of gas flow variations when the boundary condition of the pressure drop is imposed.

1.4. Durability study

The durability of FCs can be studied through a diagnostic tool. In particular, the drying and flooding faults can be detected by an analytic model or expert knowledge through fuzzy-logic, neural network, etc. [3]. There are two basic diagnosis methods of PEMFC: Model-based and Non-model based. As seen in Figure 1-9, the non-model based methods are divided into three groups: knowledge-based methods, signal-based methods, and hybrid methods. The knowledge-based methods can be divided into two groups: Artificial Intelligence methods and statistical methods [29].

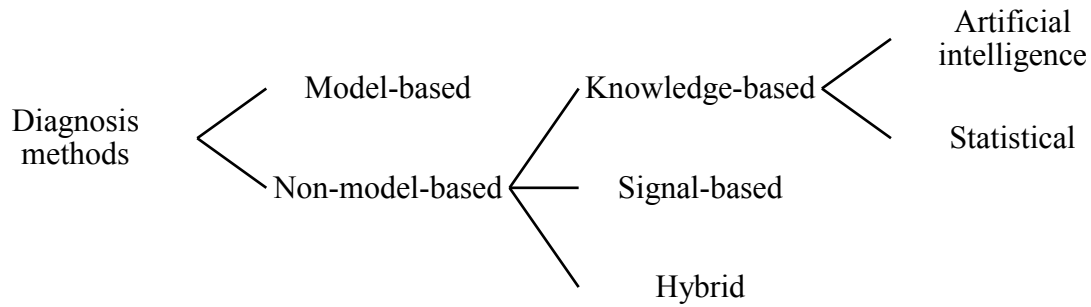


Figure 1-9. PEMFC diagnosis methods.

1.4.1. Non-model based methods

The Artificial Intelligence (AI) methods are using as the pattern recognition tools. The ability to handle noisy data is one of the most important advantages of these methods. Neural network (NN), Fuzzy Logic Control (FLC), and Neuro-fuzzy methods belong to the AI methods. In [30], the NN was used to investigate the FC state of health without providing any information about the fault type. The bigger network and more complex one must be designed to detect the faults when the number of the faults and measured variables are increased by this method. As a result, the learning procedure can be more difficult in this case.

The non-model based FLC method attempts to allocate the data points to a certain number of groups or clusters. In other words, this method works as pattern recognition. Based on these clusters, the operational conditions of the FC can be detected. This method consumes a lower time to detect the problem and it can be utilized as a real-time diagnostic tool. In [31], the evolution of the two parameters was used to develop a diagnostic tool. These parameters are the difference between the polarization and the high-frequency resistances, and the maximum absolute phase value of the Nyquist plot. Then, the fuzzy k-means algorithm was used to identify three clusters in this two-dimensional space. The clusters that were named as young, middle-aged, and old correspond to the degradation level of the FC. The dimension of the space should be increased for identifying two or more than two faults. As a result, this method is more complex for detecting more than two faults.

The adaptive neuro-fuzzy system (ANFIS) is one of the most popular methods in which the parameters of the fuzzy system are adjusted by an NN. The ANFIS has been further applied to the model-based methods [32]. The robustness and reliability of this method in real-time is the strong point of using it as a diagnostic method [29].

The statistical methods are indeed the dimension reduction methods. If the number of measured variables of the system are expressed as the dimension of the system, the more discriminating features of the system can be obtained by reducing the dimension of the system due to the correlation between the variables. Principal Component Analysis (PCA), Fisher Discriminant Analysis (FDA), and Bayesian network are the most used methods of dimension-reduction.

The correlated variables are converted to uncorrelated variables by the PCA method. In [33], seventeen different parameters of the system were analyzed by PCA to detect the faults. Four principal components were obtained by the PCA method. This method can detect a single fault at a time. Multi-PCA models can be used to detect multiple faults by separately training the variables under each fault condition. This method considers a linear correlation between variables. Therefore, the performance of this method is not good for nonlinear systems such as FCs even though it can handle the high-dimensional, highly correlated, and noisy data.

The FDA method attempts to maximize the variance between the classes while minimizing the variance within each class by determining a set of discriminant vectors. It is essential to provide the data of different operational conditions of the system and define the classes to use the FDA. This method is also linear and it provides a poor performance for the nonlinear systems. To deal with this problem some improved methods have been developed. Among the improved methods, the Kernel function based ones have shown better performance in diagnostic. However, these methods can increase the computational time compared to the linear ones [29].

In [34], the faults in air fan, cooling system, hydrogen pressure, and growth in the fuel crossover were detected by a Bayesian Network (BN) method. The BN is a probabilistic graphical model that represents a group of the system variables and their conditional dependencies by a direct acyclic graph. The BN can predict the likelihood of a cause as the contributing factor between several possible known causes. However, a large database consists of different operational conditions of the system is vital to construct the BN [29].

The signals, which are obtained from the FC, contain oscillations. Some of these oscillations provide information about the system faults. Signal processing as a tool for extracting the information from the signal can be used as a diagnostic method. In [35], the pressure drop was analyzed by Fast Fourier Transform (FFT). It was shown that there is a relation between the dominant frequency of the pressure drop inside the channels and the water transfer. However, this method suitable for stationary signals due to its constant time and frequency resolution. Therefore, the other methods capable of analyzing transitory signals were developed for the systems with transient processes such as FC.

Short-Time Fourier Transform (STFT) is a method of analyzing the signals over an interval of time. This method uses a time window to perform FFT. The basic drawback of this method is that its time window is not variant. Therefore, there is always a trade-off between the time and frequency resolutions. The Wavelet Transform (WT) is a method of analyzing the transitory signals which mitigate the trade-off between the time and frequency resolutions. Indeed, this method uses a size adjustable window. In other words, the time window becomes shorter for high frequency and vice-versa. In [36], this method was used on the stack voltage signal to detect the flooding condition of the stack. The flooding condition was detected but it was not localized. The proposed method in [36] is not adapted to a real-time diagnosis. In [37], the WT of the stack voltage signal was combined with a feature reduction method to obviate the problem of real-time diagnosis of the stack flooding condition.

Since the different non-model based methods have different advantages and disadvantages, the hybrid approaches can be used to satisfy all the diagnosis requirements of a complex system like an FC. At a glance, the basic features related to the faults can be obtained from the data by a feature extraction method such as WT, FFT, and STFT. The obtained features maybe are highly correlated. Therefore, a feature reduction method like PCA and FDA can be used to convert a high-dimensional feature space to a lower-dimensional space. Eventually, the faults can be classified by an AI method [29]. In [38], the PCA was used to reduce the correlation between the sensor measures. Then, the WT coefficients were reduced by the PCA method. Finally, a binary decision diagram was used to classify the faults. The non-model based methods demand a database of different operational conditions to be trained. Therefore, these methods are time-consuming and they can cause irreversible damages to the faulty systems during the training time[29].

1.4.2. Model-based methods

Many phenomena occur in an FC but because of their correlations, it is difficult to describe the experimental observation. As a result, the process of aging should be expressed quantitatively by an FC mathematical model. Due to a direct link between physical models and the FC phenomena, the development of such models can be very useful for developing a management system [17]. A model-based method considers the real physical aging phenomena based on the empirical or physical model. A model-based method can predict aging. Also, this method can provide degradation information about the internal physical parameters during the operation [39].

Regarding the operation of a regular PEMFC at low temperatures, diphasic water flow is inevitable in this device [40]. Liquid water droplets can clog the channels and leads to gas starvation [40]. High-temperature PEMFCs have a simpler water transfer due to their operating temperature (140-180°C) but the cost of the membrane, durability, and performance degradation are barriers in the widespread use of them [41]. Therefore, diphasic flow modeling for a regular PEMFC is indispensable. A model that takes into account the diphasic flow can be used to develop a management system.

In a regular PEMFC, high operation temperature (and a limited pressure) leads to lower water absorption of the membrane, and low operation temperature limits the reaction kinetics and ionic transport in the membrane [42]. Therefore, a strong coupling exists between the electrochemical reactions with the heat, charge, and mass transfer in a PEMFC [40]. Therefore, a model should be able to couple electrochemical, thermal, and mass transfer aspects for an accurate and comprehensive simulation [42], [43]. On the other hand, to develop and optimize the real-time control strategy, a dynamical model is necessary to evaluate the transient behavior of the fuel cell and its dynamic response [44]. A mathematical model can provide the perception of the interconnection between electrochemical parameters and different transfer mechanisms. Besides, a model allows establishing control rules leading to increased lifetime. A model, which considers all transfer phenomena and can be simulated in real-time, does not exist in the articles yet [17].

The models developed for fuel cells can be categorized in different ways: The formulation or method (empirical, semi-empirical, and analytical-mechanistic), dimension (zero, one, two, and three), and state of the model (dynamic and static). There is another way to categorize the fuel cell models that are based on their aims to emulate a single cell or a stack. The most complex methods that can model a fuel cell in detail are the analytical-mechanistic models which are also called white-box models. Some of the complex equations of the white-box models are replaced by empirical equations or mapping tables in the Semi-empirical methods. These types of methods that are also called grey-box models are obtained based on the white-box models with some simplifications. The models which used only the empirical equations are called black-box models [43], [45].

The analytical-mechanistic models can simulate the phenomena of a fuel cell in detail at the macroscopic or microscopic levels. Due to the accuracy and complexity of these models that comprise a high computational cost, they are mostly used for component design. Furthermore, these models are used to simulate a single cell or a small stack due to their high computational cost. The semi-empirical or empirical models are a systemic approach in which some or all of the phenomena are formulated by empirical expressions. These types of models are generally developed for a stack and used to develop control strategies [43].

The computational domain should be defined in a fuel cell model. A single set of equations was used for each region of a fuel cell in single-domain models. Due to the complexity of the

fuel cell modeling, multi-domain models were developed in which different sets of equations are used in each region (domain) of the fuel cell. The dimension of the model depends on its developing purpose. The higher dimensional models require a higher computation and as a result, zero-dimensional models are often used for real-time simulations [43].

The law of Fick has been used to model the mass transfer in the white-box model. The Nernst-Planck and Butler-Volmer equations have been used to model the ionic or electric charge transfer. Computational Fluid Dynamic (CFD) programs can simulate these equations in a multidimensional domain. Different steps should be accomplished in this type of simulation. The geometry of the system is defined by Computer-Aided Design (CAD) in the pre-processing step. The domain of each region or element is also determined in this step. The next step is the meshing step in which each domain is divided into subdomains. Indeed, a primitive geometry such as the pyramid, tetrahedral, prisms, and hexahedrons forms a mesh. The equations that must be solved in each domain are defined in the third step. These equations can permit to simulate the mass, heat, and charge transfer. At this step, the boundary conditions and initial conditions are defined to solve these equations [43]. Numerical simulations like CFD (computational fluid dynamic) cannot be used for real-time applications due to their high computational cost which leads to lower accuracy in real-time applications [46], [47].

The grey-box models are based on the white-box models but some of the physical phenomena are formulated by empirical equations to simplify the model. The black-box models are developed based on real experimentation on the system that is modeled [43]. The grey-box models can be also divided into three categories: parameter identification based, observer-based, and parity space methods. In a parameter identification method, the parameters of the model are identified online and these parameters can be used for fault detection. An efficient technique based on the parameter identification method is based on electrochemical impedance spectroscopy. The response of an FC to a sinusoidal perturbation is used to calculate the impedance of the FC. The impedance spectra show the dynamic behavior of FC [45].

A model runs in parallel with the real system in the observer-based method. An observer can estimate the system state variables. Then, the estimated state variables are used to calculate the system outputs. In this method, the measured values of system outputs are compared with the model outputs to generate the residuals. The systems errors can be detected by analyzing these residuals. The main problem of this method is the delay in on-line application due to the calculation time. The parity space method utilizes the parity relations based on a state-space model of the system to simplify the computation. Indeed, the residual elements (the difference between the system outputs and model outputs) of the system form a space which is called parity space or parity vectors. The parity space method utilizes parity relations based on the state-space model to simplify the computation [45]. The parity space is also called residual space. The relations or equations that generate the residuals (parity vectors) are called parity relation or parity equations. The faults of the system can be detected by analyzing the elements of this space.

The black-box models are based on system inputs and outputs. These models require many experimental data. These data are used for training procedures and model validation. The different methods were used in literature such as neural networks, FLC, and support vector machines. This type of model shows a lack of genericity and is still for off-line applications [45].

In [44], a dynamical model is proposed for the fuel cell stack in which the cells inside it were considered identical. The mass, charge, and heat transfer were modeled by the control volume approach for three parts: anode, cathode, and MEA. The mass and heat conservation equations were used in each part to model the mass and heat transfer. Finally, the Nernst equation with

an empirical model of the activation loss was used to model the output voltage. The proposed model was experimentally validated. The relative humidity of the inlet gases was not modeled. The electro-osmotic coefficient was proposed that linearly changes by the membrane water content.

In [48], a dynamical model was proposed that was formulated based on the finite volume method. Three control volumes were defined where the cathode and anode channels were considered as a lumped volume from their inlets to outlets. The momentum and energy conservation equations were developed for each part. The conventional Nernst equation was used to simulate the cell voltage but some empirical equations were used to formulate the activation loss, cathode over-voltage, and the ohmic losses. Finally, the double layer effect formulation was used to develop a dynamic model. The model was implemented in Simulink Matlab and validated by some experimental results.

In [49], a zero-dimensional model was combined with the Petri Net method to analyze the degradation in a PEMFC. This model used to predict the PEMFC reliability by modeling the stochastic and deterministic behavior. In [46], an empirical model was proposed to detect liquid water accumulation in different parts of a fuel cell. A zero-dimensional semi-empirical dynamical model was proposed in [50] to develop a sliding mode controller to control the compressor airflow, fuel cell body temperature, and output voltage by manipulating the compressor motor voltage, cooling water flow, and the anode source pressure respectively. This model simulates the stack and has no information about the cells. In [51], a zero-dimensional semi-empirical method was developed to develop a reduced-order sliding mode observer-based controller. The stack voltage and temperature were controlled by manipulating the gas flows. This model was developed for a stack and has no information about the cells. A three dimensional two-fluid non-isothermal transient model was developed in [52] to investigate the water removal during purging of a PEMFC. The Ansys Fluent was used to obtain the simulations and as a result, this model cannot be used for real-time purposes. Using the two-phase water flow, a lumped parameter zero-dimensional scalable transient model was developed in [53]. The model was able to simulate the distribution of the current density, temperature, pressure, and two-phase water flow in a segmented cell.

Fowler *et al.* [54] proposed a model based on the generalized steady-state model that has some parameters to detect the cell voltage degradation. This model is isothermal and does not consider the impact of contamination, thermal shocking and hydration cycling situations as well as the coupled effects of these factors [17]. Furthermore, this model does not consider the dynamic behavior of the cell. Zhou *et al.* [39] proposed a prediction approach for analyzing the PEMFC performance degradation based on a multi-physical aging model with a particle filter approach. Different coefficients were used in this model to describe different physical aging phenomena over time. The initial values of these coefficients were obtained by fitting the polarization curve at the beginning of life. Different physical aging phenomena including membrane conductivity losses, reduction of reactants mass transfer, and reaction activity losses were considered in this model. Laffly *et al.* [13] proposed a model which can predict the dynamic and static behavior of a PEMFC. This model uses the PEMFC static and dynamic models to predict its voltage. Due to the direct link between the model parameters with the physical phenomena, this model can investigate and study the FC aging. Indeed, a variation of the model parameter may show the aging of the PEMFC. In this paper, the FC output voltage was determined as a function of the current and time of aging. This model considers the static and dynamic behavior of the FC but is valid just for a small variation of the current. This model does not provide an accurate estimation of aging. Bressel *et al.* [55], [56] proposed an observer-based method for analyzing the degradation and predicting the FC state of health. This method can predict the degradation in diverse operating conditions. An empirical equation was used in

this study. Finally, the Kalman filter approach was used to predict the state of health, stack voltage, and degradation. This model cannot provide data about the physical phenomena that occur in the FC.

Tian *et al.* [57], [58] proposed a method to identify the failed cells. The open-circuit voltage of the cells inside a stack was measured when gas flows were suddenly stopped after 10 s supplying of hydrogen and oxygen. The quick decrease of open-circuit voltage can reveal the failed cells. This quick decrease may be because of rapid fuel consumption or gas crossover from the membrane. Narjiss *et al.* [59] proposed a method to determine the FC state of health based on the impedance spectroscopy. Low sinusoidal current signals were injected at different frequencies by controlling a full-bridge converter. The main problems, in this case, were the effect of signal injection on the stability of DC link voltage and the high ripple of extracted signals. In this study, the impact of some problems on the impedance spectroscopy was investigated. For example, a decrease in the amount of gas flow was associated with an increase in impedance. Join *et al.* [60] proposed a method to predict the output power of a stack using the static model of the PEMFC and particle filter approach. This model considers only the phenomena with time constants equal to or greater than the hour. Join *et al.* [27] completed their previous work about the model. In this study, a sensitivity analysis was provided for different parameters of the model. In [60], after obtaining parameters with curve fitting (P-t curves), the Kalman filter approach was used to predict the output power. In [27], different data sets were used to validate the model. The sensitivity analysis was performed by using the GSAT toolbox of Matlab software. Finally, the ability of the model to follow mission profiles with fast current variation was evaluated. In this case, the model could estimate an automotive profile.

In many papers, an equivalent circuit was proposed to analyze the Electrical Impedance Spectroscopy (EIS) results to detect the cell faults. The impedance of the proposed equivalent circuit is fitted on the EIS results to obtain the proposed equivalent circuit parameters. The cell faults can be detected based on the evolution of these parameters. The proposed equivalent circuit affects the fault detection power of this method [61]. The water flooding has a direct impact on the Warburg impedance in such equivalent circuits [62]. The link between the impedance of the membrane and water transfer was investigated in [63] based on EIS and an equivalent circuit. In [64], the mass transfer was modeled by adding a circuit branch to the conventional circuit. The additional circuit consists of a resistor, a capacitor, and an inductor. To identify all parameters of the proposed circuit by the EIS method, a wide frequency range must be evaluated. This wide frequency investigation takes time. As a result, other methods were proposed in the literature that utilize the impedance of certain frequencies. These methods use a part of EIS. It was revealed that the flooding and drying conditions influence Low-Frequency Resistance (LFR) and High-Frequency Resistance (HFR) respectively [65], [66]. The drying condition leads to an increase in the impedance magnitude and phase angle at all frequencies. However, the flooding condition leads to a decrease in the impedance phase angle and an increase in its magnitude at low frequencies. The HFR can be used as a reliable indicator of the drying condition [47], [67]. The phase angle of the HFR is close to zero. As a result, it is important to find an ideal value for the frequency. This ideal frequency can be changed over the lifespan of the FC. The evolution of the HFR for a single frequency is not able to detect the water flooding [47], [68]. In [61], the HFR with variable frequency was used to detect the flooding and drying conditions. The LFR was used to distinguish the flooding condition from the drying condition.

Due to the lack of a dynamical model that can simulate a stack by giving information about the cells inside it and can be simulated in real-time in literature, a 1-D lumped dynamical model is proposed in this thesis.

1.4.3. Durability enhancement tool

Lack of direct links between phenomena and FC model parameters and not taking into account all phenomena that occur in an FC are the basic problems of these methods. In this thesis, an electrochemical model is proposed. This model can consider almost all the phenomena and dynamic behavior of the FC. Besides, many parameters have a direct link with those phenomena. This model must run at the same time as the real system. Therefore, this model should be simple and should have a small time constant. Based on these reasons, a one-dimensional transient model is proposed in this thesis. Heat, mass, and charge transfers are coupled in this model. This model is introduced in the second chapter. Based on this model, it is possible to detect the occurred faults in the cells of one stack. However, a topology is required to manage the cells and supply the load. This topology must allow the cells inside a stack to be managed separately.

Multi-stack can be considered as an attempt to increase the lifetime of the fuel cell system at the cost of compactness loss. As seen in Figure 1-10, four basic topologies are used for the multi-stack or segmented FCs: series, parallel, cascade, series-parallel [3], [69], [70]. The series topology requires a low voltage ratio converter. In such a connection, the failure of a single cell means losing the whole system. Furthermore, there is no freedom degree in controlling the cells separately. The second topology, which the cells or stacks separately connect to the dc link by individual converters, provides the freedom degree in controlling the cells [71]. However, the high conversion ratio converters, which are required to increase the output voltage, provide higher stress on the semiconductor devices. This architecture is the most expensive topology due to a great requirement of the passive energy storage components. The cascade topology resolves the problem of the parallel topology. In this topology, the DC-link voltage is divided between the cells. This leads to lower stress on semiconductor devices. The series-parallel topology is as same as the parallel topology except that more cells connect to each converter. This topology inherits the advantages and disadvantages of series and parallel topologies. In such a topology, the converters with a lower voltage ratio can be used. Considering the ability of separately controlling the cells or stacks, the cascade topology can be used to manage the cells. However, connecting the cells to the high voltage DC-link while maintaining the controllability of the converters is challenging.

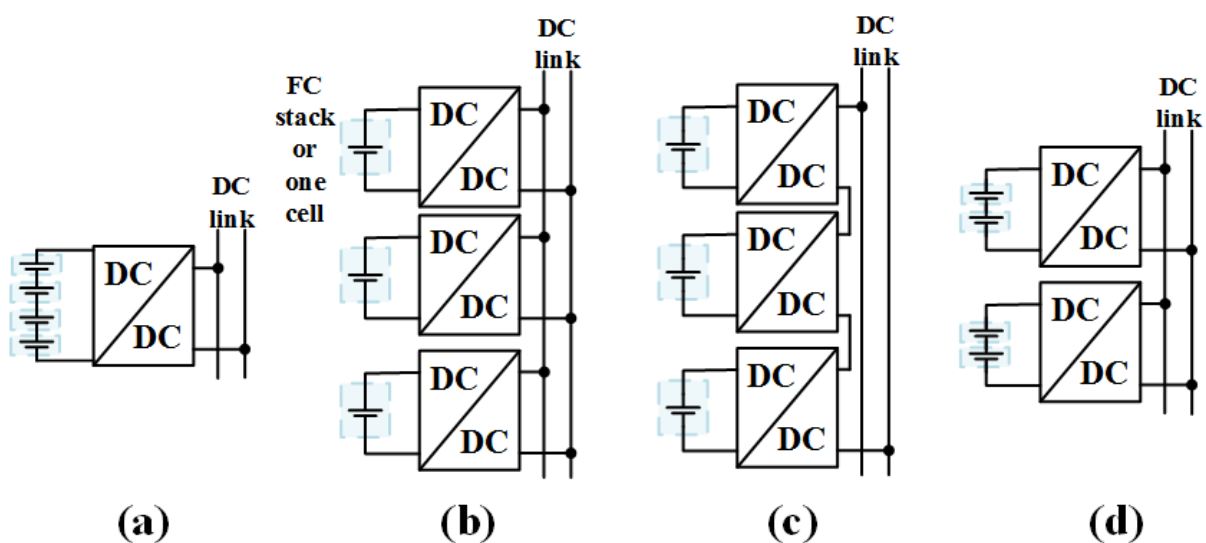


Figure 1-10. Multi stack topologies: a) Series b) Parallel c) Cascade d) Series-parallel.

In this thesis, the operating condition is controlled in such a way that the electrochemical instabilities can be avoided to improve the lifespan of a stack. The proposed model can detect the different instabilities that occur in the cells inside a stack. However, a structure is required to change the operating condition based on the model data. The water production inside a cell can be controlled by its current. Therefore, this structure should be able to change the current of a different group of cells based on the model data. As a result, this structure consists of two basic parts: Power electronics architecture, and Management system. The decisions are made by the management system based on the model data. The power electronics structure executes the decisions made by the management system.

Due to the low voltage of a cell or a small group of cells, the high voltage conversion ratio converter like isolated converters is vital but efficiency is the basic challenge [10]–[12]. In this thesis, the classical step-up DC-DC boost converters are used while their output capacitors are connected in series, inspired by the cascade topology. Multi-leg converters provide reliability along with the current ripple reduction. This solution leads to an increase in the freedom degree in management and control of the PEMFCs. The disadvantage of this serial connection is the probability of the controllability lost. In such a connection, the same load current passes through all of the capacitors. Therefore, if the input power of one cell becomes lower than the required amount, the voltage of the corresponding capacitor will decrease. In this case, the controllability will be lost if the output voltage becomes lower than the input voltage. As mentioned before, the objective is to develop a management system that separately controls the current of cells or stacks. Considering the cascade topology with N groups (Figure 1-11), if the load power (P_{load}) is constant and the DC link voltage is regulated at V_{dc} , then the load current has a constant value of i_{load} in steady-state and as a result, the supplied power by cells can be calculated as $P_k = i_{load}V_{C_k} \forall k \in \{1,2 \dots, N\}$. Assuming that the total supplied power by stacks is equal to the load power and the first group should inject a part (x) of the nominal power (P_{load}/N) whereas the other groups inject an identical value of power, the following equation can be obtained in steady-state as follows:

$$\begin{cases} P_1 = x \frac{P_{load}}{N} = i_{load}V_{C_1} \rightarrow V_{C_1} = \frac{x}{N}V_{dc} \\ P_k = \frac{N-x}{N(N-1)}P_{load} = i_{load}V_{C_k} \rightarrow V_{C_k} = \frac{N-x}{N(N-1)}V_{dc} \end{cases} \quad (1.9)$$

where k in this equation can be $\in \{2,3 \dots, N\}$. The voltage of the first capacitor must be greater than the input voltage of the corresponding converter. Thus, considering the voltage ratio of the boost converter (R_v) and (1), $x > \frac{NV_{FC}}{V_{dc}} > \frac{1}{R_v}$. Therefore, the supplied power of the first group cannot be less than $\frac{1}{R_v N}P_{load}$. Otherwise, the controllability is lost. In such conditions, a voltage equalizer or a balancing system can ensure the controllability.

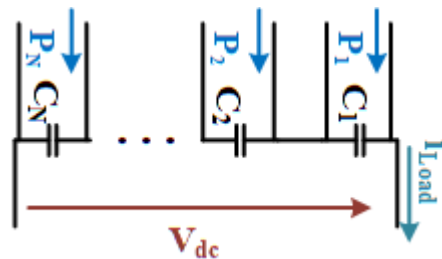


Figure 1-11. Cascade topology with different injected power by cell groups.

The equalizer in the literature can be categorized into two basic groups: with an auxiliary source and without auxiliary source [72]. The equalizers with auxiliary source use another source to compensate for the lower voltage cells. These equalizers are not efficient, especially for embedded applications. As seen in Figure 1-12, the equalizers without auxiliary sources, are categorized into two basic groups: dissipative and non-dissipative equalizers [72]. Dissipative equalizers use resistance to decrease the voltage of the higher voltage cells. These equalizers waste much energy. Therefore, the efficiency is very low. However, the low cost, simple implementation, and small size are their advantages [73], [74]. The non-dissipative equalizers can be divided into three groups: capacitor-based [74]–[80], converter based [72], [81]–[94] and other type equalizers [95], [96]. A control approach is usually adopted for switches of a specific structure to balance the voltages in the third group of equalizers.

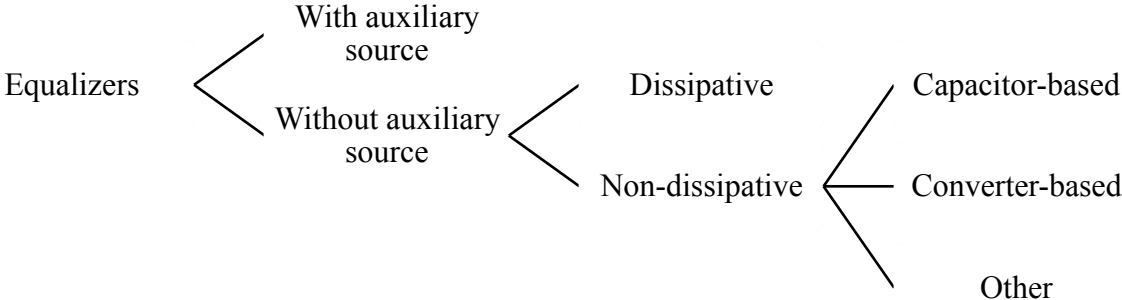


Figure 1-12. Different types of equalizers.

Several capacitors are connected to cells by several switches in the capacitor-based topologies. The cells are periodically connected to these capacitors, and this operation continues to the point where all the cells and capacitors reach the same voltage. These equalizers require numerous amount of switches and they are not cost-effective for a large number of cells or high power applications. Furthermore, these equalizers can balance the voltages through several repeated operations. As a result, they need much time to balance the voltages. The maximum of the balancing current can be controlled by sizing the capacitor capacitances. Therefore, the high efficiency in balancing can be obtained independently of imbalance states [74]–[79]. The capacitors of each level of a multi-level converter were frequently connected to next or previous level capacitors by using the numerous amount of switch in [79]. In this topology, the switches and capacitors in the multi-level converter were used to balance the voltage of capacitors in each level without adding another device. To overcome the problem of balancing time, the resonance phenomenon can be used. Using the resonance in such topologies, the balancing speed can be increased simultaneously with achieving the benefits of soft switching [80].

The converter based equalizer can be categorized into three groups: cell to stack equalizers [72], stack to cell equalizers [81], [87]–[93], stack to stack equalizers[94], and cell to cell equalizers [82]–[86].

A stack to cell equalizer with a flyback converter was used to equalize the voltage of series lithium-Ion batteries in [91]. A stack to stack equalizer was used in this topology to realize the modular approach.

A forward-flyback resonant inverter was used to send energy from the series cell to cells in [81]. A voltage multiplier circuit was connected to cells. This circuit is used two diodes for each cell to automatically select the lower-voltage cells and send energy to them. The required amount of switches was minimized in this topology at a cost of lower efficiency due to the use of two diodes for each cell. In this topology, the number of switches is independent of the number of cells. Similar topology with a buck converter on the primary side of the transformer

was used in [88] for photovoltaic application. The forward-flyback converter in [81] the proposed was divided by a bidirectional converter in [89]. Therefore, the design became more flexible and circuit implementation was simplified. In [92], a half-bridge converter was used on the primary side of a transformer to send energy from the series-connected cell to lower-voltage cells. A multi-stacked current doubler was connected to the secondary side of the transformer in connecting with cells. The number of diodes and inductances must be increased by increasing the number of cells. Since this topology can be implemented with two switches independent of cell number without a multi-winding transformer, the circuit design and implementation can be simplified. In [87], [90] an improved push-pull converter with a clamping capacitor was used to send energy from the series cells to lower-voltage cells. A multi-winding transformer was used in this topology and H-bridge converters were used in the secondary windings of the transformer. This topology needs to measure the voltage to drive the required H-bridge converters. The balancing current can be very high in this topology and as a result, the balancing time can be reduced.

For the battery applications, it is not necessary to have a large balancing current, because the voltage difference among cells slowly increases. Therefore, there is much time to balance the cells with the lower current to decrease the losses [74]. However, in such applications of which the voltage balancing between output capacitors of DC-DC converters is required to ensure the controllability of the converters, the balancing time is the most important parameter. On the other hand, when the difference between cell voltages is very high, using the resonance can be dangerous for power electronic devices due to the high current peak. Regarding the possible inability of a cell or a set of cells in injecting the nominal power in a stack, a large difference between the output capacitor voltages is possible in the FC applications. As a result, a new equalizer is proposed in this thesis. The proposed equalizer can send energy to the lower voltage cells. This topology can quickly reach the steady-state condition by using a small number of switches and ensure the controllability in the worst conditions. The number of controlled switches in some converter-based equalizers depends on the cell numbers [72], [85]–[87], [90], [91], [94]. These equalizers are not effective in terms of cost and volume. In the proposed equalizer, the number of controlled switches is independent of the cell number.

Due to dynamic constraints, the hybridization of a fuel cell with an energy storage system is required to supply a given load, especially for transport or stationary applications [97]–[103]. Different type of this hybridization and their energy management systems were reviewed in [97], [98]. The different types of power electronic converters that are used in this hybridization were reviewed in [104]. Generally, the FC has a slow dynamic due to its auxiliaries. Hence, hybridization with the storage devices can be a good way to satisfy different load profiles. The battery has a high energy density and a higher power density than the FC. Therefore, the FC/Battery hybridization has been used in some papers [100], [105]–[107]. Contrary to the batteries, supercapacitors (SCs) have a high power density and a lower energy density than the batteries. As a result, the FC/SC hybrid system has been widely used in literature due to the ability of the SC in compensating for the slow dynamic of the FC [100], [108], [109]. To benefit from the advantages of both storage systems, the FC/SC/Battery hybridization has been used in some papers [101], [110]–[115]. In terms of energy management, two types of categorization can be considered. The first one is based on fuel consumption management or approaches to achieving the maximum efficiency of the FC [98], [111]. The main objective in [107], [113]–[115] was to develop an energy management strategy to improve fuel consumption. In this thesis, the objective is to develop a management system for PEMFCs in which energy management can be implemented while curing the defective cell groups. The second type of categorization is based on control strategies such as PID, operational modes, FLC, predictive control, etc. [98].

In [108], the difference between the load power and FC power was used to regulate the dc-link voltage. The charging mode of the SC starts when the load power was lower than the 0.98 of FC power. Based on the equations of the different converters, the duty cycles were generated. Since the FC injected power is constant, this method cannot be useful for a dynamic load profile. In [111], a proportional-integral controller was used to determine the FC power based on the difference between the batteries' State of Charge (SOC) and its reference. To determine the power of the battery, a proportional controller was used based on the difference between the SOC of the SC and its reference. The power of SC was obtained based on the difference of demanded power and the sum of two other power. In [105], the power-sharing between the battery and Fc was performed by applying the operations modes. Indeed, power-sharing was performed based on the driving cycle and the amount of power. The low and high amounts of load power are supplied by the battery and FC respectively. Both FC and battery should supply the load for a higher amount of load power or during the transient conditions. In [112], a state machine was used to share power between three sources. A power-sharing rate between the sources was defined for each state. The conditions of switching between the states are based on the SOC of the battery and SC. Energy management based on the state machine was proposed in [106] for a hybrid system consist of multi-stack and a battery bank. The objective of the proposed state machine is that the least number of stacks shall be used and the stacks shall work far from their open-circuit voltage, whereas the depth of discharge of the battery is limited. The SOC range of the battery and comparison between the load power and the sum of the stacks and battery powers specified the switching conditions between the states. In [110] an energy management system based on the FLC method was proposed for a predefined driving cycle. The proposed FLC has two inputs (SOC of the battery and FC injected power) and two outputs (SOC of the SC and the sum of battery and SC power). A genetic algorithm optimizes the membership functions based on the three different driving cycles. This optimization is performed offline due to the large computation. A high-pass filter was used to share the second output of the fuzzy-logic between battery and SC. The probabilistic support vector machine was used in this paper to classify and distinguish these three different driving cycles in real-time. The basic drawback of the FLC is the necessity of a great numerical memory. In [109], two methodologies based on Markov chains and NN were proposed to predict the power demand. The model predictive control was used for energy management in this paper. The proposed model predictive control was formulated as a nonlinear optimization problem that was solved by dynamic programming. The objective of this method was to minimize fuel consumption and to maintain the SOC of the SC based on the predicted load power demand.

The conventional hybridizing FC with SC is used in this thesis to respond to the high dynamic load profile. A bidirectional DC-DC boost converter is used with the SC to stabilize the DC bus voltage. For simplicity, the decoupling method based on a Low-pass filter is used to share energy between the FC and SC.

1.5. Conclusions

An overview of the thesis context was provided in this chapter. The main goal of this thesis is to propose an FC management system to improve its durability. As explained in this chapter, the proposed system consists of three basic parts. The focus of this chapter was on the problem statement and bibliography.

The proposed model is well explained in the second chapter, the power electronics structure is introduced in the third chapter, and the fourth chapter is about the management system. The proposed system considered in this thesis is shown in Figure 1-13.

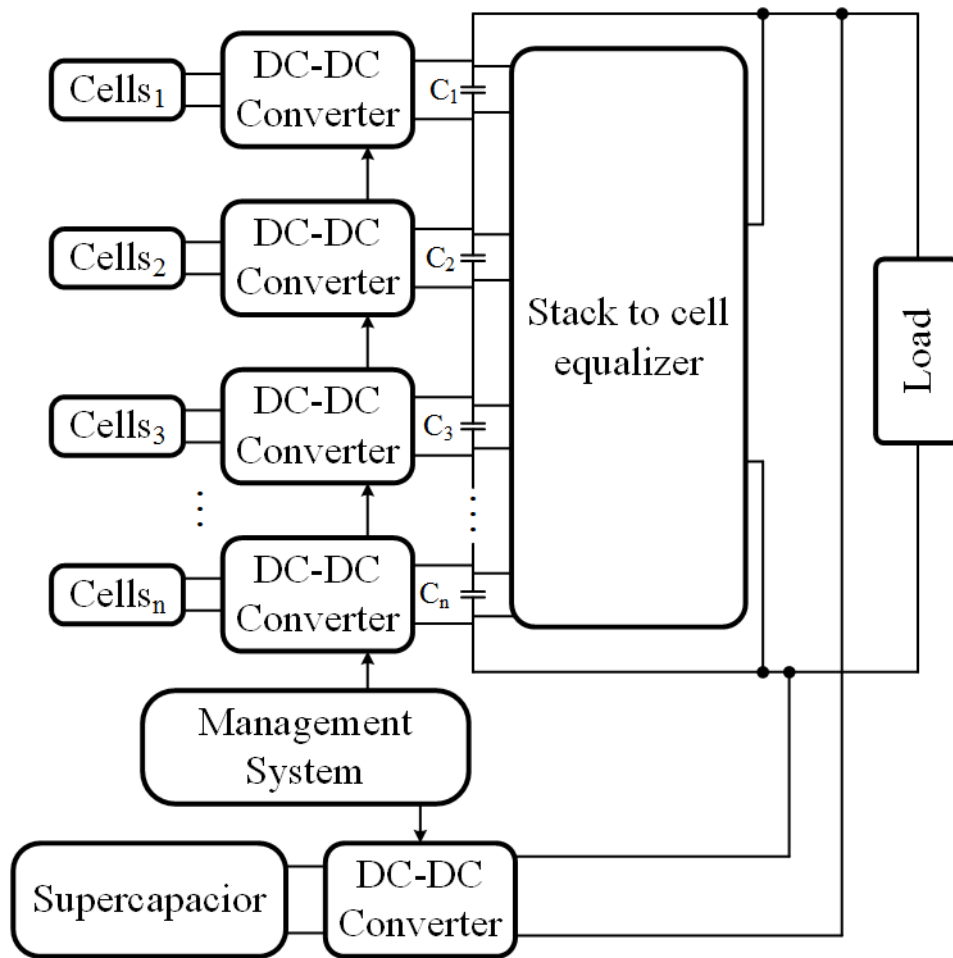


Figure 1-13. Proposed structure to improve the durability of a stack.

Chapter 2

Polymer Electrolyte Membrane Fuel cell: Modeling and Experimental validation

2.1. Introduction

This chapter aims to propose a one-dimensional transient model for PEMFC that can be used to simulate a PEMFC in real-time. Furthermore, the proposed model provides different state variables that can be used to observe the operational conditions of a PEMFC. The basic aim of developing this model is to detect the heterogeneities that occurred for different cells inside a stack. Therefore, this model must simulate one cell inside a stack.

Many attempts have been realized to understand and predict the heterogeneities of operation and degradation of a single cell [21], [22], [116]–[123]. These heterogeneities are mainly due to the variation of reactive gases, water concentrations along the channels, and temperature variations. The maximum current density appears when the best compromise between hydration of the membrane/ionomer and oxygen concentration occurs. For standard operating conditions, the input of the cathode channel is generally too dry ($RH < 100\%$) and its output has a low oxygen concentration. It was verified by a segmented cell that the maximum current density appears in the middle of the cell. Furthermore, local degradations can occur due to moisture cycling of the membrane at the gas inlet or fuel starvation phenomenon. The fuel starvation is a local absence of hydrogen at the anode side due to flooding or the presence of another gas. This phenomenon is responsible for the local degradation of the cathode.

Although operational heterogeneities and degradations between the inlet and outlet of a single cell were studied thanks to segmented cells, heterogeneities between the different cells of a stack have not been well explained and modeled. The origin of this type of heterogeneity can be as follows:

1. Heterogeneity of the used materials. For instance, the Membrane Electrode Assemblies (MEAs) are not all identical, or the manufacturing tolerance of bipolar plates or gaskets is not precise enough. Similarly, the heterogeneity can arise from the errors of the stack assembling.
2. Bad distribution of gas flows between the different cells. This bad distribution can be caused by various reasons. For instance, undersized intake manifolds can create a significant pressure drop between the first and last cells, especially for the U-shaped configuration [124]–[127]. Some cells can be susceptible to the intrusion of the GDL into channels during compression [128]. For low current densities, the unsteady nature of the diphasic flow can be enough to create a bad flow distribution when the pressure drop is low between the input and the output of cells [129], [130]. Finally, the bad

distribution of flows can have a thermal origin as explained in the following paragraph [131].

3. Temperature heterogeneity between the cells. This heterogeneity can come from poor thermal insulation of endplates or it can be the consequence of premature aging of a cell, which will then produce more heat in comparison to other cells. An improperly sized cooling system can also cause temperature heterogeneity. The channels of a colder cell contain more liquid water. Therefore, the colder cells provide higher resistance to gas flows. The lower gas flow rate compared to the other cells leads to less evacuation of the produced water especially in vapor form. This is a snowball phenomenon: The more liquid water exists in the channels, the more liquid water accumulates there.
4. Heterogeneity of degradation. This heterogeneity can appear during the aging of the stack. If a cell degrades prematurely and its electrical performance becomes weaker than other cells, it will dissipate more heat and its temperature will increase. Therefore, less liquid water will be in the supply channels and the gas flow will increase. This may lead to drying conditions that will cause a performance decrease and therefore more heat production. The drying of a cell is the second possible instability.

These two instabilities (flooding and drying) result from the coupling between heat, mass, and charge transfer and can be initiated by the heterogeneity of degradation, gas flow distribution, or temperature. These heterogeneities can appear in a stack for a fundamental reason that each cell in a stack is subjected to the same pressure drop. The cells are not fed by the same gas flow rates. These instabilities can barely appear in a single cell when the gas flow rate is imposed. The flow rate passing through a cell can decrease when it clogs in a stack. Similarly, if the liquid water quantity in a cell decreased compared to the other cells, the flow rate passing through it would increase and this higher flow rate leads to the drying instability.

The boundary condition of the gas flow rates is usually imposed on a single cell in the literature although the pressure drop is identical between the cells inside a stack. The effect of imposed pressure drop boundary condition in a stack compared to the imposed flow rate boundary condition is illustrated in Figure 2-1. In this figure, the oxygen stoichiometry and the pressure drop at the cathode side are plotted as a function of time for the operation of a single-cell. The applied dry air flow rate is depicted in blue in this figure. The results with the applied pressure drop are shown in black.

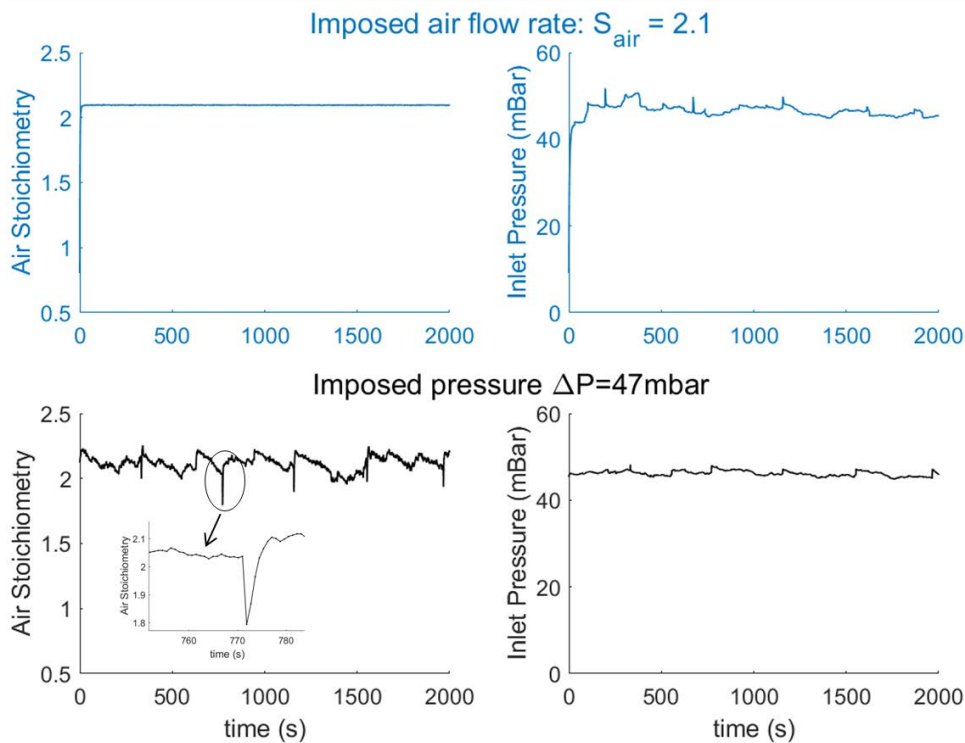


Figure 2-1. Air stoichiometry and pressure drop on the cathode side as a function of time for a single cell as described in [117]. Current density is equal to $0.5\text{A}/\text{cm}^2$, $T=65^\circ\text{C}$. $P_{out}=\text{atmospheric pressure}$.

Notably, the operation of a cell with the applied pressure drop leads to a significant variation of the airflow rate in time. As a result, it can arise electrical instability and /or the fuel starvation when it occurs on the anode side. For a boundary condition of imposed flow rate, the pressure increases to evacuate the droplet when it appears and clogs the channel. For a boundary condition of imposed pressure drop, the behavior is not the same. The dynamic of clogging and unclogging is slower and therefore the operation is less stable. Thus, the operation of a cell inside a stack is always less stable than outside of a stack for a condition of imposed flow rate. **Therefore, the boundary condition of imposed pressure drop must be respected for modeling a cell inside a stack.**

One simple solution to compensate for the improper distribution of the gas flow rate between the different cells is to impose an excess amount of gas (stoichiometry) to provide the minimum flow rate for the cells with minimum flows. However, the gases must be properly humidified to prevent the cells, which have the maximum flows, from drying out. The humidifying of gases is an expensive part of the system and the present trend is to simplify the balance of plant. Another solution to compensate for the improper distribution of the gas flow rate is sizing the channels in such a way that they can create a significant pressure drop. A significant pressure drop facilitates the evacuation of the liquid water and as a result, it decreases the sensitivity of the flow rate through a cell to the present amount of liquid water [132], [133]. The disadvantage of this solution is the higher energy consumption of the air compressor or hydrogen recirculation pump. There is an optimum value of the pressure drops. If the pressure drops are too low, the channels can be blocked with liquid water and if these drops are too high, the cost (CAPEX and OPEX) of the compression system is too high. However, the optimum value of the pressure drop depends on the current density. Therefore, a usual strategy is to increase the stoichiometry for the low current densities to keep a minimum pressure drop.

Figure 2-2 represents the flow rate of evacuated water from the anode side (in blue) and the cathode side (in green) for a single cell whose anode and cathode plates are thermally controlled

independently. In Figure 2-2 (a), the temperature of the plates is the same and in Figure 2-2 (b), (a) temperature gradient of 5°C is imposed between the two plates with a warmer anode. The flow of produced water by the electrochemical reaction is shown in red in this figure.

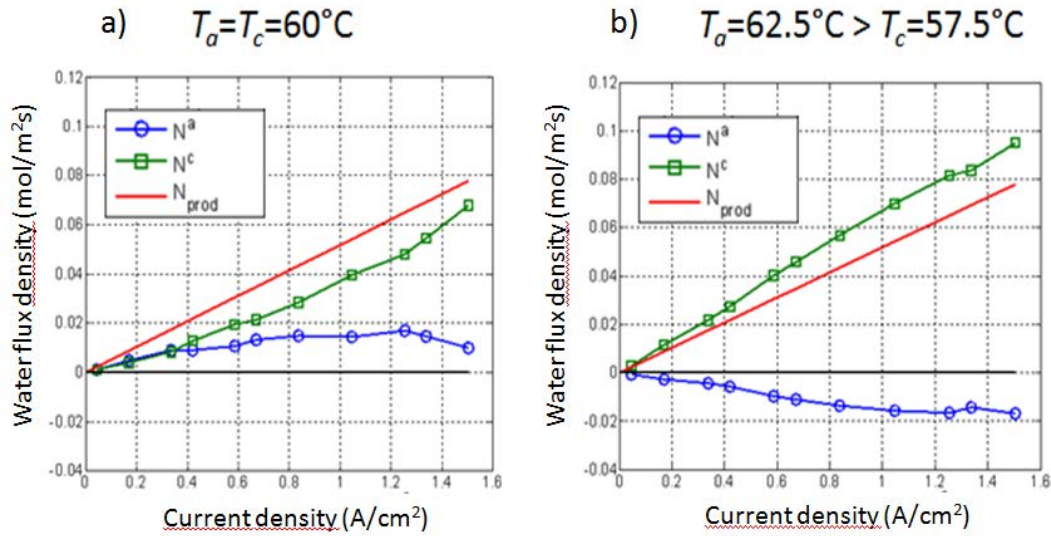


Figure 2-2. Distribution of the produced water flow between the anode and cathode compartments for two different thermal configurations: a) The same temperature of the plates. b) A temperature gradient of 5°C with a warmer anode (the negative water flux at the anode (blue curve) means that the inlet water vapor that comes from the H₂ humidifier is even drained towards the cathode) [19].

Notably, the distribution of the produced water flow rate between the anode and cathode is very sensitive to thermal boundary conditions. The water is essentially transferred from the electrode to the channels in vapor form according to a diffusion mechanism due to the saturated vapor pressure gradient that originates from the temperature gradient [19], [20]. Therefore, it can be expected that a warmer cell can disturb the water flow distribution of adjacent cells due to the temperature gradient that is created. **Therefore, it is important to take into account the thermal coupling between the adjacent cells to model a cell inside a stack.**

The main objective of this chapter is to propose a simple model that can detect the instabilities of a cell inside a stack in real-time. As mentioned earlier, these instabilities are linked to water transfer. The diphasic flow should be characterized to detect the mentioned instabilities.

In this chapter, the diphasic flow in the anode and cathode compartment is characterized in such a way that the flow distributions heterogeneities between the cells can be predicted. Numerous models have been carried out to describe diphasic flow in the fuel cell channels [130], [134], [135]. This type of flow is very complex. Since the flow of liquid water changes from the inlet to the outlet, it is possible to have a flow of water droplets in the inlet and a liquid film at the outlet [132]. Wettability, wall roughness, and interaction with GDL affect this flow. Considering this complexity and intending to develop a model that can be implemented in real-time [136], the orientation is toward developing a porous media type model which is characterized by intrinsic permeability and relative permeability of the gas and liquid water [137]. To estimate the model parameters, a simple method is proposed in this chapter.

This model also provides liquid water saturation in the channels. The saturation indicates the quantity of the present liquid water in the anode and cathode compartment. The proposed model is simple enough to be solved in real-time. As a result, it is suitable for system diagnosis and control or simultaneous modeling of several cells of a stack. This model can explain the mechanism of the degradation propagation from cell to cell in a stack. Due to the direct impact

of the temperature on the water transfer model, a model for characterizing the temperature of the different parts of a cell is also presented in this chapter. To introduce a complete model, the oxygen and charge transfer models are also explained in this chapter. These models are coupled and they can affect each other. For simplicity and simulating the model in real-time, it is tried to keep models as simple as possible. Hence, there are many simplifications, especially in the charge transfer model.

2.2. Heat transfer model

The heat transfer mechanism can be summarized by an equivalent electrical scheme as demonstrated in Figure 2-3. In this model, the MEA is isothermal and T_m is the average temperature of anode and cathode electrodes, and membrane. In other words, the thermal resistance of the electrodes and membrane are considered very low compared to the GDL thermal resistance. T_m , T_a , and T_c are the temperature of the MEA, anode plate, and cathode plate respectively. As seen in this figure, three heat sources are considered for a cell. The heat source associated with the MEA is used to model the heat generation by the reaction and Joule effect in the MEA. This heat flux can be calculated as follows:

$$\phi_{MEA} = \frac{ILW}{2F} LHV_{H_2} - UILW \quad (2.1)$$

where I is the current density, L and W are respectively the length and width of the active area of the cell, F is the Faraday constant ($F=96485.332 \text{ C/mol}$), U is the cell potential, and LHV_{H_2} is the lower heating value of Hydrogen (242 kJ/mol). As seen in this equation, more heat is generated for the higher value of the current density. It should be noted that the potential of the cell can be considered as an input of the model to provide a more accurate model for fault detection; otherwise, the potential is calculated in the charge transfer Section. The cell potential is measured by a voltage sensor when it is considered as an input of the model.

Two other heat sources that are connected to channels are used to model the absorbed or released thermal energy due to the water phase change. To calculate these heat fluxes, the water balance must be calculated in the channels to find the water phase change flow rate. These heat fluxes can be obtained by multiplying the water phase change flow rate to the latent heat of the water ($L_v=40.68 \text{ kJ/mol}$) as follows:

$$\begin{cases} \phi_a^{th} = Df_a L_v \\ \phi_c^{th} = Df_c L_v \end{cases} \quad (2.2)$$

where Df_a and Df_c are the water phase change flow rates in the anode and cathode channels respectively that can be calculated as follows:

$$\begin{cases} Df_a = N_{H_2Ovap}^{a,in} - N_{H_2Ovap}^{a,out} + N_{H_2Ovap}^{a,el \rightarrow ch} \\ Df_c = N_{H_2Ovap}^{c,in} - N_{H_2Ovap}^{c,out} + N_{H_2Ovap}^{c,el \rightarrow ch} \end{cases} \quad (2.3)$$

where $N_{H_2Ovap}^{a,in}$, $N_{H_2Ovap}^{a,out}$ are respectively the vapor water flow rate at the input and output of the anode channel, and $N_{H_2Ovap}^{a,el \rightarrow ch}$ is the vapor water flow rate that is transferred from the anode electrode to the anode channel. Similarly, $N_{H_2Ovap}^{c,in}$ and $N_{H_2Ovap}^{c,out}$ are the vapor water flow rate at the input and output of the cathode channel and $N_{H_2Ovap}^{c,el \rightarrow ch}$ is the vapor water flow rate that is

transferred from the cathode electrode to the cathode channel. These flow rates are obtained from the water transfer model that will be explained in the following sections.

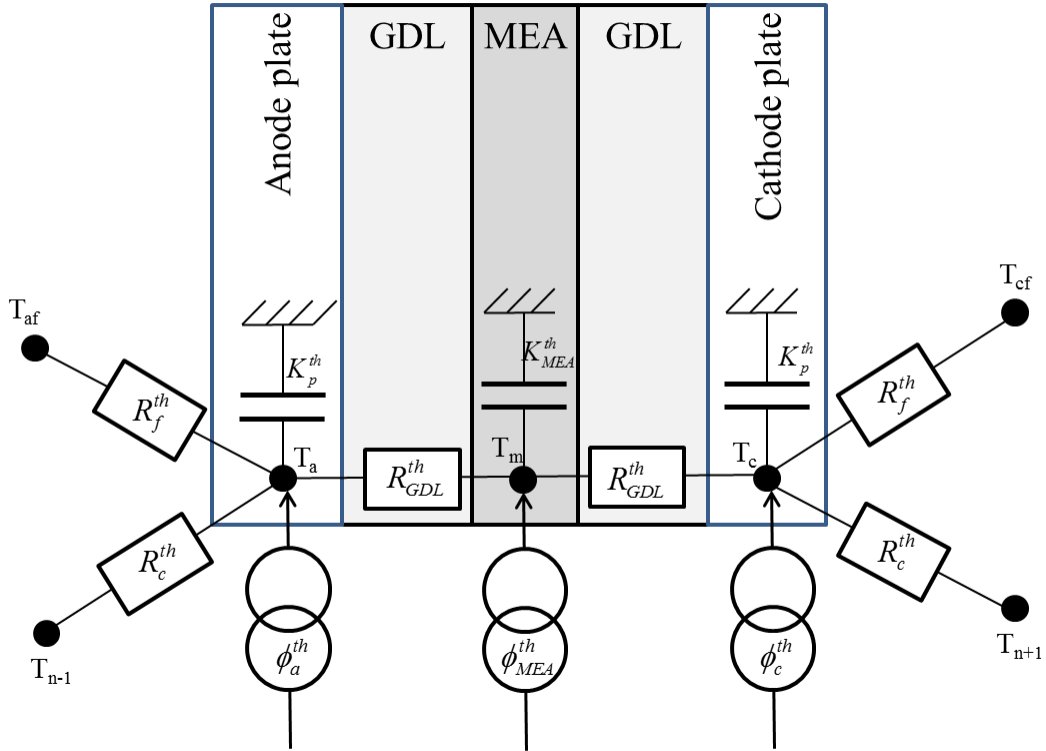


Figure 2-3. Heat transfer model in a cell. The coupling with the cooling fluid and the neighbor cells is achieved thanks to thermal resistances. The thermal inertia of the MEA and plates are considered. Regarding a very low Biot number (R_{GDL}^{th}/R_m^{th}), the MEA is assumed isothermal. Three thermal sources are considered.

As seen in Figure 2-3, simple thermal resistances are used to model the heat transfer between the channels and the MEA. The thermal resistance of the GDL can be calculated as follows [28]:

$$R_{GDL}^{th} = \frac{e_{GDL}}{\lambda_{GDL}LW} \quad (2.4)$$

where e_{GDL} is the thickness of the GDL, and λ_{GDL} is the effective thermal conductivity of the GDL. The thermal impact of the adjacent cells and the cooling fluid are also considered by using thermal resistances (R_c^{th} and R_f^{th} respectively). These resistances depend on the materials and construction technics. T_{af} and T_{cf} indicate the anode and cathode side cooling fluid temperatures respectively. T_{n-1} and T_{n+1} indicate the temperature of the preceding cathode and following anode of the neighbor cells in the stack. Considering the thermal capacity of the MEA, its temperature can be calculated from the following differential equation:

$$K_{MEA}^{th} \frac{dT_m}{dt} = \phi_{AME}^{th} + \frac{T_a - T_m}{R_{GDL}^{th}} + \frac{T_c - T_m}{R_{GDL}^{th}} \quad (2.5)$$

where K_{MEA}^{th} is the thermal capacitance of the MEA that can be calculated from the following equation:

$$K_{MEA}^{th} = \rho_{MEA} C_{MEA} V_{MEA} \quad (2.6)$$

where ρ_{MEA} is the volumetric mass density (kg/m^3) of the MEA, C_{MEA} is its specific heat capacity ($\frac{J}{kg^\circ K}$), and V_{MEA} is its volume. Considering the membrane thickness (e_m), its volume can be calculated ($V_{MEA} = e_m LW$). The thermal capacity of the anode and cathode channels can be calculated as follows:

$$K_p^{th} = \rho_p C_p V_p \quad (2.7)$$

where ρ_p , C_p , and V_p are respectively the volumetric mass density, specific heat capacity, and volume of the plate. Considering the thickness of the plate (e_p), its volume can be calculated ($V_p = e_p LW$). Thus, the cathode and anode channel temperatures can be calculated as follows:

$$\begin{aligned} K_p^{th} \frac{dT_a}{dt} &= \phi_a^{th} - \frac{T_a - T_m}{R_{GDL}^{th}} + \frac{T_{af} - T_a}{R_f^{th}} + \frac{T_{n-1} - T_a}{R_c^{th}} \\ K_p^{th} \frac{dT_c}{dt} &= \phi_c^{th} - \frac{T_c - T_m}{R_{GDL}^{th}} + \frac{T_{cf} - T_c}{R_f^{th}} + \frac{T_{n+1} - T_c}{R_c^{th}} \end{aligned} \quad (2.8)$$

Further information about the heat transfer model can be found in [28].

2.3. Mass transfer

2.3.1. Oxygen transfer

The oxygen transfer mechanism in the perpendicular direction to the MEA is summarized in Figure 2-4 by an electrical equivalent circuit. The concentration gradient of a species in a mixture creates molecular transport. This type of transport is called transport by diffusion. The main driving force of oxygen movement in the perpendicular direction to the membrane is supposed to be the diffusion. As seen in Figure 2-4, the diminution of the oxygen concentration from the cathode channel to the cathode electrode is modeled by a resistance. This resistance can be calculated as follows [138]:

$$R_{O_2}^{diff} = \frac{e_{GDL}}{LWD_{O_2}^{T_c}} \quad (2.9)$$

where $D_{O_2}^{T_c}$ is the effective oxygen diffusion coefficient in the GDL that depends on the temperature. This coefficient can be calculated as follows:

$$D_{O_2}^{T_c} = D_{O_2}^{GDL} \left(\frac{T_c}{T_0} \right)^{1.832} \quad (2.10)$$

where T_0 is the standard temperature ($25^\circ C$) and $D_{O_2}^{GDL}$ is the oxygen diffusion coefficient through the cathode GDL at temperature T_0 that can be calculated as follows:

$$D_{O_2}^{GDL} = D_{O_2}^{0,GDL} \frac{P_0}{P} \quad (2.11)$$

where P_0 is the atmospheric pressure, $D_{O_2}^{0,GDL}$ is the oxygen diffusion coefficient through the cathode side GDL without the temperature and pressure effects, and P is the total pressure in the cathode channel.

Given the oxygen concentration in the cathode channel ($C_{O_2}^{c,ch}$), the oxygen concentration in the electrode of the cathode ($C_{O_2}^{c,el}$) can be calculated by the following equation:

$$C_{O_2}^{c,el} = C_{O_2}^{c,ch} - R_{O_2}^{diff} \frac{ILW}{4F} \quad (2.12)$$

In other words, the diffusion time of oxygen in the perpendicular direction to the membrane is ignored. This model is interested in a longer time constant than the time constant of the oxygen diffusion in the perpendicular direction to the membrane ($D_{O_2}^{GDL} / e_{GDL}^2 \geq 100Hz$).

The concentration of the oxygen in the cathode channel can be calculated from the following equation [138]:

$$\left(V_{ch}^c (1 - S_c) \right) \frac{dC_{O_2}^{c,ch}}{dt} = N_{O_2}^{in} - N_{O_2}^{out} - \frac{ILW}{4F} \quad (2.13)$$

where S_c is the water saturation in the cathode channel, $N_{O_2}^{in}$ is the molar oxygen flow rate at the inlet of the cathode channel, $N_{O_2}^{out}$ is the molar oxygen flow rate at the outlet of the cathode channel, and V_c is the volume of cathode channels. Considering the cathode channel depth ($e_{c,ch}$), the volume of the cathode channels can be estimated by $V_{ch}^c = 0.5LWe_{c,ch}$. The saturation level indicates how much of the cathode channel volume is filled with liquid water. Regarding the objective of this thesis to simulate a cell inside a stack, the total flow rate of dry gases (N_{air}^{in}) must be obtained as a function of pressure drop inside the channels. This flow rate is calculated in the following section.

The oxygen molar flow rates at the inlet and outlet of the cathode channel are unknown in (2.13). The molar flow of oxygen at the outlet of the cathode channel should be calculated as a function of the oxygen concentration. Considering the pressure at the output of the cathode channel (P^{out}), the following equation can be obtained based on the relation between the concentration and pressure and by taking into account the vapor water molar fraction:

$$C_{O_2}^{c,ch,out} = \frac{P^{out}}{RT_c} \frac{N_{O_2}^{out}}{N_{O_2}^{out} + N_{N_2}^{out} + N_{H_2Ovap}^{c,out}} \quad (2.14)$$

Therefore:

$$N_{O_2}^{out} = \frac{C_{O_2}^{c,ch,out}}{\frac{P^{out}}{RT_c} - C_{O_2}^{c,ch,out}} \left[N_{N_2}^{out} + N_{H_2Ovap}^{c,out} \right] \quad (2.15)$$

Considering the mean concentration is equal to the inlet-outlet average:

$$C_{O_2}^{c,ch} = \frac{C_{O_2}^{c,ch,in} + C_{O_2}^{c,ch,out}}{2} \quad (2.16)$$

Thus, the molar flow of oxygen at the outlet of the cathode channel as a function of the oxygen concentration is as in the following equation:

$$N_{O_2}^{out} = \frac{2C_{O_2}^{c,ch} - C_{O_2}^{c,ch,in}}{\frac{P^{out}}{RT_c} - 2C_{O_2}^{c,ch} - C_{O_2}^{c,ch,in}} \left[N_{N_2}^{out} + N_{H_2Ovap}^{c,out} \right] \quad (2.17)$$

It should be noticed that the output pressure is equal to atmospheric pressure. The nitrogen flow rate at the outlet of the cathode is equal to its value at the inlet of the cathode channel that is about 0.79 of the dry airflow at the inlet. Therefore, the oxygen flow rate at the inlet and outlet of the cathode channel can be calculated as follows:

$$\left\{ \begin{array}{l} N_{O_2}^{in} = 0.21N_{air}^{in} \\ N_{O_2}^{out} = \frac{2C_{O_2}^{c,ch} - C_{O_2}^{c,ch,in}}{\frac{P^{out}}{RT_c} - 2C_{O_2}^{c,ch} - C_{O_2}^{c,ch,in}} \left[\frac{79}{100} + \frac{C_{H_2O}^{c,ch,out}}{\frac{P^{out}}{RT_c} - C_{H_2O}^{c,ch,out}} \right] N_{air}^{in} \end{array} \right. \quad (2.18)$$

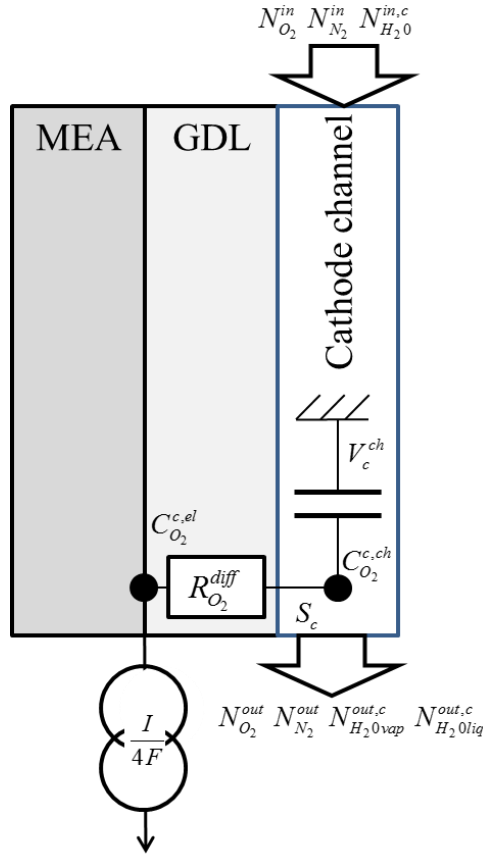


Figure 2-4. Oxygen transfer model in the perpendicular direction to the MEA. Because of its very short time constant ($F > 50\text{Hz}$), the oxygen storage in the GDL or electrode is not described.

2.3.2. Water transfer

The model for water transfer in the fuel cell should be investigated in two directions: the channel (anode or cathode) direction between the inlet and outlet and perpendicular to the membrane.

2.3.2.1. Water transfer through the MEA

The electrical equivalent circuit of the model of water transfer through the MEA is shown in Figure 2-5.

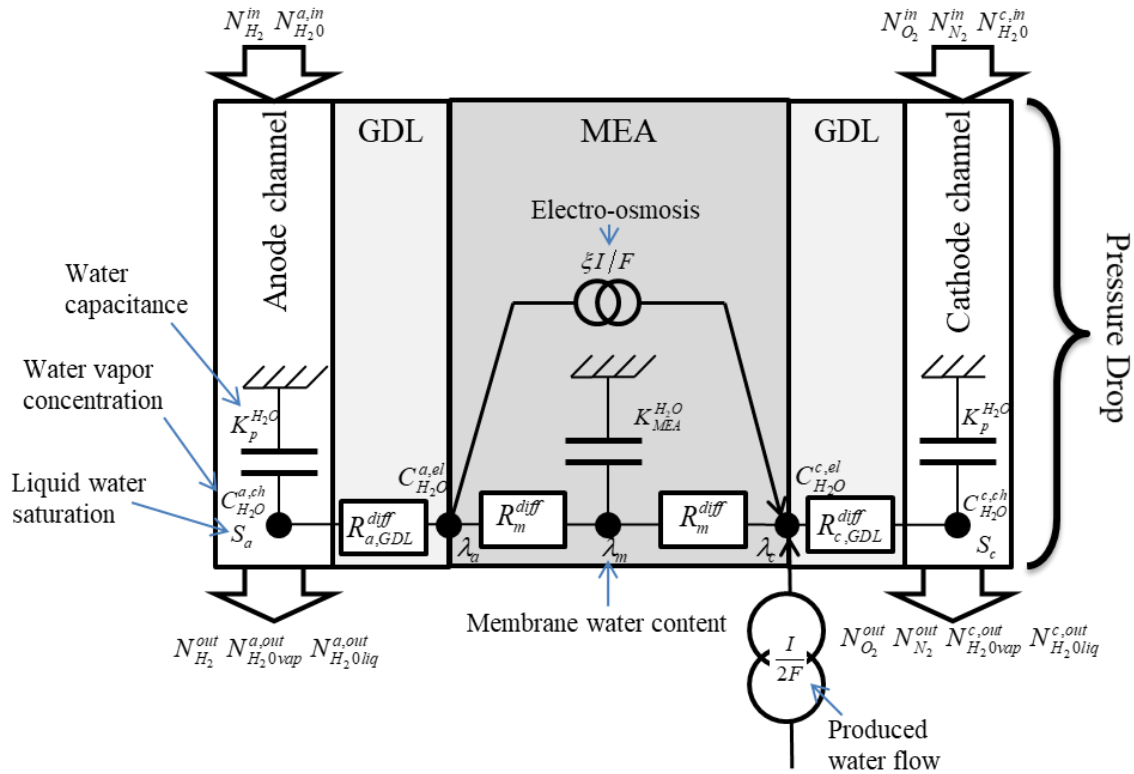


Figure 2-5. Electrical equivalent circuit of the water transfer model in the direction perpendicular to the membrane. Three different water storages are considered in the MEA and channels.

The water can be transferred in the perpendicular direction to the membrane by diffusion and electro-osmosis based on the springer model [28], [138], [139]. The transfer of liquid in a porous medium due to an electrical field is called electro-osmosis flow of water. This type of water transfer can bring the water molecules from the anode side to the cathode side. To model this type of water transfer, a simple coefficient ξ is used and the whole amount of proton generation is multiplied to this coefficient to obtain the whole water transfer by electro-osmosis from the anode to the cathode. As seen in Figure 2-5, the MEA discretized into three points of the membrane and two electrodes. For the purpose of simplicity, the electrodes are considered as interfaces. The volumetric characteristics of the electrodes can add more complexity to the model without adding any new fundamental qualitative features. To calculate different parameters and especially the water content of the membrane, the water balance must be written at the anode and cathode sides. It is inevitable to explain the sorption law for the MEA parts for the aim of the water balance expression. Water sorption is defined as the adsorbed amount of water by the media in equilibrium with the vapor or liquid water at a given temperature. The water sorption curve usually demonstrates the water content as a function of water activity (or relative humidity). In this thesis, the sorption law for the different parts of the MEA is linearized

to simplify the whole model of the system. The linear sorption law for the electrodes of the MEA is as follows [28], [139]:

$$\begin{cases} \lambda_a = 14 \frac{C_{H_2O}^{a,el}}{C_{sat}^{T_m}} \\ \lambda_c = 14 \frac{C_{H_2O}^{c,el}}{C_{sat}^{T_m}} \end{cases} \quad (2.19)$$

where λ_a and λ_c are the water content of the anode and cathode electrodes respectively, $C_{H_2O}^{a,el}$ and $C_{H_2O}^{c,el}$ are the water vapor concentration in the anode and cathode electrodes, and $C_{sat}^{T_m}$ is the concentration of saturated water vapor at the membrane temperature. The concentration of saturated water vapor can be calculated as follows:

$$C_{sat}^T = 10^5 \frac{e^{\frac{13.669 - 5096.23}{T}}}{RT} \quad (2.20)$$

In this equation, R is the universal gas constant ($8.314 \frac{J}{mol^\circ K}$), T is the temperature at which the concentration of saturated water vapor is calculated. For instance, T equal to T_m , T_a , and T_c is used to calculate the concentration of saturated water vapor in the membrane, anode channel, and cathode channel respectively.

The linear sorption law for the membrane can be written as follows:

$$C_{H_2O}^m = \frac{\rho_{dry}}{EW} \lambda_m \quad (2.21)$$

where $C_{H_2O}^m$ is the water concentration in the membrane, ρ_{dry} is the volumetric mass of a dry membrane, and EW is its equivalent weight (kg/mol).

Based on Figure 2-5, the water balance at the anode side is as follows:

$$\frac{C_{H_2O}^{a,ch} - C_{H_2O}^{a,el}}{R_{a,GDL}^{diff,H_2O}} + \frac{\rho_{dry}}{EW} \frac{\lambda_m - \lambda_a}{R_m^{diff}} - \xi \frac{I}{F} LW = 0 \quad (2.22)$$

where $C_{H_2O}^{a,ch}$ is the water vapor concentration in the anode channel, $R_{a,GDL}^{diff,H_2O}$ is the resistance of the GDL to the diffusion of the water vapor, R_m^{diff} is the membrane resistance to the diffusion, and ξ is the electro-osmosis coefficient. Notable that the liquid water transfer inside the GDL is ignored in this model for the sake of simplicity. Similar to the resistance of the GDL to the oxygen diffusion, the resistance of the GDL to the diffusion of the water can be calculated as follows:

$$R_{a,GDL}^{diff,H_2O} = \frac{e_{GDL}}{D_{H_2O}^{a,GDL} LW \frac{P_0}{P} \left(\frac{T_a}{T_0} \right)^{1.832}} \quad (2.23)$$

where $D_{H_2O}^{a,GDL}$ is the effective water vapor diffusion coefficient through the anodic GDL without the temperature effect. The water balance equation at the cathode side is similar to this equation:

$$\frac{C_{H_2O}^{c, ch} - C_{H_2O}^{c, el}}{R_{c, GDL}^{diff, H_2O}} + \frac{\rho_{dry}}{EW} \frac{\lambda_m - \lambda_c}{R_m^{diff}} + (1 + 2\xi) \frac{I}{2F} LW = 0 \quad (2.24)$$

where $C_{H_2O}^{c, ch}$ is the water vapor concentration in the cathode channel. In a similar way of calculating the diffusion resistance of the GDL to the oxygen, the GDL diffusion resistance at the cathode side can be calculated from the following equation:

$$R_{c, GDL}^{diff, H_2O} = \frac{e_{GDL}}{D_{H_2O}^{c, GDL} LW \frac{P_0}{P} \left(\frac{T_c}{T_0} \right)^{1.832}} \quad (2.25)$$

where $D_{H_2O}^{c, GDL}$ is the effective water diffusion coefficient through the cathode side GDL without the temperature effect. The membrane diffusion resistance can be calculated similarly:

$$R_m^{diff}(\lambda_m, T_m) = \frac{\frac{e_m}{2}}{LW D_0(T_m) \frac{\lambda_m}{14}} \quad (2.26)$$

where $D_0(T)$ is the water diffusion coefficient in the membrane that depends on the temperature but that is independent of the water content. This coefficient can be obtained by the following equation:

$$D_0(T_m) = D_{0m} \exp \left[2416 \left(\frac{1}{303} - \frac{1}{T_m} \right) \right] \quad (2.27)$$

where D_{0m} is the water diffusion coefficient through the membrane without the temperature effect. By substituting (2.33) in (2.22), the water concentration in the anode electrode can be obtained:

$$C_{H_2O}^{a, el} = \frac{\frac{C_{H_2O}^{a, ch}}{R_{a, GDL}^{diff, H_2O}} + \frac{\rho_{dry}}{EW} \frac{\lambda_m}{R_m^{diff}} - \xi \frac{I}{F} LW}{\frac{1}{R_m^{diff} \frac{C_{sat}^{T_m}}{14} \frac{EW}{\rho_{dry}}} + \frac{1}{R_{a, GDL}^{diff, H_2O}}} \leq C_{sat}^{T_m} \quad (2.28)$$

As seen in this equation, if the numerator is less than zero, there will be no solution. As a result, there can be a law for the current density as follows:

$$I \leq \frac{FC_{H_2O}^{a, ch}}{\xi LWR_{GDL}^{diff, H_2O}} + \frac{F\rho_{dry}}{\xi LWEW} \frac{\lambda_m}{R_m^{diff}} \quad (2.29)$$

The water vapor concentration in the cathode electrode can be obtained from the following equation employing a similar approach:

$$C_{H_2O}^{c, el} = \frac{\frac{C_{H_2O}^{c, ch}}{R_{c, GDL}^{diff, H_2O}} + \frac{\rho_{dry}}{EW} \frac{\lambda_m}{R_m^{diff}} + (2\xi + 1) \frac{I}{2F} LW}{\frac{\rho_{dry}}{EW} \frac{14}{R_m^{diff} C_{sat}^{T_m}} + \frac{1}{R_{c, GDL}^{diff, H_2O}}} \leq C_{sat}^{T_M} \quad (2.30)$$

Based on the water balance, the water vapor flow rate from the electrode to channel in the anode ($N_{H_2Ovap}^{a,el\rightarrow ch}$) and cathode ($N_{H_2Ovap}^{c,el\rightarrow ch}$) sides can be calculated as follows:

$$\begin{cases} N_{H_2Ovap}^{a,el\rightarrow ch} = \frac{\rho_{dry}}{EW} \frac{\lambda_m - \lambda_a}{R_m^{diff}} - \xi \frac{I}{F} LW = \frac{C_{H_2O}^{a,el} - C_{H_2O}^{a,ch}}{R_{a,GDL}^{diff,H_2O}} \\ N_{H_2Ovap}^{c,el\rightarrow ch} = \frac{\rho_{dry}}{EW} \frac{\lambda_m - \lambda_c}{R_m^{diff}} + (1 + 2\xi) \frac{I}{2F} LW = \frac{C_{H_2O}^{c,el} - C_{H_2O}^{c,ch}}{R_{c,GDL}^{diff,H_2O}} \end{cases} \quad (2.31)$$

The accumulation of water in the membrane can be calculated thanks to a water balance:

$$e_m LW \frac{d\lambda_m}{dt} = \frac{\lambda_c - \lambda_m}{R_m^{diff}} + \frac{\lambda_a - \lambda_m}{R_m^{diff}} \quad (2.32)$$

2.3.2.2. Water transfer down the channel direction

(a) Diphasic flow modeling

The model must be simple enough to be solved in real-time but it must also describe the physics of the flow as best as possible. In this thesis, it is proposed to assimilate the flow field as a porous medium characterized by an intrinsic permeability, and the relative permeability functions of the gas ($f_g(s)$) and liquid water ($f_{liq}(s)$). These functions depend on the saturation (S) levels. The saturation is defined by the ratio of liquid volume to the total volume. The flow rates of reactive gases, water vapor, and liquid water depend on the position between the inlet and outlet of the feeding plates. To keep the equations only in one dimension, the inlet-outlet averages of these quantities will be considered.

Based on Darcy's hypothesis that the volume flow rate is proportional to the pressure drop, the following equation can be written for the gas flow:

$$\frac{N_g^m + N_{H_2Ovap}^m}{\frac{P^m}{RT}} = \frac{k_g f_g(S)}{\mu_{mix}(T)} \Delta P \quad (2.33)$$

where N_g^m is the average molar flow rate of the reactive gas (H_2 or dry air) (mol/s), $N_{H_2Ovap}^m$ is the average flow rate of the water vapor (mol/s), P^m ($P^m = P_{atm} + \Delta P/2$) is the average absolute pressure (Pa), T is the average temperature (K), R is the perfect gas constant (SI), k_g is the intrinsic permeability of the porous medium being estimated (m^3), $f_g(S)$ is the relative permeability of the gas as a function of the saturation (S) being estimated (without unit), $\mu_{mix}(T)$ is the viscosity of the gas-water vapor mixture as a function of the temperature (Pa.s), and ΔP is the pressure drop between the inlet and outlet of the plate (Pa). This method is proposed in this thesis to be able to calculate the flow rates as a function of pressure drops inside the channels. As a result of the imposed pressure drop, this model can simulate the behavior of one cell inside its stack environment.

The average molar flow rate of the reactive gas and water vapor can be calculated as follows:

$$\begin{cases} N_g^m = \frac{(N_g^{in} + N_g^{out})}{2} \\ N_{H_2Ovap}^m = \frac{(N_{H_2Ovap}^{in} + N_{H_2Ovap}^{out})}{2} \end{cases} \quad (2.34)$$

where N_g^{in} and N_g^{out} are respectively the flow rates of the gas (H₂ or dry air) at the input and output of the (anode or cathode) channel, $N_{H_2Ovap}^{in}$ and $N_{H_2Ovap}^{out}$ are the water vapor flow rates at the input and output of the anode or cathode channels respectively.

The procedure is the same for the liquid water flow rate:

$$\frac{N_{H_2Oliq}^m}{M_{H_2O}} = \frac{k_{liq} f_{liq}(S)}{\rho_{liq} \mu_{H_2Oliq}(T)} \Delta P \quad (2.35)$$

Where k_{liq} is the intrinsic permeability in principle equal to k_g , $f_{liq}(S)$ is the relative permeability of the liquid, ρ_{liq} is the density of the liquid water (1000 kg/m³ at 5°C), M_{H_2O} is the molar mass of the water (18 g/mol), and $\mu_{H_2Oliq}(T)$ is the viscosity of liquid water as a function of temperature (Pa.s). The viscosity of liquid water as a function of the temperature can be calculated as follows:

$$\mu_{H_2Oliq}(T) = 1.9675 \times 10^{-6} e^{\left(\frac{1.8296 \times 10^3}{T}\right)} \quad (2.36)$$

(b) Estimation of intrinsic and relative permeability

The three unknown parameters and functions that must be estimated for a given channel geometry are the intrinsic permeability, the gas relative permeability $f_g(S)$, and the liquid water relative permeability $f_{liq}(S)$. To identify the intrinsic permeability and these two functions, a method is proposed in this section. This method is realized by imposing the gas flows (hydrogen and humid air) in an initially dry cell, then recording the variation of the pressure drop as a function of time following a current step. To have a cell with its channels initially in dry conditions, the cell should be supplied by dry gases for a long time before running the experiment. The intrinsic permeability of the gas is obtained from (2.33) when the channels are dry ($S=0$, $f_g(S)=1$). Relative permeability of the gas and liquid water are obtained by the evolution of the pressure drop over time before the liquid flow starts and thanks to the pseudo-steady state.

(c) Experimental set-up

The anode and cathode feed plates consist of five parallel straight channels with a length of 300 mm and a width of 1mm. The depth of anode and cathode channels is 0.47 mm and 0.51 mm respectively. The rib separating two channels has a width of 1 mm. MEAs with a length of 300 mm and a width of 10 mm of active surface area provided by IonPower. The platinum loads at the anode and cathode are 0.1 and 0.2 mg/cm² respectively. The GDL used are SGL 34BCs 240 μm thick and compressed to 170 μm using PTFE flat gaskets. The temperature of the anode

and cathode plates is independently controlled by two thermostatically controlled tank and a platinum sensor located on each plate. The air and hydrogen flows are humidified by two extremely stable membrane humidifiers regulated in temperature by a circulating tank. The humidity at the cathode inlet is measured using a chilled mirror sensor (Mitchell) that has an accuracy of (better than) 0.1°C on the dew temperature measuring. The air and hydrogen outlets are at the atmospheric pressure. Pressure drop is measured at the terminals of the anode and cathode compartments using two Honeywell pressure sensors.

The relative humidity at the cathode inlet is imposed at a value close to 100% and the anode is supplied with dry hydrogen. Besides, a temperature gradient is imposed between the anode and cathode: the temperature of the anode plate is regulated at 67.5°C while the temperature of the cathode plate is regulated at 62.5°C. This temperature gradient ensures that 100% of the produced water goes to the cathode (as seen in Figure 2-2). In this way, the molar flow rate of liquid water appearing on the cathode compartment is strictly equal to the sum of the water produced by the electrochemical reaction plus the humidification water supplied minus the water vapor flux at the outlet:

$$N_{H_2O_{liq}}^c = \frac{ILW}{2F} + \frac{P_{sat}(T_{dp}^{in})}{P_0 + \Delta P_c - P_{sat}(T_{dp}^{in})} N_{air}^{c,in} - \frac{P_{sat}(T_{dp}^{out})}{P_0 - P_{sat}(T_{dp}^{out})} N_{air}^{c,out} \quad (2.37)$$

where $P_{sat}(T_{dp}^{in})$ is the saturated vapor pressure of the water at the dew temperature measured at the inlet, $P_{sat}(T_{dp}^{out}) = P_{sat}(T_c)$ is the saturated vapor pressure of the water at the cathode plate temperature, $N_{air}^{c,in}$ is the dry airflow rate at the cathode inlet, and $N_{air}^{c,out} = N_{air}^{c,in} - ILW/4F$ is the dry airflow at the cathode outlet, in other words, the flow at the inlet minus the flow of consumed oxygen.

Six air stoichiometry (1.8, 2, 2, 2.25, 2.5, 2.75 & 3) and eight currents (5A, 7.5A, 10A, 12.5A, 15A, 20A, 25A & 30A) are considered.

(d) Experimental results

The experimental results for the air stoichiometry of 2 are presented in Figure 2-6. There is no liquid water in the channels ($S=0$) and the pressure drop is stable over the time before applying the current ($t < 175s$). A slight decrease of the pressure drop over the running time ($175s < t < 180s$) can be observed due to the consumption of the oxygen and consequently a reduction in the average volume flow rate through the cell to generate the current. Then the pressure drop monotonically increases to a specific value and then it changes stochastically around an average value. This monotonous phase of pressure drop increase is called imbibing. It was observed that no liquid water came out of the cathode channel during this phase (imbibing). Then, droplets of water appear and partially block the channels without leaving the cell. The lack of a rapid time variation may indicate the immobility of the water droplets. From a certain quantity of liquid water in the channels, the pressure drop varies stochastically around an average value. The water droplets are moving and create an unsteady diphasic flow.

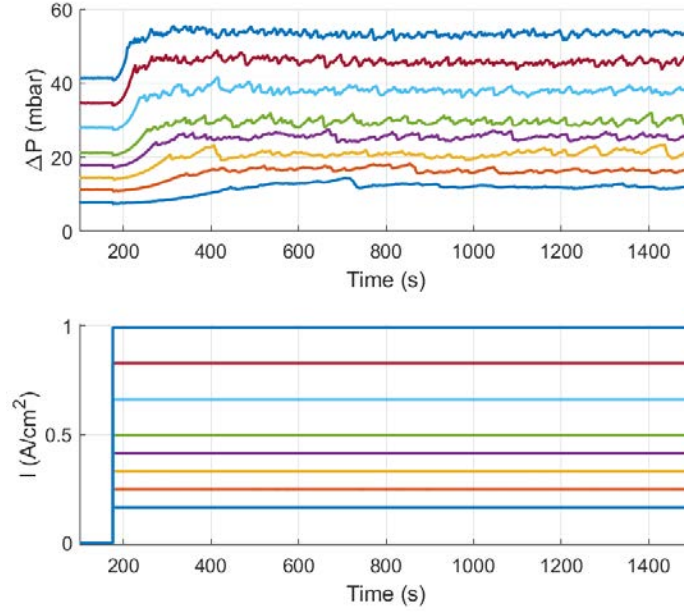


Figure 2-6. Pressure drop at the cathode side as a function of time following a current step and considering an applied air flow rate. The saturation of liquid water is initially zero. Eight current densities $S_{air}=2 S_{H_2}=I$. $T_{anode}=67.5^\circ C$. $T_{cathode}=62.5^\circ C$. $HR_{anode}=0\%$. $HR_{cathode}\sim 100\%$ (measured as a function of time)

(e) Monophasic flow

The monophasic flow ($S_c=0$) for the time $t < 175s$ allows to determine the intrinsic permeability k_c of the porous medium corresponding to the feeding plates according to (2.38):

$$\frac{N_{air}^{in} + N_{H_2O}^{in}}{\frac{P_0 + \Delta P_c / 2}{RT_c}} = \frac{k_g^c}{\mu_{mix}(T_c)} \Delta P_c \quad (2.38)$$

The molar flow rate of air and water vapor are constant. The average pressure P^m is equal to the outlet pressure P_{atm} plus half the pressure drop ($\Delta P_c / 2$). The viscosity of the mixture of air and water vapor $\mu_{mix}(T_c)$ is obtained by the mixing law from [140]. The experimental result shown in Figure 2-6 allows determining the intrinsic permeability of $1.06 \cdot 10^{-13} m^3$ for the five straight channels in parallel with a depth of 0.51 mm combined with the GDL SGL 35BC that is compressed to 170 μm .

(f) Imbibing

Figure 2-7 shows a magnification of the imbibing phase, just after the current generation, for the different stoichiometry and current densities. During the imbibing phase, droplets of liquid water appear in the channels. Thus, the passage of the gas is blocked but droplets stay immobile due to surface tension forces.

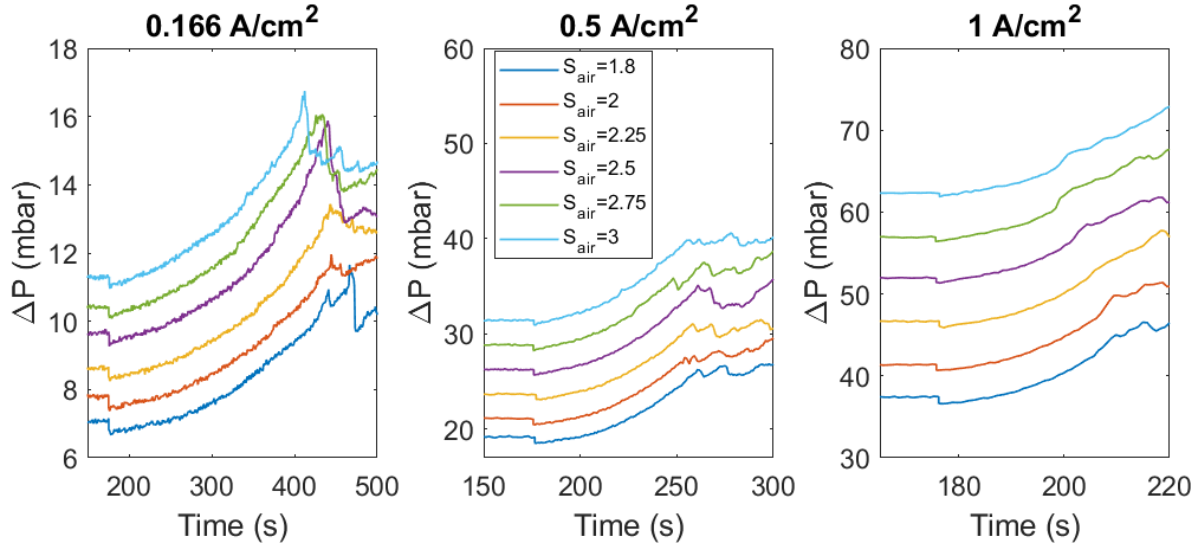


Figure 2-7. Imbibing experiment: the current is generated at $t=175s$. The stochastic variations following by the regular increase of the pressure drop (no liquid flow) is a sign of the two-phase flow.

It is observed that the required time to make the water droplets move depends slightly on the stoichiometry. As seen in Figure 2-7, the higher the current, the shorter the time it takes to make the water droplets move. During the imbibing phase, as long as the pressure drop is regular, no liquid water is coming out of the cathode. Therefore, it is possible to calculate the mass of liquid water $M_{H_2Oliq}^c$ in the cathode compartment as a function of time by integrating (2.37):

$$M_{H_2Oliq}^c(t) = M_{H_2O} \times \int_0^t \left[\frac{ILW}{2F} + \frac{P_{sat}(T_{dp}^{in})}{P_0 + \Delta P_c - P_{sat}(T_{dp}^{in})} N_{air}^{c,in} - \frac{P_{sat}(T_{dp}^{out})}{P_0 - P_{sat}(T_{dp}^{out})} N_{air}^{c,out} \right] dt \quad (2.39)$$

Finally, the volume of liquid water and the saturation that is calculated without taking into account the volume of the GDL can be deduced:

$$S_c = \frac{\text{liquid water volume}}{\text{channel volume}} = \frac{\rho_{liq} M_{H_2Oliq}^c(t)}{V_{ch}} \quad (2.40)$$

(g) Estimation of the relative permeability of the gas f_g

The relative permeability is determined during the imbibing phase. The molar flow rate of nitrogen is constant. The average flow rate of oxygen is obtained as a function of the current ($N_{O_2}^m = N_{O_2}^{in} - \frac{I}{8F}$). The average flow rate of water vapor is obtained by considering that nitrogen and oxygen are saturated at the outlet and measuring the dew point temperature at the inlet:

$$\left\{ \begin{array}{l} N_{H_2Ovap}^{c,in} = \frac{P_{sat}(T_{dp}^{in})}{P_0 + \Delta P_c - P_{sat}(T_{dp}^{in})} (N_{O_2}^{in} + N_{N_2}^{in}) \\ N_{H_2Ovap}^{c,out} = \frac{P_{sat}(T_c)}{P_0 - P_{sat}(T_c)} \left(N_{O_2}^{in} - \frac{ILW}{4F} + N_{N_2}^{in} \right) \\ N_{H_2Ovap}^m = \frac{N_{H_2Ovap}^{c,in} + N_{H_2Ovap}^{c,out}}{2} \end{array} \right. \quad (2.41)$$

where $N_{O_2}^{in}$ and $N_{N_2}^{in}$ are respectively the flow rate of oxygen and nitrogen at the inlet of the cathode channels. $N_{H_2Ovap}^{c,in}$ and $N_{H_2Ovap}^{c,out}$ are the corresponding water vapor flow rates. The average pressure P^m is obtained from the pressure drop (where $P^{c,m} = P_{atm} + \Delta P_c / 2$). The average flow rate of oxygen can be calculated as a function of the current density ($N_{O_2}^m = N_{O_2}^{in} - \frac{ILW}{8F}$). The flow rate of Nitrogen is constant. The viscosity of the gas mixture can be calculated as explained in [140]. The saturation as a function of time (S^*) is deduced from (2.33), (2.39), and (2.40) since the flow of liquid water at the outlet is zero during the imbibing phase. The relative permeability of the gas as a function of saturation is depicted in Figure 2-8 for the 48 experiments (eight different currents and six different values of the air stoichiometry).

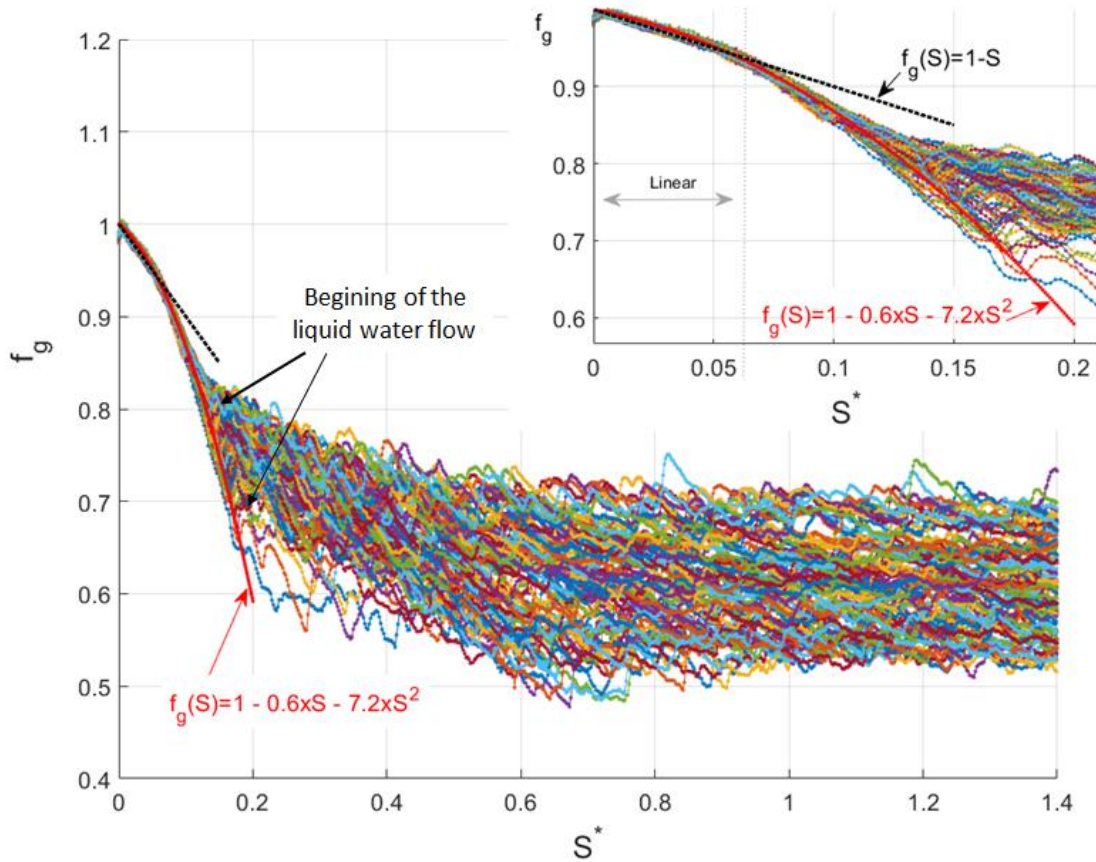


Figure 2-8. Relative permeability of the gas as a function of the saturation for the 48 experiments. All the experimental results are superimposed until the start of the two-phase flow.

As seen in Figure 2-8, the 48 curves are well superimposed as far as the liquid flow rate has not started. These results can be fitted by a second-degree (quadratic) polynomial. Notice that the relative permeability of the gas is linear for the low saturation levels ($S < 0.05$):

$$f_g^c(S_c) = 1 - S_c \quad S_c < 0.05 \quad (2.42)$$

The following equation is obtained for the considered channel geometry and used materials:

$$f_g^c(S_c) = 1 - 0.6 \times S_c - 7.2 \times S_c^2 \quad (2.43)$$

(h) Operation on pseudo-steady-state

Once critical saturation is reached, the liquid water begins to move and the diphasic flow, which is inherently unsteady, produces a stochastic variation in the pressure drop around an average value. It is assumed that the average value of the pressure drop for the determined diphasic flow is constant and the standard deviation of random variations around this average value is not modeled to keep the proposed model as simple as possible.

From the average pressure drop in pseudo-steady-state, it is possible to calculate the relative permeability of the gas based on (2.33) and to deduce the average saturation according to (2.43). Under the same approach, which was applied during the imbibing phase, the total liquid water flow leaving the cathode can be obtained by (2.37). Figure 2-9 demonstrates the logarithm of the liquid relative permeability as a function of the logarithm of the average saturation in steady-state for three different values of the current density. As seen in this figure, the liquid water relative permeability not only depends on the saturation but also on the current density. Unfortunately, the intrinsic liquid relative permeability has not been found in this thesis. This porous media approach failed to describe the liquid water flow and additional work needs to be done to better model it.

In the following, the relative permeability of the liquid water in the channels is only defined as a function of the saturation to avoid complexity and at least to get qualitative results:

$$\begin{cases} f_{liq}^a(S_a) = S_a^\alpha \\ f_{liq}^c(S_c) = S_c^\alpha \end{cases} \quad (2.44)$$

α is chosen equal to 3 in good agreement with figure 2.9

This law of relative permeability for the liquid flow combined with the relative permeability law for the gas expressed by (2.43) makes it possible to calculate the average flow rate of gas and liquid as a function of the applied pressure drop and saturation.

Remark: this parameter estimation procedure has been applied to characterize the AXANE fuel cell but the results were not satisfactory due to the inability to apply a temperature gradient between the anode and cathode of this fuel cell. Indeed to apply the proposed identification method, it is necessary to have a cell whose two plate temperatures can be separately controlled to create a temperature gradient. This is not possible with a stack, a dedicated device is needed but it is not complicated to set it up.

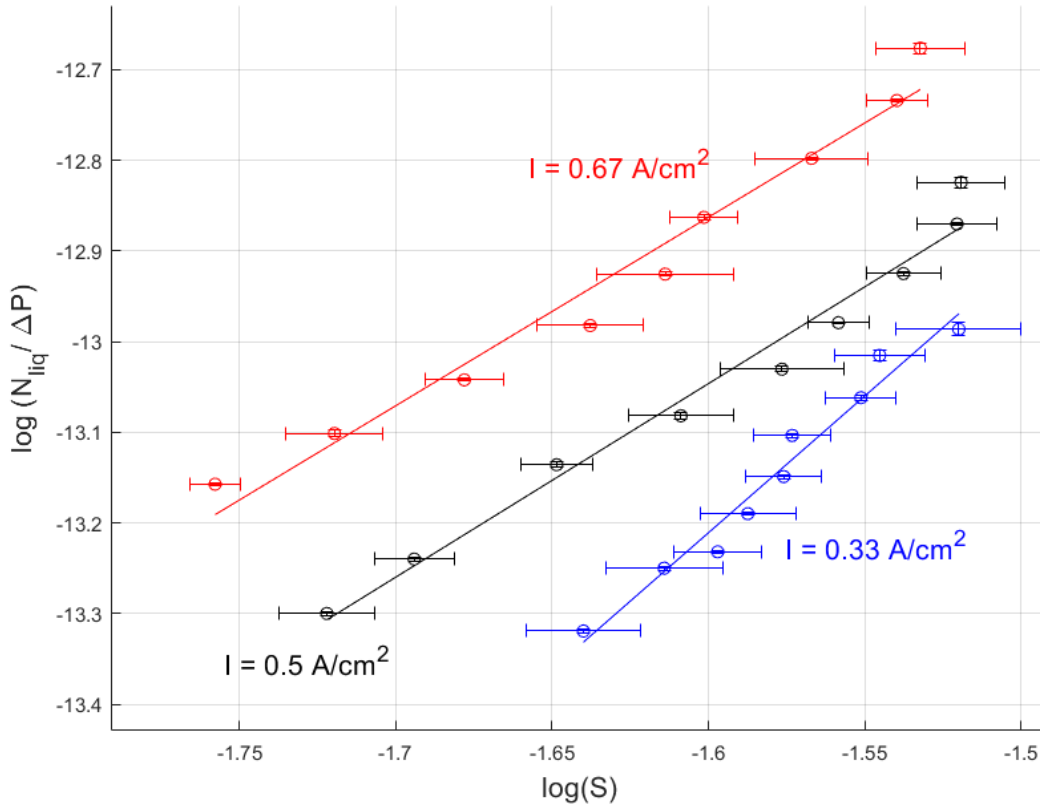


Figure 2-9. Logarithm of the liquid water flow rate (mol/s) divided by the pressure drop (*mbar*) as a function of the logarithm of the average saturation in steady-state, for three current densities. Each measurement point 'o' is the average of 10 measurements made under the same conditions and the error bar corresponds to the standard deviation. The non-superimposable results lead to a deduction that the liquid relative permeability depends on an additional parameter. Indeed, the airflow produces a constraint on the liquid that changes its relative permeability.

(i) Water balance in the cathode compartment

The liquid water amount in the channel increases only once the water vapor concentration reaches the saturation level. Therefore, it is required to have some cases to model the water transfer in the channel. The first case can be considered when the saturation in the channel is higher than zero and the water vapor concentration in the cathode channel ($C_{H_2O}^{c, ch}(T_c)$) is equal to the concentration of the saturated water vapor at the temperature of the cathode ($C_{sat}(T_c)$). To obtain the saturation as a function of time, a water balance is carried out in the cathode compartment. In this model, the storage term of water in vapor form is neglected.

$$\left\{ \begin{array}{l} \text{.Case } C_{H_2O}^{c, ch}(T_c) = C_{sat}^{T_c} \quad \& \quad S_c > 0 \\ V_{ch}^c \frac{dS_c}{dt} = \frac{M_{H_2O}}{\rho_{H_2Oliq}} \left[N_{H_2Ovap}^{c, in} - N_{H_2Ovap}^{c, out} - N_{H_2Oliq}^{c, out} + N_{H_2Ovap}^{c, el \rightarrow ch} - V_{ch}^c \left(\frac{dC_{sat}^{T_c}}{dT_c} \frac{dT_c}{dt} \right) \right] \\ \frac{dC_{H_2O}^{c, ch}}{dt} = \frac{dC_{sat}^{T_c}}{dT_c} \frac{dT_c}{dt} \end{array} \right. \quad (2.45)$$

where $S(t=0) = S_0$, $N_{H_2Ovap}^{c,in} = \frac{P_{sat}(T_{dp}^{in})}{P_0 + \Delta P - P_{sat}(T_{dp}^{in})} N_{air}^{in}$ is the inlet water vapor flow rate,

N_{air}^{in} is the inlet dry air flow rate, $N_{H_2Ovap}^{c,out} = \frac{P_{sat}(T_c)}{P_0 - P_{sat}(T_c)} \left(N_{air}^{in} - \frac{ILW}{4F} \right)$ is the outlet water

vapor flow rate, and $N_{H_2Oliq}^{c,out}$ is the liquid water flow rate at the outlet of the cathode channel. It is assumed here that the air is saturated at the outlet. Otherwise, the saturation is zero. To determine this flow rate, the water transport model must be solved in a perpendicular direction

to the membrane (Section 2.3.2.1). In this equation, $\frac{dC_{sat}^{T_c}}{dT_c}$ is calculated as follows:

$$\frac{dC_{sat}^{T_c}}{dT_c} = C_{sat}^{T_c} \left(\frac{5096.23}{T_c^2} - \frac{1}{T_c} \right) \quad (2.46)$$

The inlet dry airflow is obtained based on Darcy's law for the gas:

$$N_{air}^m + N_{H_2Ovap}^m = \frac{k_c f_g^c(S_c)}{\mu_{mix}(T_c)} \Delta P_c \frac{P_c^m}{RT_c} \quad (2.47)$$

The average flows are calculated as the average input/output flows:

$$\frac{1}{2} (N_{air}^{in} + N_{air}^{out}) + \frac{1}{2} (N_{H_2Ovap}^{c,in} + N_{H_2Ovap}^{c,out}) = \frac{k_c f_g^c(S_c)}{\mu_{mix}(T_c)} \Delta P_c \frac{P_0 + \Delta P_c / 2}{RT_c} \quad (2.48)$$

The inlet dry airflow rate is deduced from this equation as a function of the pressure drop ΔP , current I , the humidifying temperature T_{dp}^{in} , and the cell temperature T_c :

$$N_{air}^{in} = \frac{\frac{k_c f_g^c(S_c)}{\mu_{mix}(T_c)} \Delta P_c \frac{P_0 + \Delta P_c / 2}{RT_c} + \left[1 + \frac{P_{sat}(T_c)}{P_0 - P_{sat}(T_c)} \right] \frac{ILW}{8F}}{1 + \frac{1}{2} \frac{P_{sat}(T_{dp}^{in})}{P_0 + \Delta P_c - P_{sat}(T_{dp}^{in})} + \frac{1}{2} \frac{P_{sat}(T_c)}{P_0 - P_{sat}(T_c)}} \quad (2.49)$$

The second case can be considered when the saturation in the channel is equal to zero and the water concentration in the cathode channel is lower than the concentration of the saturated water vapor at the temperature of the cathode. In this case, the saturation and concentration can be calculated as follows:

$$\left\{ \begin{array}{l} \text{Case } C_{H_2O}^{c,ch}(T_c) < C_{sat}^{T_c} \quad \& \quad S_c = 0 \\ \frac{dS_c}{dt} = 0 \\ V_{ch}^c \frac{dC_{H_2O}^{c,ch}}{dt} = N_{H_2Ovap}^{c,in} - N_{H_2Ovap}^{c,out} - N_{H_2Oliq}^{c,out} + N_{H_2Ovap}^{c,el \rightarrow ch} \end{array} \right. \quad (2.50)$$

The last case can be considered when the saturation in the channel is equal to zero and the water concentration in the cathode channel is equal to the concentration of the saturated water

vapor at the temperature of the cathode. Two subcases can be considered. The first subcase means liquid water generation in the channel. In this subcase, the water vapor balance should be higher than zero. This case is to deal with the numerical problems and discontinuity in the solving method. The derivative equations of the system are as follows in this case:

$$\left\{ \begin{array}{l}
 \text{Case } C_{H_2O}^{c,ch}(T_c) = C_{sat}^{T_c} \quad \& \quad S_c = 0 \\
 \text{if } \left[N_{H_2Ovap}^{c,in} - N_{H_2Ovap}^{c,out} - N_{H_2Oliq}^{c,out} + N_{H_2Ovap}^{c,el \rightarrow ch} - V_{ch}^c \left(\frac{dC_{sat}^{T_c}}{dT_c} \frac{dT_c}{dt} \right) \right] > 0 \\
 V_{ch}^c \frac{dS_c}{dt} = \frac{M_{H_2O}}{\rho_{H_2Oliq}} \left[N_{H_2Ovap}^{c,in} - N_{H_2Ovap}^{c,out} - N_{H_2Oliq}^{c,out} + N_{H_2Ovap}^{c,el \rightarrow ch} - V_{ch}^c \left(\frac{dC_{sat}^{T_c}}{dT_c} \frac{dT_c}{dt} \right) \right] \\
 \frac{dC_{H_2O}^{c,ch}}{dt} = \frac{dC_{sat}^{T_c}}{dT_c} \frac{dT_c}{dt} \\
 \text{else} \\
 \frac{dS_c}{dt} = 0 \\
 V_{ch}^c \frac{dC_{H_2O}^{c,ch}}{dt} = N_{H_2Ovap}^{c,in} - N_{H_2Ovap}^{c,out} - N_{H_2Oliq}^{c,out} + N_{H_2Ovap}^{c,el \rightarrow ch}
 \end{array} \right. \quad (2.51)$$

(j) Water balance in the anode compartment

Based on Darcy's hypothesis, the volume flow rate can be written as follows:

$$\frac{N_{H_2}^m + N_{H_2Ovap}^{a,m}}{P_0 + \frac{\Delta P_a}{2}} = \frac{k_g^a f_g^a(S_a)}{\mu_{mix}(T_a)} \frac{\Delta P_a}{RT_a} \quad (2.52)$$

where $N_{H_2}^m$ is the average value of the hydrogen flow rate in the anode channel and $N_{H_2Ovap}^{a,m}$ is the average flow rate of the water vapor in the anode channel. These parameters can be calculated as follows:

$$\left\{ \begin{array}{l}
 N_{H_2}^m = N_{H_2}^{in} - \frac{ILW}{4F} \\
 N_{H_2Ovap}^{a,m} = \frac{N_{H_2Ovap}^{a,in} + N_{H_2Ovap}^{a,out}}{2}
 \end{array} \right. \quad (2.53)$$

Knowing the relative humidity at the inlet of the anode channel:

$$RH_a^{in} = \frac{N_{H_2Ovap}^{a,in}}{N_{H_2}^{in} + N_{H_2Ovap}^{a,in}} \frac{P_a}{P_{sat}(T_a)} \quad (2.54)$$

the water vapor flow rate at the inlet of the anode channel can be deduced as a function of the Hydrogen flow rate at the inlet of the anode channel:

$$N_{H_2Ovap}^{a,in} = \frac{RH_a^{in} P_{sat}(T_a)}{P_0 + \Delta P_a - RH_a^{in} P_{sat}(T_a)} N_{H_2}^{in} \quad (2.55)$$

where $P_{sat}(T_a)$ is the saturated vapor pressure of the water at the anode plate temperature. Considering the saturated condition at the outlet of the anode channel, the water flow rate at the outlet can be calculated as follows:

$$N_{H_2Ovap}^{a,out} = \frac{P_{sat}(T_a)}{P_0 - P_{sat}(T_a)} \left[N_{H_2}^{in} - \frac{ILW}{2F} \right] \quad (2.56)$$

Using (2.52)-(2.56), the dry hydrogen flow rate at the inlet of the anode channel can be obtained as follows:

$$N_{H_2}^{in} = \frac{\left(\frac{P_0 + \frac{\Delta P_a}{2} k_a f_g^a(S_a)}{RT_a} \frac{\Delta P_a}{\mu_{mix}(T_a)} \right) + \frac{ILW}{4F} \left(\frac{P_0}{P_0 - P_{sat}(T_a)} \right)}{1 + \frac{1}{2} \left(\frac{RH_a^{in} P_{sat}(T_a)}{P_0 + \Delta P_a - RH_a^{in} P_{sat}(T_a)} + \frac{P_{sat}(T_a)}{P_0 - P_{sat}(T_a)} \right)} \quad (2.57)$$

Using this equation and (2.55)-(2.56), the water vapor flow rate at the inlet and outlet of the anode channel can be obtained. The liquid water flow rate at the outlet of anode channel ($N_{H_2Oliq}^{a,out}$) can be calculated by (2.35) for the anode side. The relative permeability for the gas phase at the anode side should be identified in a similar way of the relative permeability identification at the cathode side. Since the relative permeability identification was not the basic objective of this thesis, a possible function as in the following equation is used for $f_g^a(S_a)$:

$$f_g^a(S_a) = (1 - S_a)^\alpha \quad (2.58)$$

In a similar way to the cathode channel, three cases are considered to model the water transfer inside the anode channel. The first case can be considered when the saturation in the anode channel is equal to zero and the water concentration in the anode channel ($C_{H_2O}^{a,ch}(T_a)$) is lower than the concentration of the saturated water vapor at the anode temperature ($C_{sat}(T_a)$):

$$\left\{ \begin{array}{l} \text{Case } C_{H_2O}^{a,ch}(T_a) < C_{sat}^{T_a} \quad \& \quad S_a = 0 \\ \frac{dS_a}{dt} = 0 \\ V_{ch}^a \frac{dC_{H_2O}^{a,ch}}{dt} = \left[N_{H_2Ovap}^{a,in} - N_{H_2Ovap}^{a,out} - N_{H_2Oliq}^{a,out} + N_{H_2Ovap}^{a,el \rightarrow ch} \right] \end{array} \right. \quad (2.59)$$

Considering the anode channel depth ($e_{a,ch}$), the volume of the anode channels can be estimated by $V_{ch}^a = 0.5LWe_{a,ch}$. The second case is similar to the first case of the cathode side. In this case, the saturation in the anode side is higher than zero and the water concentration in the anode channel is equal to the concentration of the saturated water at the temperature of the anode. The derivative equations for this case are as follows:

$$\left\{ \begin{array}{l} \text{.Case } C_{H_2O}^{a,ch}(T_a) = C_{sat}^{T_a} \quad \& \quad S_a > 0 \\ V_{ch}^a \frac{dS_a}{dt} = \frac{M_{H_2O}}{\rho_{H_2Oliq}} \left[N_{H_2Ovap}^{a,in} - N_{H_2Ovap}^{a,out} - N_{H_2Oliq}^{a,out} + N_{H_2Ovap}^{a,el \rightarrow ch} - V_{ch}^a \left(\frac{dC_{sat}^{T_a}}{dT_a} \frac{dT_a}{dt} \right) \right] \\ \frac{dC_{H_2O}^{a,ch}}{dt} = \frac{dC_{sat}^{T_a}}{dT_a} \frac{dT_a}{dt} \end{array} \right. \quad (2.60)$$

Where dT_a/dt is the result of the heat transfer model and $\frac{dC_{sat}^{T_a}}{dT_a}$ is calculated as follows:

$$\frac{dC_{sat}^{T_a}}{dT_a} = C_{sat}^{T_a} \left(\frac{5096.23}{T_a^2} - \frac{1}{T_a} \right) \quad (2.61)$$

The third case is similar to the third case of the cathode side. This case is summarized in the following equation:

$$\left\{ \begin{array}{l} \text{.Case } C_{H_2O}^{a,ch}(T_a) = C_{sat}^{T_a} \quad \& \quad S_a = 0 \\ \text{if } \left[N_{H_2Ovap}^{a,in} - N_{H_2Ovap}^{a,out} - N_{H_2Oliq}^{a,out} + N_{H_2Ovap}^{a,el \rightarrow ch} - V_{ch}^a \left(\frac{dC_{sat}^{T_a}}{dT_a} \frac{dT_a}{dt} \right) \right] > 0 \\ V_{ch}^a \frac{dS_a}{dt} = \frac{M_{H_2O}}{\rho_{H_2Oliq}} \left[N_{H_2Ovap}^{a,in} - N_{H_2Ovap}^{a,out} - N_{H_2Oliq}^{a,out} + N_{H_2Ovap}^{a,el \rightarrow ch} - V_{ch}^a \left(\frac{dC_{sat}^{T_a}}{dT_a} \frac{dT_a}{dt} \right) \right] \\ \frac{dC_{H_2O}^{a,ch}}{dt} = \frac{dC_{sat}^{T_a}}{dT_a} \frac{dT_a}{dt} \\ \text{else} \\ \frac{dS_a}{dt} = 0 \\ V_{ch}^a \frac{dC_{H_2O}^{a,ch}}{dt} = N_{H_2Ovap}^{a,in} - N_{H_2Ovap}^{a,out} - N_{H_2Oliq}^{a,out} + N_{el \rightarrow ch}^a \end{array} \right. \quad (2.62)$$

(k) Response to a current step for an imposed pressure condition

As mentioned before (Figure 2-6), the transfer of water in the perpendicular direction to the membrane is highly dependent on the temperature field. If the anode plate is hotter than the anode electrode, all the produced water flow will be discharged to the cathode. This particular thermal boundary condition is used to determine the flow of water discharged on the cathode side. As in the parameter estimations of the diphasic flow model, the temperatures of the anode and cathode plates are imposed to 67.5°C and 62.5°C respectively. Under these conditions, all the produced water flow is evacuated from the cathode side ($N_{H_2Ovap}^{el \rightarrow ch} = ILW/2F$).

Figure 2-10 (c) shows the time evolution of the experimental stoichiometry of the air St_{air} after imposing a current step for a boundary condition of imposed pressure. The pressure drop is experimentally regulated by a pressure controller. This device was mounted before the membrane humidifier to avoid condensation problems. The cathode compartment is initially dry ($S_0=0$). It can be seen that the pressure drop ΔP changes slightly over time (Figure 2-10 (a)).

This can be explained by the fact that the pressure controller imposes a constant pressure before the membrane humidifier. As the flow rate decreases due to the appearance of the liquid water in the cell, the pressure drop in the humidifier slightly decreases (~ 1.5 mbar), and therefore the pressure at the inlet of the fuel cell ΔP increases. For this reason, the experimental measurement of $\Delta P(t)$, which is shown in Figure 2-10 (a), is considered as an input of the model. Figure 2-10 (c) shows ten experimental results (in black) that have been obtained under the same conditions. Because of the stochastic nature of the airflow, it is useful to perform the same experiment several times. Considering the imposed pressure drop condition as Figure 2-10 (a), the experimental results are compared to the simulation results in Figure 2-10 (c). The simulation result is obtained by the numerical resolution of (2.47)-(2.51). The model also predicts the evolution of the saturation over time (Figure 2-10 (b)).

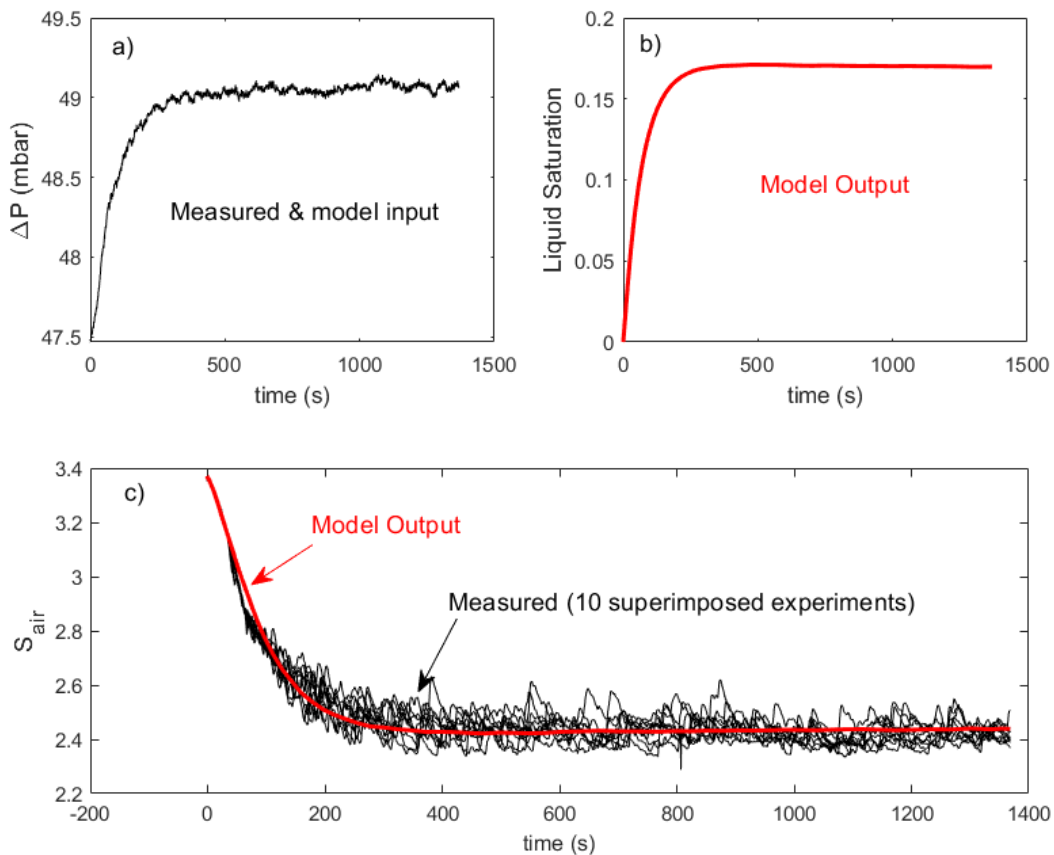


Figure 2-10. Response to a current step of 0.67 A/cm². The cathode compartment is initially dry ($S_c=0$). $T_{dp}=60^\circ\text{C}$. $T_c=62.5^\circ\text{C}$. $T_a=67.5^\circ\text{C}$. At time $t=0$ the average current density increases from 0 to 0.67 A/cm². a) applied pressure drop on the cathode side. b) Simulation result of liquid water saturation in the cathode channel. c) Air stoichiometry as a function of time. This simulation has been performed using the accurate liquid relative permeability corresponding to the current density (red curve in Figure 2-9).

In summary, the proposed model associated with the method of estimating its parameters (intrinsic and relative permeability) makes it possible to simulate the two-phase flow in the channels. Some improvement has to be done to correctly model the liquid flow, but these first results are rather encouraging. The fast stochastic variations of the flow rate around the average value are not modeled. However, these fast variations around the average flow rate are often responsible for transitory periods of fuel starvation. This model is therefore not complete, but it allows evaluating average flow rates. The lower this average flow rate (Stoichiometry close

to 1), the higher the risk of fuel starvation. The characterization and modeling of the fast variations in the flow rate around the average value will also be the subject of future studies.

2.4. Charge transfer

The materials and gases near the active catalytic sites can produce faradic currents. One of the most important electrochemical couples that has a huge impact on the potential of the cell is the water oxidation/oxygen reduction. Considering this reaction as the main reaction and neglecting other reactions to produce faradic current, the equivalent circuit of the charge transfer model is depicted in Figure 2-11.

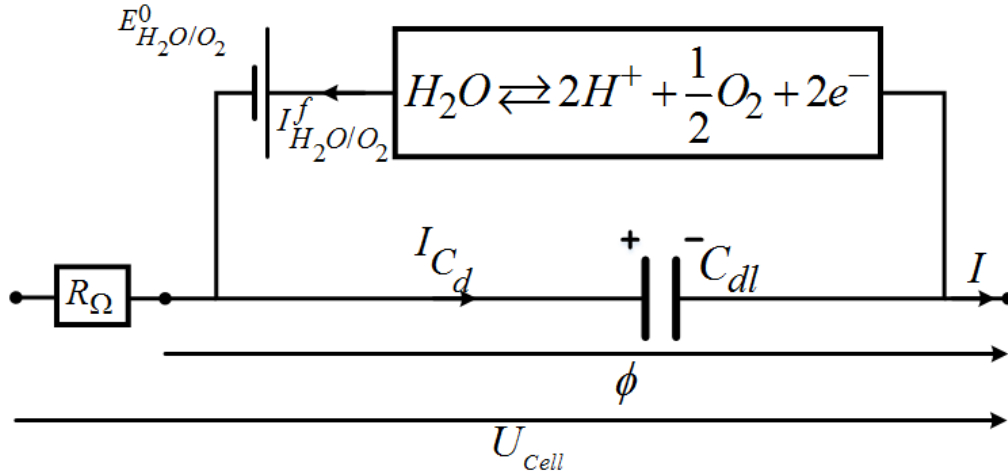


Figure 2-11. Electrical equivalent circuit of the charge transfer model.

The Nernst equation can be used to calculate the potential of an electrochemical reaction. Based on the Nernst equation, the potential of the water oxidation/oxygen reduction can be calculated as follows [119]:

$$E_{H_2O/O_2}^0 = E_{H_2O/O_2}^{ref} + \frac{RT_m}{4F} \ln \left(\frac{C_{O_2}^{c,el}}{C_{O_2}^{ref}} \right) - \frac{RT_m}{2F} \ln \left(\frac{C_{H_2O}^{c,el}}{C_{H_2O}^{ref}} \right) \quad (2.63)$$

where E_{H_2O/O_2}^{ref} is the standard cell potential, $C_{O_2}^{ref}$ and $C_{H_2O}^{ref}$ are respectively the reference values of the oxygen and water concentrations for obtaining the standard cell potential, $C_{H_2O}^{c,el}$ is the water concentration in the cathode electrode which is calculated in the preceding section. The reference values of the oxygen and water concentrations can be calculated as follows:

$$\begin{cases} C_{O_2}^{ref} = 0.21 \frac{P_0}{RT_{ref}} \\ C_{H_2O}^{ref} = \frac{P_0}{RT_{ref}} e^{\left(13.669 - \frac{5096.23}{T_{ref}} \right)} \end{cases} \quad (2.64)$$

where T_{ref} is equal to 333°K. Considering the potential of the water oxidation/oxygen reduction, the faradic current density is given by the Butler-Volmer law [119]:

$$I_{H_2O/O_2}^f = LW\gamma I_0^{H_2O/O_2} \left[\frac{C_{H_2O}^{c,el}}{C_{H_2O}^{ref}} e^{\frac{F\alpha_{H_2O/O_2}^{ox,Pt}}{RT_m}(\phi - E_{H_2O/O_2}^0)} - \frac{C_{O_2}^{c,el}}{C_{O_2}^{ref}} e^{-\frac{F\alpha_{H_2O/O_2}^{red,Pt}}{RT_m}(\phi - E_{H_2O/O_2}^0)} \right] \quad (2.65)$$

where $I_0^{H_2O/O_2}$ is the exchange current density (A/m^2), γ is the roughness factor of the electrode, ϕ is the cathode electrode potential, $\alpha_{H_2O/O_2}^{ox,Pt}$ is the anodic charge transfer coefficient, and $\alpha_{H_2O/O_2}^{red,Pt}$ is the cathodic charge transfer coefficient. The current density of the cell can be obtained by the Kirchhoff law [119]:

$$I = I_{C_{dl}} - I_{H_2O/O_2}^f \quad (2.66)$$

where $I_{C_{dl}}$ is the current which passes through the double-layer capacitance of the cell and which can be obtained from the following equation [119]:

$$I_{C_{dl}} = -LWC_{dl} \frac{d\phi}{dt} \quad (2.67)$$

where C_{dl} is the double-layer capacity of the cell. The voltage of the cell can be calculated with the calculated current from the following equation [119]:

$$U_{cell} = \phi - R_{\Omega}ILW \quad (2.68)$$

where R_{Ω} is the ohmic resistance which is the sum of two resistances:

$$R_{\Omega} = R_m + R_e \quad (2.69)$$

where R_e is the electrical resistance of the cell to the electrons and R_m is the membrane and electrodes protonic resistance which depends on the water content of the membrane and its temperature [138]:

$$R_m = \frac{e_m}{3 \times 10^{-1} e^{\left[\frac{1263}{303} \left(\frac{1}{T_m} - \frac{1}{T_m} \right) \right]}} \left[\frac{1}{(5.139\lambda_a - 3.26)^+} + \frac{1}{(5.139\lambda_m - 3.26)^+} + \frac{1}{(5.139\lambda_c - 3.26)^+} \right] \quad (2.70)$$

As seen in this equation, the membrane thickness is divided into three parts. The water content of the membrane, anode, and cathode is taken into account to calculate the resistance of three parts. These resistances are in series and as a result, the equivalent resistance is equal to the sum of all the individual resistors.

2.5. Hydrogen starvation detection

The droplets of water inside the channel can block the active sites. In this case, the fuel starvation can occur for the cell. Therefore, the hydrogen flow rate at the outlet of the channel must be positive to avoid fuel starvation. The hydrogen flow rate at the outlet of the channel can be calculated based on (2.57). Considering (2.58) as the permeability function, the hydrogen flow rate at the outlet of the anode channel is as follows:

$$N_{H_2}^{out} = N_{H_2}^{in} - \frac{ILW}{2F} = \frac{\left(\frac{P_0 + \frac{\Delta P_a}{2} k_a (1 - S_a)^\alpha}{RT_a \mu_{mix}(T_a)} \Delta P_a \right) + \frac{ILW}{4F} \left(\frac{P_0}{P_0 - P_{sat}(T_a)} \right)}{1 + \frac{1}{2} \left(\frac{RH_a^{in} P_{sat}(T_a)}{P_0 + \Delta P_a - RH_a^{in} P_{sat}(T_a)} + \frac{P_{sat}(T_a)}{P_0 - P_{sat}(T_a)} \right)} - \frac{ILW}{2F} \quad (2.71)$$

The positive hydrogen flow rate at the outlet of the channel leads to the appearance of a condition on the saturation level in the channel to avoid the fuel starvation:

$$S_a \leq 1 - \sqrt[\alpha]{\left(\frac{ILW}{2F} + \frac{ILW}{4F} \left(\frac{RH_a^{in} P_{sat}(T_a)}{P_0 + \Delta P_a - RH_a^{in} P_{sat}(T_a)} - 1 \right) \right)} \frac{RT_a \mu_{mix}(T_a)}{k_a \left(P_0 + \frac{\Delta P_a}{2} \right) \Delta P_a} \quad (2.72)$$

Based on the equations that were explained in this chapter, a model is developed as follows:

$$\frac{d}{dt} \begin{pmatrix} T_a \\ T_c \\ T_m \\ C_{O_2}^{c,ch} \\ S_a \\ S_c \\ C_{H_2O}^{a,ch} \\ C_{H_2O}^{c,ch} \\ \lambda_m \\ \phi \end{pmatrix} = \Gamma \begin{pmatrix} T_a \\ T_c \\ T_m \\ C_{O_2}^{c,ch} \\ S_a \\ S_c \\ C_{H_2O}^{a,ch} \\ C_{H_2O}^{c,ch} \\ \lambda_m \\ \phi \end{pmatrix} \quad (2.73)$$

The input/output parameters of the model are shown in Figure 2-12 along with the state variables. As seen in this figure and considering (2.66) and (2.68), the voltage of the cell can be obtained as a function of its current and vice versa. In addition to the current or voltage as input, the temperature of the adjacent cells, the cooling temperature at the anode and cathode side, the pressure drop inside the channels, the relative humidity at the anode channel inlet, and the concentration at the cathode channel inlet are the inputs of this model. Notable that, a more accurate model can be obtained for the state variables by taking the measured voltage and current as input parameters.

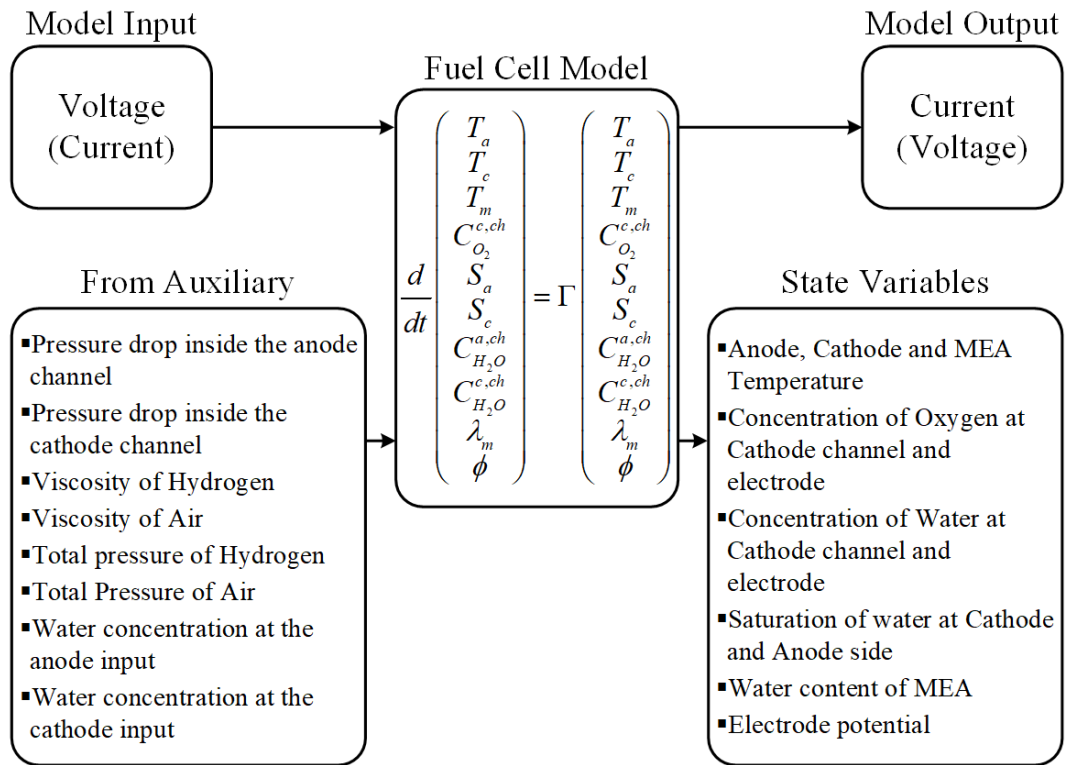


Figure 2-12. Block diagram of the reduced-order transient PEMFC model

Since the cooling fluid temperature of each side can be separately defined, this model can be used to investigate the impact of a temperature gradient on a cell. Since the pressure drop inside the channels along with the temperature of the neighboring cells is the input of the model, this model can be used to simulate a stack. For instance, three cells connected by linking the inputs of one cell model to another cell model output as seen in Figure 2-13 to simulate a stack. In this figure, the same pressure drops and current are used for the cells while they are electrically connected in series. Notable that the pressure drop between to channels is neglected and as a result, all the cells are under the same pressure drops. However, it is easy to impose different pressure drops or this difference between the pressure drops inside the cell channels can be modeled by some simple resistances between the channels.

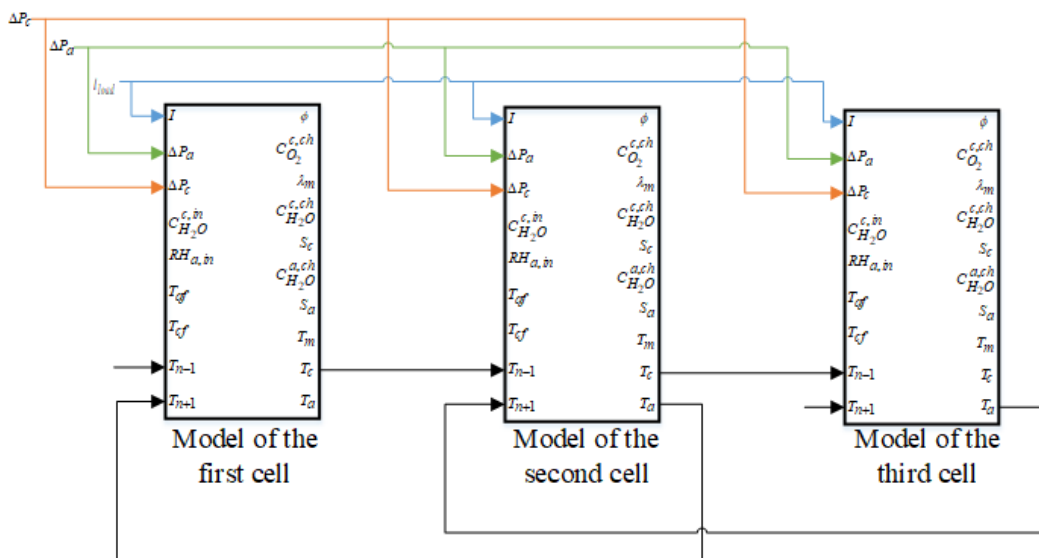


Figure 2-13. Stack simulation (The cells are under the same pressure drop and they are thermally connected.).

2.6. Simulation Results

To evaluate the proposed fuel cell model, the Matlab tool is used. This system of differential equations is solved by a numerical calculation. Matlab solver can solve such a system of equations based on the Runge-Kutta method. There are different methods in Matlab that can solve the Ordinary Differential Equation (ODE). The proposed model can force down the solver step size to an unreasonably small level due to the if-else lathers that must be used to consider the different conditions of saturation level and water concentration in the channels. Such systems are called Stiff ODE. Since ode15s has shown the best performance for most of the Stiff ODE problems, this method is used to solve the proposed model.

2.6.1. Simulation of one cell

The parameters that are used for the simulation purpose are shown in Table 2.1. In the proposed simulation, the current density is increased from zero to 2 A/cm^2 in 600 s then is decreased to zero. As seen in Figure 2-14, the boundary condition of the pressure drops inside the anode and cathode channels is considered in this simulation.

Table 2.1. Parameters of the model for simulations

Parameter	Unit	Value	Description	Origin
L	m	0.3	Channel length	Measurement
W	m	0.01	Channel width	Measurement
e_{GDL}	m	2.5×10^{-4}	GDL thickness	Equivalent 1D value considering 2D diffusion between the channel and the rib
λ_{GDL}	$W/(m \text{ } ^\circ K)$	0.3	Effective thermal conductivity of GDL	[28]
ρ_{MEA}	kg/m^3	2020	Volumetric mass density of the membrane	Nafion 212
C_{MEA}	$J/(kg \text{ } ^\circ K)$	1000	Specific heat capacity of the MEA	PTFE value
e_{MEA}	m	5×10^{-5}	Membrane thickness	Nafion 212
D_{0m}	m^2/s	4×10^{-10}	Water diffusion coefficient through the membrane	[119]
$D_{H_2O}^{a,GDL}$	m^2/s	25×10^{-6}	Effective water diffusion coefficient through the anodic GDL	[119]
$D_{H_2O}^{c,GDL}$	m^2/s	12×10^{-6}	Effective water diffusion coefficient through the cathode GDL	[119]

$D_{O_2}^{0,GDL}$	m^2/s	12×10^{-6}	Effective oxygen diffusion coefficient through the cathode GDL	[119]
ρ_p	kg/m^3	2000	Plate volumetric mass density	graphite
C_p	$J/(kg \text{ } ^\circ K)$	7200	Specific heat capacity of plates	graphite
e_p	m	2×10^{-3}	Plate thickness	Assumption
R_f^{th}	$^\circ K/W$	$R_{GDL}^{th}/3$	Thermal resistance	Assumption
R_c^{th}	$^\circ K/W$	R_{GDL}^{th}	Thermal resistance	Assumption
$e_{c,ch}$	m	5.1×10^{-4}	Cathode Channel depth	The value that has been used for estimating the relative permeabilities
$e_{a,ch}$	m	4.7×10^{-4}	Anode channel depth	The value that has been used for estimating the relative permeabilities
ρ_{dry}	kg/m^3	2020	The volumetric mass density of the dry membrane	Nafion 212
EW	kg	1.1	The equivalent weight of the membrane	Nafion 212
ξ	-	0.45	Electro-osmosis coefficient	[141]
R_e	Ω	$2 \times 10^{-6} \Omega$	Electronic resistance	Assumption
C_{dl}	F	$200 F$	Double-layer capacitance	Assumption
γ	-	200	Roughness factor of the electrode	Assumption
$I_0^{H_2O \setminus O_2}$	A/m^2	0.05	Exchange current density	Assumption
$E_{H_2O \setminus O_2}^{ref}$	V	0.95	Open-circuit voltage of the cell	Assumption
$\alpha_{H_2O \setminus O_2}^{ox,Pt}$	-	1	Anodic charge transfer coefficient	Assumption
$\alpha_{H_2O \setminus O_2}^{red,Pt}$	-	1	Cathodic charge transfer coefficient	Assumption
k_g^a	m^3/s	1.5×10^{-14}	Intrinsic permeability of the gas at the anode side	Measured

k_g^c	m^3/s	1×10^{-13}	Intrinsic permeability of the gas at the cathode side	Measured
α	-	3		Measured
$k_{liq}^c = k_{liq}^a$	m^3/s	8.8394×10^{-15}	Intrinsic permeability of the liquid water	Assumption

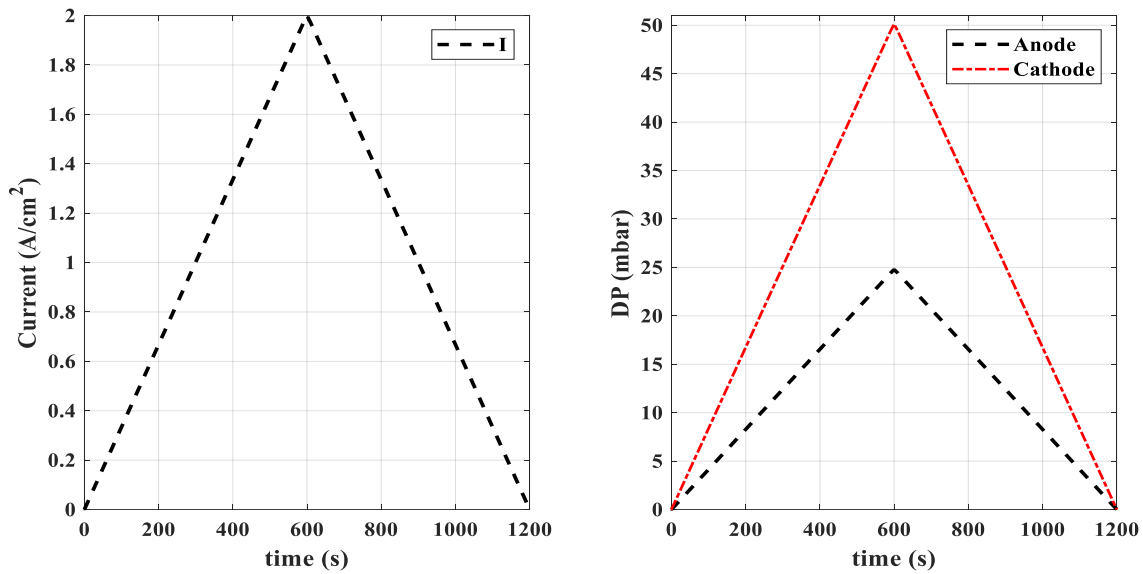


Figure 2-14. Applied current density and inlet/outlet pressure drop.

The dew point temperature at the cathode and anode inlets are applied with bubblers at 50°C (cathode and anode). The temperature of the cooling fluid is set to 60°C as the temperature of the neighboring cells.

The simulation results of the potential and the output voltage of the cells are depicted in Figure 2-15. The difference between the potential and voltage is due to the Joule resistance. I-V characteristic can be drawn based on this obtained voltage. The I-V characteristic of the cell is demonstrated in Figure 2-16. As seen in this figure, the polarization curves based on the increasing and decreasing of the current are slightly different. This difference is explained by the lower airflow when decreasing the current density. This lower airflow is a consequence of the appearance of liquid water in the channels when the pressure loss is kept constant. The hydration time constant of the membrane is well considered. In practice, this difference is rather related to the formation of platinum oxides at high potentials which are less active for oxygen reduction reaction than the bare platinum.

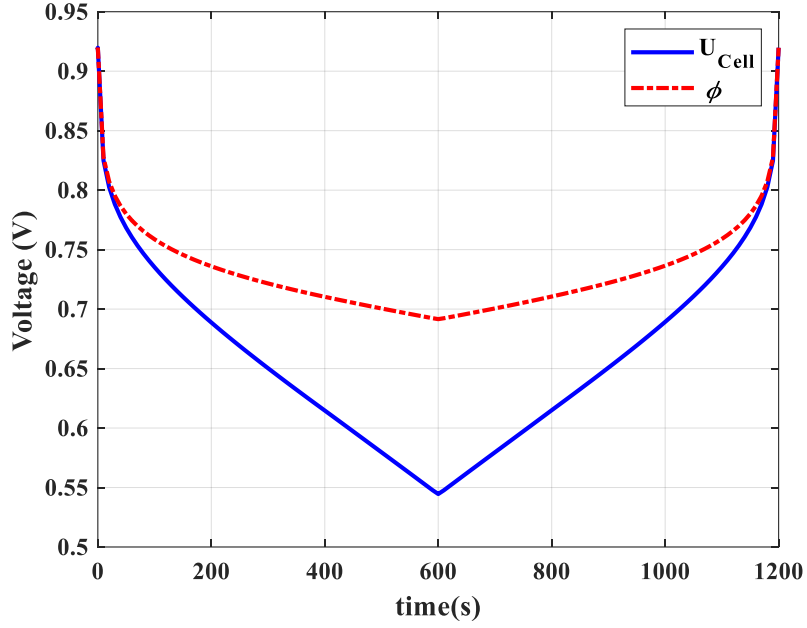


Figure 2-15. Simulation result of the voltage of the cell and cathode potential.

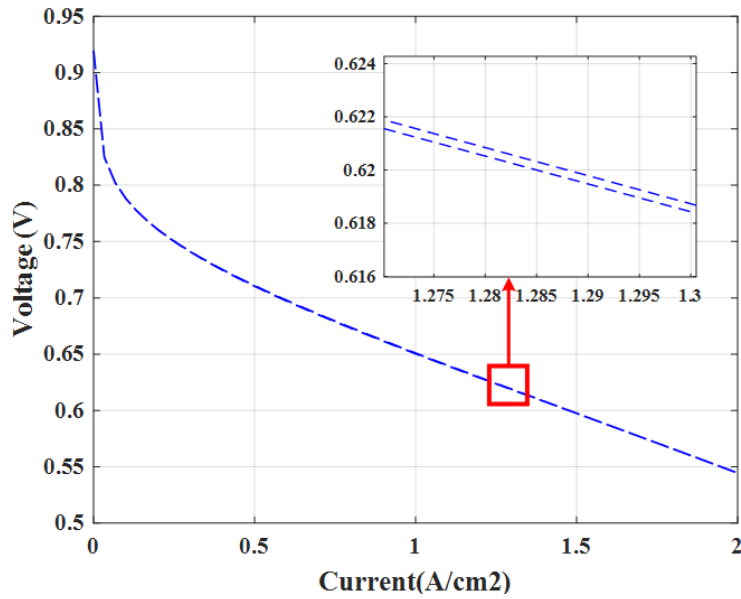


Figure 2-16. I-V characteristic simulation of a single cell. A higher saturation level inside the channels leads to a lower airflow during the decreasing the current. As a result, a negligible voltage difference exists between the increasing and decreasing current densities.

The temperature of the anode, cathode, and the MEA is shown in Figure 2-17. As seen in this figure, the temperature is increased by increasing the applied current and vice versa. The stoichiometry of Hydrogen and air can be calculated as follows:

$$\begin{cases} St_{H_2} = \frac{N_{H_2}^{in}}{ILW/2F} \\ St_{O_2} = \frac{0.21N_{air}^{in}}{ILW/4F} \end{cases} \quad (2.74)$$

where $ILW/2F$ and $ILW/4F$ are respectively the molar flow rate of hydrogen and oxygen that participate in the reaction. These two parameters are also shown in Figure 2-17. The stoichiometry of oxygen and hydrogen respectively move around 2.5 and 1.5 due to the appearance of liquid water inside the channels. The presence of liquid water in the channels is verified by the liquid water flow rate at the outlet of the channels as shown in Figure 2-17. The presence of the liquid water in the cathode and anode channels can be further confirmed by the liquid water saturation in the channels. The saturation level is depicted in Figure 2-18 during the simulation. As seen in this figure, the relative humidity in the channels is kept close to one due to the high relative humidity of the inlet gases. However, the relative humidity in the electrodes is decreased by increasing the current density and pressure drop due to the temperature rise. The relative humidity in the channels can be calculated by the water vapor concentration in the channels:

$$\begin{cases} RH^{a,ch} = \frac{C_{H_2O}^{a,ch}}{C_{sat}^{T_a}} \\ RH^{c,ch} = \frac{C_{H_2O}^{c,ch}}{C_{sat}^{T_c}} \end{cases} \quad (2.75)$$

where $C_{sat}^{T_a}$ and $C_{sat}^{T_c}$ are calculated by (2.20). The relative humidity in the electrodes can be calculated as follows:

$$\begin{cases} RH^{a,el} = \frac{C_{H_2O}^{a,el}}{C_{sat}^{T_m}} \\ RH^{c,el} = \frac{C_{H_2O}^{c,el}}{C_{sat}^{T_m}} \end{cases} \quad (2.76)$$

where $C_{sat}^{T_m}$ is calculated by (2.20). Since the membrane temperature is higher than the anode and cathode channels temperatures, the concentration of the saturated water in the electrodes is higher than its value in the channels. As a result, the relative humidity in the electrodes decreases for the high value of the membrane temperature. The water content simulation results are also provided in Figure 2-18. As the temperature increases due to the increase in the current density, the concentration of the saturated vapor increases. As a result, even despite the increase in water concentration in the electrodes, the water content decreases. The total water flow-rate and membrane to channel water flow-rates are shown in Figure 2-19.

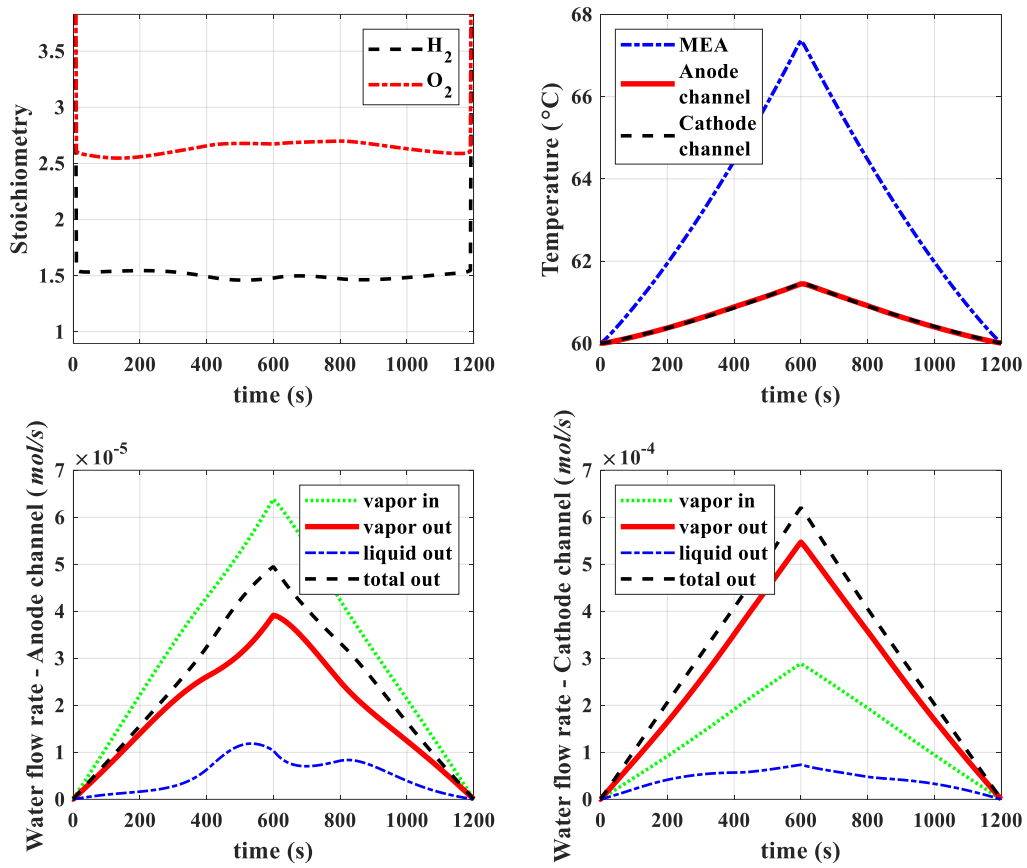


Figure 2-17. Simulation results of the stoichiometry, temperatures, and water flow-rates in the anode and cathode sides.

The simulation results of the oxygen concentration in the cathode electrode and channel are demonstrated in Figure 2-20. The oxygen concentration in the cathode electrode is the result of both the increased water vapor concentration with temperature and the diffusion limitation through the GDL.

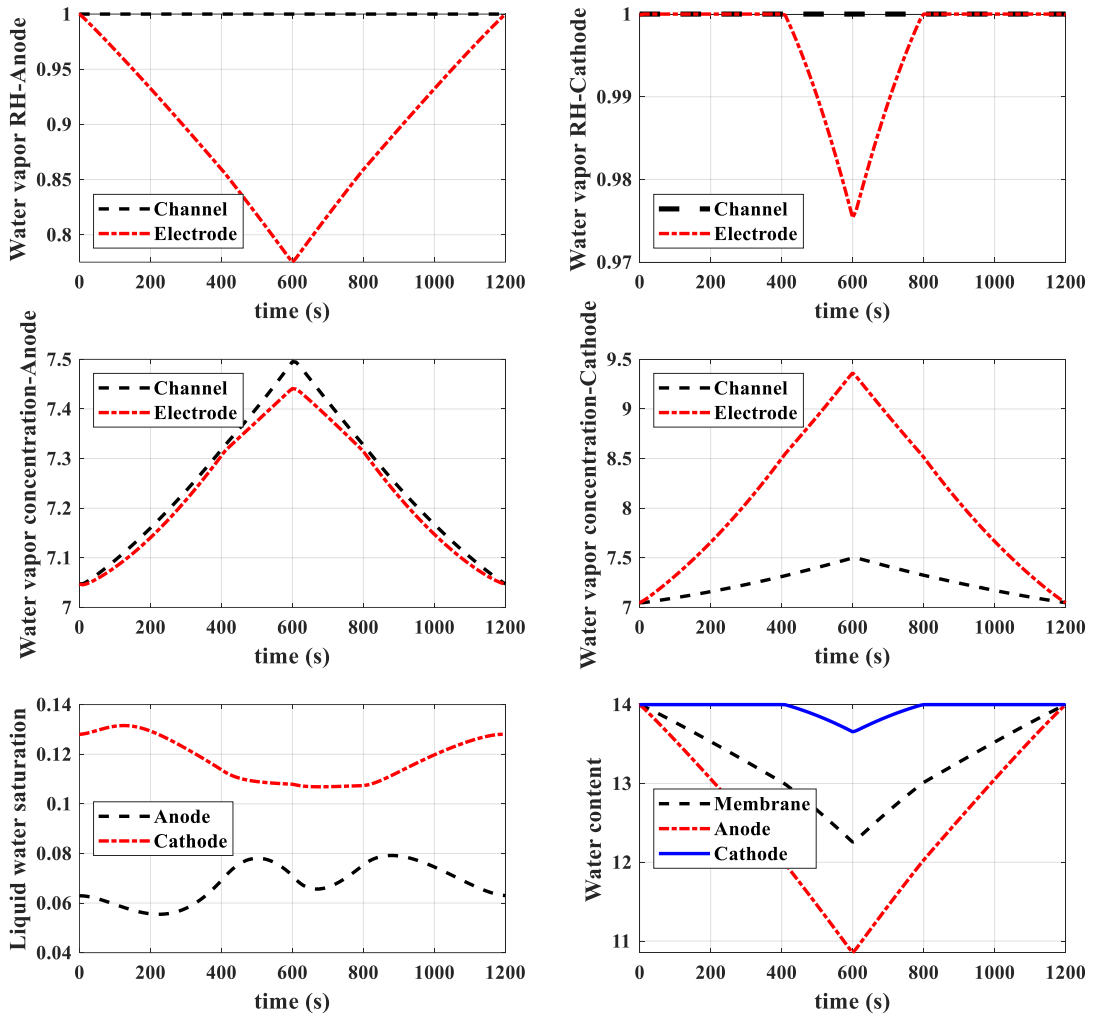


Figure 2-18. Simulation results of the water vapor relative humidity and concentration, liquid water saturation in the channels, and water content.

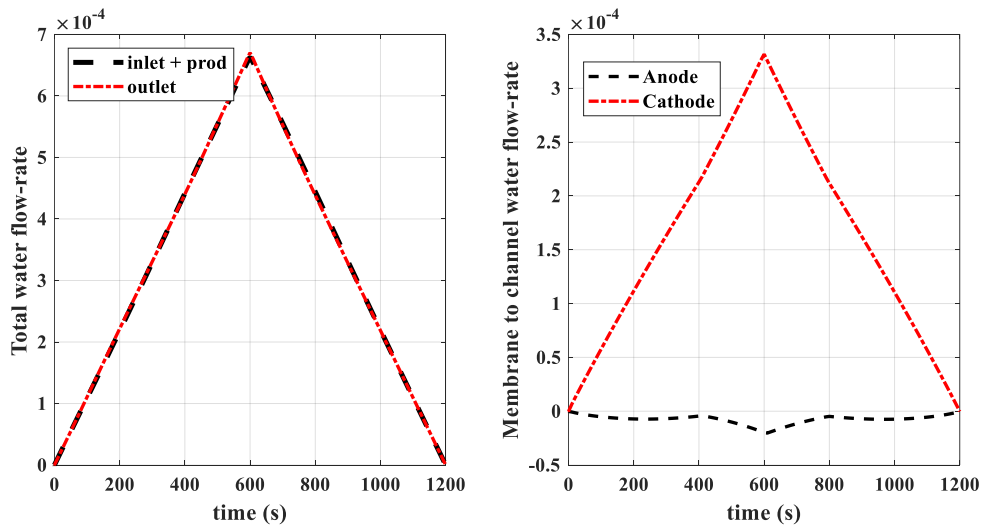


Figure 2-19. Simulation results of the total water flow-rates and membrane to channel water flow-rates

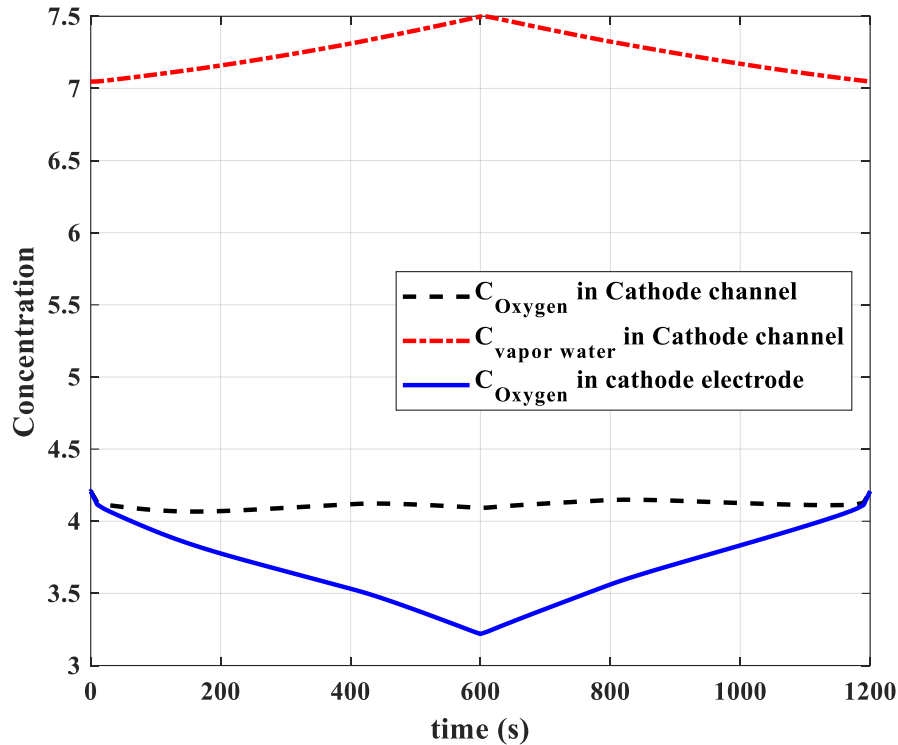


Figure 2-20. Simulation results of the oxygen concentration

These primary simulation results show how the model behaves. However, it is necessary to compare it with experimental results to initially estimate the unknown parameters, then in a second time to validate the model. It is an extra perspective.

The last simulation was for one cell in which the pressure drop inside the channels was the boundary condition. In the following simulation, the propagation of a fault from a cell to adjacent cells is simulated.

2.6.2. Stack simulation

Based on the structure depicted in Figure 2-21 and Figure 2-13, a stack consisting of 5 cells is modeled. Five cells are assumed to be connected in series. The parameters of the cell models are the same as illustrated in Table 2.1. The dew point temperature at the cathode and anode inlets are applied with bubblers at 50°C (cathode and anode). Two simulations are performed for this stack. The temperature of the cooling fluid is set to 60°C. As seen in Figure 2-21, the stack is insulated from the ambient and clamping plates. As a result, the anode side of the first cell and cathode side of the last cell are just connected to cooling fluid. Three simulations are performed to evaluate the capability of the model in simulating a stack.

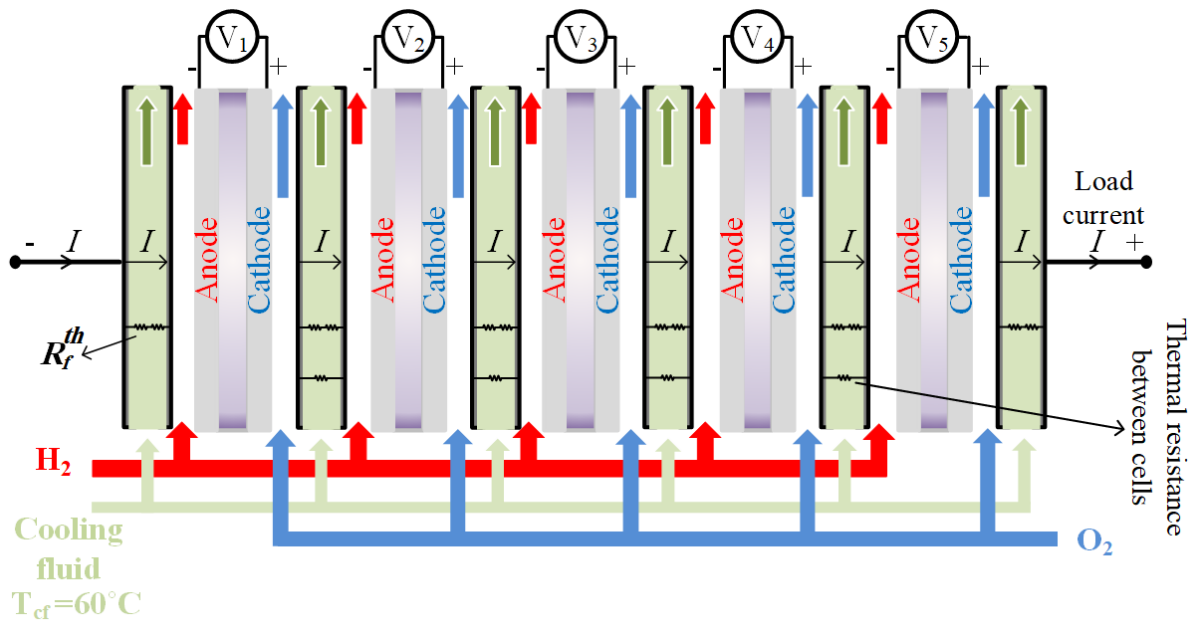


Figure 2-21. Block diagram of a stack model consisting of 5 cells

In the first simulation, the cooling fluid temperatures of the third cell is increased from 60°C to 75°C at 500 s to simulate a transient clogging of the cooling flow channels. These temperatures decreased to their nominal value of 60°C at 3500 s. A slope of 0.08 is used to increase or decrease the temperatures. The same load current of 30 A passes through all cells in this simulation. The pressure drop inside the anode and cathode channel is fixed to 11 *mbar* and 25 *mbar* respectively. The increase in the cooling fluid temperature leads to an increase in the temperature of the anode and cathode plates of the third cell (Figure 2-22). This temperature increase impacts on the adjacent cells. Since the temperature change is very intense, it impacts both sides of the adjacent cells. The effect of these temperature increases is more on the anode plate of the fourth cell and the cathode plate of the second cell. As seen in Figure 2-22, a temperature gradient appears between the anode and cathode of the second and fourth cells. The second and fourth cells also impact the first and fifth cells respectively. The anode plate of the fourth/fifth cell is warmer than its cathode plate. But the cathode plate of the first/second cell is warmer than its anode plate. These temperature gradients lead to the liquid water saturation level changes. As seen in Figure 2-23, the anode channel/cathode channel saturation level of the first and second cells increased/decreased due to their temperature gradients. Besides, the anode channel/cathode channel saturation level of the first and second cells decreased/increased due to their temperature gradients. The higher temperature changes, the higher saturation level changes. These saturation levels inversely influence dry gas flow rates. In other words, the saturation level increase leads to a reduction in the dry gas flow rate. The dry gas flow rate has a transient behavior once the saturation level approaches to zero or increased from zero. Since the water droplet appearance or disappearance is a time-consuming process, the viscosity and the water vapor concentration change influence the dry gas flow rates before the saturation level changes. For instance, the dry air flow rate of the third cell initially decreases after 500 s due to the viscosity and water vapor flow rate changes. Then it increases due to the decrease of the water saturation in the cathode channel of the third cell. Regarding the changes in the dry gas flow rates (Figure 2-24), the stoichiometry of hydrogen and oxygen changes.

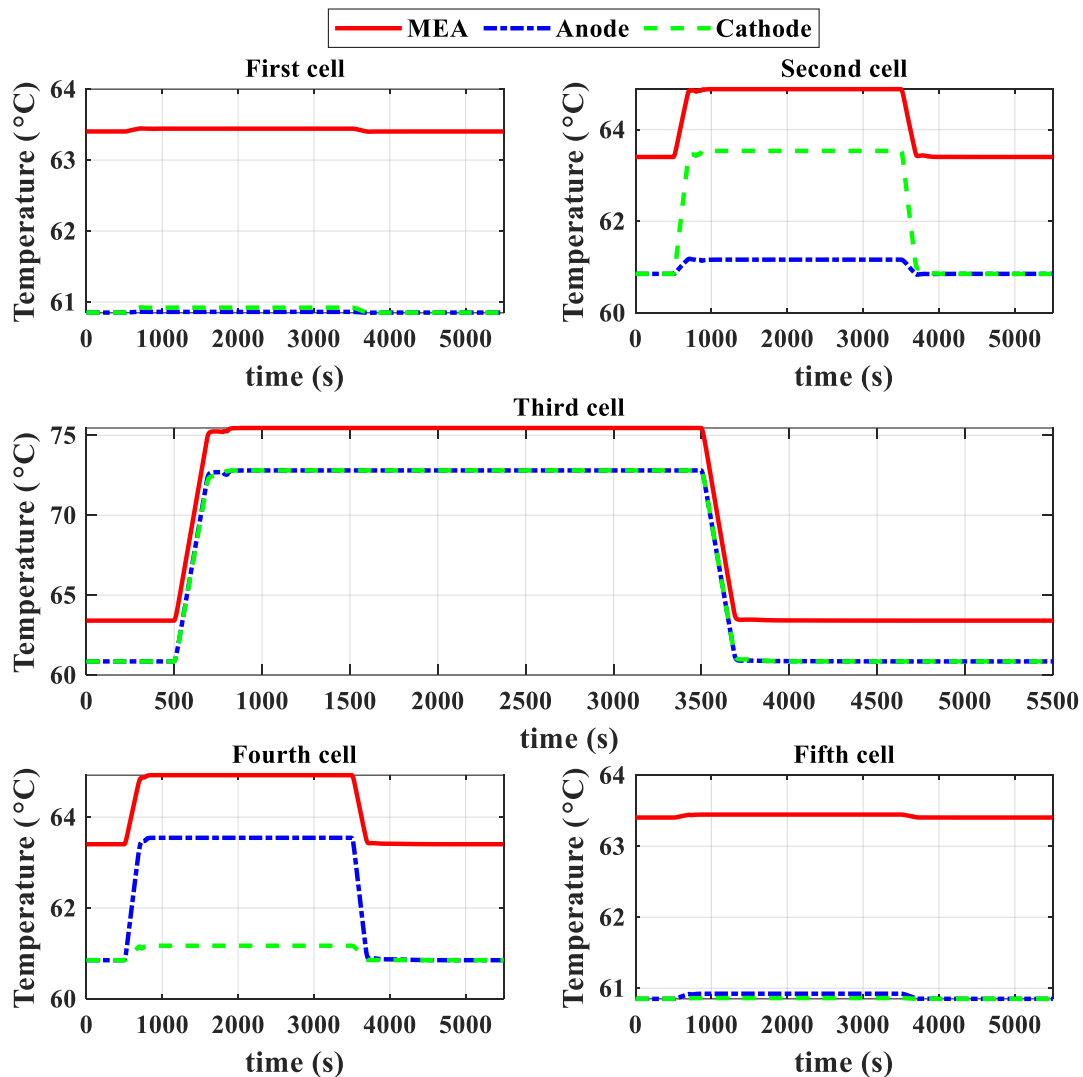


Figure 2-22. Simulation results of the cell temperatures when the cooling fluid temperatures of the third cell increased from 60 °C to 75 °C at 500 s and decreased to its nominal value of 60 °C at 3500 s. A constant current of 30A passing through the cells (The air and hydrogen pressure drops are applied).

Since both side temperatures of the third cell increased (in the interval of 500 s and 3500 s), its membrane water content decreases as shown in Figure 2-24. The changes in this parameter for the other cells are not strictly sensible compared to the third cell. Since the membrane water content of the third cell is lower than its value for the other cells in the interval of [500 s-3500 s], its membrane becomes more resistive and as a result its voltage lower than others (Figure 2-24). As a result, the stack voltage decreases for the interval of the fault as depicted in Figure 2-25. The applied current density of the cells is also shown in this figure.

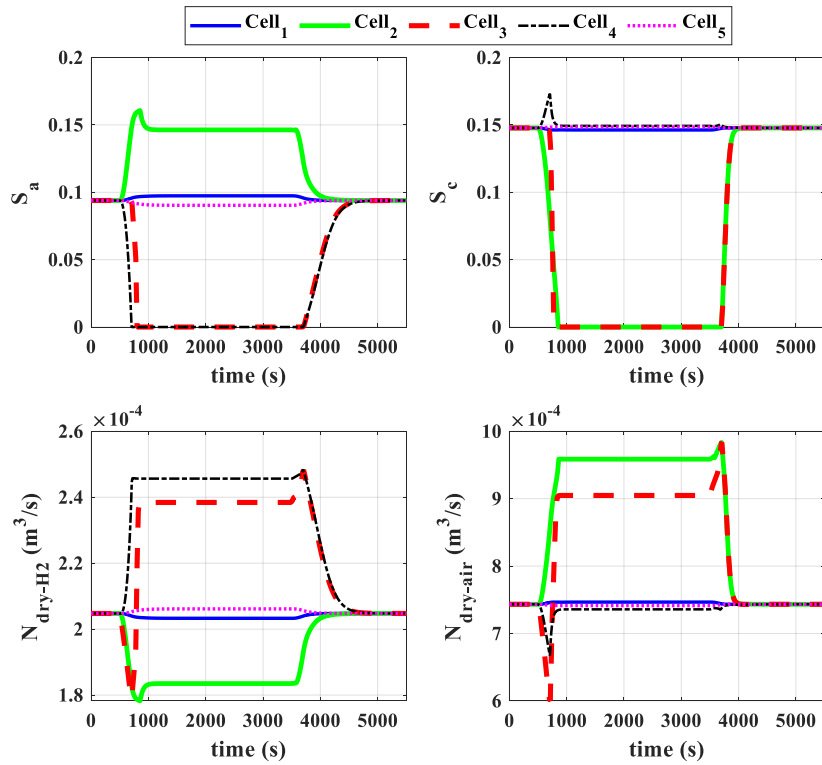


Figure 2-23. Simulation results of the dry gas flow rates and saturation level inside the channels when the cooling fluid temperatures of the third cell increased from 60 °C to 75 °C at 500 s and decreased to its nominal value of 60 °C at 3500 s. A constant current of 30A passing through the cells (The air and hydrogen pressure drops are applied).

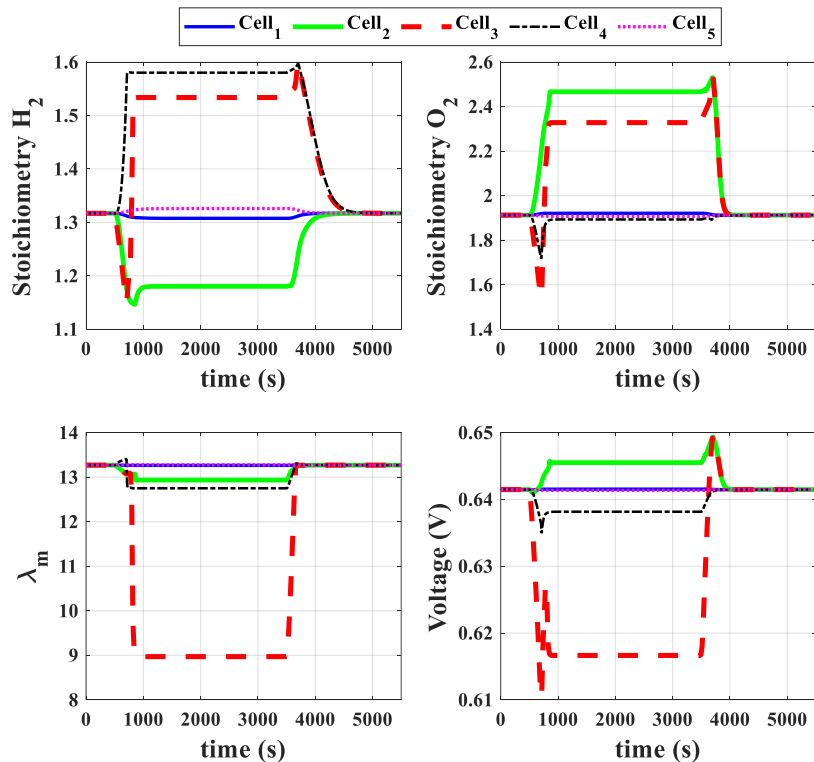


Figure 2-24. Simulation results of the stoichiometry of hydrogen and oxygen, membrane water content, and the cell voltages when the cooling fluid temperatures of the third cell increased from 60 °C to 75 °C at 500 s and decreased to its nominal value of 60 °C at 3500 s. A constant current of 30A passing through the cells (The air and hydrogen pressure drops are applied).

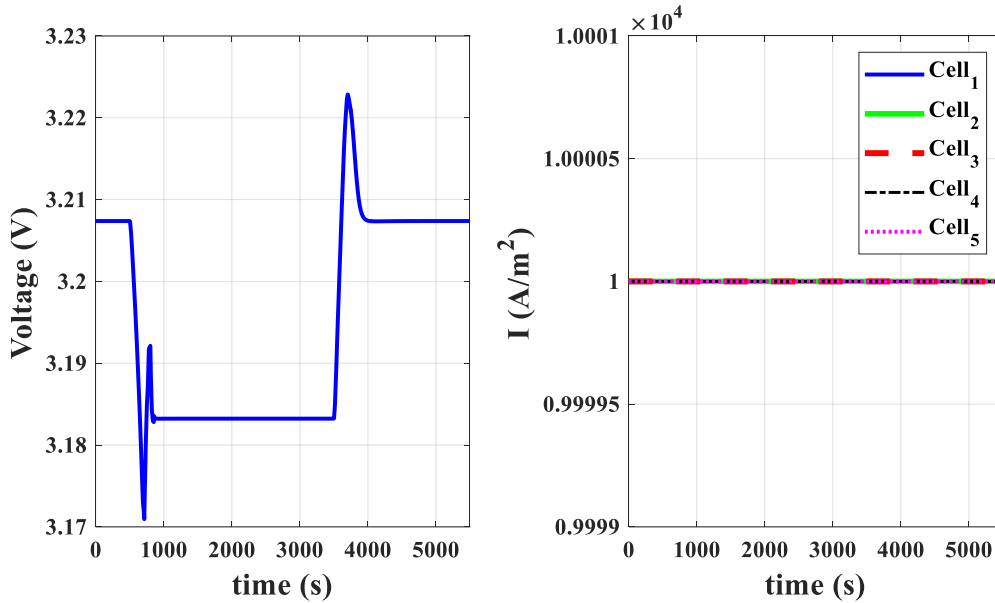


Figure 2-25. Simulation results of the stack voltage and applied current densities when the cooling fluid temperatures of the third cell increased from 60 °C to 75 °C at 500 s and decreased to its nominal value of 60 °C at 3500 s. A constant current of 30A passing through the cells (The air and hydrogen pressure drops are applied).

In the second simulation, the same load current of 10 A passes through all of the cells and the exchange current density of the third cell decreases from its nominal value (Table 2.1) to 10^{-6} times of it at 500 s to simulate for example an electrochemical degradation. The pressure drop inside the anode and cathode channel is fixed to 2.7 mbar and 6.8 mbar respectively. The other parameters are the same as Table 2.1 except R_c^{th} . In this simulation, this parameter is equal to $R_{GDL}^{th}/10$. As seen in Figure 2-26, the temperature of the third cell increases due to the change of the exchange current density. This temperature rise influences the cathode and anode sides of the second and fourth cells respectively. Due to this temperature gradient produced by the faulty third cell, the saturation level in the anode channel of the second cell and the saturation level in the cathode side of the fourth cell increased (Figure 2-27). Furthermore, the saturation level in the cathode side of the second cell and the saturation level inside the anode channel of the fourth cell decreased.

The temperature effect on the first and fifth cells is negligible. As seen in Figure 2-27, the saturation level changes influence the dry gas flow rates. Increasing the saturation level inside the channels leads to a decrease in the corresponding dry gas flow rate and vice versa. For instance, the increase of the saturation level inside the anode channel of the second cell leads to a decrease in its hydrogen flow rate. This phenomenon can lead to a fuel starvation event in the second cell, in turn leading to a drop in its exchange current density and heating of this cell. Here a mechanism is shown that explains the propagation of degradations from cell to cell because of the thermal coupling. The membrane water content of the cells is also shown in Figure 2-28. As seen in this figure, the membrane water content of the third cell is slightly decreased due to the increase of its temperature. The change of this parameter for the other cells is negligible. The lower membrane water content leads to an increase in its protonic resistance. As a result, the third cell voltage decreases again because of drying. The stack voltage and the applied current density of the cells are shown in Figure 2-29.

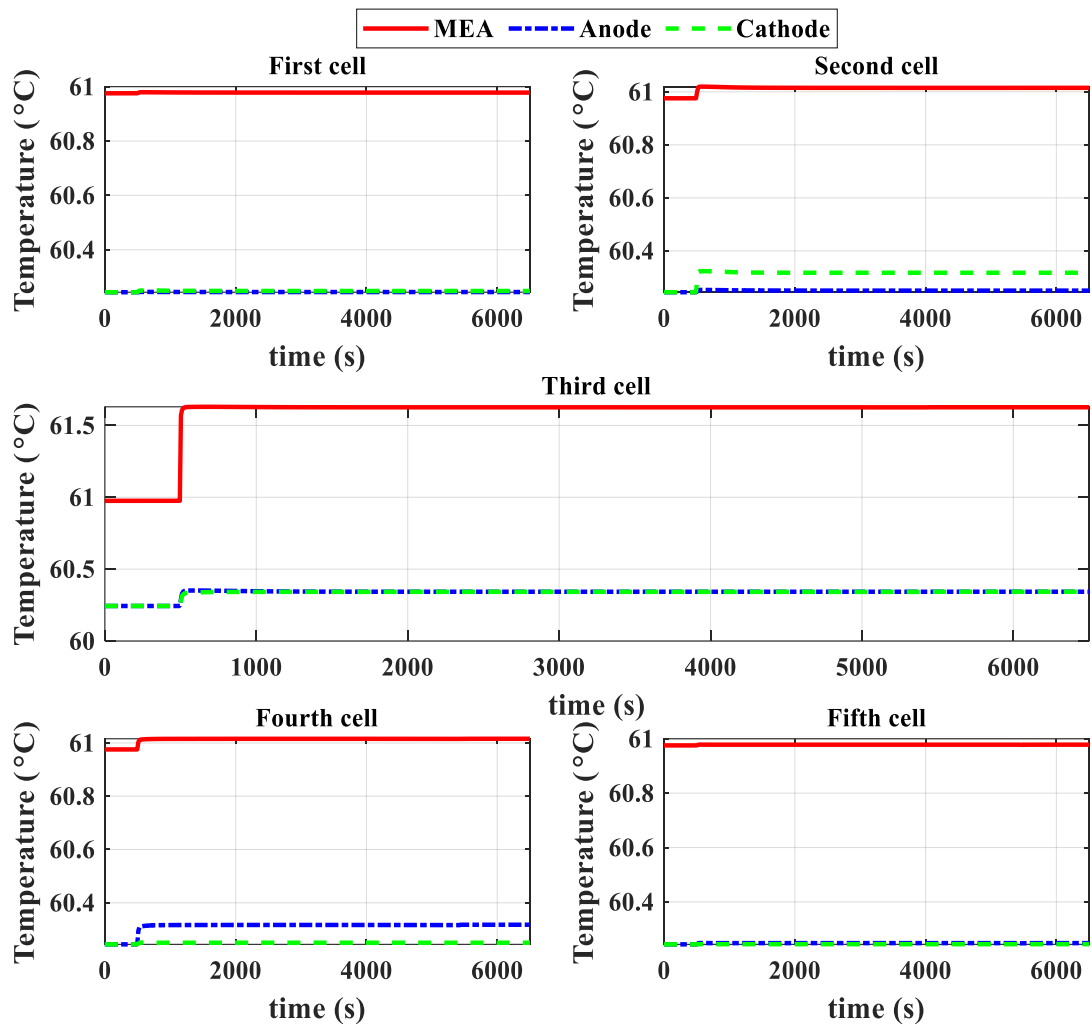


Figure 2-26. Simulation results of the cell temperatures when the exchange current density of the third cell decreased from its nominal value to 10^{-6} times of it at 500 s. A constant current of 10 A passes through the cells (The air and hydrogen pressure drops are applied).

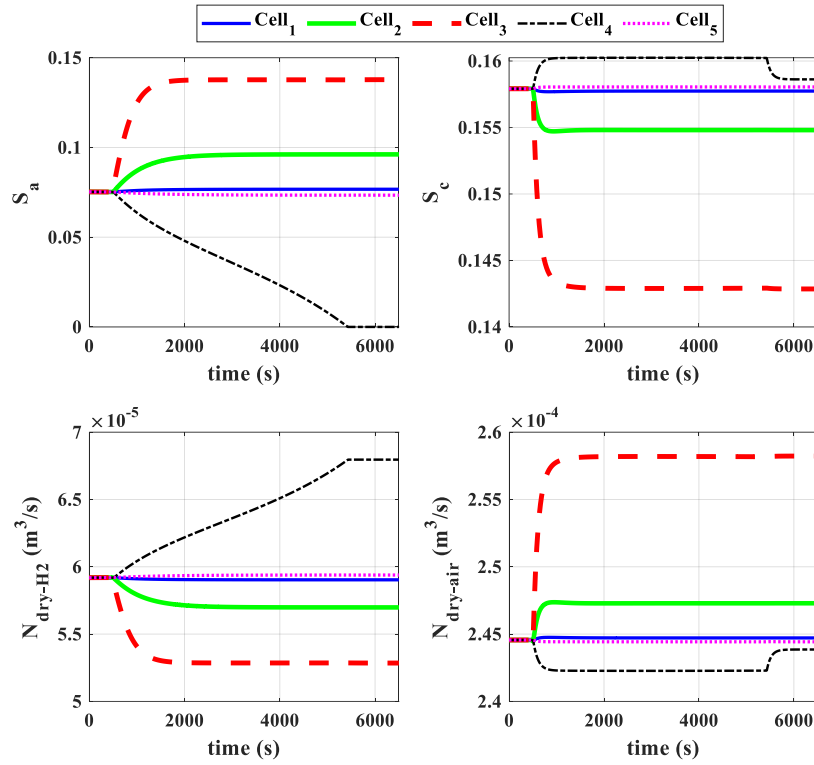


Figure 2-27. Simulation results of the dry gas flow rates and the saturation level inside the channels when the exchange current density of the third cell decreased from its nominal value to 10^{-6} times of it at 500 s. A constant current of 10 A passes through the cells (The air and hydrogen pressure drops are applied).

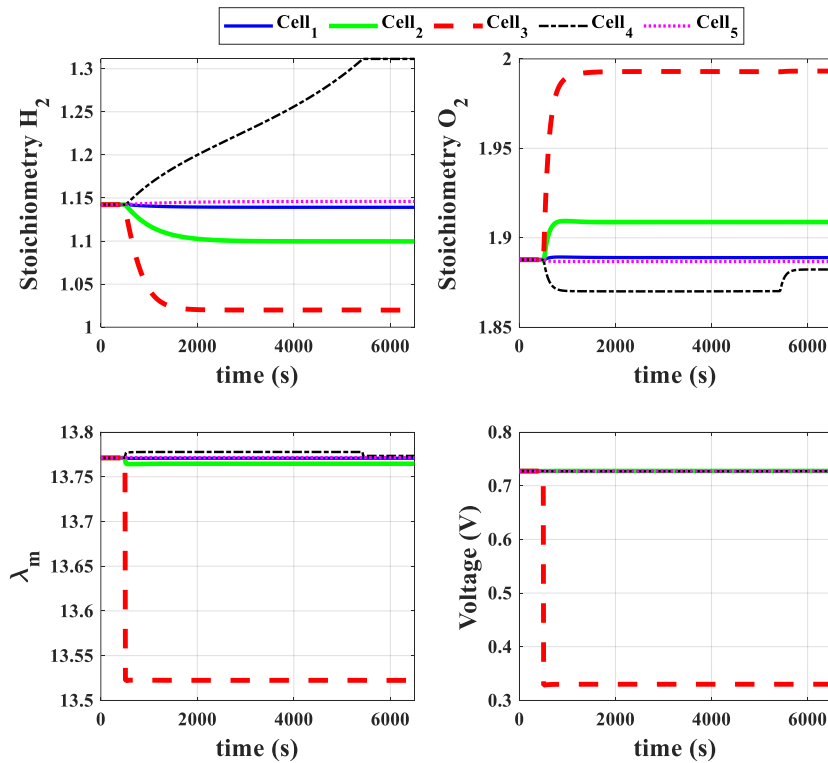


Figure 2-28. Simulation results of the cell voltages, membrane water content, and the stoichiometry of hydrogen and oxygen when the exchange current density of the third cell decreased from its nominal value to 10^{-6} times of it at 500 s. A constant current of 10 A passes through the cells (The air and hydrogen pressure drops are applied). The gas flow rates are highly sensitive to temperature gradients in these very low-pressure drops (low current density).

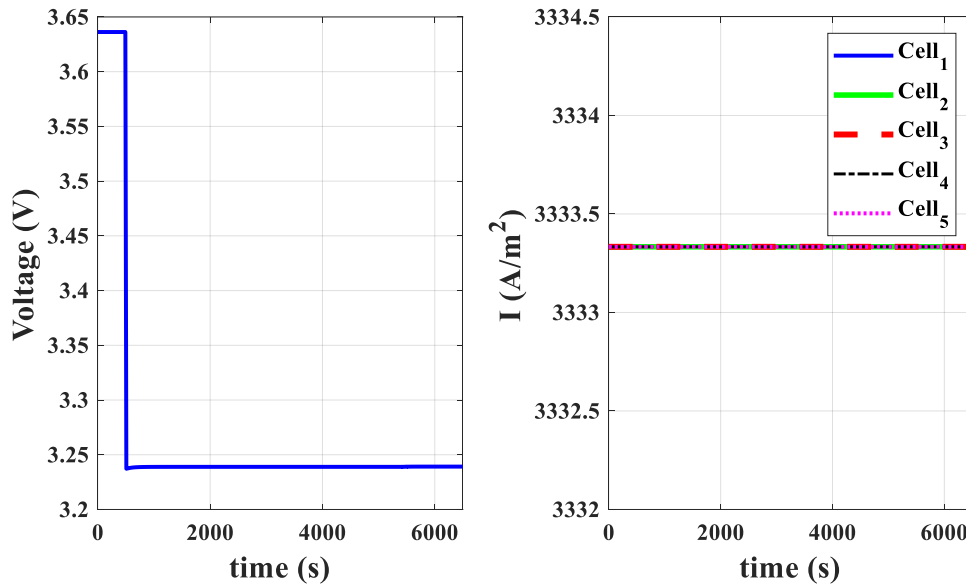


Figure 2-29. Simulation results of the stack voltage and applied current densities when the exchange current density of the third cell decreased from its nominal value to 10^{-6} times of it at 500 s. A constant current of 30A passing through the cells (The air and hydrogen pressure drops are applied).

The conditions, assumptions, and parameters of the third simulation are the same as the second simulation but the stack is not thermally insulated in this simulation. It is assumed that the anode side of the first cell and cathode side of the fifth cell are in contact with the clamping plates by a thermal resistance equal to R_{GDL}^h . The clamping plates are supposed to have a constant temperature of 58 °C. Due to this assumption, the first and fifth cells initially have a temperature gradient as seen in Figure 2-30. This temperature gradient leads to a different saturation level inside their channels than the other cells (Figure 2-31). The impact of the exchange current density changes is the same as the second simulation. It can be noticed that the hydrogen stoichiometry of the first cell is low from the beginning because of the thermal coupling with the clamping plate (Figure 2-32). The same behavior can be seen for the oxygen stoichiometry of the fifth cell. Here we have modeled the well-known end-cell issue. It can be noticed that if the fifth cell can be submitted to voltage instabilities because of oxygen starvation, the situation of the first cell (cold anode) is more critical because H₂ starvation will lead to irreversible degradation of the cathode. The benefits of thermal insulation of the endplates can be understood. The stack voltage and the applied current density of the cells are shown in Figure 2-33 during this simulation.

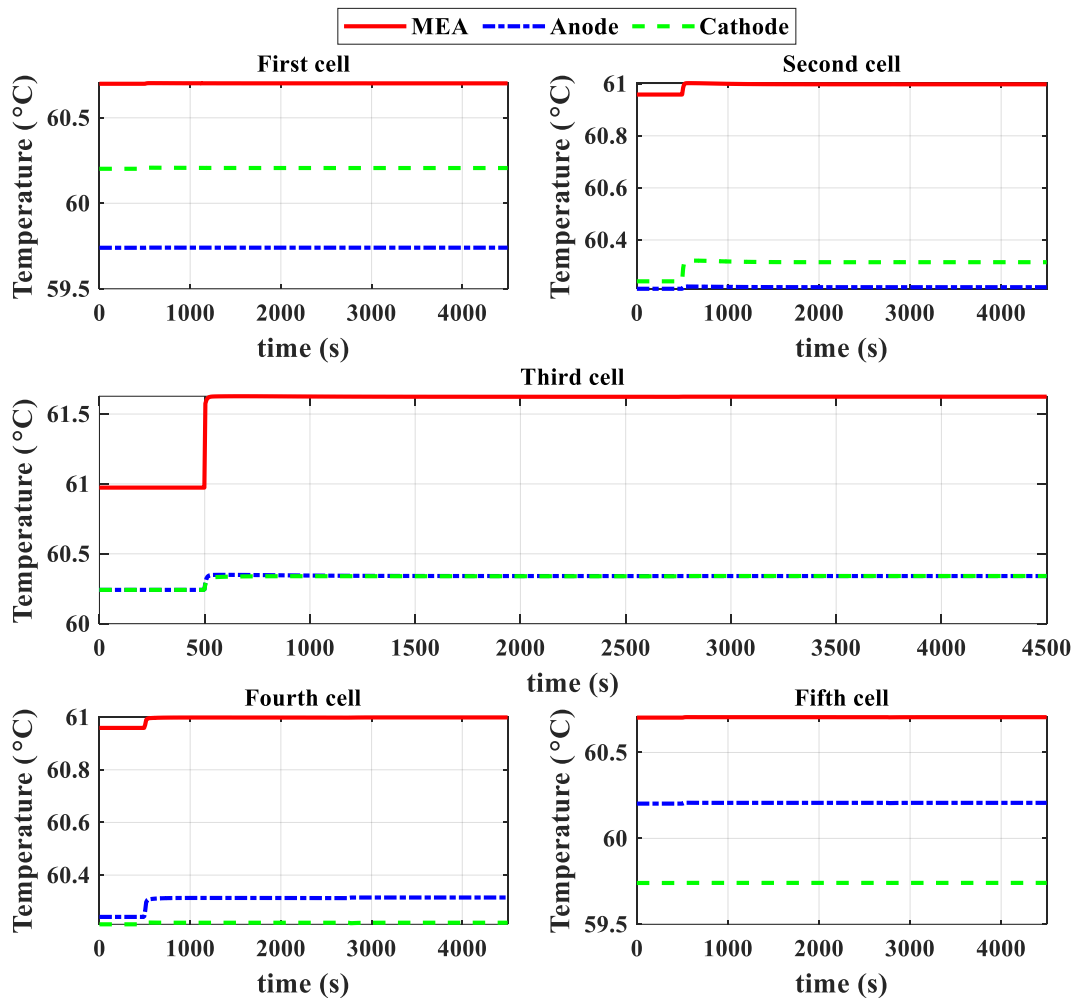


Figure 2-30. Simulation results of the cell temperatures when the exchange current density of the third cell decreased from its nominal value to 10^{-6} times of it at 500 s. A constant current of 10 A passes through the cells of the non-insulated stack (The air and hydrogen pressure drops are applied). The initial temperature gradient inside the end cells can be noticed.

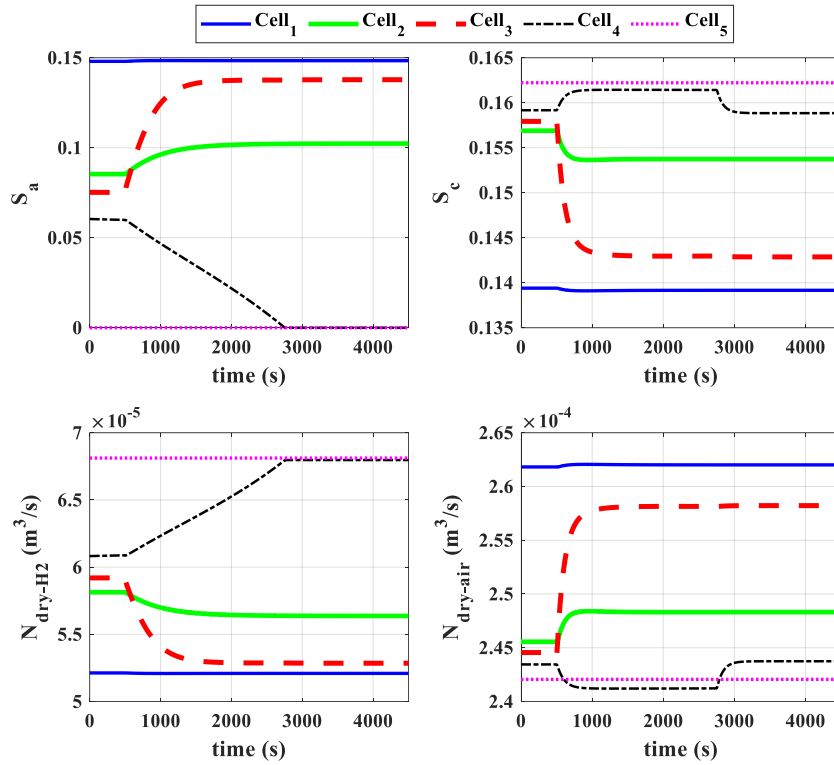


Figure 2-31. Simulation results of the dry gas flow rates and the saturation level inside the channels when the exchange current density of the third cell decreased from its nominal value to 10^{-6} times of it at 500 s. A constant current of 10 A passes through the cells of the non-insulated stack (The air and hydrogen pressure drops are applied).

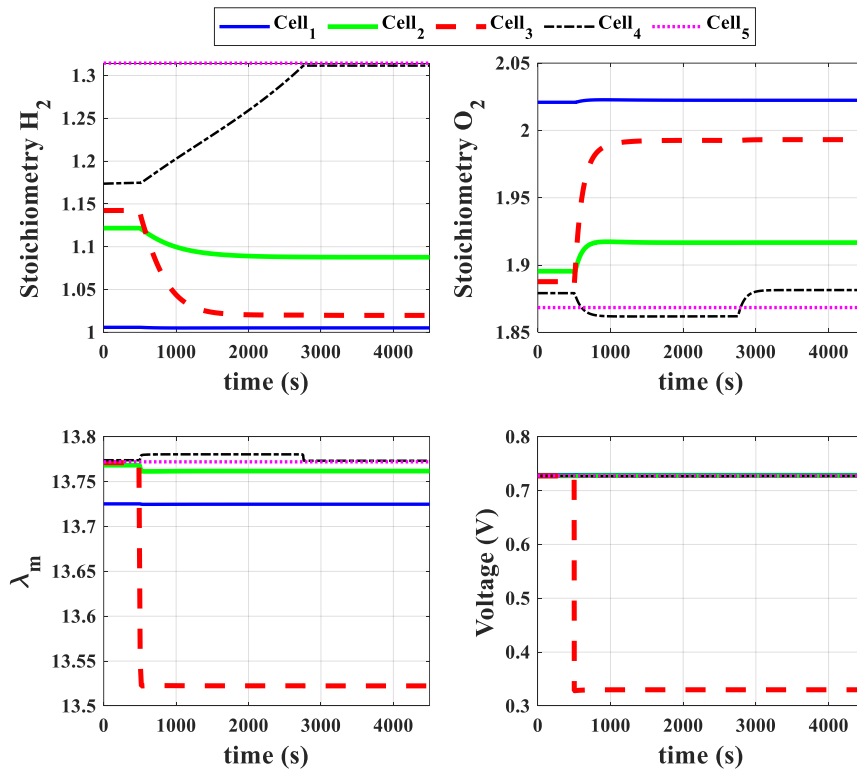


Figure 2-32. Simulation results of the cell voltages, membrane water content, and the stoichiometry of hydrogen and oxygen when the exchange current density of the third cell decreased from its nominal value to 10^{-6} times of it at 500 s. A constant current of 10 A passes through the cells of the non-insulated stack (The air and hydrogen pressure drops are applied). This very low hydrogen stoichiometry of the first cell is a consequence of the thermal coupling with the clamping plate.

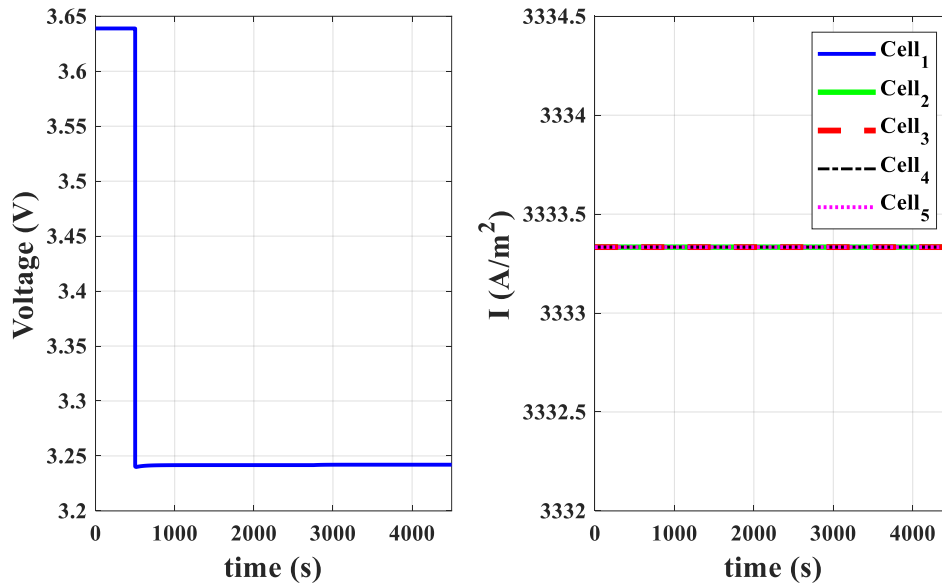


Figure 2-33. Simulation results of the stack voltage and applied current densities when the exchange current density of the third cell decreased from its nominal value to 10^{-6} times of it at 500 s. A constant current of 10 A passes through the cells of the non-insulated stack (The air and hydrogen pressure drops are applied).

2.7. Conclusions

A real-time reduced-order transient model of a cell in its surrounding stack was developed in this chapter. The boundary conditions considered are imposed pressure drops for the gases, and the thermal coupling with neighboring cells is described. This allows modeling a stack by assembling several cells. A mechanism for the propagation of the degradations from a cell to its neighboring one has been proposed and simulated. The main difficulty not completely solved rigorously is the description of the liquid water flow in the channels. It has been observed that the liquid relative permeability depends not only on the saturation but on another additional parameter. The parameters of this model that couple transfers of mass, heat, and charges are numerous and their estimation must be correctly carried out to allow an effective validation. This will be a part of another thesis. This model was successfully implemented on the dSAPCE version 1005 in the LEMTA laboratory with a sample rate of 1kHz.

Chapter 3

Power electronics Structure

3.1. Introduction

The objective of this chapter is to propose a power electronics structure which can realize the goals of the FCMS. This structure should allow the management of the cell groups individually. As mentioned in Chapter One, the conventional boost converter is connected to cell groups for simplicity. To further increase the output voltage, the output capacitors of boost converters are connected in series inspired by the cascade connection of multi-stacks. Loss of controllability is possible in this case. To prevent this possibility, an equalizer is proposed. The proposed power electronics architecture to realize the fuel cell management system is shown in Figure 3-1. As seen in this figure, the total number of cells inside one stack is broken into different groups of cells. Each group is connected to the DC-DC boost converter. These boost converters allow to separately manage cells. To ensure the controllability of different boost converters, an equalizer based on the multi-winding transformer is proposed in this thesis. To regulate the DC bus voltage, the SC with the conventional bidirectional boost converter is used.

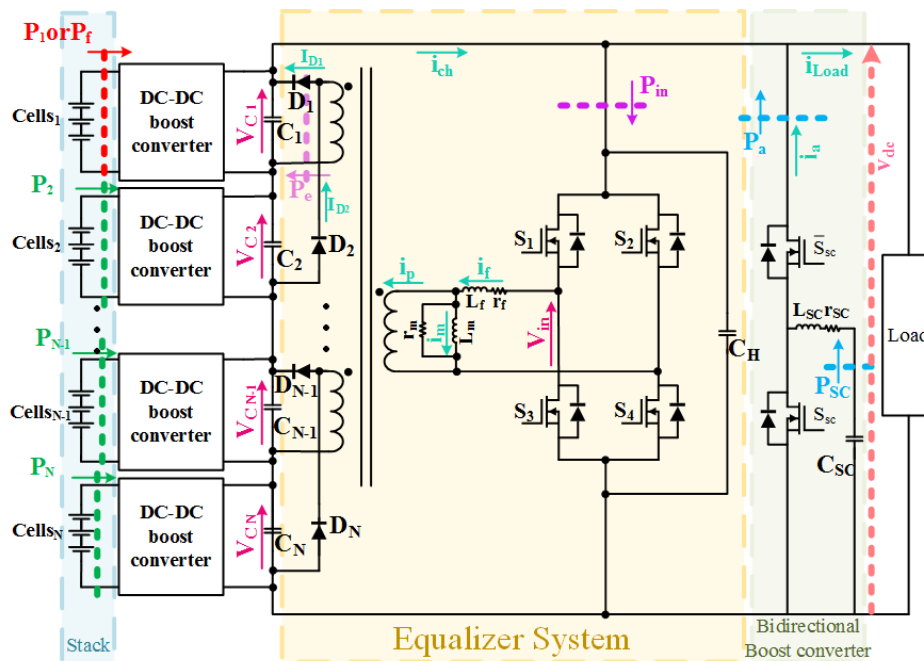


Figure 3-1. Proposed power electronics architecture to realize the fuel cell management system.

An accurate model of the system can be used to perform the sizing or stability analysis. In [80], an equivalent model was derived from the proposed equalizer to select the best value of capacitances and the switching frequency. There are three basic approaches to investigate the dynamic behavior of the system: Discrete-time model, Switching model, and Average model. In [142], these three approaches were used to investigate the dynamic behavior of a boost

converter with a sliding mode current controller. In [143], the stability of a boost converter based on the discrete-time model, and the average model was investigated when a hysteresis current controller was used. The dynamic behavior of a boost converter with an LC filter was investigated based on the discrete-time model approach in [144]. In [144], the output voltage and current of the boost converter were controlled based on the dynamic separation. The discrete-time model cannot be used especially for a complex system with different switches and switching frequencies. For such systems, the average model can be used to study the dynamic behavior of the system. In [145], an interleaved-boost full-bridge converter was modeled by defining the state-space model of the system over different operation modes. In this paper, the switching period was divided into operation modes. The state-space model was updated for each mode and the average of the states was calculated by considering the time of each operation mode. Therefore, this model can be very complex. In [146], an average model was proposed to perform the stability analysis for a hybrid wave and photovoltaic power generation system. The average model of each system and control method were used to obtain an overall average model for the hybrid system. Then, the stability analysis based on the eigenvalues of the proposed average state-space model has been used to verify the stable operation of the system under various operating conditions. An average model based on the state-space equations of the system was introduced for a balancer in [84]. This balancer can equalize the voltage between two SC banks. Indeed, the proposed balancer was a synchronous buck-boost topology that can transfer the stored energy in the inductor of the converter to the banks and vice versa. In such a connection, there is no intermediary AC power stage. For systems with AC power stage, the average values of AC variables are equal to zero. This last property involves an order reduction to establish the average model. To deal with this phenomenon, the DC terms and the first-order terms of Fourier series of state variables were used in [147]. Since the transformer current of a dual active bridge converter is purely AC, its DC component is equal to zero. Therefore, the switching frequency terms in the Fourier series of state variables were used to capture the effect of the transformer current on the system dynamics in [147]. In [148], [149], a dynamical average model was proposed for an isolated boost converter. In this converter, the average value of the transformer leakage current over each period of switching is equal to zero. Therefore, the energy cannot be transferred through the transformer by using this average value in the average state-space model. The equation of the average value of the leakage current was obtained over a half period. Since the leakage current of the isolated boost converter is symmetric, this equation is valid for any half periods. As a result, the obtained average value is not equal to zero and the energy can be transferred through the transformer even in the average model. The main disadvantage of this approach is the assumption in which the transformer current waveform must be symmetrical.

In this thesis, the proposed equalizer includes an AC power stage but the current waveforms can be asymmetrical (Figure 3-2). Thus, a reduced-order average model is proposed in which the symmetrical waveform of the transformer current is not mandatory. Moreover, the proposed average model takes into account the cross-coupling effect due to the serial connection of output capacitors. Dynamic stability analysis of the system is also performed based on the proposed model. This model can be also used for sizing and designing. The validity of the proposed method is verified by the experiments. The functionalities of the management system are experimentally validated in three different operating conditions of the cells.

The rest of this paper is organized as follows: The proposed power electronics structure is explained in Section 3.2. The control methods, which are used for different parts of the proposed structure is explained in Section 3.3. An average dynamical model is also proposed and provided in Section 3.2 and 3.3. The simulation and experimental results are provided in Section 3.4 and 3.5 to evaluate the effectiveness of the proposed structure and the proposed model. The

stability analysis of the proposed control method is also investigated in Section 3.6. Finally, conclusions are listed in Section 3.7.

3.2. Proposed power electronics structure

As seen in Figure 3-1, the energy can be transferred from the series capacitors to the lower voltage capacitors by the equalizer. Indeed, this equalizer is an isolated DC-DC converter. The H-bridge inverter can send energy to even or odd-numbered cells through a High Frequency (HF) transformer. To stabilize the input voltage of the H-bridge inverter, a film capacitor (C_H) is used. Regarding the embedded application, an SC bank regulates the standard voltage of 48 v for DC link voltage (V_{dc}). The SC bank is connected to the DC link through a bidirectional converter. It is assumed that the cells inside one stack are broken down into some groups of cells with an identical number of cells. Furthermore, it is assumed that only one group of cells has a problem at a moment. In the worst condition, one group of cells can inject no power. The DC link voltage is converted to an AC voltage on the primary side of the HF transformer by the H-bridge inverter. This AC voltage is shown by V_{in} .

3.2.1. Operation Modes

In this section, the following assumptions are considered in the operation analysis for simplicity:

1. Turn ratio for all secondary windings is the same and equal to $m = \frac{N_2}{k N_1}$ and k is the coupling coefficient.
2. The coupling coefficient between the primary and secondary windings are identical and equal to k .
3. The coupling coefficient between the secondary windings is unitary.
4. The DC bus voltage is controlled to a reference constant value.
5. The switches are considered as the ideal devices. The diode voltage drops are taken into account but their dynamical resistance is assumed zero.

The theoretical waveforms of the proposed equalizer in steady-state are shown in Figure 3-2 when C_1 (and C_2) are the lower voltage capacitors between odd and even-numbered capacitors respectively. As seen in this figure, based on the proposed switching commands for the H-bridge inverter, a symmetrical square waveform (V_{in}) is applied on the primary side of the HF transformer with a variable duty cycle (d). Therefore, the odd\even numbered diodes can be naturally turned on during the positive\negative part of this square wave because of the diode structure and the polarity of secondary windings. The diode corresponding to the lower voltage capacitor between odd\even numbered diodes is automatically turned on during the positive\negative part of the input voltage of the HF transformer. Due to the same polarity of the secondary windings, a voltage equal to the lower voltage between the odd\even numbered capacitor voltages is induced to all secondary windings when an odd\even numbered diode starts to conduct. Therefore, other odd\even numbered diodes are negatively biased during the conduction of one diode. Theoretical waveforms of the proposed equalizer are shown in Figure 3-2a when the first capacitor has the lowest voltage and in Figure 3-2b when the first and second capacitors have the lower voltage between odd\even numbered capacitors and other capacitors have the same voltage. As seen in those figures, the transformer current waveform can be symmetrical or not. To be more general, the second case is presented as the operation modes as follows:

- 1) Mode 1 [t_0-t_1 : Figure 3-3 (a)]: Before t_0 two switches S_1 and S_2 were on. At t_0 , S_2 is turned off and S_4 is turned on. Therefore, a positive voltage is applied to the primary side of the transformer. This voltage is induced in the secondary windings. This voltage leads to the reverse-biased of the even-numbered diodes. Based on the reason mentioned above, only diode D_1 , which connects to the lower voltage capacitor between odd-numbered capacitors, conducts current. As a result, the energy through the leakage inductance of the transformer is transferred to the capacitor C_1 . Therefore, the leakage current and voltage of C_1 is increased. The derivative equations of the system are as follows:

$$\begin{cases} L_m \frac{di_m}{dt} = \frac{V_{C_1} + V_d}{m} \\ L_f \frac{di_f}{dt} = V_{in} - \frac{V_{C_1} + V_d}{m} - r_f i_f \\ C_1 \frac{dV_{C_1}}{dt} = \frac{\left(i_f - i_m - \frac{V_{C_1} + V_d}{mr_m} \right)}{m} - i_{load} + \frac{P_1}{V_{C_1}} \\ C_j \frac{dV_{C_j}}{dt} = \frac{P_j}{V_{C_j}} - i_{load} \quad j = 2, 3, 4 \end{cases} \quad (3.1)$$

where L_m and L_f are respectively the magnetic and leakage inductances, r_f is the leakage resistance to model the copper losses and r_m is to model the iron losses, i_m is the magnetizing current, i_f is the leakage current, V_d is the diode drop voltage, V_{in} is the input voltage at the primary side of the transformer, V_{C_j} is the voltage of C_j , P_j is the injected power by the boost converter corresponding to the j^{th} fuel cell, and i_{load} is the load current.

- 2) Mode 2 [t_1-t_2 : Figure 3-3 (b)]: S_4 is turned off and S_2 is turned on as a synchronous rectifier in this mode. Therefore, the primary side of the transformer is short-circuited. In other words, the input voltage of the HF transformer is equal to zero. The diode D_1 continues to conduct but the current passing through it, which is proportional to the leakage current, is linearly decreased. The derivative equations in this mode are as follows:

$$\begin{cases} L_m \frac{di_m}{dt} = \frac{V_{C_1} + V_d}{m} \\ L_f \frac{di_f}{dt} = -\frac{V_{C_1} + V_d}{m} - r_f i_f \\ C_1 \frac{dV_{C_1}}{dt} = \frac{\left(i_f - i_m - \frac{V_{C_1} + V_d}{mr_m} \right)}{m} - i_{load} + \frac{P_1}{V_{C_1}} \\ C_j \frac{dV_{C_j}}{dt} = \frac{P_j}{V_{C_j}} - i_{load} \quad j = 2, 3, 4 \end{cases} \quad (3.2)$$

The switching frequency of the H-bridge inverter is chosen as low as enough in such a way that the diode D_1 can be turned off before the end of this mode t_2 . As a result, the

derivative equations of the system during the interval of $[t_f, t_2]$ are as following when the diode is off:

$$\begin{cases} L_m \frac{di_m}{dt} = r_m (i_f - i_m) \\ L_f \frac{di_f}{dt} = -r_f i_f - r_m (i_f - i_m) \\ C_j \frac{dV_{C_j}}{dt} = \frac{P_j}{V_{C_j}} - i_{load} \quad j = 1, 2, 3, 4 \end{cases} \quad (3.3)$$

- 3) Mode 3 $[t_2-t_3]$: Figure 3-3(c): S_1 is turned off and S_3 is turned on in this mode. A negative voltage appears on the primary side of the transformer. In other words, V_{in} has a negative value. This mode like mode 1 has the same effect on the even-numbered capacitors. The voltage of C_2 is the lowest voltage between the even-numbered capacitors. Therefore, the diode D_2 is turned on and the voltage of C_2 starts to increase. The leakage current is negative but its absolute value is decreased over this mode. The derivative equations of the system are as follows:

$$\begin{cases} L_m \frac{di_m}{dt} = -\frac{V_{C_2} + V_d}{m} \\ L_f \frac{di_f}{dt} = V_{in} + \frac{V_{C_2} + V_d}{m} - r_f i_f \\ C_2 \frac{dV_{C_2}}{dt} = -\frac{\left(i_f - i_m + \frac{V_{C_2} + V_d}{mr_m} \right)}{m} - i_{load} + \frac{P_2}{V_{C_2}} \\ C_j \frac{dV_{C_j}}{dt} = \frac{P_j}{V_{C_j}} - i_{load} \quad j = 1, 3, 4 \end{cases} \quad (3.4)$$

It can be noted that this mod does not exist for Figure 3-2a.

- 4) Mode 4 $[t_3-t_4]$: Figure 3-3(d): This mode is similar to mode 2 but due to an applied negative voltage to the primary side of the HF transformer, the even-numbered diodes can be turned on. Since the second capacitor is assumed to be the lower voltage capacitor between the even-numbered capacitors, the second diode begins to conduct the current. The derivative equation of the system before the diode stops to conduct is as following during the interval of $[t_3, t_{fe}]$:

$$\left\{ \begin{array}{l} L_m \frac{di_m}{dt} = -\frac{V_{C_2} + V_d}{m} \\ L_f \frac{di_f}{dt} = \frac{V_{C_2} + V_d}{m} - r_f i_f \\ C_2 \frac{dV_{C_2}}{dt} = -\frac{\left(i_f - i_m + \frac{V_{C_2} + V_d}{mr_m} \right)}{m} - i_{load} + \frac{P_2}{V_{C_2}} \\ C_j \frac{dV_{C_j}}{dt} = \frac{P_j}{V_{C_j}} - i_{load} \quad j=1,3,4 \end{array} \right. \quad (3.5)$$

Throughout $[t_{fe}, t_4]$ the derivative equations of the system are changed as (3.3) when the diode D_2 is off in this mode. Moreover, this mod does not take place for Figure 3-2a.

Based on these modes, the power can be transferred from the series connection of capacitors to the lower voltage capacitors. A state-space model can be developed by (3.1)-(3.5) for the equalizer. Any losses in the transformer reduce the power that is received by lower-voltage cells. The transformer leakage inductance can also affect its transmitting power by affecting its input current. Therefore, the transformer design has a key role in this topology.

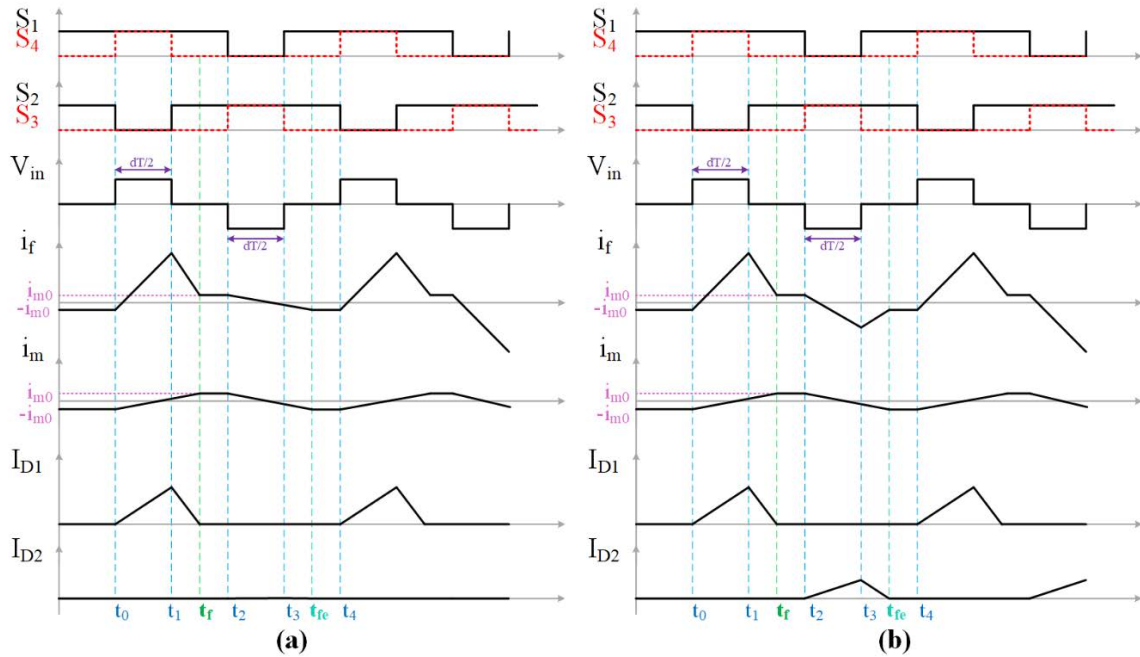


Figure 3-2. Theoretical waveforms in the steady-state of the proposed equalizer whereas: a) V_{c1} is the lowest voltage between all capacitors b) V_{c1}/V_{c2} is the lowest voltage between the odd\even numbered capacitors.

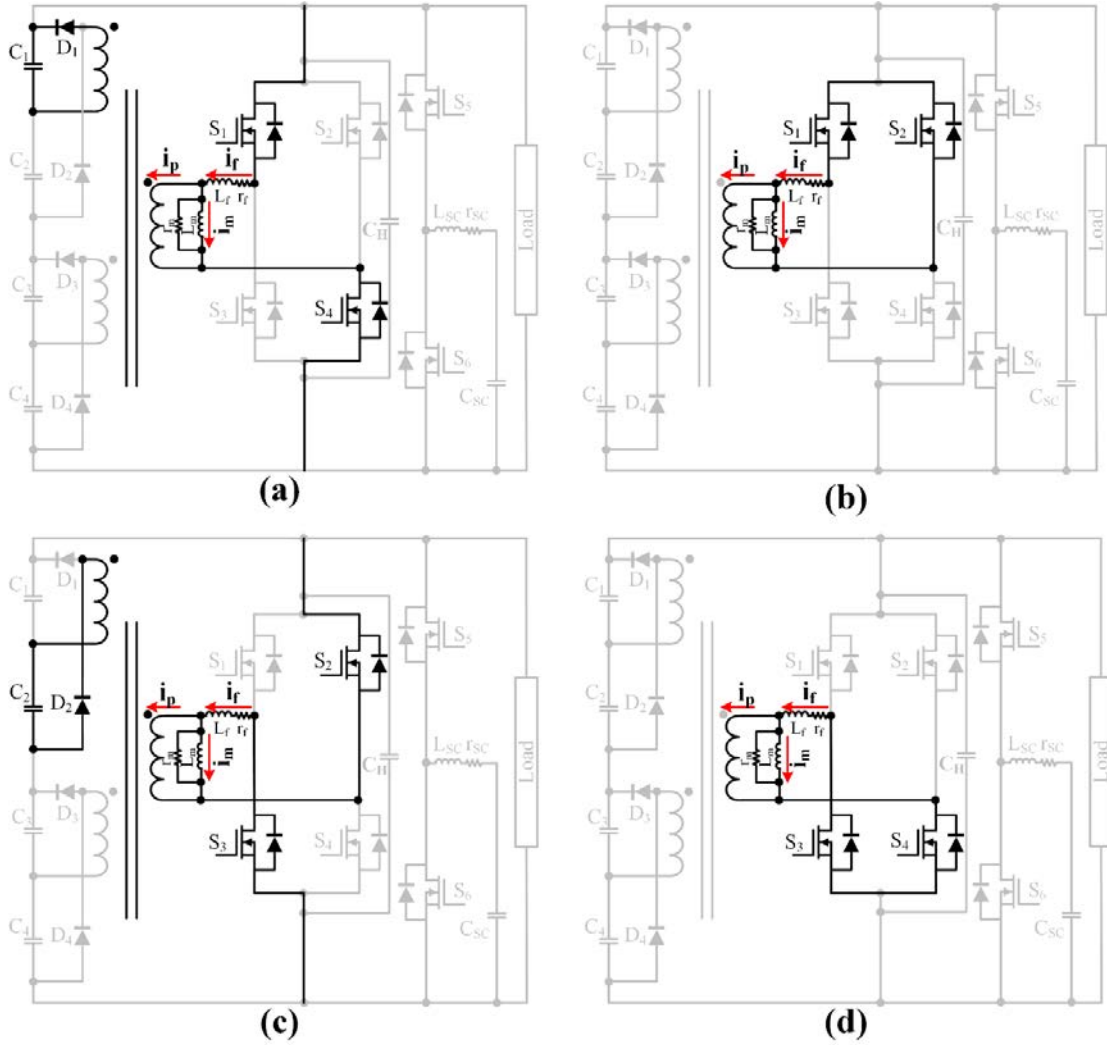


Figure 3-3. Different operation modes of the proposed equalizer. (a) Mode 1: $t_0 < t < t_1$. (b) Mode 2: $t_1 < t < t_2$. (c) Mode 3: $t_2 < t < t_3$. (d) Mode 4: $t_3 < t < t_4$.

3.2.2. Design consideration

The magnetizing inductance of the transformer must be maximized to reduce the magnetizing current. For instance, L_m and L_f of a core with two windings can be calculated by the following equation:

$$\begin{cases} L_m = k^2 L_1 \\ L_f = (1 - k^2) L_1 \end{cases} \quad (3.6)$$

Where k is the coupling coefficient and L_1 can be calculated by:

$$L_1 = \frac{N^2}{\mathfrak{R}} \quad (3.7)$$

N is the number of turns and \mathfrak{R} is the reluctance of the core. As seen in this equation, increasing the number of turns and decreasing the reluctance lead to an increase in the magnetizing inductance. Increasing the number of turns increases the volume of the transformer and, therefore, increases the hysteresis losses. Furthermore, increasing the number of turns also increases the wire length that leads to an increase of the wire resistance and, consequently, the

copper losses. The reluctance is inversely proportional to the permeability. Hence, selecting a core with high permeability can make it possible to increase the magnetizing inductance with a lower volume. This also increases the leakage inductance. However, the leakage inductance affects the maximum transmitting power through the transformer in each cycle. This power is also the most important parameter in reducing the equalizing time. To obtain this power in the steady-state by considering the first group of cells as the faulty cells, the diode current can be used to calculate the transferred energy. Therefore, the transferred energy can be calculated as follows:

$$W_e = V_{C_1} \int_{t_0}^{t_f} i_D(t) dt = V_{C_1} \int_{t_0}^{t_f} \frac{i_f - i_m - \frac{V_{C_1} + V_d}{m r_m}}{m} dt \quad (3.8)$$

Where W_e is the energy received by the faulted cell, V_{C_1} is the voltage of the first capacitor, and i_D is the corresponding diode current that is on. Based on Figure 3-2, this equation can be solved by dividing its time interval into two intervals:

$$W_e = \left(\int_{t_0}^{t_1} \frac{i_f - i_m}{m} dt + \int_{t_1}^{t_f} \frac{i_f - i_m}{m} dt - \frac{V_{C_1} + V_d}{m r_m} (t_f - t_0) \right) \quad (3.9)$$

Assuming that the time constant of L_f/r_f is much larger than $t_f - t_1$, the magnetizing and leakage current functions can be obtained based on (3.1) in the interval $[t_0, t_1]$ as follows:

$$\begin{cases} i_f(t) = -i_{m0} \left(1 - \frac{t}{\frac{L_f}{r_f}} \right) + \frac{\sum_j V_{C_j} - \frac{V_d + V_{C_1}}{m}}{L_f} t \\ i_m(t) = -i_{m0} + \frac{V_d + V_{C_1}}{m L_m} (t - t_0) \end{cases} \quad (3.10)$$

Where $-i_{m0}$ is the magnetizing current at t_0 . The magnetizing current value at t_f is equal to i_{m0} . Keeping the same assumption of the time constant and based on (3.2), the magnetizing and leakage current can be calculated throughout $[t_1, t_f]$ as follows:

$$\begin{cases} i_f(t) = i_{m0} \left(1 - \frac{t - t_1}{\frac{L_f}{r_f}} \right) + \frac{V_d + V_{C_1}}{m L_f} (t_f - t_1) - \frac{V_d + V_{C_1}}{m L_f} (t - t_1) \\ i_m(t) = i_{m0} + \frac{V_d + V_{C_1}}{m L_m} (t - t_f) \end{cases} \quad (3.11)$$

Substituting (3.10) and (3.11) in (3.9), two terms are unknown in the subsequent equation: $t_1 - t_0$, $t_2 - t_1$. The duration of $t_1 - t_0$ is equal to $dT/2$ where $T = 1/F$ and F is the switching frequency of the H-bridge inverter, and d is its duty cycle. The second duration can be calculated employing the diode current equation throughout $[t_0, t_f]$. The diode current can be calculated from the following equation:

$$\frac{di_D}{dt} = \frac{di_f}{dt} - \frac{di_m}{dt} - \frac{V_{C_1} + V_d}{m r_m} \quad (3.12)$$

Two equations can be obtained for the maximum value of the diode current by integrating (3.12) over two intervals of $[t_0, t_1]$ and $[t_1, t_2]$ and using (3.10) and (3.11). Using these two equations, the time duration of $t_2 - t_1$ is obtained with one unknown parameter (i_{m0}). This parameter is obtained from the magnetizing current equation throughout $[t_0, t_2]$ as follows:

$$i_{m0} = -i_{m0} + \frac{V_d + V_{C_1}}{m L_m} (t_2 - t_0) \rightarrow i_{m0} = \frac{V_d + V_{C_1}}{2m L_m} ((t_f - t_1) + (t_1 - t_0)) \quad (3.13)$$

Thus, an equation for the transferred energy is obtained by replacing (3.10) and (3.11) in (3.9) and using (3.12) and (3.13) which all of the parameters are known. The transferred power is obtained from the transferred energy equation and the time duration of one switching period. The equation of the transferred power is as follows:

$$P_{e1} = \frac{dV_{C_1}}{8F^2 m^2} \left(\frac{\frac{dF(mV_{dc} - B_1)}{L_f} - \frac{dFB_1}{L_m} - \frac{16F^3 L_m (m r_m V_{dc} - 2L_f B_1)}{r_m (-4FL_f L_m + 4FL_C r_m - dr_f r_m)}}{\frac{d^2 F r_f (-m r_m V_{dc} + 2L_f B_1)}{L_f (4FL_f L_m - 4FL_C r_m + dr_f r_m)} - \frac{d(-4FL_C + 2dr_f) A_1}{4L_f L_m B_1 (4FL_f L_m - 4FL_C r_m + dr_f r_m)^2}} \right) \quad (3.14)$$

This power is received by the first capacitor. As seen in this equation, the transferred power in steady-state depends on the leakage and magnetizing inductances, capacitor voltages, frequency, duty cycle, iron losses, copper losses, and transformer turn ratio. It should be noted that A_i , B_i , and $L_i \forall i \in \{1, 2, \dots, N\}$ can be calculated as follows:

$$\begin{cases} A_i = (4FL_m r_m (mV_{dc} - (V_{C_i} + V_d)) + dr_f r_m (V_{C_i} + V_d) - 4FL_f (L_m + r_m)(V_{C_i} + V_d))^2 \\ B_i = (V_{C_i} + V_d) \\ L_C = L_f + L_m \end{cases} \quad (3.15)$$

A similar equation can be obtained for the transferred power to one of the even-numbered capacitors. Considering the second capacitor as a lower voltage capacitor among the even-numbered capacitors, the transferred power can be calculated as follows:

$$P_{e2} = \frac{dV_{C_2}}{8F^2 m^2} \left(\frac{\frac{dF(mV_{dc} - B_2)}{L_f} - \frac{dFB_2}{L_m} - \frac{16F^3 L_m (m r_m V_{dc} - 2L_f B_2)}{r_m (-4FL_f L_m + 4FL_C r_m - dr_f r_m)}}{\frac{d^2 F r_f (-m r_m V_{dc} + 2L_f B_2)}{L_f (4FL_f L_m - 4FL_C r_m + dr_f r_m)} - \frac{d(-4FL_C + 2dr_f) A_2}{4L_f L_m (4FL_f L_m - 4FL_C r_m + dr_f r_m)^2} B_2} \right) \quad (3.16)$$

This power is received by the second capacitor. It can be noted that this power is negligible in the case of Figure 3-2a. To obtain a dynamical average model, the power that is consumed by the equalizer is also required. To calculate this power, the losses inside the system should be added to $P_{e1} + P_{e2}$. The injected power to the equalizer can be calculated as follows:

$$P_{in} = P_{e_1} + P_{e_2} + \frac{\bar{V}_{p_1}^2 + \bar{V}_{p_2}^2}{r_m} + r_f (\bar{I}_{f_1}^2 + \bar{I}_{f_2}^2) \quad (3.17)$$

where \bar{I}_{f_1} is the RMS value of the leakage current of the transformer due to the transmitting energy to the first capacitor, and \bar{V}_{p_1} is the RMS voltage on the primary side of the transformer due to the transmitting energy to the first capacitor that is the RMS value of $\frac{V_d + V_{C_1}}{m}$ throughout $t_f - t_0$ in the switching period as follows:

$$\begin{cases} \bar{I}_{f_1}^2 = \frac{1}{T} \int_{t_0}^{t_f} (i_f(t))^2 dt = \frac{1}{T} \left(\int_{t_0}^{t_1} (i_f(t))^2 dt + \int_{t_1}^{t_f} (i_f(t))^2 dt \right) \\ \bar{V}_{p_1}^2 = \frac{1}{T} \int_{t_0}^{t_f} \left(\frac{V_d + V_{C_1}}{m} \right)^2 dt = \frac{(t_f - t_0)}{T} \left(\frac{V_d + V_{C_1}}{m} \right)^2 \end{cases} \quad (3.18)$$

\bar{I}_{f_2} and \bar{V}_{p_2} are the RMS value of the leakage current of the transformer and the RMS voltage on the primary side of the transformer due to the transmitting energy to the second capacitor that can be similarly calculated in the interval of $[t_2, t_{fe}]$ as follows:

$$\begin{cases} \bar{I}_{f_2}^2 = \frac{1}{T} \int_{t_2}^{t_{fe}} (i_f(t))^2 dt = \frac{1}{T} \left(\int_{t_2}^{t_3} (i_f(t))^2 dt + \int_{t_3}^{t_{fe}} (i_f(t))^2 dt \right) \\ \bar{V}_{p_2}^2 = \frac{1}{T} \int_{t_2}^{t_{fe}} \left(\frac{V_d + V_{C_2}}{m} \right)^2 dt = \frac{(t_{fe} - t_2)}{T} \left(\frac{V_d + V_{C_2}}{m} \right)^2 \end{cases} \quad (3.19)$$

It should be noticed that this current is negligible in the case of Figure 3-2a. The current i_{ch} , which is passed through the series connection of the capacitors, can be calculated as follows:

$$i_{ch} = i_{load} + \frac{P_{in}}{V_{dc}} - i_a \quad (3.20)$$

where i_{load} is the load current, and i_a is the current that is injected by the SC. Calculating the received power by the capacitors, a dynamical average model based on the derivative equations of the system can be obtained as follows:

$$\begin{cases} C_1 \frac{dV_{C_1}}{dt} = \frac{P_1 + P_{e1}}{V_{C_1}} - i_{ch} \\ C_2 \frac{dV_{C_2}}{dt} = \frac{P_2 + P_{e2}}{V_{C_2}} - i_{ch} \\ C_j \frac{dV_{C_j}}{dt} = \frac{P_j}{V_{C_j}} - i_{ch} \quad \forall j \in \{3, 4, \dots, n\} \end{cases} \quad (3.21)$$

By substituting (3.14)-(3.20) in (3.21), the resulting equations form a system of equations. V_{C_j} can be determined by solving this system numerically. Then, P_{e_i} where $i \in \{1, 2\}$ can be calculated by (3.14)-(3.16). For simplicity in the theoretical approach, the first cell is only supposed to have a problem. Assuming that four capacitors are in series and all the cell groups can inject the rated power of 126 W except the first group, the results of the theoretical equations are shown in Figure 3-4. The first group injects no power in this case. Other information is

summarized in Table 3.1. In this condition, the first capacitor voltage (V_{C_1}) is decreased. To investigate the impact of the leakage inductance on the transferred power to the lower voltage capacitor, the duty cycle of the H-bridge inverter is assumed to be 0.4 and the coupling coefficient is changed. Using (3.14), (3.20), and (3.21), the transferred power and the leakage inductance are calculated for different values of the coupling coefficient. The amount of transferred power as a function of the leakage inductance is shown in Figure 3-4 (a). As seen in this figure, the amount of power is decreased by increasing the leakage inductance. Thus, the leakage inductance should be minimized in one hand. On the other hand, large leakage inductance is required to limit the overshoot of the current. Therefore, there must be a trade-off between the peak of current and maximum transferred power through the transformer.

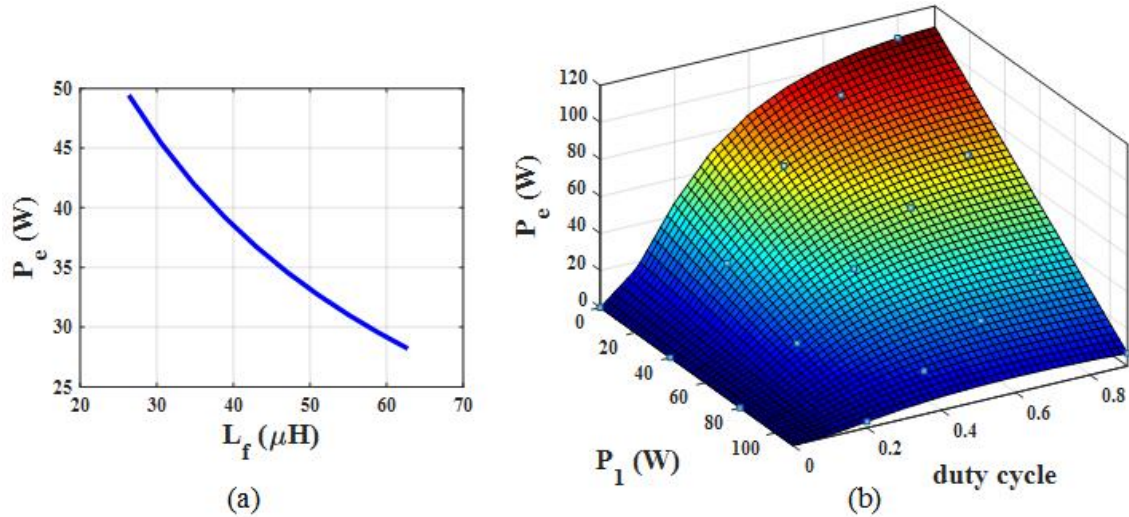


Figure 3-4. The amount of transferred power through the transformer of the proposed equalizer in steady state: (a) Changes in the amount of leakage inductance, when the duty cycle of H-bridge inverter is equal to 0.4 and the first group, injects no power. (b) Changes in the amount of supplied power by the faulted cell and changes in the duty cycle.

To check the effectiveness of the proposed equalizer, it is assumed that the first group of cells cannot inject the nominal power. The injected power by the first cell is changed from zero to nominal power. The other cell groups inject the nominal power. In this condition, the transferred power is calculated by changing the duty cycle of the H-bridge inverter based on (3.14), (3.20), and (3.21). The transferred power by changing the duty cycle of the H-bridge inverter for different values of the first cell group injected power is shown in Figure 3-4 (b). As seen in this figure, the further reduction in injected power by the first group of cells can be compensated by increasing the duty cycle of the H-bridge inverter. In other words, the transferred power through the transformer is increased by increasing the duty cycle of the H-bridge inverter when the injected power of the faulty cell was decreased.

To select a magnetic core based on the constraints mentioned above, the worst condition is taken into account. In this condition, one group of cells should be short-circuited. Thus, one group can inject no power while the other groups inject the nominal power. In this condition, the output voltage of the boost converter connected to the faulted cell decreased and the controllability is lost. The equalizer should send the power to this capacitor to ensure controllability. The Leakage inductance of the transformer has an impact on the primary and secondary transformer side currents. Considering the first group of cells as the faulted cells, the first capacitor voltage is equal to zero in this condition. As a result and based on (3.10) and (3.13), the leakage current in transient conditions can be calculated as follows:

$$i_f = \frac{\sum_j V_{C_j}}{L_f} t \quad (3.22)$$

Table 3.1. The parameters of the proposed system.

Symbol	Unit	Value	Description
C	μF	4700	Electrochemical
A_L	nH/turns ²	12500	Planar transformer core
N_1	turns	1	Primary winding turns
N_2	turns	4	Secondary winding turns
k	-	0.98	Coupling coefficient
F	kHz	40	Switching frequency of the H-bridge
V_C	V	12	Nominal output voltages of boosts
V_d	V	0	Drop voltage of diodes
P_{FC}	W	126	Nominal injected power of different cells
η	-	1	Efficiency of the equalizer system
Controller parameters			
ω_f	Rad/s	$2\pi 10^3$	Cut-off radian frequency of the filter
K_p	-	0.1	Proportional gain of the controller
λ	Rad/s	7500	
k_i	Rad/s	7500	
F_s	kHz	29	Switching frequency of the boost converters
K_{SC}	Rad/s	0.08	
C_{SC}	F	165	Capacitance of the SC

Assuming that the DC link voltage is controlled to have a constant value of 48 V, the maximum of the leakage current can be calculated as follows based on Figure 3-2:

$$i_{f_{\max}} = \frac{48}{L_f} \frac{dT}{2} \quad (3.23)$$

Using (3.10), (3.12), and (3.13), the maximum current of the diode can be calculated as follows:

$$i_{D_{\max}} = \frac{48}{L_f} \frac{dT}{2m} \quad (3.24)$$

In the worst case, the duty cycle is equal to the maximum value of one. The maximum of the leakage current in the transient conditions for different values of the leakage inductance is shown in Figure 3-5. As seen in this figure, the peak of the leakage current is very high. Indeed, a low-pass filter can cope with this problem and control the rate of duty-cycle change. Furthermore, a current protection circuit will be detailed in the next section.

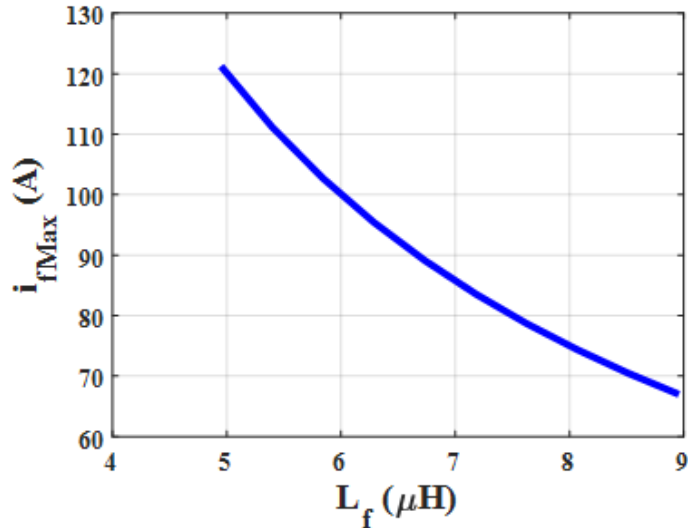


Figure 3-5. Impact of the leakage inductance on the maximum of leakage current in transient conditions.

The leakage current in steady-state can be used to determine the rating of the semiconductor devices. Considering a proportional gain to control the duty cycle of the H-bridge inverter in closed-loop, the maximum of the leakage and diode currents can be calculated by (3.10) and (3.12)-(3.21). These currents are shown in Figure 3-6 by changing the leakage inductance of the transformer when the first group of cells can inject no power and other groups can inject the nominal power. As seen in this figure, if the leakage inductance is equal to $5 \mu\text{H}$, the current rating of the H-bridge inverter switches should be very higher than 15 A and the current rating of the diodes should be higher than 60 A. Therefore, there is a trade-off between the current rating of the semiconductor devices and the maximum power that can be transferred through the transformer.

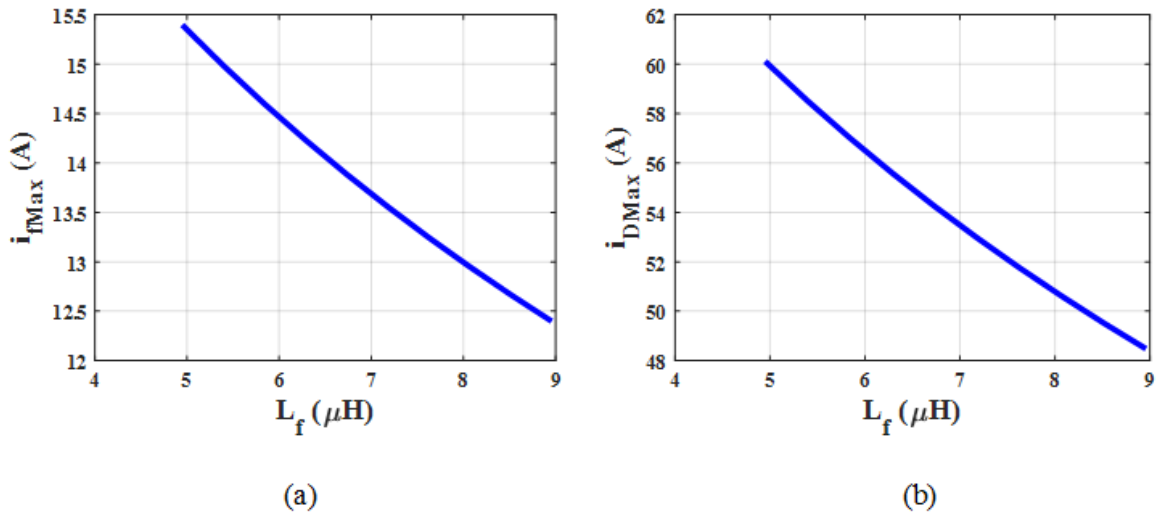


Figure 3-6. Influence of the leakage inductance on a) the maximum of leakage current b) the maximum of the diode current in steady-state.

The coupling coefficient of 0.99 is assumed based on previous experiences. Replacing (3.6) in (3.14) and using (3.20) and (3.21), the value of L_l can be calculated to send the nominal power by the equalizer. Equation (3.7) can be used to select the magnetic core by knowing L_l . It is essential to minimize the volume of the transformer to reduce its losses. Therefore, the desired core can be chosen among the magnetic core in the market by using (3.7) and the

classical equation of the minimum number of turns to minimize the transformer volume. Considering these design constraints, the devices used to make simulation and obtain experimental results are shown in Table 3.1.

3.3. Control Method

3.3.1. Equalizer controller

To control the duty cycle of the H-bridge inverter in closed-loop, a simple proportional control is used. As seen in Figure 3-7, the maximum voltage among the output capacitors connected to the boost converters of different groups of cells is compared with the lowest voltage and this difference is multiplied by the proportional gain to obtain the duty cycle. This controller is also able to decrease the maximum voltage on each output capacitor and can consequently reduce the stress on the capacitors and semiconductor devices. A low-pass filter is used in this controller to control the dynamical behavior of the equalizer. Due to the possibility of a large external perturbation during the transient states, this controller can impose a high value of duty cycle that leads to conduct a high value of current in semiconductors. To model such a control system, the derivative equation of the filter is used as follows:

$$\frac{dy}{dt} = \omega_f (V_{C_{\max}} - V_{C_{\min}} - y) \quad (3.25)$$

where y is the output of the filter, ω_f is the cut-off frequency of the filter, $V_{C_{\min}}$ and $V_{C_{\max}}$ are the minimum and maximum voltages among the capacitor voltages respectively. As a result, the duty cycle of the H-bridge inverter is calculated as follows:

$$d = K_p y \quad (3.26)$$

In this thesis, a protection circuit is also proposed to dynamically control the maximum value of the duty cycle and indirectly control the maximum value of the current. As seen in Figure 3-7, this protection is implemented by considering the derivative equation of leakage inductance of the transformer. Based on Figure 3-2, the leakage current of the transformer can be positively/negatively reached its maximum during the positive/negative part of the input voltage of the transformer. The time interval of $[t_0, t_1]$ or $[t_2, t_3]$ is equal to $dT/2$ where T is $1/F$ and F is the switching frequency. Therefore, the maximum duty cycle can be deduced from the model as following regardless of the losses:

$$L_f \frac{I_{\max}}{dT/2} = \Delta V \quad (3.27)$$

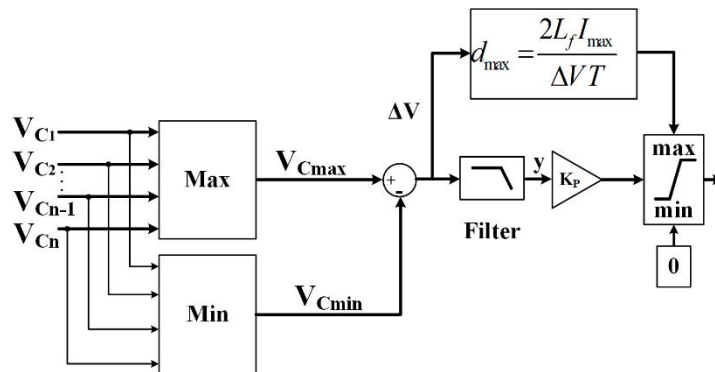


Figure 3-7. Schematic diagram of the control method used to determine the duty cycle (d) of the H-bridge inverter.

3.3.2. DC bus voltage regulator

To regulate the DC bus voltage, an SC is connected to the DC bus by a bidirectional boost converter as depicted in Figure 3-1. The state-space model of the super-capacitor with a boost converter is as follows:

$$\begin{cases} L_{SC} \frac{di_{SC}}{dt} = v_{sc} - (1-d_{SC})V_{dc} - r_{SC}i_{SC} \\ C_{SC} \frac{dv_{SC}}{dt} = -i_{SC} \end{cases} \quad (3.28)$$

where L_{sc} is the inductance connected to the boost converter of the SC and r_{sc} is its resistance, v_{sc} is the SC voltage, and i_{sc} is its current. Therefore, the injected average current to the DC bus by the SC can be calculated as follows:

$$i_a = (1-d_{SC})i_{SC} \quad (3.29)$$

In this thesis, a hierarchical control method with two loops is used to regulate the DC bus voltage. This method includes an outer loop (energy loop) and an inner loop.

3.3.2.1. Outer loop

To control the DC bus voltage, a controller based on the flatness theory is used in this paper. This controller is deeply studied in [150], [151]. The stored energy in the DC link is used as the output variable of this controller. This energy can be calculated as follows:

$$y_{dc} = \frac{1}{2} C_{eq} V_{dc}^2 \quad (3.30)$$

where $C_{eq}=C/N$ is the equivalent capacitor of series-connected capacitors. The derivation of this energy is as follows:

$$\dot{y}_{dc} = \sum_{j=1}^n P_j + P_a - P_{load} \quad (3.31)$$

Where P_a is the power injected to DC bus by the SC. Hence:

$$P_a = \dot{y}_{dc} + P_{load} - \sum_{j=1}^n P_j \quad (3.32)$$

Considering the losses of the boost converter in the resistance of its inductance, this power can be calculated as follows:

$$P_a = P_{SC} - r_{SC} \left(\frac{P_{SC}}{v_{sc}} \right)^2 - L_{SC} \left(\frac{P_{SC}}{v_{sc}} \right) \frac{d \left(\frac{P_{SC}}{v_{sc}} \right)}{dt} \quad (3.33)$$

where P_{sc} is the injected power by the SC. As seen in Figure 3-8, this control is realized by two loops. The inner loop is the power loop and the energy loop is an outer loop. Based on the energy stored in the DC bus, the energy loop can control the voltage of the DC bus. Assuming that the outer loop (energy loop) is slower enough than the inner loop (power loop), the variation of the magnetic energy can be neglected in (3.33). Furthermore, the injected power by SC can be rewritten as follows:

$$P_{SC} = 2P_{max} \left(1 - \sqrt{1 - \frac{P_a}{P_{max}}} \right) \quad (3.34)$$

Where P_{max} is as follows:

$$P_{max} = \frac{v_{SC}^2}{4r_{SC}} \quad (3.35)$$

Using (3.31)-(3.35), the power that must be injected by the SC to regulate the DC link voltage is obtained. This control can operate if the inner loop that controls the power of SC is as fast enough. To ensure that the electrostatic energy follows its reference, a second-order dynamical law is used to generate the reference of power. We set:

$$\dot{y}_{dc_{ref}} - \dot{y}_{dc} + K_1 (y_{dc_{ref}} - y_{dc}) + K_2 \int (y_{dc_{ref}} - y_{dc}) = 0 \quad (3.36)$$

Where K_1 and K_2 are the controlling parameters with $K_1 = 2\zeta\omega_n$, and $K_2 = \omega_n^2$ (where ω_n is the desired cutoff radian frequency of the voltage control loop [152]). \dot{y}_{dc} is obtained from (3.36). (3.32) and (3.36) allow obtaining the SC power reference. The inner loop goal is to control the power delivered by the SC to track its reference.

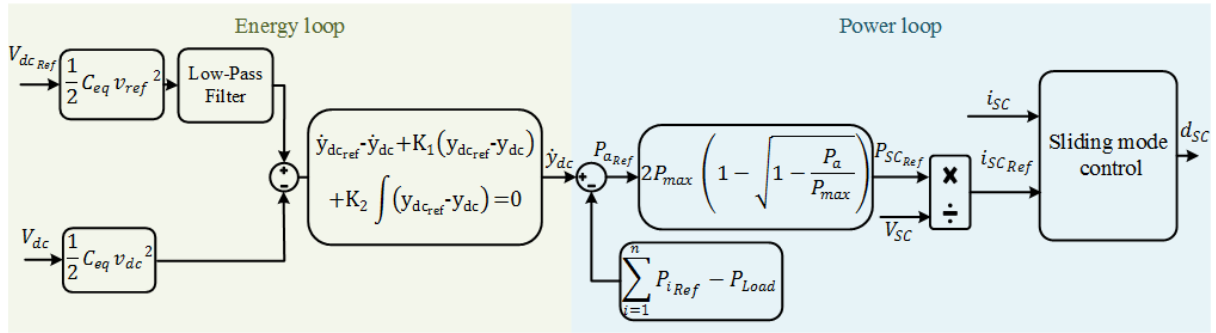


Figure 3-8. Schematic diagram of the voltage controller.

3.3.2.2. Inner loop

Assuming that the dynamic of the SC voltage variations is slow in comparison to the DC bus voltage variations, the SC voltage can be considered as a constant value for the design of the DC bus control. As a result, the reference current of the SC can be obtained by dividing its reference power to its voltage. The reference power, which must be injected to the DC bus, can be calculated by (3.32) and the result of the outer loop. Then, the reference power of the SC is calculated by (3.34). In this thesis, the sliding mode control method is used to control the current. The main reason behind take this control method is its dynamic which is independent of the operating point. A sliding surface is defined as follows:

$$s = i_{SC} - i_{SC_{ref}} + k_i \int (i_{SC} - i_{SC_{ref}}) \quad (3.37)$$

To ensure the zero steady-state error, an integral term is used in this sliding surface [153]. The associated reaching condition is defined as follows:

$$\dot{s}(x) = -\lambda s(x) \quad (3.38)$$

where λ is a positive constant that determines the speed of attraction to the sliding surface. By differentiating (30) and using (31), the following equation is obtained:

$$\frac{di_{SC}}{dt} + k_i (i_{SC} - i_{SCref}) = -\lambda s(x) \quad (3.39)$$

Using this equation and (3.34), the equivalent duty cycle of the SC converter can be calculated as follows:

$$d_{SC} = \frac{L_{SC}}{V_{dc}} \left[\frac{V_{dc} - v_{sc} + r_{SC} i_{SC}}{L_{SC}} - k_i (i_{SC} - i_{SCref}) - \lambda (i_{SC} - i_{SCref} + k_i \int (i_{SC} - i_{SCref})) \right] \quad (3.40)$$

As seen in Figure 3-9, saturation controls the maximum value of the duty cycle. To prevent the integration wind-up in this control, an anti-windup method is proposed in this thesis. This method guarantees that the control is not stuck on the maximum value imposed by the saturation during the startup and transient conditions. To realize this method, the difference between the duty cycle value before and after saturation is multiplied by a gain (k_{aw}). Then, the resulting value is subtracted from $i_{SC} - i_{SCref}$.

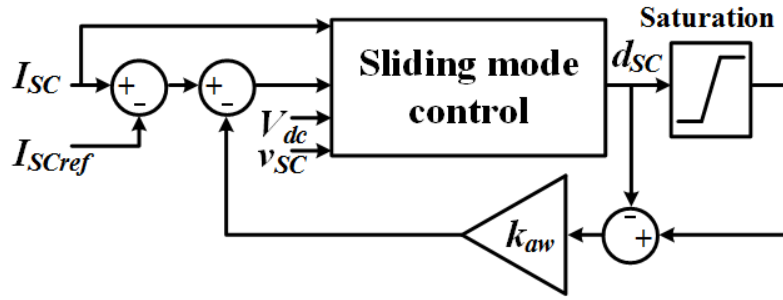


Figure 3-9. Proposed anti-windup control scheme.

3.3.2.3. Capacitance sizing

The optimum value of the capacitance is also a key factor in reducing the size of the system. In [150], a method was proposed to calculate the minimum value of the capacitance. Based on this method, the worst condition is considered. In this condition, the SC and DC link voltages are in their minimum values and a step in the load power from the highest negative value to the highest positive value is applied as shown in Figure 3-10. Due to the negative value of the load power (recovery mode), the fuel cells inject no power and when this step occurs, the S_{SC} switch is turned on to compensate this power and regulate the DC bus voltage. During this time, the energy is stored in the inductor of the supercapacitor boost converter and no energy is injected to the DC bus. As a result, the DC bus voltage is decreased during this time. Because the S_{SC} is turned on during the interval of $[t_i, t_m]$, the following equation based on (3.31) can be written:

$$\begin{cases} \dot{y}_{dc}(t) = -P_{load}(t) \\ \dot{y}_{dc,ref}(t) = 0 \\ y_{dc,ref}(t) = y_{dc,ref}(t_i) \end{cases} \quad (3.41)$$

The stored energy in the DC bus can be obtained from the integral of its derivative in this interval. Based on (3.41) and (3.36), the derivative of the stored energy in the DC bus can be rewritten during the interval of $[t_i, t_m]$. The integral part of (3.36) can be neglected in this short time interval. As a result, the derivative of the DC bus stored energy is changed as follows:

$$\begin{cases} y_{dc}(t) = y_{dc,ref}(t_i) - P_{load,max}(t - t_i) \\ \dot{y}_{dc}(t) = K_1(y_{dc,ref}(t_i) - y_{dc}(t)) \end{cases} \quad (3.42)$$

Assuming the slow dynamics of the supercapacitor voltage and regarding (3.33) and (3.34), the current of supercapacitor can be calculated as follows:

$$i_{SC,ref}(t) = \frac{v_{SC,min}^2}{2r_{SC}} \left(1 - \sqrt{1 - \frac{4r_{SC}(1 + K_1(t - t_i))}{v_{SC,min}^2}} \right) \quad (3.43)$$

Furthermore, an equation for the current of supercapacitor can be obtained by solving the differential equation of the inductor of the boost converter connected to the supercapacitor as follows:

$$i_{SC}(t) = - \left(i_{min} + \frac{v_{SC,min}}{r_{SC}} \right) \exp \left(- \frac{r_{SC}}{L_{SC}} (t - t_i) \right) + \frac{v_{SC,min}}{r_{SC}} \quad (3.44)$$

The time interval of $t_m - t_i$ and $i_{SC,max}$ can be obtained by solving (3.42) and (3.43) when $t = t_m$. using this interval and (3.41), an equation can be obtained for the capacitance value as follows:

$$C_{eq} = \frac{2P_{load,max}(t_m - t_i)}{V_{dc}(t_i)^2 - V_{dc}(t_m)^2} \quad (3.45)$$

where C_{eq} is the equivalent capacitance of the series connection of the boost converter output capacitors. $V_{dc}(t_m)$ can be rewritten as follows:

$$V_{dc}(t_m) = V_{dc}(t_i) - \Delta V \quad (3.46)$$

where ΔV is the voltage drop. The minimum value of the capacitor can be obtained by solving (3.42)-(3.45) numerically. In this application, the maximum voltage drop in DC link is 7 V and as a result, the minimum value of the four capacitors in series connection is 4.7 mF for a variation of the load power from -400 W to 400 W. The other parameters are shown in Table 3.1. A simulation in the same condition is performed and the load power is changed from -400 W to 400. The DC bus voltage is shown in Figure 3-11. As seen in this figure, the voltage drop in this condition is close to the maximum value in the analytical approach.

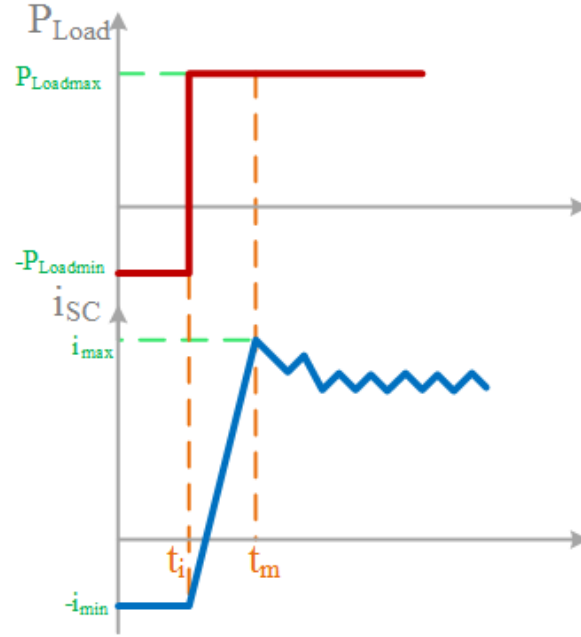


Figure 3-10. Maximum step load to calculate the minimum value of the capacitors.

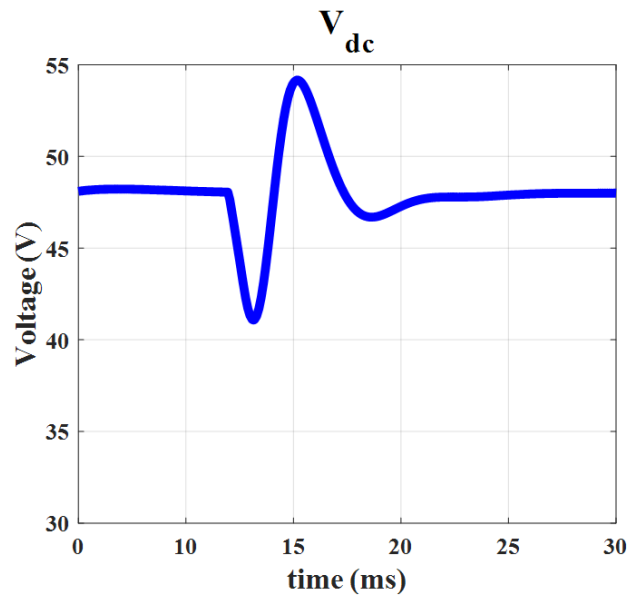


Figure 3-11. DC bus voltage drop when load power is changed from -400 W to 400 W, the capacitance of the boost converter output capacitors is 4.7 mF and the SC voltage is equal to half of its nominal voltage (24).

3.3.3. SC voltage controller

A similar approach is used to control the voltage of SC. The stored energy in SC is used to controls its voltage. This energy can be calculated as follows:

$$y_{SC} = \frac{1}{2} C_{SC} v_{sc}^2 \quad (3.47)$$

where C_{SC} is the capacitance of the SC. Considering that the dynamic of the DC bus voltage loop is widely greater than the dynamic of the SC voltage loop, the derivation of this energy is as follows:

$$\dot{y}_{SC} = -P_{SC} \approx \sum_{j=1}^n P_j - P_{load} \quad (3.48)$$

\dot{y}_{SC} is the power of the SC (P_{SC}) that should be transferred to the SC (negative) or injected by it (positive). The total power of cell groups that must be injected in the steady-state can be obtained by this equation. A simple proportional gain controller is used to ensure that stored energy in the SC follows its reference:

$$\dot{y}_{SC_{ref}} - \dot{y}_{sc} + K_{sc} (y_{SC_{ref}} - y_{SC}) = 0 \quad (3.49)$$

The proportional gain K_{SC} , which represents the cutoff radian frequency of the SC voltage loop, should respect the low dynamic assumption of the SC voltage loop. Based on (3.48), the total power that should be injected by the cell groups can be calculated. As seen in Figure 3-12, a rate limiter is used to respect the dynamical constraint imposed by the fuel cell auxiliaries. V_i and i_i are the voltage and current of the i^{th} group of cells. d_i is the duty cycle of the boost converter connected to the i^{th} group of cells.

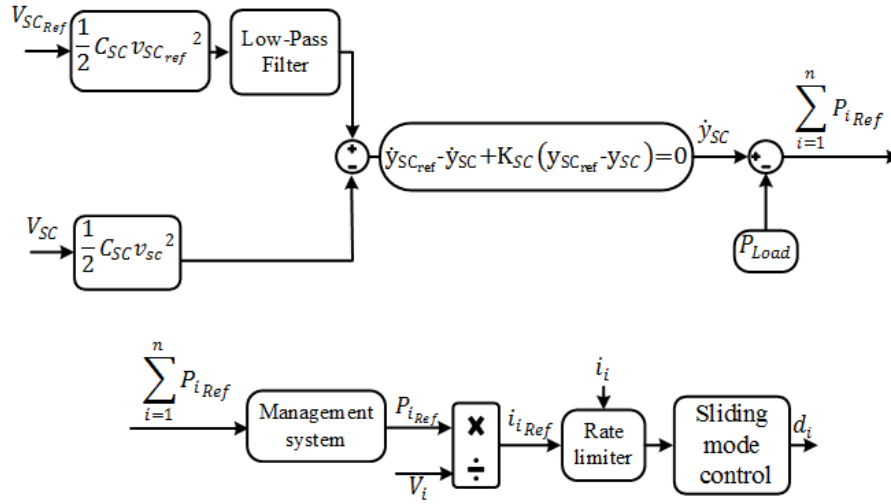


Figure 3-12. Schematic diagram of the SC voltage controller.

To control the power delivered by each group of cells, the sliding mode controller is used. The parameter of this controller is chosen in such a way that this controller is as fast as enough.

3.4. Simulation results

Based on the proposed state-space model, a simulation is made by four capacitors in series in Matlab/Simulink to preliminary verify the validity of the proposed equalizer theories. For a precise study of the proposed system, the H-bridge inverter is controlled in the open-loop mode and its duty cycle is set to 0.4 in the first simulation. It is assumed that the PEMFCs connected to the first and second capacitors can inject half of the nominal power and the other cells inject the nominal power (126 W). The voltage and current waveforms on the primary side of the transformer for $d=0.4$ are shown in Figure 3-13. As seen in this figure, the current is linear and the power can be transmitted through the transformer. These results are also in agreement with the theoretical waveforms.

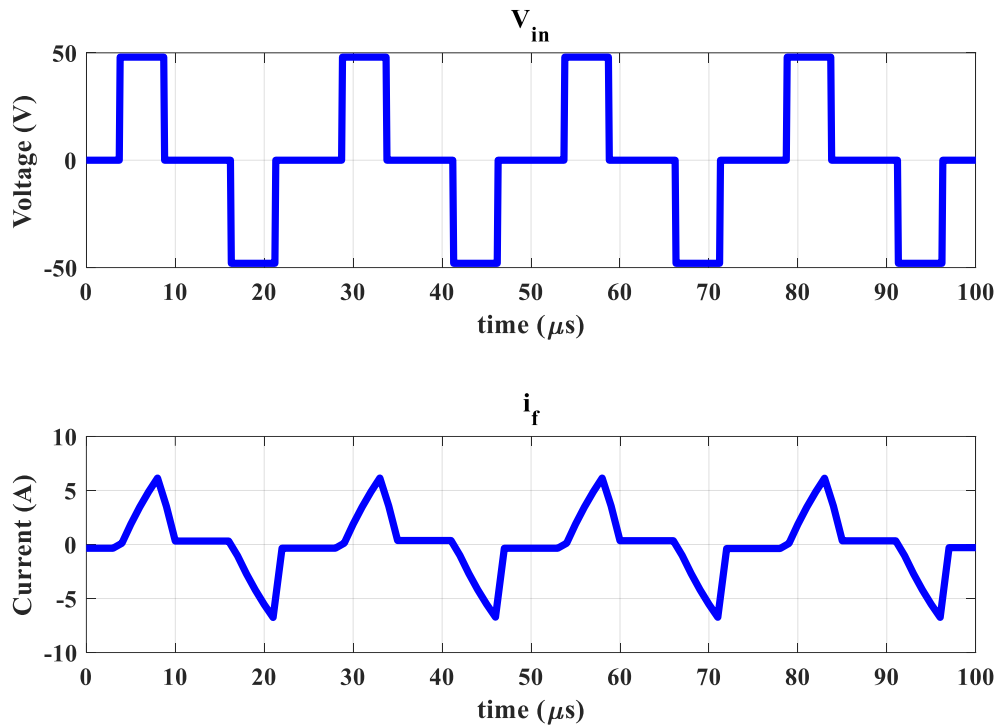


Figure 3-13. Simulation results of voltage and current waveforms on the primary side of the transformer for $d=0.4$.

The voltage changes of different capacitors in closed-loop are shown in Figure 3-14 when the cells inject nominal power except the first cell in the second simulation. The first cell is turned off and it can inject no power in this simulation.

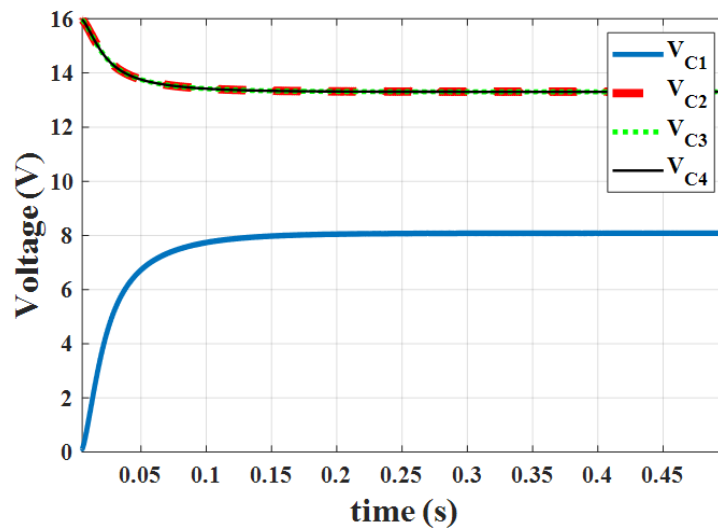


Figure 3-14. Simulation results of the Output capacitor voltages in closed-loop when the first group of cells injects no power.

To evaluate the behavior of the average model, two other simulations are performed when four groups of the cells inside the stack are connected to four boost converters. The injected power by the first group is changed from 63W to 100W at 0.05s during the third simulation. The injected power of the other cells is fixed to nominal power (126 W) during this simulation. The parameters that are used to make simulation results are shown in Table 3.1. To study the dynamical behavior of the average model, the state-space model of the system based on (3.1)-(3.5) is also simulated with the same parameters. The results of the third simulation are shown

in Figure 3-15 and Figure 3-16 As seen in these figures, the average model results are consistent with the results of the state space model. The voltage change of the output capacitor of the boost converters connected to the different groups of the cells is shown in Figure 3-15. The difference between the two models is due to the linearizing method which was used to calculate (3.14). Indeed, the transformer current has an exponential form which has been approximated by the first-order polynomial based on the Taylor series. For the proposed average model, the power of the balancing system defined by (3.14) is a bit overestimated; consequently, the obtained voltage is a bit higher than the switching model or state-space model. The voltage of the DC bus ($\sum_j V_{C_j}$) is shown in Figure 3-16 during this simulation. As seen in this figure, the DC voltage is regulated near the reference voltage (48 V). Notable that the power of the fuel cell is reduced slowly and this undershoot is eliminate when the real low dynamic of the fuel cell is taken into account. Therefore, this simulation was accomplished in the worst condition.

The condition for the fourth simulation is similar to the third simulation except for the injected power by the second cell. This power is set to 100W in the fourth simulation. The voltage changes of different capacitors are shown in Figure 3-17. The DC bus voltage is shown in Figure 3-18 during this simulation. As seen in these figures, the average model corresponds with the state-space model of the system.

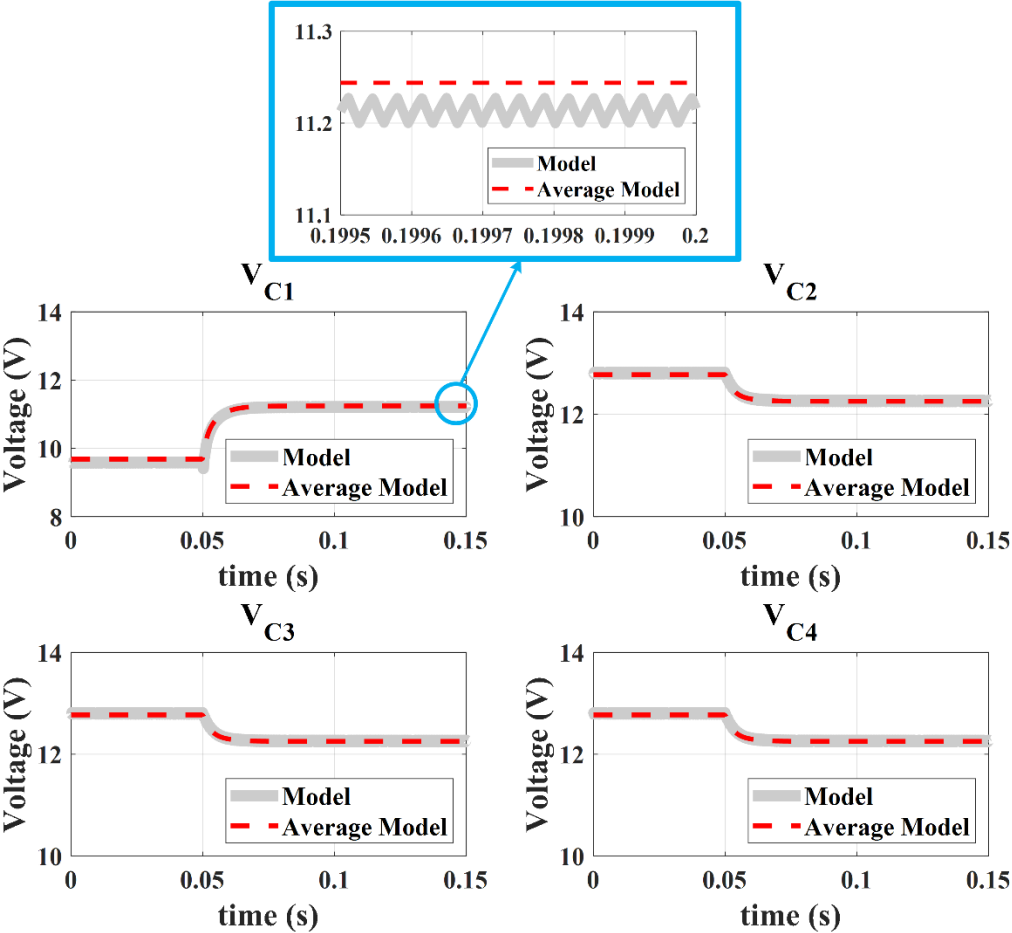


Figure 3-15. Simulation results of the voltage changes of the boost converters output capacitors connected to the cells in closed-loop when P_I is increased from 63W to 100W and the other groups of cells inject the nominal power.

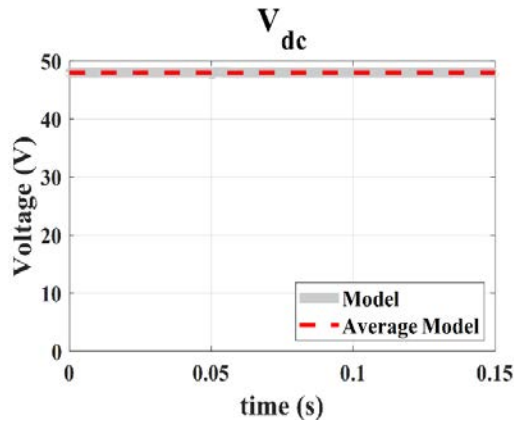


Figure 3-16. The dc bus voltage in closed-loop when the first cell power is increased from 63W to 100W and the other groups of cells inject the nominal power.

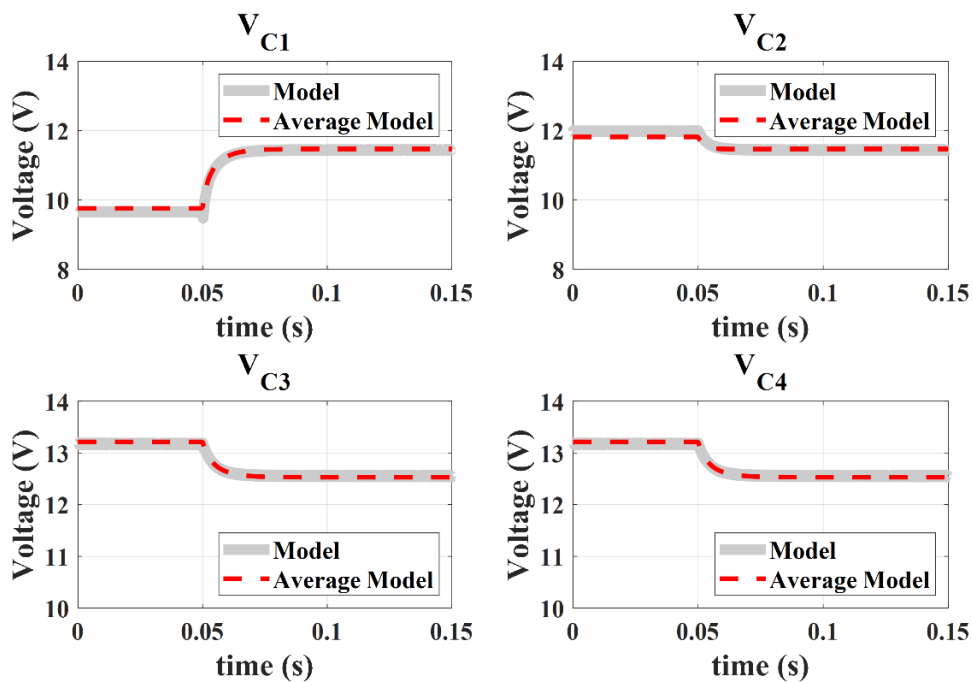


Figure 3-17. 1 Simulation results of the voltage changes of the boost converters output capacitors connected to the cells in closed-loop when P1 is changed from 63W to 100W, P2 is set to 100W, and the other groups of the cells inject the nominal power.

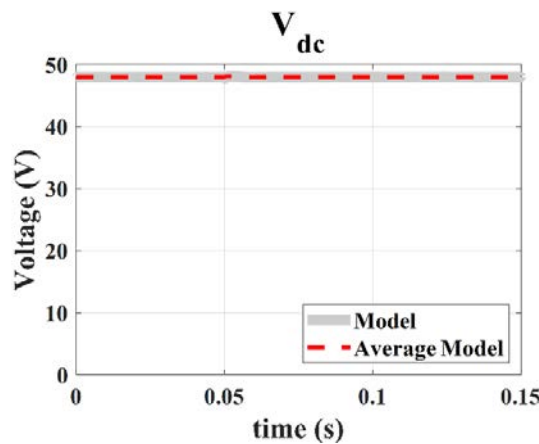


Figure 3-18. The dc bus voltage in closed-loop when the first cell power is changed from 63W to 100W, the injected power of the second cell is set to 100W, and the other groups of the cells inject the nominal power.

3.5. Experimental results

To further verify the proposed system and validation of the theoretical analysis, simulation results, and the proposed models, the experiments are conducted on a laboratory prototype as demonstrated in Figure 3-19. A dSPACE 1005 with the FPGA board is used to receive the captured data and send the commands. Four programmable power supplies are used to emulate the PEMFCs. These power supplies are connected to four boost converters, the output capacitors of the boosts are connected in series. The part number used in this prototype are listed in Table 3.2. The proposed balancing system connects to these capacitors. Notably, a planar transformer is built to implement the equalizer of the test bench. Each winding turn of this transformer means a printed circuit board. On each printed circuit board, a copper line with a width of 21.5 mm and a thickness of 35 μm is rotated in such a way that the circuits can be placed in the window of the magnetic core. This design is used to minimize leakage inductance. The turn number of primary and secondary windings are shown in Table 3.1.

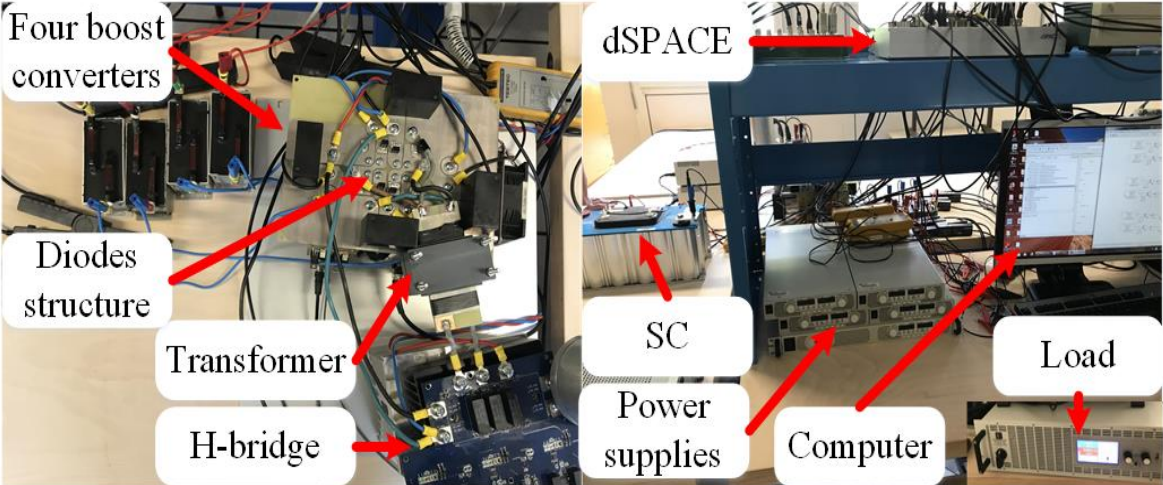


Figure 3-19. Test bench of the proposed system.

Table 3.2. Parameters of the used devices in the test bench.

	Unit	Value
FC	Power supply	TDK GENH 750W
	Inductance	(1mH)
Boost converter	Switches	IGBT
	Capacitor	Electrochemical (4700 μF)
	Diodes	DSS2x121-0045B
Equalizer	Magnetic core	B66295G Material N87
	H-bridge switches	SiCMOSFET CCS050M12CM2
	Capacitor	film (220 μF)

The first experiment conditions are similar to the first simulation. The cell groups inject nominal power except the first and second cell groups. These cell groups inject half of the nominal power. The voltage and current waveforms on the primary side of the transformer for $d=0.4$ are shown in Figure 3-20. As seen in this figure, the results are in agreement with the simulation results and the power can be transferred to the first and second capacitors during the positive and negative part of the input voltage respectively.

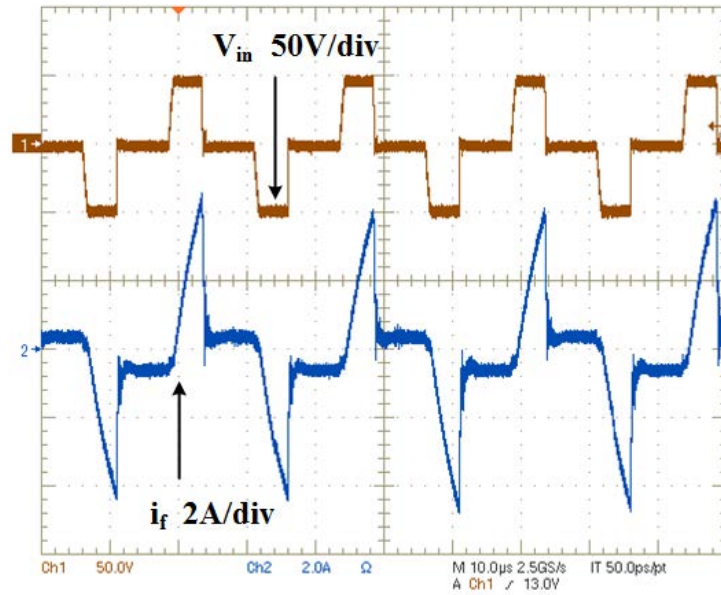


Figure 3-20. Experimental waveforms of the current and voltage on the primary side of the transformer when first and second fuel cells inject the half of nominal power and duty cycle of H-bridge inverter is equal to 0.4.

The second experiment conditions are similar to the second simulation. The first power supply is turned off and as a result, it can inject no power. The other cells inject nominal power. The voltage changes of different capacitors are shown in Figure 3-21 when the duty-cycle of H-bridge inverter is controlled in closed-loop with the same parameter of simulation.

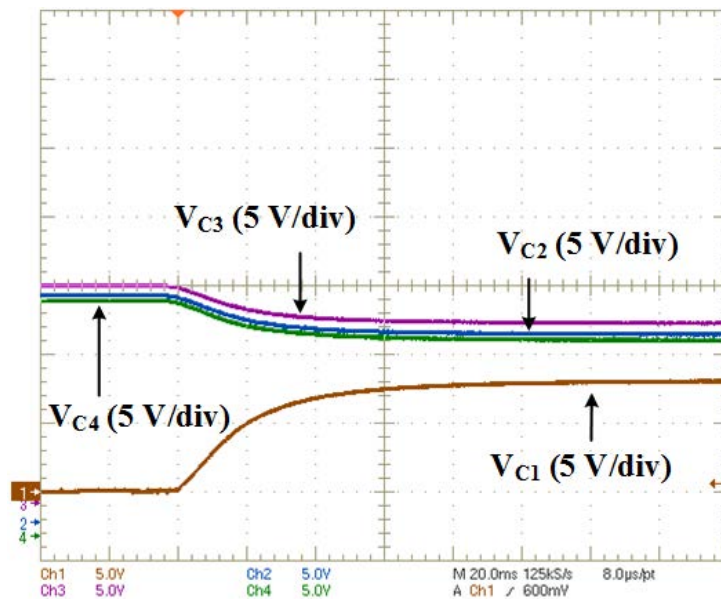


Figure 3-21. Experimental results of the Output capacitor voltages when the first group of cells injects no power.

To validate the proposed model for the design purpose, the capacitor voltages are measured when the first cell can inject half of the nominal power. In this experiment, the duty cycle is changed in the open-loop from 0.3 to 0.9. These voltages are also numerically calculated by (3.21) and (3.28). The output power of each boost converter is measured. These powers are used in these theoretical equations. The results of the experiment and theoretical equations are shown in Table 3.3. In this table, the error V_{C_1} is the relative error of the first capacitor voltage. In this table, the error is the root mean square of the relative errors as follows:

$$Error = \sqrt{\sum_{j=1}^4 \left(\frac{V_{C_{jth}} - V_{C_{jexp}}}{V_{C_{jth}}} \right)^2} \quad (3.50)$$

where $V_{C_{jth}}$ and $V_{C_{jexp}}$ are respectively the theoretical and experimental voltage of the j^{th} capacitor.

Table 3.3. Theory and experimental capacitor voltages (V) comparison

Duty cycle	0.3	0.4	0.5	0.6	0.7	0.8	0.9
$V_{C_{1th}}$	10.05	10.58	10.92	11.13	11.28	11.38	11.46
$V_{C_{2th}}$	12.72	12.54	12.43	12.35	12.31	12.27	12.25
$V_{C_{3th}}$	12.32	12.14	12.04	11.97	11.92	11.89	11.86
$V_{C_{4th}}$	12.92	12.74	12.63	12.55	12.51	12.47	12.44
$V_{C_{1ex}}$	10	10.5	10.9	11.1	11.3	11.3	11.4
$V_{C_{2ex}}$	12.7	12.5	12.3	12.2	12.2	12.1	12.1
$V_{C_{3ex}}$	12.4	12.1	12	12	12	12	12
$V_{C_{4ex}}$	13	12.8	12.6	12.5	12.5	12.4	12.4
Error (%)	1.04	1.00	1.14	1.33	1.13	1.89	1.81
Error V_{C_1} (%)	0.50	0.76	0.18	0.27	0.18	0.70	0.52

The same assumption of the third simulation is used to accomplish the third experiment. The experimental results of the output capacitors voltage changes are shown in Figure 3-22 (a) when the first cell power is increased from 63W to 100W. As seen in this figure, the voltage of the first capacitor is increased because of the increasing the corresponding cell injected power. The voltage of the other capacitors changed in such a way that the sum of voltage is fixed to 48V. The average model results are also shown in Figure 3-22 (b) in the same conditions for a better view. These results are verified by the experimental results. There is always an error between the simulation and experiment results in steady-state. The error between voltages of the capacitors is in a reasonable range and less than 3 percent. This error is caused by not considering all losses.

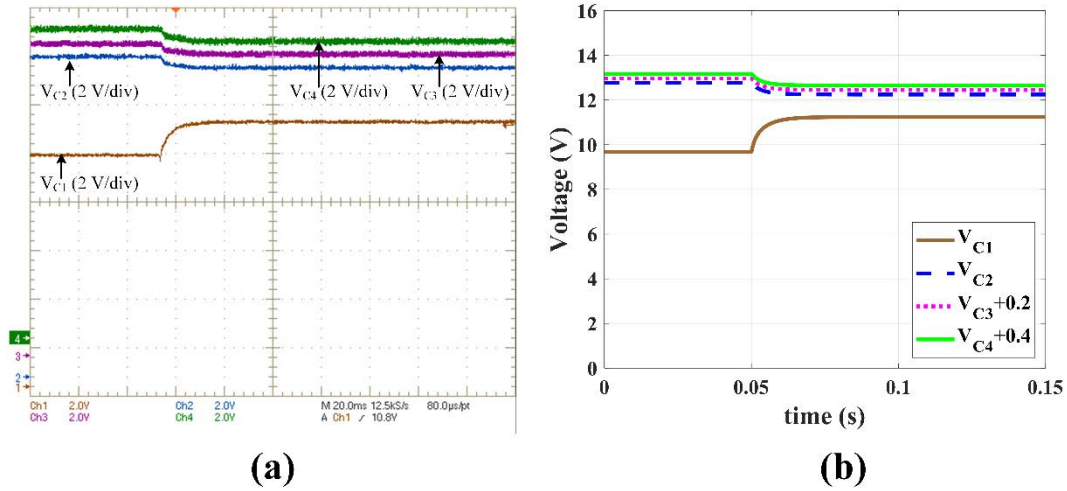


Figure 3-22. Voltage changes of the boost converters output capacitors connected to the cells in closed-loop when P_1 is increased from 63W to 100W, and P_2 is set to the nominal power: a) Experimental results b) Simulation results of the average model.

The fourth experiment is accomplished in the same condition as the fourth simulation. The experimental results of the voltage changes of output capacitors are shown in Figure 3-23(a). To provide a better view, the average model results are also shown in Figure 3-23(b) in the same conditions. As seen in this figure, the experimental results are in agreement with the simulation results. Based on the experimental and simulation results, the proposed model for the management system is valid and it can be used to study and analyze the stability of the system.

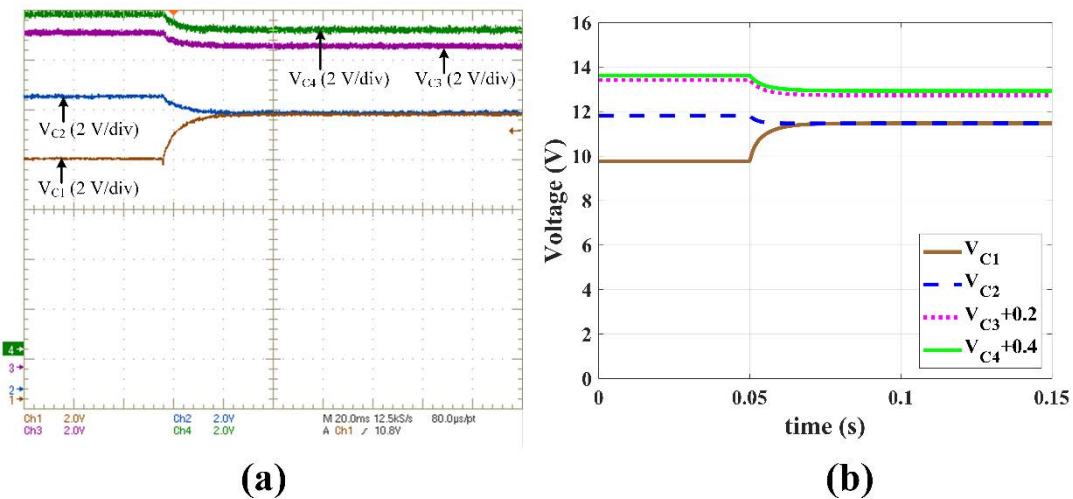


Figure 3-23. Voltage changes of the boost converters output capacitors in closed-loop when P_1 is changed from 63W to 100W, and P_2 is set to 100W: a) Experimental results b) Simulation results of the average model.

The main objective of the proposed equalizer system is to guarantee the controllability of DC-DC converters connected to fuel cells for applying energy management (Figure 3-1). The drying and flooding conditions are the most critical conditions for the membrane of the PEMFC. In these conditions, the energy management system must function properly to compensate for the faults. If one cell suffers from drying, it should be short-circuited to produce more water by keeping constant gas flow rates. This leads to a decrease in gas stoichiometry for this particular cell and consequently membrane humidification. On the contrary, no current should be

generated by a cell in flooding conditions to let it dry. In other words, the power generated by the cell should be controlled near zero. In the following, it is assumed that the first cell experiences these conditions among four other healthy cells.

The capacitor voltages are shown in Figure 3-24 (a) and the transformer voltage and current on the primary side are shown in Figure 3-24 (b) in the flooding condition of the first PEMFC. As seen in these figures, the current of the first PEMFC cannot be set to zero before running the equalizer system. As seen in Figure 3-24, when the square wave voltage is supplied on the primary side of the transformer by the H-bridge inverter, the current of the first PEMFC reaches to zero after about 40 ms with the used parameters for the controller. Indeed, the boost converter connected to the first PEMFC will be controllable after this time. Furthermore, the capacitor voltage connected to the first PEMFC is increased and other capacitor voltages are decreased.

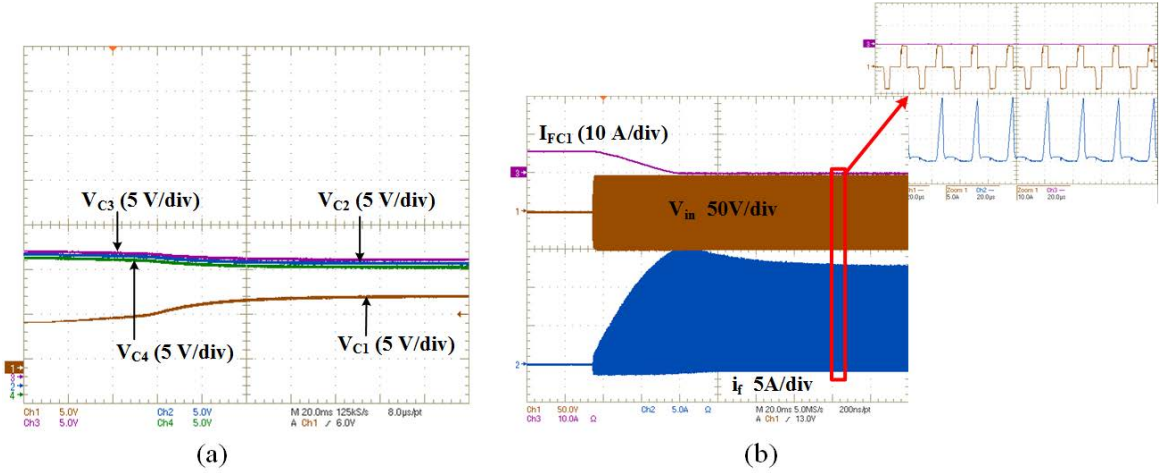


Figure 3-24. Experimental results of the proposed equalizer during the flooding condition of the first cell. (a) Output capacitor voltages. (b) Voltage and current on the primary side of the transformer and current of the first cell.

The output capacitor voltages of the boost converters in the drying condition of the first PEMFC are shown in Figure 3-25 (a). In this condition, the voltage and current on the primary side of the transformer are also shown in Figure 3-25 (b). As seen in this figure, the first capacitor voltage is increased from zero to 8 volts but the short-circuit conditions are maintained for the first PEMFC. For this experiment, the maximum current of the power supply is limited to 20A.

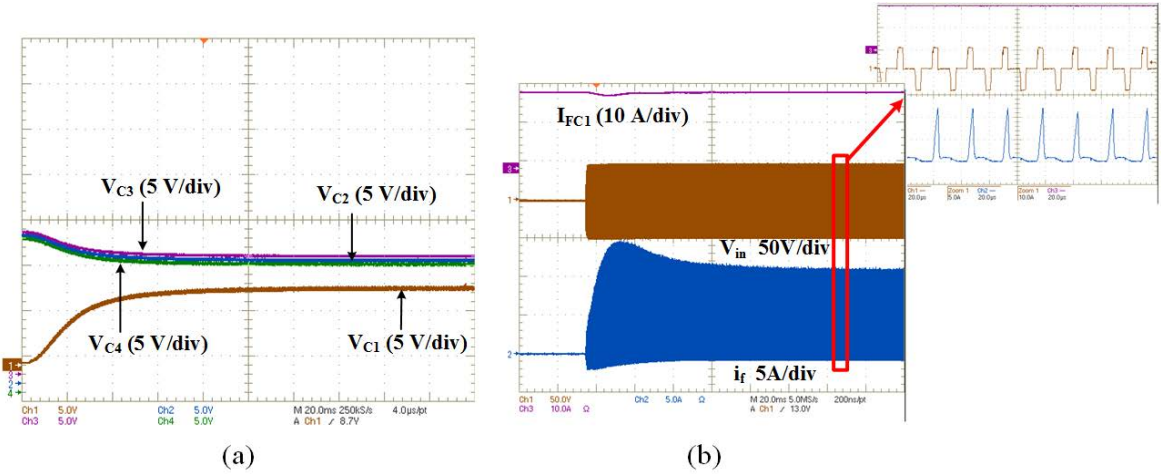


Figure 3-25. Experimental results of the proposed equalizer during the drying condition of the first cell. (a) Output capacitor voltages. (b) Voltage and current on the primary side of the transformer.

3.6. Stability analysis

Since the average model is valid and it can estimate the behavior of the system in closed-loop, this model can be used to analyze the stability of the system. By obtaining the eigenvalues of the Jacobian matrix of this model, the local stability around the equilibrium point can be analyzed. Furthermore, this model can be used to size the parameters of the different controllers in such a way that the stability of the system is ensured. The poles of the sliding mode controller (current controller) should be at least less than one-tenth of the switching radian frequency of the boost converters or bidirectional converter connected to the SC. The switching frequency of these converters is equal to 30 kHz. Therefore, the λ and k_i of the sliding mode controller should be lower than 18850 *rad/s*. Due to the noise in real conditions, 7500 *rad/s* is used for these two parameters. As mentioned before, the power loop of the DC bus voltage controller should be faster than the energy loop. As a result, the cutoff radian frequency of the energy loop should be lower than one-tenth of the current control loop. Therefore, ω_n equal to 500 *rad/s* is used to obtain K_1 and K_2 . The damping ratio of 0.7 is used to obtain the best behavior. The control of the SC voltage should respect the slow dynamic of the fuel cell. A rate limiter of 4 *A/s* limits the dynamic of current change to respect the dynamic of the fuel cell. The equalizer system controller should be faster than the DC link voltage controller to ensure the controllability of boost converters even in transient conditions. However, the cut-off frequency of the equalizer controller should be lower than one-tenth of its switching radian frequency. The switching frequency of the H-bridge inverter is equal to 40 kHz. The equalizer controller must be fast enough to guarantee the controllability of the boost converters in transient conditions. The equalizer controller can be saturated in transient conditions even with the dynamic saturation and anti-windup. As a result, the cut-off frequency of $2\pi \cdot 10^3$ *rad/s* is used for the equalizer controller. The dynamic variations of the SC voltage will be neglected in the stability study due to the slow dynamic of the SC voltage and the powers delivered by the fuel cells are supposed to be constant.

To evaluate the stability of the system, the power of the first cell is changed from zero W to 100 W with steps of 10 W. The other cell powers are fixed to 126 W. The other parameters that are used for this simulation is shown in Table I. The voltage change of the output capacitor of the boost converters connected to cells in this simulation is shown in Figure 3-26. As seen in this figure, the voltage of the first cell is increased by increasing the injected power of the first cell. The voltage of other cells is decreased to fix the DC bus voltage to 48 V. The eigenvalues of the closed-loop system are depicted in Figure 3-27. These eigenvalues with negative real parts prove the stability of the system. As seen in this figure, the different groups of eigenvalues are shown in different circles with different colors and numbers. The purple circles show the eigenvalues that strongly depend on the parameters of the voltage and current controllers. The place of eigenvalues inside the purple circle numbered 1 and 2, can be changed by changing the parameters of the current sliding mode controllers. The multiple eigenvalues in the same place are shown by a circle around the multiplication sign as shown in circle numbered one. The place of eigenvalues inside the purple circle numbered 3 and 2 can be changed by changing the natural radian frequency of the second-order system used to find K_1 and K_2 in (3.36). The blue circles specify the place of eigenvalues that depend on the parameters of the equalizer system controller. The place of eigenvalues inside the blue circle numbered 4 can be changed by the operating point and all parameters of equalizer controller consist of the proportional gain and the cut-off frequency that used for finding the duty cycle of H-bridge inverter. The place of eigenvalues inside the blue circle numbered 5 strongly depends on the operating point and the proportional gain (K_p) of the equalizer system controller.

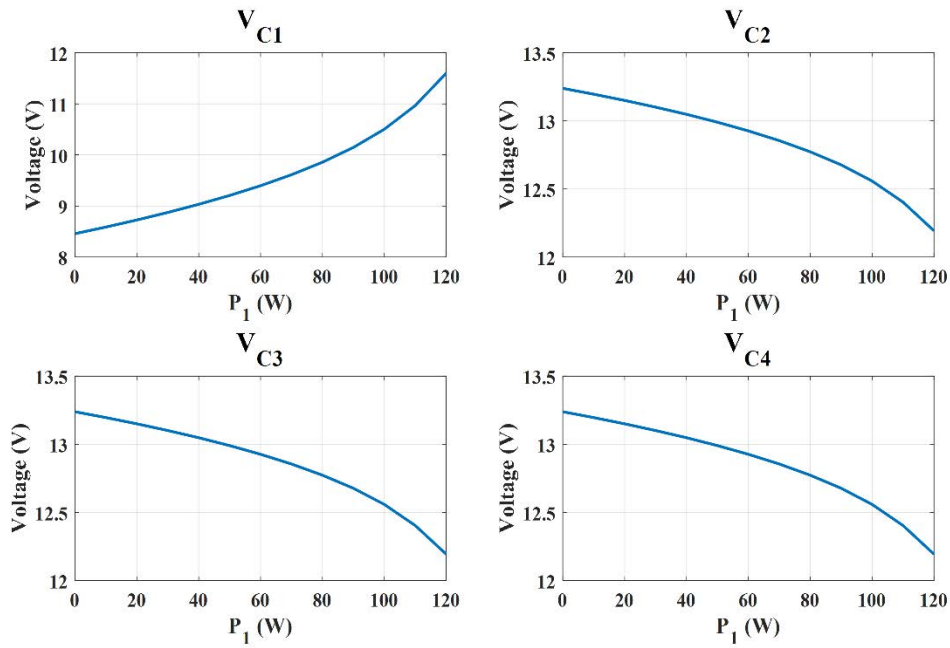


Figure 3-26. Steady-state voltage changes of the boost converters' output capacitor connected to fuel cells in closed-loop by changing the injected power of the first group of cells while the other groups inject the nominal power of 126 W.

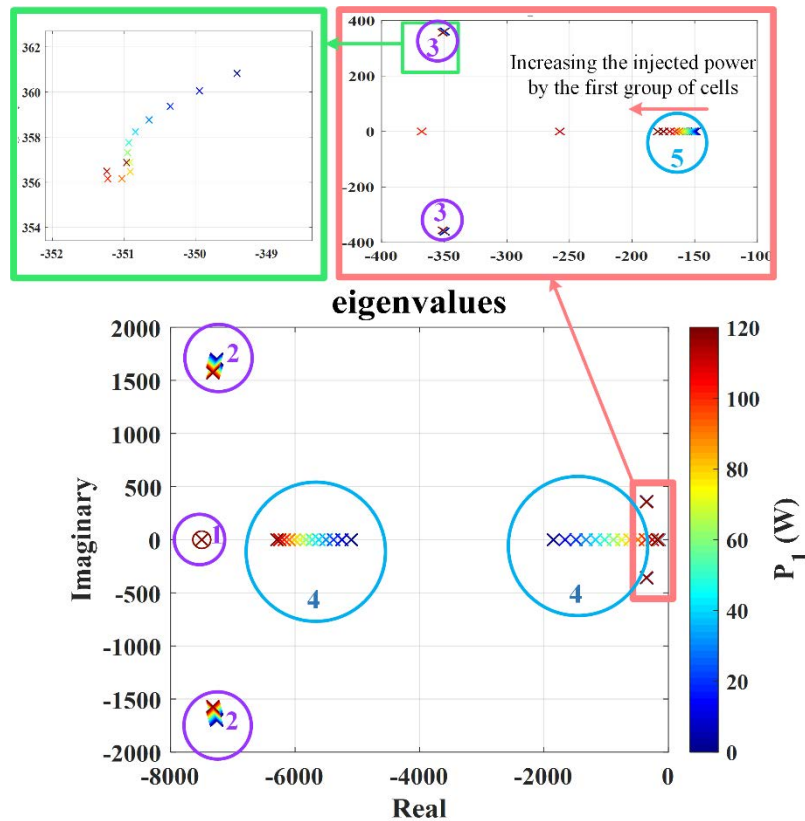


Figure 3-27. Eigenvalues of the closed-loop system by changing the injected power of the first group of cells while the other groups inject the nominal power of 126 W.

To prove the stability of the system when two groups of the cells are in the fault conditions, the power of the second group of cells is fixed to 50 W that is a little bit lower than the half of nominal power. The injected power of the first group of cells is increased from zero W to 40W while the injected power by the other groups is set to 126 W. The steady-state value of the output capacitor voltages by changing the first cells injected power is shown in Figure 3-28. As

seen in this figure, the voltage of the first cell is increased by increasing the injected power of the first cell. The voltage of other cells is decreased to fix the DC link voltage near 48 V. The eigenvalues of the closed-loop system are shown in Figure 3-29. These eigenvalues with negative real parts prove the stability of the system.

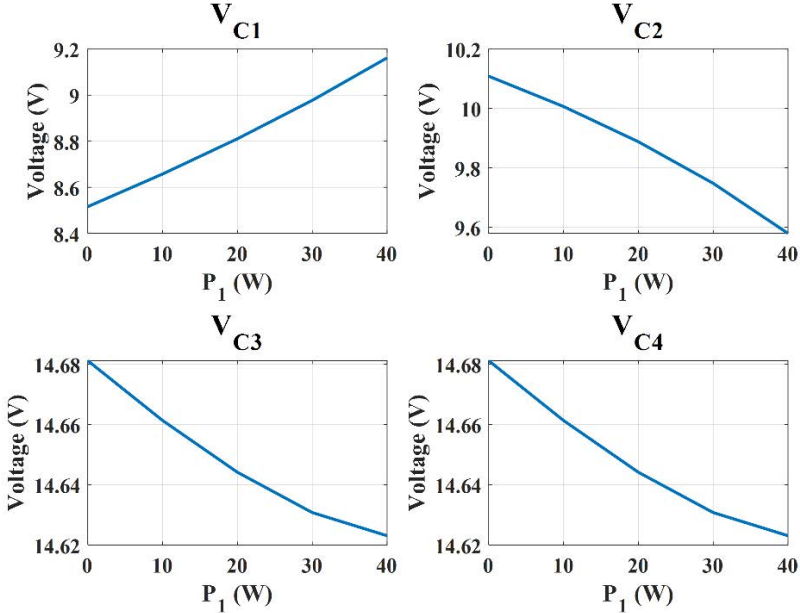


Figure 3-28. Steady-State voltage changes of the boost converters’ output capacitor connected to fuel cells in closed-loop by changing the injected power of the first group of cells while the second group of cells injects 50 W and the other groups inject the nominal power of 126 W.

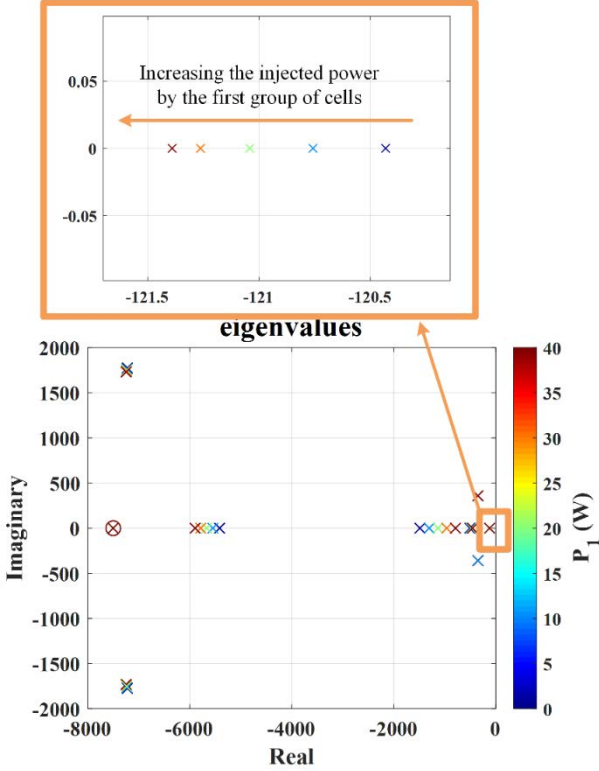


Figure 3-29. Dominant eigenvalues of the closed-loop system by changing the injected power of the first group of cells while the second group of cells injects 50 W and the other groups inject the nominal power of 126 W.

The other issue that needs to be addressed is the robustness of the control method. Robustness is the ability of the closed-loop system in being insensitive to perturbations and tolerating the component variation. To assess the robustness of the controller, the eigenvalues of the system are studied under changing some parameters of the system. If the real part of eigenvalues remains negative, it can be proved that it is a robust controller. In this system, the capacitor change can have an important effect on the stability of the system. The capacitance can be changed by aging and temperature effect.

To check the robustness of the control method, the capacitance of the first capacitor is changed from 2.35 mF to 9.4 mF . The injected power of the first cell is fixed to zero W and the other cells inject the nominal power. The same parameters as Table 3.1 are used for the controller. The evolution of the eigenvalues of the system is depicted in Figure 3-30. The dominant eigenvalue of the system becomes less negative by further decreasing the capacitance value from 4 mF . The place of multiple eigenvalues that are seen in this figure strongly depends on the control parameters and operating point.

The permeability of the magnetic core and the coupling coefficient between the windings of the transformer are two other parameters that their values can have an impact on stability. The permeability change depends on the manufacturing process. In [154], it has been concluded that the permeability is constant for a wide range of temperature. However, the initial permeability is changed by increasing the temperature based on the datasheet of the used core. The effect of permeability change on the location of the poles is so small. The coupling coefficient can be changed due to the manufacturing process. To evaluate the impact of this parameter, the power of the first group of cells is fixed to zero Watt while the other cells inject the nominal power. The coupling coefficient is changed from 0.7 to 0.97. The parameters of the controller are as same as before. The dominant eigenvalue of the system during the change of the coupling coefficient is also depicted in Figure 3-31.

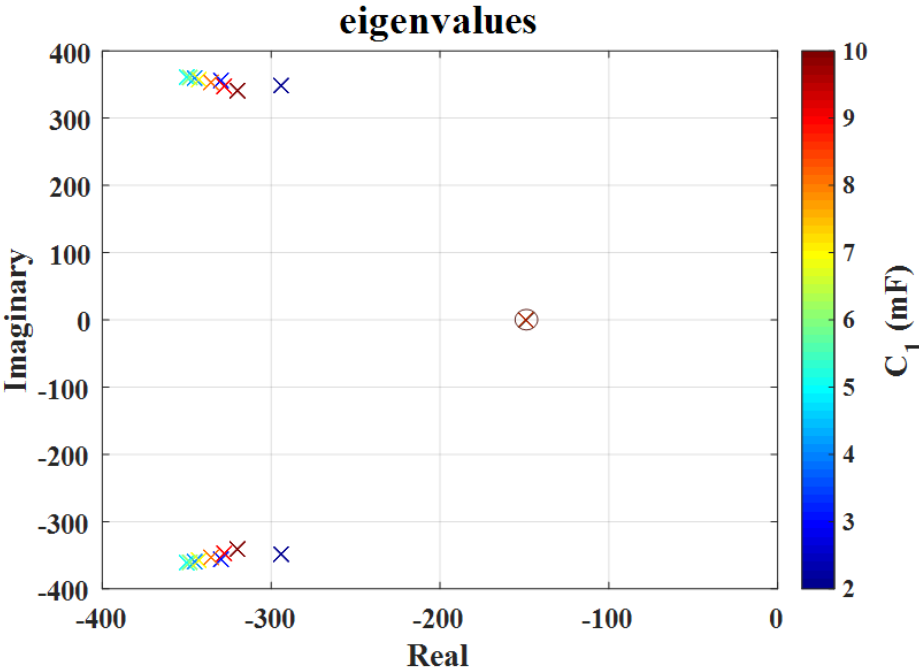


Figure 3-30. Dominant eigenvalues of the closed-loop system by changing the capacitance value of the first capacitor when the power of the first group of cells is equal to zero W and the other groups inject the nominal power of 126 W.

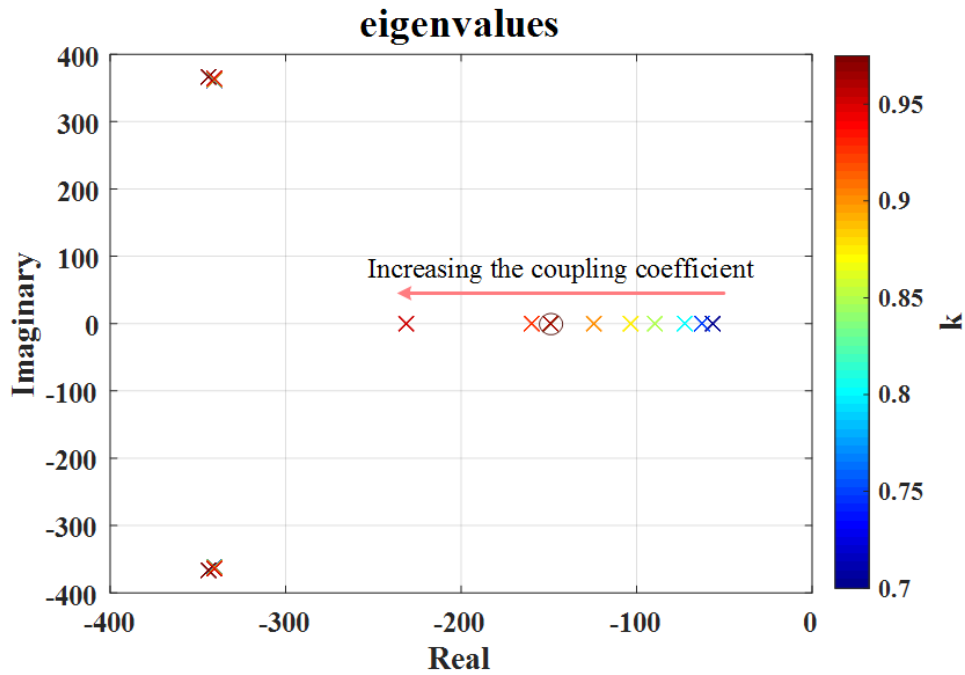


Figure 3-31. Dominant eigenvalues of the closed-loop system by changing the coupling coefficient when the power of the first group of cells is equal to zero W and the other groups inject the nominal power of 126 W.

As seen in the previous results, the real part of the eigenvalues of the system has always a negative value of less than -50. This value depends strongly on the equalizer controller parameters.

3.7. Conclusions

In this chapter, a power electronics architecture is proposed to implement the FCMS. Using this architecture, energy management can be performed even in the fault mode of the cells, and while the system is trying to cure a cell. An equalizer based on the multi-winding transformer was proposed to ensure the controllability of boost converters in a series connection of their output capacitors. The validation of the proposed system was investigated through the simulation and experimental results. The validity of the theoretical model was confirmed using the experimental results. Therefore, this model can be used to predict the behavior of the equalizer system. In other words, the theoretical equations can be used for sizing the system. The experimental results confirm the effectiveness of the equalizer system in maintaining the control ability of the boost converters when a cell is not able to supply the nominal power.

To investigate the dynamical properties of the system and to prove its stability, a dynamical average model is proposed taking into account the order reduction induced by the presence of the HF transformer and cross-coupling effects due to the serial connection of output capacitors. The validity of the reduced model is verified through the simulation and experimental results. The stability analysis based on the proposed model proved the asymptotic stability of the system in different conditions. The robustness of this control method was also investigated based on the stability analysis by changing some of the system parameters. The experimental results, which show the behavior of the system in different operating conditions, validated the effectiveness of the proposed topology. These results also confirmed that the controllability and the DC-link voltage regulation are always ensured even during drying or flooding conditions concerning one of the cell groups in which the power injected by each group of cells is modified to improve durability.

Chapter 4

Management system

4.1. Introduction

The last piece of the FCMS puzzle is to develop a management strategy. Based on the developed model in Chapter 2, the instabilities of the cells inside one stack can be detected. The results of the proposed method must lead to commands which can drive the proposed power electronics structure in Chapter 3. This chapter aims to explain the management strategy. Indeed, the FCMS works as a diagnosis system which can counteract the electrochemical instability of cells to cure it. As discussed in the first chapter, a model can be used to diagnose the origin of the cell instabilities due to its direct link with physical phenomena. The idea of cell instability detection is to trace some parameters of the proposed model. The deviation of these parameters from their average values between the cells can be interpreted as different instabilities. Then, the desired decisions are taken and the power injected by the cells is adjusted to cure the defected cells. In this chapter, such a management system is explained and validated. This chapter is organized as follows: The proposed management system is explained in Section 4.2 after a short introduction in Section 4.1. The simulation results are presented in Section 4.3 for two different conditions of the first group of cells when three other groups work normally. In Section 4.4, the whole system is experimentally examined from the energy management point of view. Eventually, the conclusions are listed in Section 4.5.

4.2. Proposed management system

The schematic diagram of the system to implement the proposed management system is depicted in Figure 4-1. As demonstrated in this diagram, the reference power of different cells is adjusted by the management system. The control loop box in this figure is the control method which was developed and explained in Chapter 3. The PEMFC RT-simulation is the real-time simulation of the model that was proposed in Chapter 2.

Since the essential objective of this thesis is to attack three main cause of cell failure consisting of drying and flooding conditions and aging, three model parameters which have a link to these phenomena are used to detect these instabilities. These three parameters are the stoichiometry of Hydrogen (St_{H_2}), the stoichiometry of Oxygen (St_{O_2}), and the water content of the membrane (λ_m). The water content is the number of the water molecule in the active site of (SO_3^-). Reducing this parameter can be an indicator of drying. However, this parameter is not useful to detect the gas starvation problem originated from the flooding condition of cells. The origin of the gas starvation is inside the gas channels. As a result, the stoichiometry of Oxygen and Hydrogen is used to detect the flooding condition of cells. It is also possible to distinguish which part of the cell was drowned utilizing these two parameters. The main reason for choosing these two parameters is their direct relation with the liquid water level inside the anode and cathode channels. Because of the strongly nonlinear relationship of these parameters with the

corresponding phenomena and the value of injected power by cells, it is very challenging to control the system based on the white-box methods. As a result, the black-box methods can be used to control the injected power by the cells based on the selected model parameters. Among the black-box methods, FLC can be implemented with a lower level of complexity. Robustness, fast performance, and design simplicity are among the most important advantages of this method [2], [155], [156].

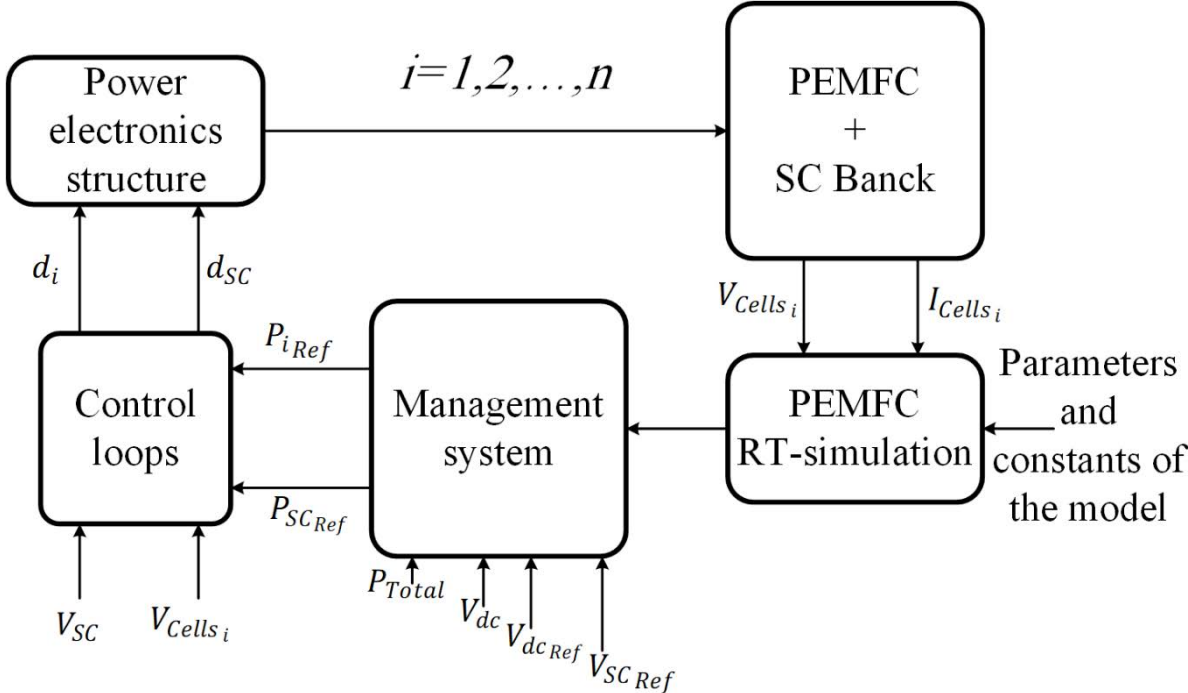


Figure 4-1. Block diagram of the proposed management strategy.

As demonstrated in Figure 4-2, the FLC method consists of four main parts: 1) fuzzification, 2) rule-based reasoning, 3) inference and 4) defuzzification. The FLC inputs turn to fuzzy language in the fuzzification part. Then the outputs in the inference section are made based on the laws in rule-base. In the Defuzzification part, quantifiable results are produced from the outputs of the inference part [2]. The widespread use of this method as a diagnostic tool was investigated in Chapter 1.

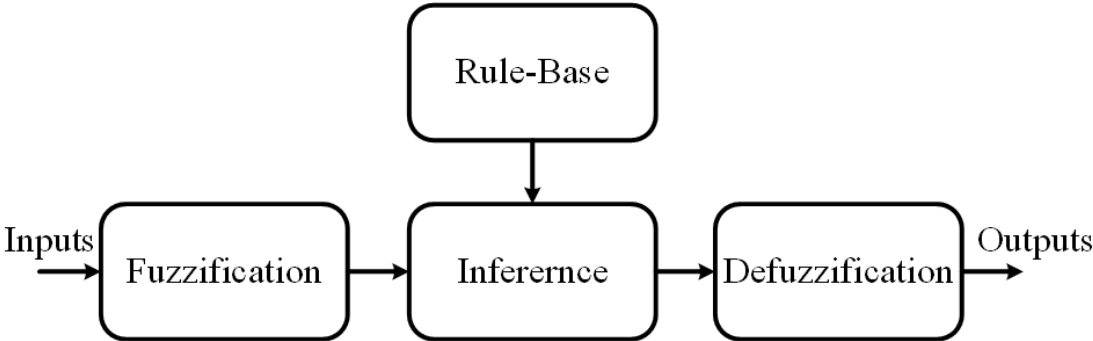


Figure 4-2. Block diagram of the FLC.

Mamdani-type FLC consists of five steps: Fuzzification, apply fuzzy operator, apply the implication method, apply the aggregation method, and defuzzification [157].

In the first step, a real scalar value is converted to fuzzy linguistic variables. Indeed, a given interval of a scalar input variable is divided into several fuzzy linguistic sets. Each set or each

membership has its function to map a numeric variable to a linguistic variable with a degree of truth (weight). There are different types of membership functions: sigmoid, Trapezoid, triangle, etc. For instance in Figure 4-3, the 'a' is 20% Normal and 80% belongs to the Dried subset. These values are the weight of the 'a' in each subset. Generally, the weight or degree of truth is shown by $\mu(z)$ ($\mu(\lambda_m)$ in Figure 4-3). A trapezoid-shaped curve is used as a function for each set or memberships in this figure.

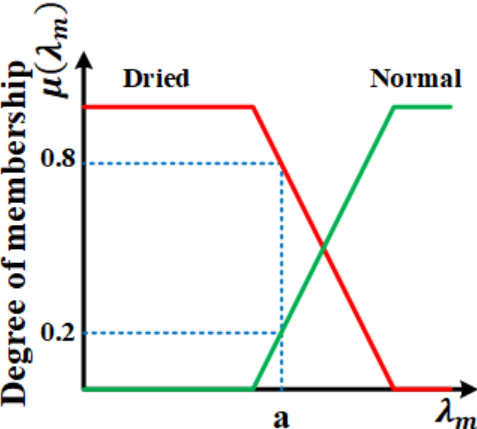


Figure 4-3. Fuzzification

Since an FLC can have more than one input variable and each variable has its own fuzzy linguistic sets, the rule-base might use the logical operators to deduce the output. The most common operators are AND, OR, and NOT operations. Because these logical operators are also used to derive the output weight (degree of truth) from the weight of input variables, they have to be formulated. The AND operation can be applied by min or product function. The OR operation is realized by max or probabilistic OR functions. The Not operation is applied by subtracting the weight of fuzzy sets from one. In this thesis, the min and max functions are used because of their simplicity, effectiveness, and widespread use. Figure 4-4 demonstrated the application of the min function to implement the AND operator. This figure reveals a simplified example in which the membrane water content and stoichiometry of hydrogen are used as indicators of drying and flooding conditions respectively [157], [158].

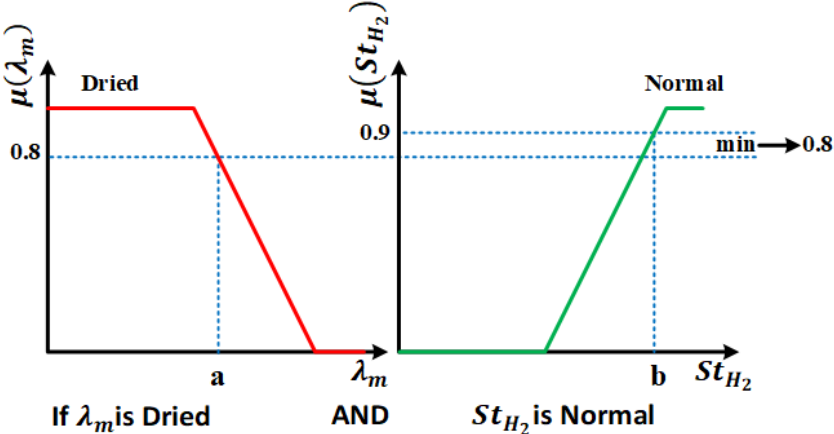


Figure 4-4. Applying the fuzzy operator

The rule base contains rules in the form of If-Then and each output is another fuzzy linguistic set defined by an appropriate membership function. This fuzzy output set must be reshaped by the result of the last step (applying the fuzzy operator). This process is called implication in

which the input is a number and output is a fuzzy set. Two methods can reshape an output fuzzy set: min, which truncates the output fuzzy set, and product, which scales the output fuzzy set. This process is accomplished for each rule. Generally, the intersection or union graphically performs the combination of the fuzzy sets. The union and intersection are implemented by OR and AND operators respectively [159].

In this thesis, the minimum method (min) is used to implement the implication regarding the widespread use of this method. The implication based on the min method is shown in Figure 4-5. As can be seen in this figure, a scalar value, which is obtained from the Fuzzy AND operator, can reshape the fuzzy output set. In this figure, a and b are the inputs of fuzzy logic [157], [160].

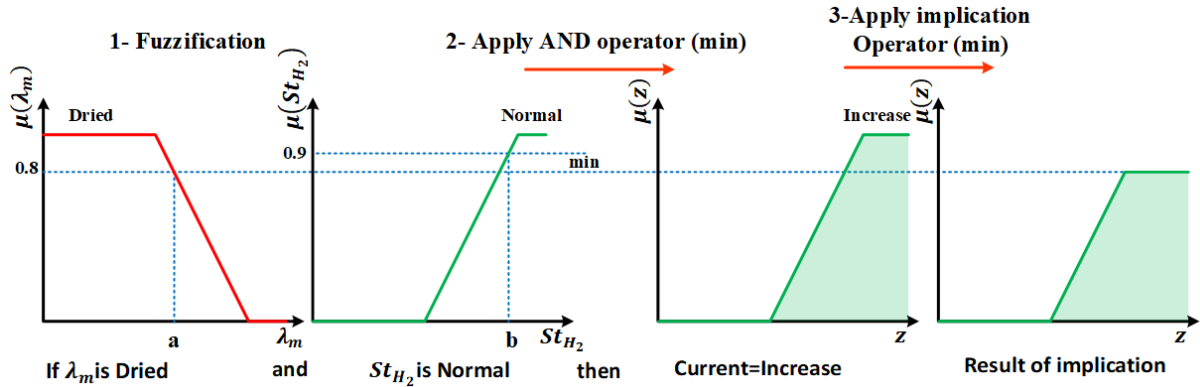


Figure 4-5. Implication method

The fuzzy output is the result of deducing all the rules in the rules base. As a result, the output of all rules must be combined to produce the output. The fuzzy rules output can be combined through an aggregation method to obtain a single fuzzy set as an output reference. The aggregation operation can be implemented by sum, max, or probabilistic OR functions. As the max function is well accepted, this function is used to aggregate the output of fuzzy rules in this thesis. For instance, Figure 4-6 demonstrates the aggregation of the outputs of four fuzzy rules. As seen in this figure, the output of the aggregation is a new fuzzy set [158].

This fuzzy set must be converted to a scalar quantity to be used. This conversion is performed in the last step of the fuzzy process. This step is called defuzzification and like its name, it is the opposite of the fuzzification. In other words, the defuzzification is a process in which a fuzzy set is mapped to a scalar value. There are many defuzzification methods in the literature: Center of gravity (centroid), Center of area, fuzzy mean, middle of maximum, weighted average, etc. The centroid method is used in this thesis due to its privileges over other methods. This method is the most prevalent among other methods. The algebraic equation, which expresses this method, is as follows [157], [158]:

$$Z^* = \frac{\int \mu(z) \cdot z \, dz}{\int \mu(z) \, dz} \quad (4.1)$$

where $\mu(z)$ is the weight of output fuzzy set (z) and Z^* is the output of the fuzzy logic controller as seen in Figure 4-6. In this figure, the z is the change in the reference current. It should be noticed that the discrete version of this equation is the weighted average method expression [157], [158]:

$$Z^* = \frac{\sum \mu(\bar{z}) \cdot \bar{z}}{\sum \mu(\bar{z})} \quad (4.2)$$

where \bar{z} is the centroid of each symmetric membership function. This method is limited to symmetrical membership functions [157].

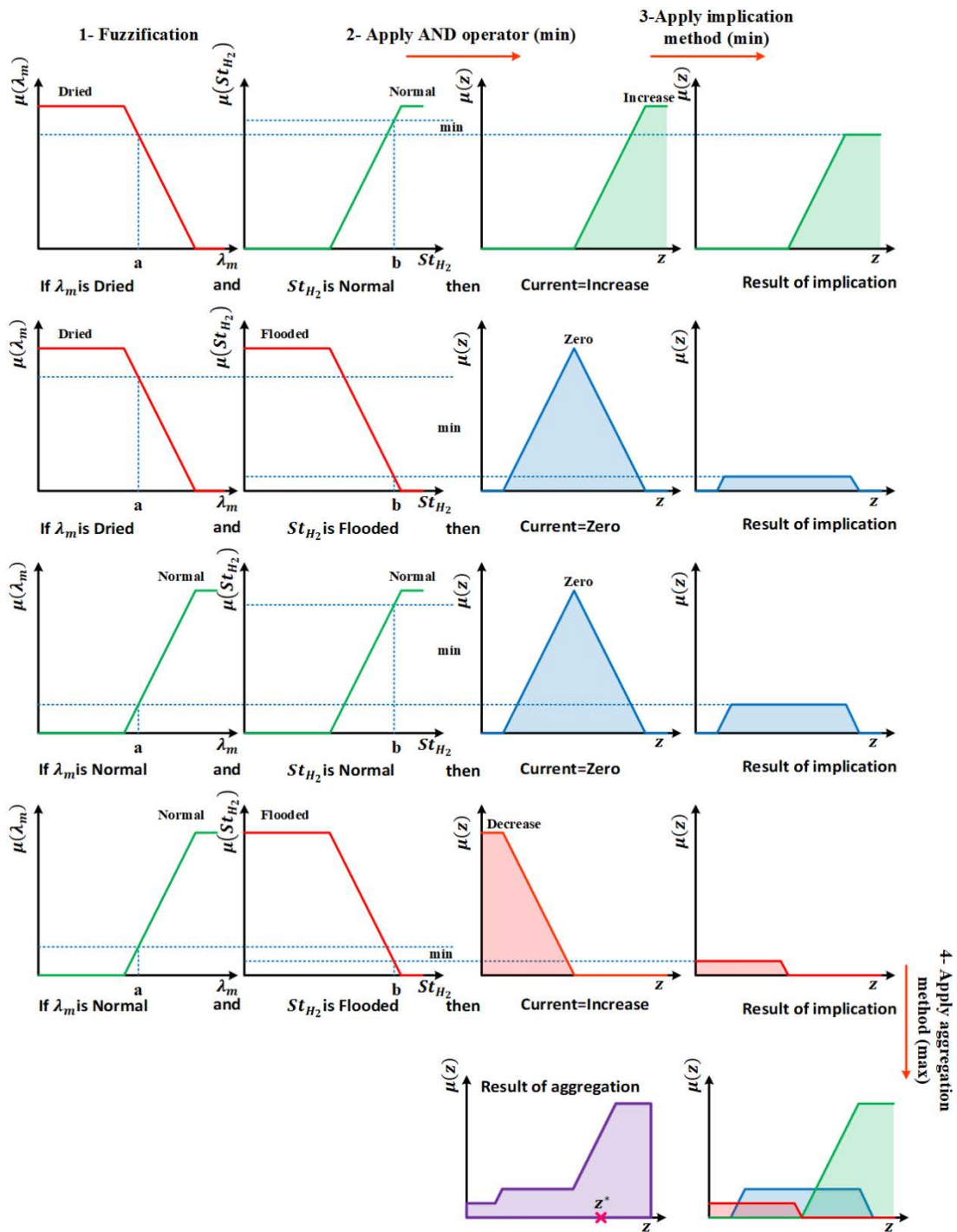


Figure 4-6. Aggregation method

The block diagram of the FCMS strategy to deal with the flooding and drying conditions of different cells inside one stack is depicted in Figure 4-7. As seen in this figure, the three model parameters are normalized by their average value. These normalized values are the inputs of the FLC. The normalized value of the injected electrical power change by different cells (ΔP_{e_i}) is the output of the FLC. The total power supplied by different cell groups must be equal to the

load power in the steady-state as explained in Chapter 3 to ensure a steady-state condition for the SC. However, each group of cells has own FLC and ΔP_e and as a result, the sum of reference powers is not necessarily equal to the load power. Therefore the last part of this management approach assures that the total power supplied by cell groups to be equal to the load power in steady-state while considering the maximum injectable power of cell groups. In other words, the total reference power must be distinguished from the total injected power due to the disturbances (ΔP_{e_i}) imposed by the FCMS. As seen in this figure, ζ is used to limit the maximum amount of injected power change. This parameter has a value between zero and one. In other words, $\frac{P_{Total_{ref}}}{n}$ and ζ are used to convert the normalized value of electrical power change to an absolute value. To obtain the reference current of each cell group, the reference value of power is divided by the measured voltage of each cell group (V_i). Then the reference current passes through a low-pass filter with a cutoff angular frequency of $\omega_{f_{Iref}}$ to respect the dynamic of the fuel cell and its auxiliaries. The reference current (I_{ref_i}) should be applied by the power electronics structure that was explained in Chapter 3. The current (I_{cells_i}) and voltage (V_i) of each cell group are measured and applied to the fuel cell model that was developed in Chapter 2. As seen in Figure 4-7, any change in the output of the FLC leads to its input change due to an external current loop. The external current loop ensures that the current passing through each cell group is equal to its reference value. As a result, the FLC should be slow enough (slower than the outer loop i.e. the SC voltage controller) to respect the dynamic of the fuel cell.

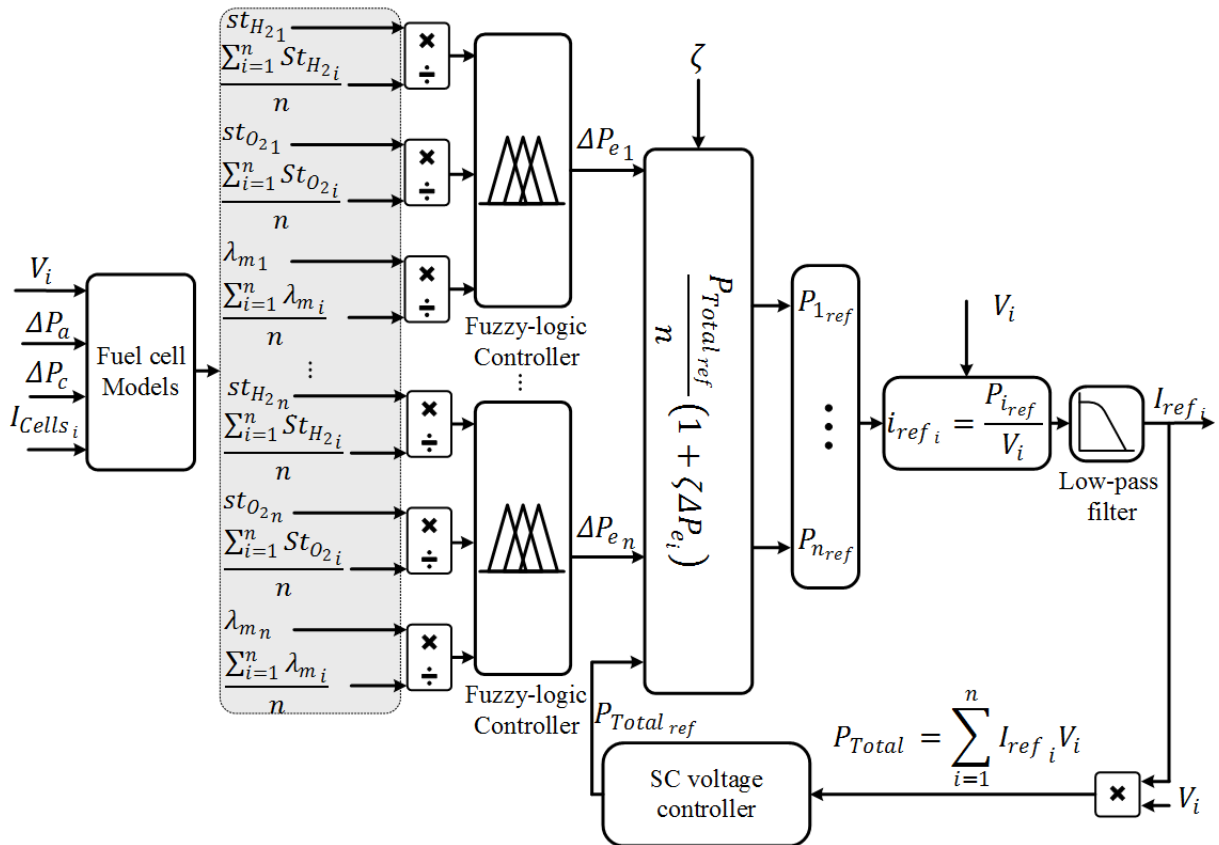


Figure 4-7. Block diagram of the FCMS strategy.

As seen in Figure 4-7, the cell group currents, voltages, and the pressure drop inside the anode and cathode channels are the input of the fuel cell model that can be measured in an experimental test bench. Since the power is applied and the voltage is an output of the model,

the current can be obtained. In other words, the developed model in Chapter 2 can be used to generate the required voltage in Figure 4-7 and the required cell group currents can be calculated by knowing the imposed power. However, the pressure drops must be applied to the cell group models. Indeed, the total flow rate of Hydrogen and Oxygen is applied based on the reference stoichiometry of them in an experimental test bench. The applied flow rates lead to the pressure drop inside the channels that can be measured. However, the conversion of the flow rate to the pressure drop can be easily calculated in a simulation. The total flow rate of air and hydrogen can be applied to a stack. The total reference flow rates can be calculated from the total reference stoichiometry of air and hydrogen as follows:

$$N_{H_2 Total ref} = st_{H_2 ref} \sum_{i=1}^n \frac{I_{cells i} LW}{2F}$$

$$N_{O_2 Total ref} = \frac{1}{0.21} st_{O_2 ref} \sum_{i=1}^n \frac{I_{cells i} LW}{4F} \quad (4.3)$$

These total flow rates must be converted to the pressure drop inside the channels to be used as the inputs of the fuel cell model developed in Chapter 2. Regarding the strong nonlinear relation between the total flow rates and the pressure drops inside the channels, finding an implicit equation is out of this thesis interests due to its application only for the simulation purposes. However, an algorithm detailed in Figure 4-8 is developed to find the pressure drops as a function of total flow rates.

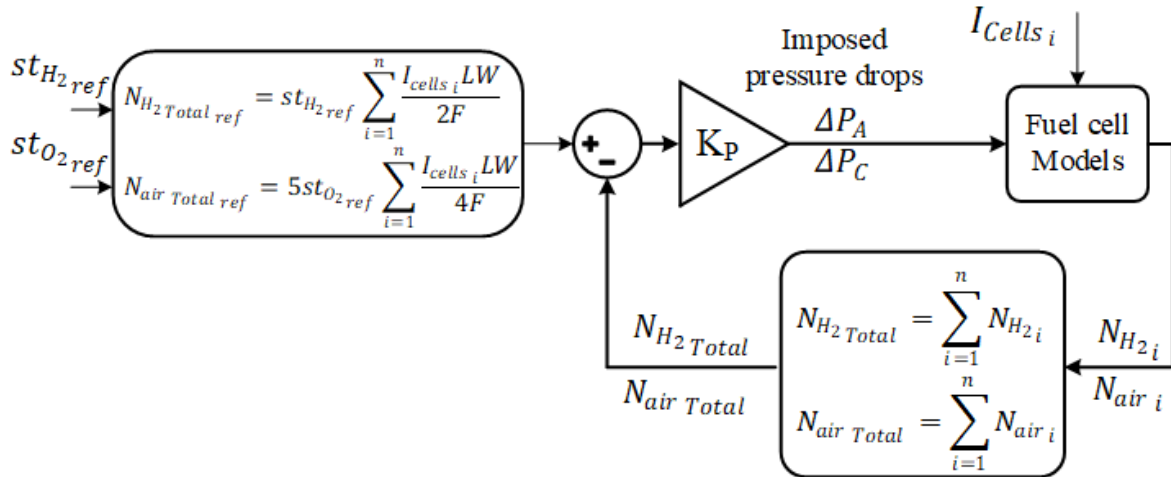


Figure 4-8. Block diagram of the second part of the FC management.

Since the management system requires the total power and this power is applied by the SC voltage controller, this controller should be considered in the simulation. To avoid introducing the power electronics part models in the management system model, the derivation of the energy in the SC described by (3.48) is used as a control input. By integrating this equation, the stored energy in the SC can be obtained and its voltage can be calculated as demonstrated in Figure 4-9. Compared to the SC voltage controller presented in Chapter 3, an integrator term is added to the trajectory planning part of the SC voltage control strategy to cancel the static error between the SC voltage and its reference. Indeed, the FCMS generates a static error between the total reference power demanded by the SC controller and the supplied one by the cell groups. This voltage control loop has an interconnection with the external current loop of fuel cell groups. Therefore, the voltage control loop should be slower than the fuel cell current loop but it must be fast enough to quickly reject the applied perturbation by the FCMS.

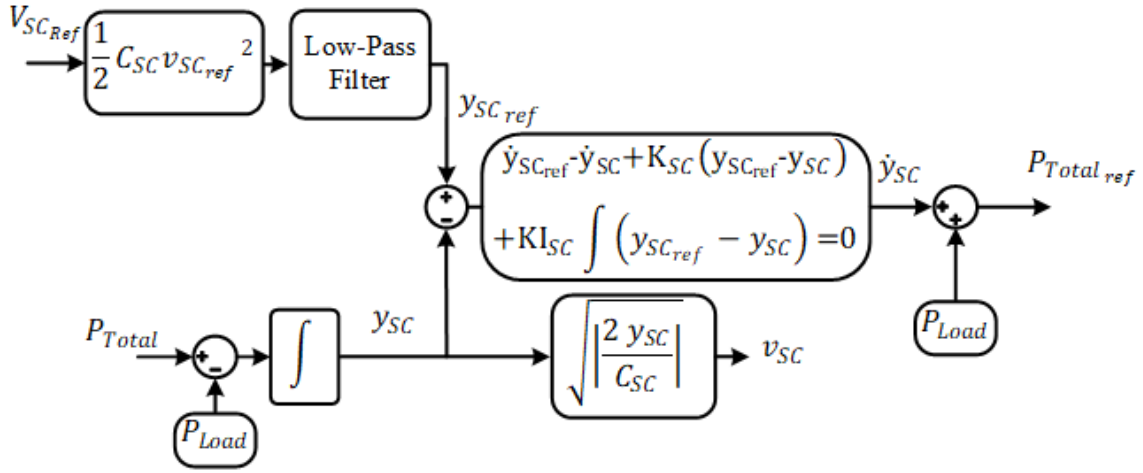


Figure 4-9. Schematic diagram of the SC voltage controller that is used for the management system simulation purposes.

4.3. Simulation results

To verify the effectiveness of the proposed strategy several simulations are performed. The first step is to describe the FLC. The membership functions of the inputs and output of the FLC are shown in Figure 4-10. Mamdani fuzzy inference system is used to implement the FLC. These functions and their intervals were obtained through a trial and error procedure. for the sake of simplicity, the number of membership functions for each input and output was tried to be as low as possible. Different trapezoidal membership functions (with different intervals and around different points) were used for the inputs and output. As a result, twenty different FLCs were developed. However, the rule base was the same for all of the developed FLCs. The dynamic behavior of the system was assessed for each FLC by simulations. The simulation was iterated for the normal, drying, and flooding conditions of the first cell group. The other cell groups were always in the normal operational condition. The FLCs with the minimum oscillation during the transient condition were compared by their static error. Since the normalized parameters are the input of the FLCs, the mean square of the input parameter deviations from one at the steady-state was used as the static error:

$$Error = \frac{1}{3N} \sqrt{\sum_{i=1}^N (1 - \lambda_{m_i})^2 + (1 - St_{H_{2_i}})^2 + (1 - St_{O_{2_i}})^2} \quad (4.4)$$

where N is the number of cell groups.

The universe of discourse for the inputs and output of the FLC is shown in Table 4.1. This table shows the rules in the rule base part of the FLC. As seen in this table, the electrical power change is more affected by the normalized value of the water content when this value is less than one. The next priority in changing the injected power of the cell belongs to the normalized value of Hydrogen stoichiometry. In other words, the Negative (N) water content means the cell is about to be dried (or is already dried) and thus the power should be increased to produce more water (to reduce the cell stoichiometry). However, the magnitude of this change depends on the two other inputs of the FLC. The Negative (N) stoichiometry means that a high amount of liquid water appeared in the channels and therefore, the power should be decreased to produce less water (to increase the stoichiometry). Conversely, the Positive (P) Stoichiometry means that the cell is about to be dried. The electrical power of the cell should be increased to reduce the stoichiometry when the stoichiometry is Positive. The Zero (Z) state of the inputs

means that they have a normal value and as a result, the supplied power should not be changed (Z or Zero) in this case. For instance, the change in the output power is Positive Big (PB) when the water content is Negative (N) and one of the stoichiometries or both of them are Positive (P). The output power change is kept PB even when the oxygen stoichiometry is Negative (N) and two other inputs are Positive (P) due to the priority of the water content and hydrogen stoichiometry. Due to considered priorities, the output power change is Positive Small (PS) when the stoichiometry of hydrogen and oxygen are respectively Negative (N) and Positive and the water content is Negative (N). Notably, a separate FLC with the same features is used for each group of cells, and the FLC runs every 100 s.

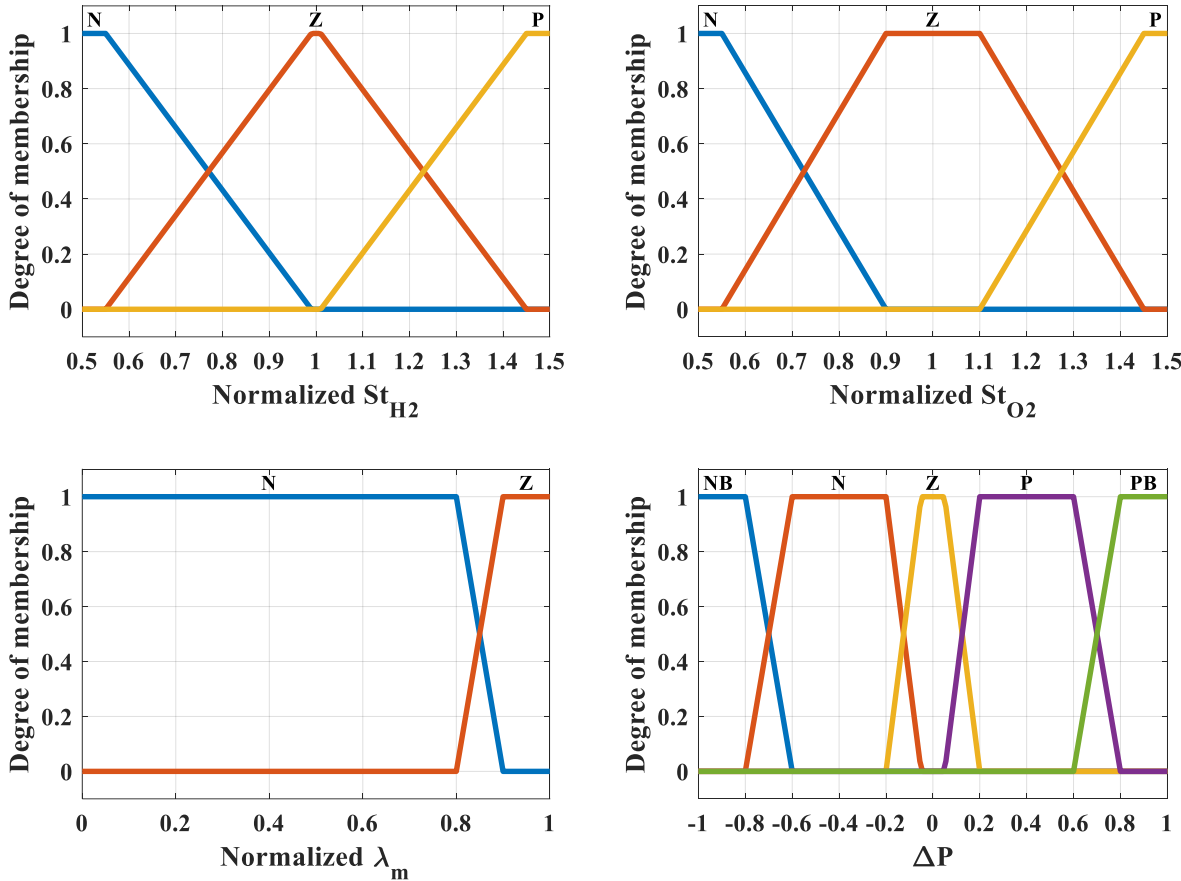


Figure 4-10. Membership functions: inputs (St_{H_2} , St_{O_2} , and λ_m) and output (ΔP_e).

Four groups of cells are considered for simulations. The cell groups are not thermally connected (to each other) for the sake of simplicity in result assessment. The temperature of the adjacent cells for each group of cells is equal to 60 °C. The first group is considered as a defective group. The control parameters are shown in Table 4.2. As demonstrated in Figure 4-7, the measured value of voltages and current of each cell group is required. Since the voltage value is not available in the simulation and the different cell conditions affect this value, it should also be simulated. In the second chapter, the current and voltage of the fuel cell were the model input and output respectively. The proposed model can simulate the cell voltage concerning the operating condition of the cell. It should be noticed that the model, which is used to realize FCMS, is based on the proposed model in Chapter 2 but the voltage of the cell is a measured parameter to take into account the aging in the real test bench.

Table 4.1. Rule base of the fuzzy logic controller

Rule No.	If St_{H2}	& If St_{O2}	& If λ_m	Then ΔP_e
1	Z	Z	Z	Z
2	P	Z	Z	PS
3	N	Z	Z	NS
4	Z	N	Z	NS
5	P	N	Z	Z
6	N	N	Z	NB
7	Z	P	Z	PS
8	P	P	Z	PB
9	N	P	Z	Z
10	Z	Z	N	PB
11	P	Z	N	PB
12	N	Z	N	PS
13	Z	N	N	PS
14	P	N	N	PB
15	N	N	N	PS
16	Z	P	N	PB
17	P	P	N	PB
18	N	P	N	PS

Table 4.2. Control parameters.

Parameter	Unit	Value
ζ	-	0.3
$\omega_{f_{Iref}}$	Rad/s	2π
K_P	-	0.1
K_{SC}	Rad/s	0.2π
KI_{SC}	Rad ² /s ²	0.01
$\omega_{f_{Vsc}}$	Rad/s	0.1π

The cooling fluid temperature of the first group is increased at 1000 s in the first simulation. A slope of 0.08 from 60 °C to 75 °C increases the cooling fluid temperatures. The load power of 235 W is applied and this power is shared equally between the cells. In this simulation, the applied pressure drop in the anode and cathode channels is equal to 11 *mbar* and 25 *mbar* respectively. The dew point temperature at the cathode and anode inlets are applied with bubblers at 50°C (cathode and anode). The other model parameters are shown in Table 2.1. Due

to the temperature rise as seen in Figure 4-11, the water saturation in the anode and cathode side of the first group of cells decreases to zero (Figure 4-12). This lower saturation level leads to the gas flow rate increase (Figure 4-12). Therefore, the stoichiometry of hydrogen and oxygen increased as shown in Figure 4-13. The gas flow rates and consequently the stoichiometries are initially reduced due to the delay in temperature rise and disappearance of the water droplets. The decrease in the flow rates is due to the viscosity change due to temperature change and the change of the vapor water flow rate. Then the water droplets disappear and as a result, the flow rates decrease. The membrane water content of the first group is also depicted in the figure. The water content decreased due to the cooling fluid temperature rises. This reduction makes the membrane more resistive and as a result, the cell voltage of the first group decreased (Figure 4-13). This condition is the drying condition that was explained in Chapter 1. The normalized value of the stoichiometries and the membrane water content are shown in Figure 4-14. The injected power by the cell groups is also shown in this figure.

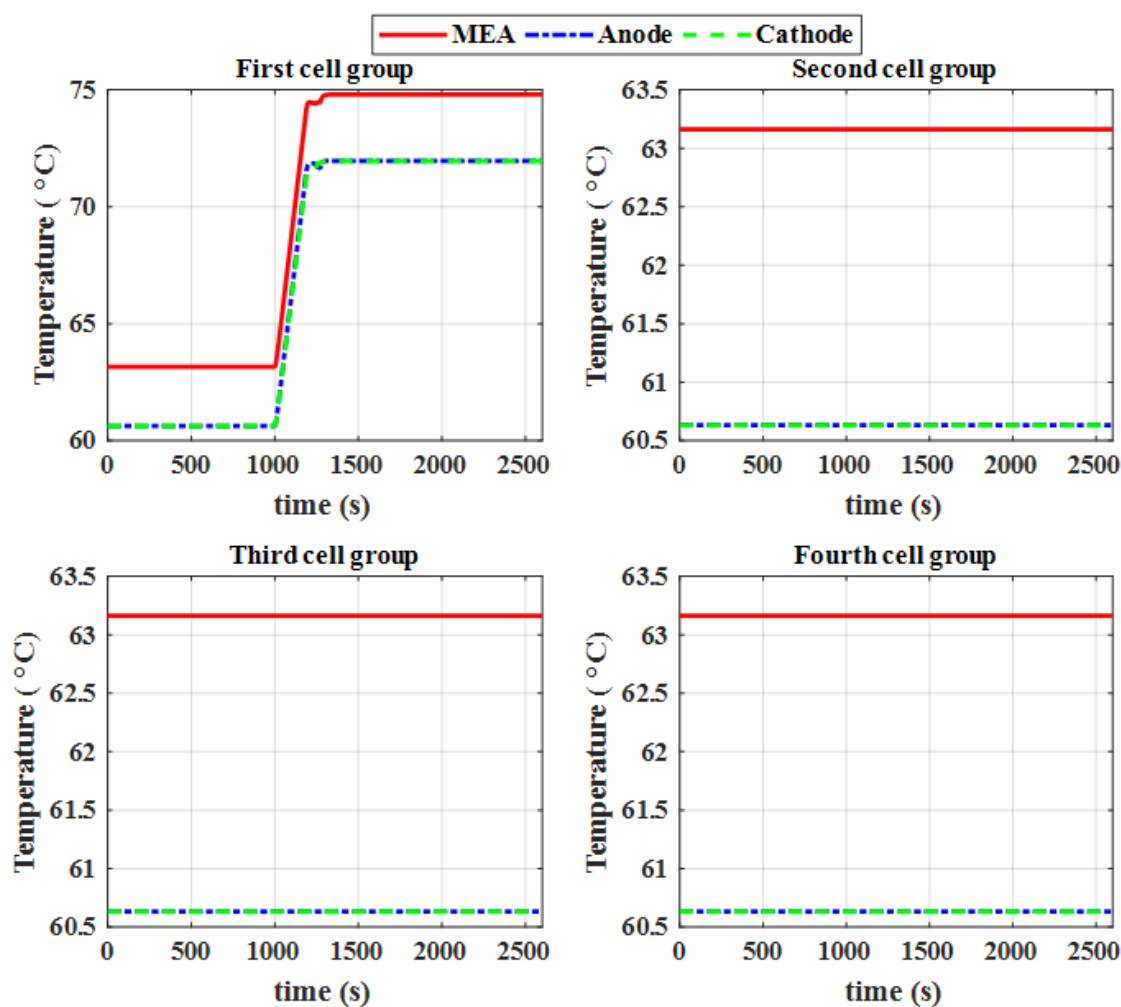


Figure 4-11. Simulation results of the cell temperatures when the cooling fluid temperatures of the first group increased at 1000 s and when a constant current of 30A passing through the cells (The air and hydrogen pressure drops are applied).

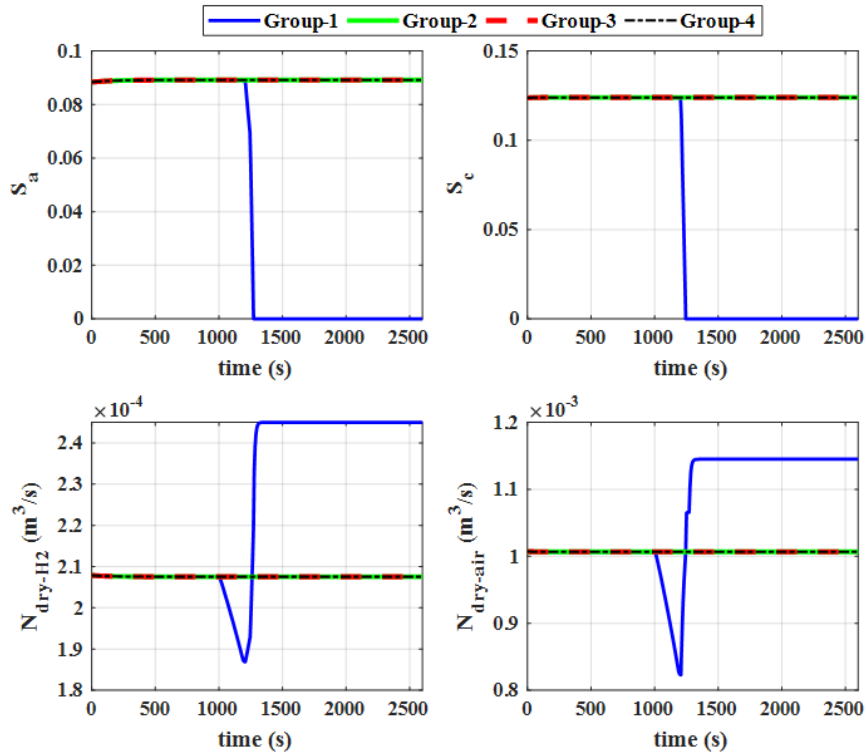


Figure 4-12. Simulation results of the dry gas flow rates and the saturation level inside the channels when the cooling fluid temperatures of the first group increased at 1000 s and when a constant current of 30A passing through the cells (The air and hydrogen pressure drops are applied).

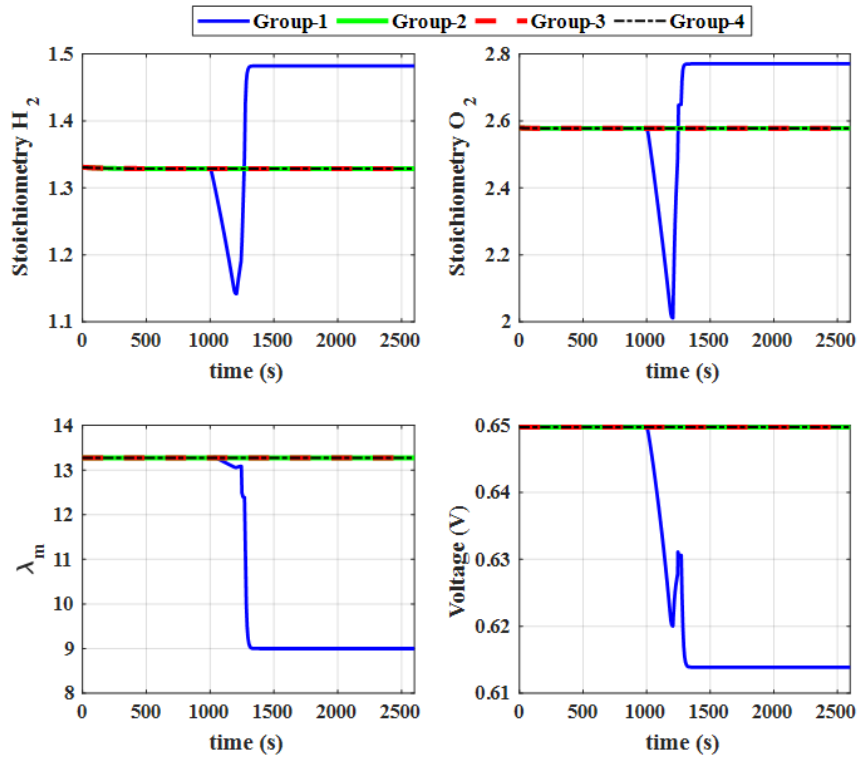


Figure 4-13. Simulation results of FLC inputs and the cell voltages when the cooling fluid temperatures of the first group increased at 1000 s and when a constant current of 30A passing through the cells (The air and hydrogen pressure drops are applied).

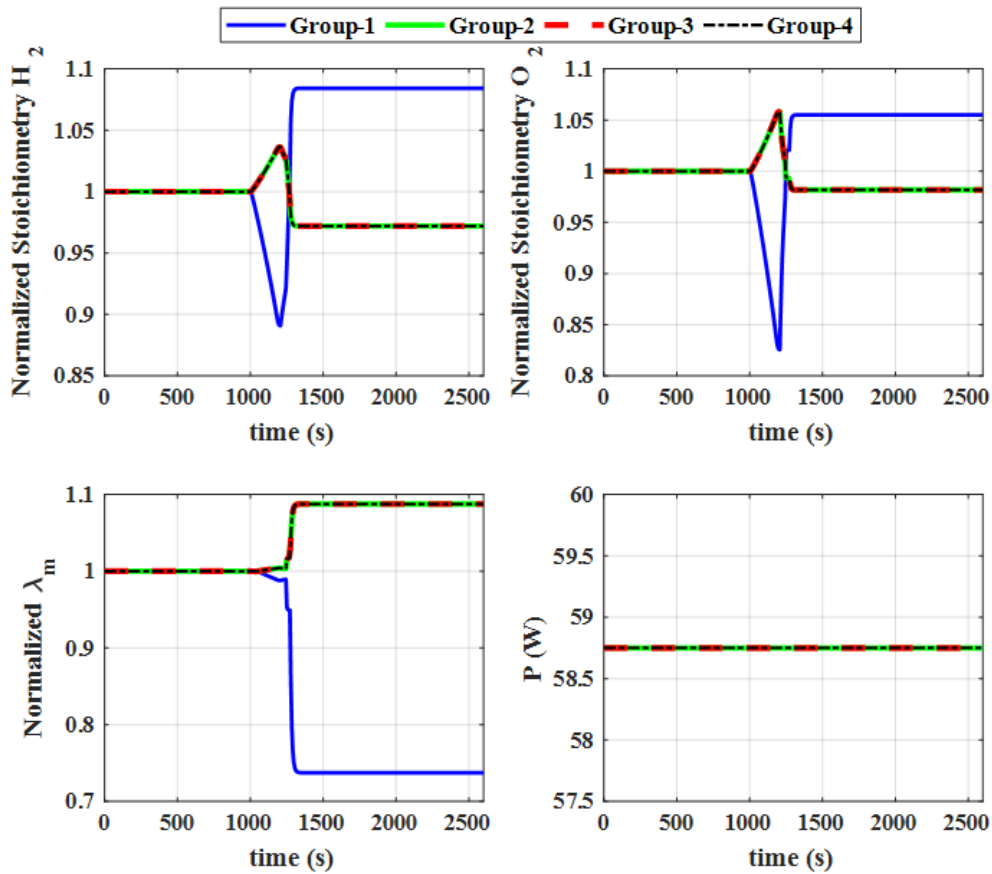


Figure 4-14. Simulation results of the normalized value of FLC inputs when the cooling fluid temperatures of the first group increased at 1000 s and when a constant current of 30A passing through the cells (The air and hydrogen pressure drops are applied).

The second simulation is performed with the same parameters and in the same condition as the first simulation in steady-state. The load power of 235 W is applied in this simulation. However, the injected power by different groups of cells is controlled by the FCMS. The normalized value of the three inputs of the FLC is shown in Figure 4-15. The applied power is also shown in this figure. As seen in this figure, the membrane water content of the first group is decreased after 1000 s. The FCMS consequently increases the electrical power injected by the first group to produce more water. It should be noted that decreasing the local stoichiometry can also deal with this issue. It takes about 200 s for the cooling fluid temperatures to reach their final value due to the slope of 0.08. As a result, the FCMS has only controlled the changing rate of FLC inputs during this time. After this interval, the FCMS increases the membrane water content of the first group by increasing the supplied power by the first group. However, this power rise leads to reducing the stoichiometry of hydrogen and oxygen. Because of this drastic reduction of stoichiometry, the FCMS slightly reduces the injected power by the first group. To keep all three inputs of the FLC at the closest possible value to one, the FCMS has reached the final value of injected powers by the cell groups after some oscillations. The absolute value of FLC inputs is shown in Figure 4-16. The single-cell voltages are also shown in this figure.

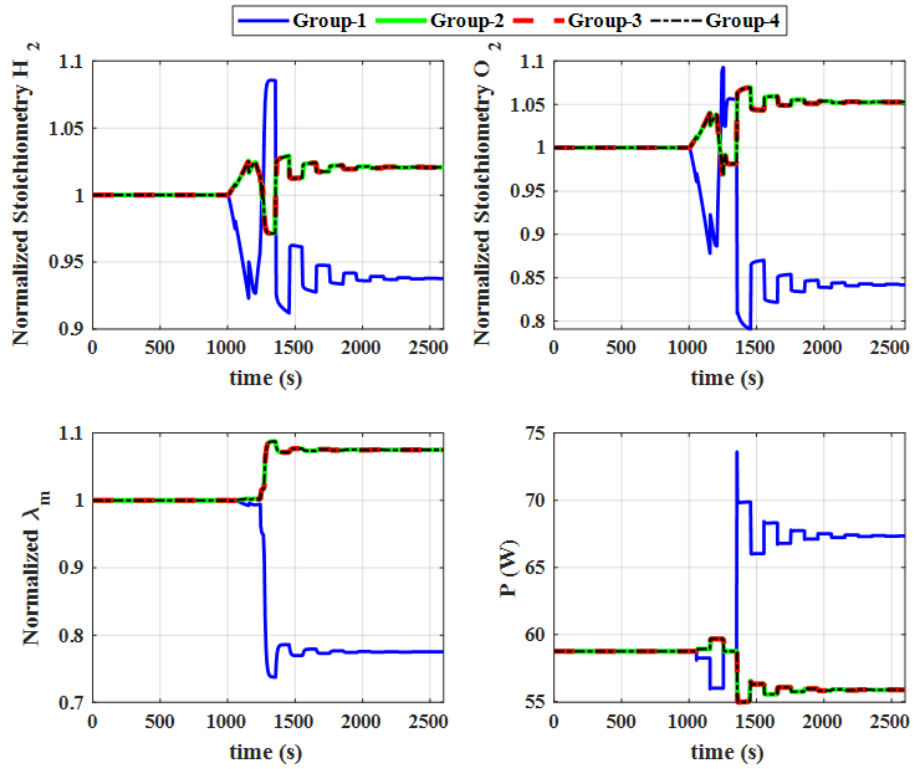


Figure 4-15. Simulation results of the normalized value of FLC inputs and the reference power that should be injected by the cell groups when the cooling fluid temperatures of the first group increased at 1000 s and when the FCMS controls the injected power of cells groups (The air and hydrogen pressure drops are applied).

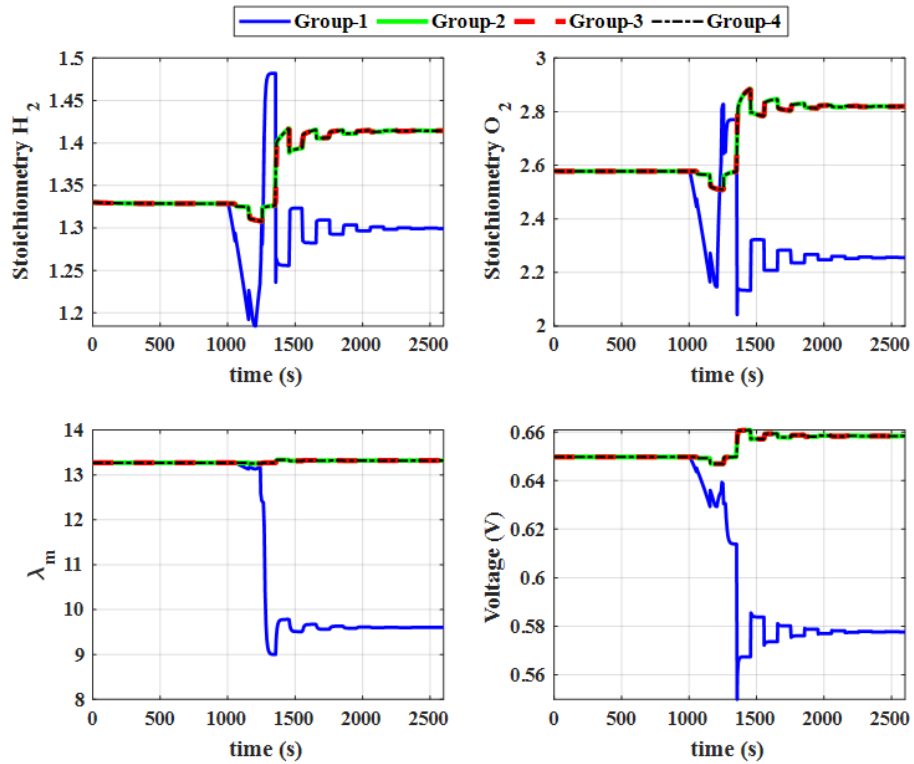


Figure 4-16. Simulation results of the FLC inputs and the single-cell voltages when the cooling fluid temperatures of the first group increased at 1000 s and when the FCMS controls the injected power of cells groups (The air and hydrogen pressure drops are applied).

The temperature of the cell groups is shown in Figure 4-17. Due to this temperature changes resulted from the high-temperature rise of the cooling fluids, the saturation level at the anode and cathode channel of the first group decreased to zero (Figure 4-19) like the first simulation. However, the saturation in the channels of the other groups decreased due to the reduction of the injected power. As a result, the flow rate of dry gases changes concerning the amount of saturation change (Figure 4-19). Regarding the reduction in the supplied power of cell groups except for the first group, the membrane and plate temperatures reduced as seen in Figure 4-17.

Regarding Figure 4-9, the reference of the total power and the total injected power by cell groups are shown in Figure 4-19. As seen in this figure, the SC voltage changes during the transient conditions to regulate the DC link voltage. The reference total power demanded by the SC voltage controller is adjusted to compensate for the disturbance generated by the FCMS. The total voltage of the cell groups is depicted in Figure 4-20 during the second simulation. As seen in this figure, the overall stack voltage is reduced. However, this reduction is negligible compared to the large change in the current injected by the first group. The current density injected by cell groups is also shown in Figure 4-20 which is changed due to reference power change demanded by the FCMS and the SC voltage controller. In other words, the FCMS and the SC voltage controller change the reference power, and then, this power is divided by the voltage of the cell groups to make a reference value for their current. Then, the current is applied to the fuel cell model and can change the voltage of the cell group. Thus, a transient is conceivable for the reference and real of the powers and currents.

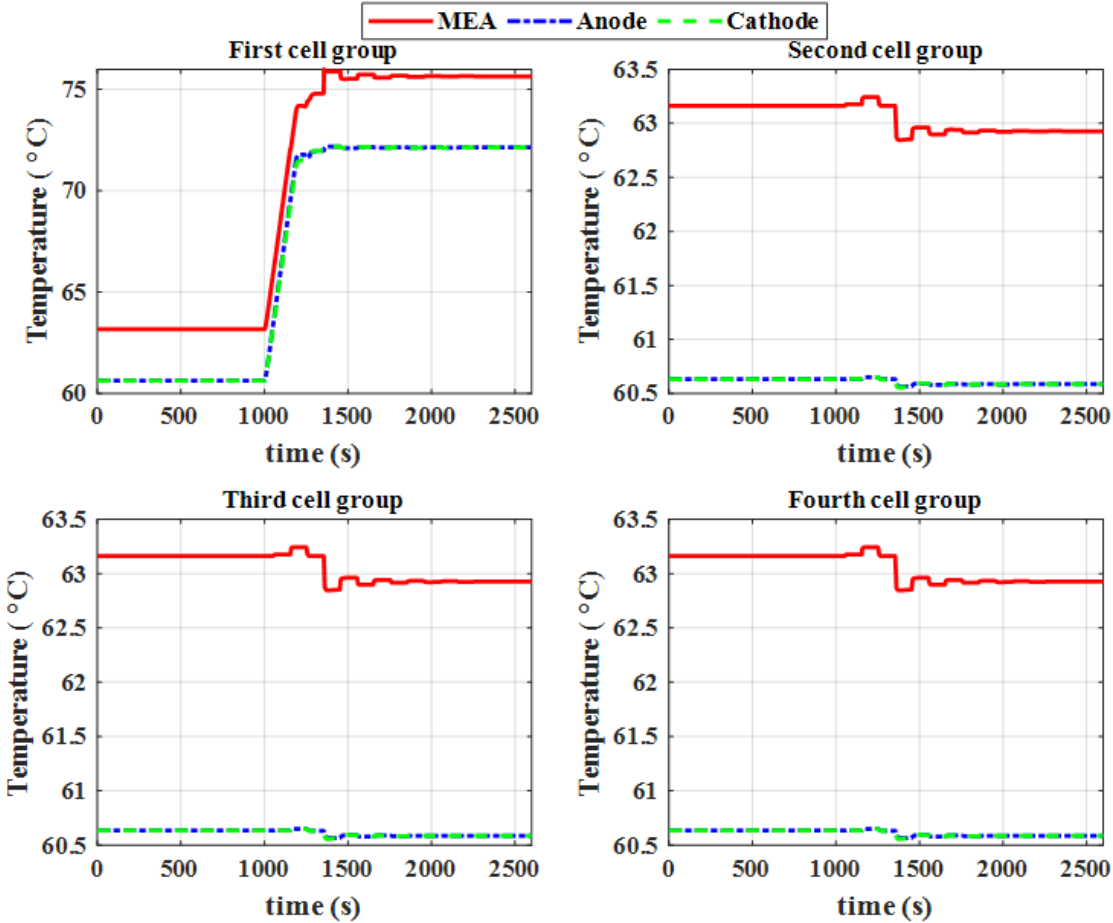


Figure 4-17. Simulation results of the cell temperatures when the cooling fluid temperatures of the first group increased at 1000 s and when the FCMS controls the injected power of cell groups (The air and hydrogen pressure drops are applied).

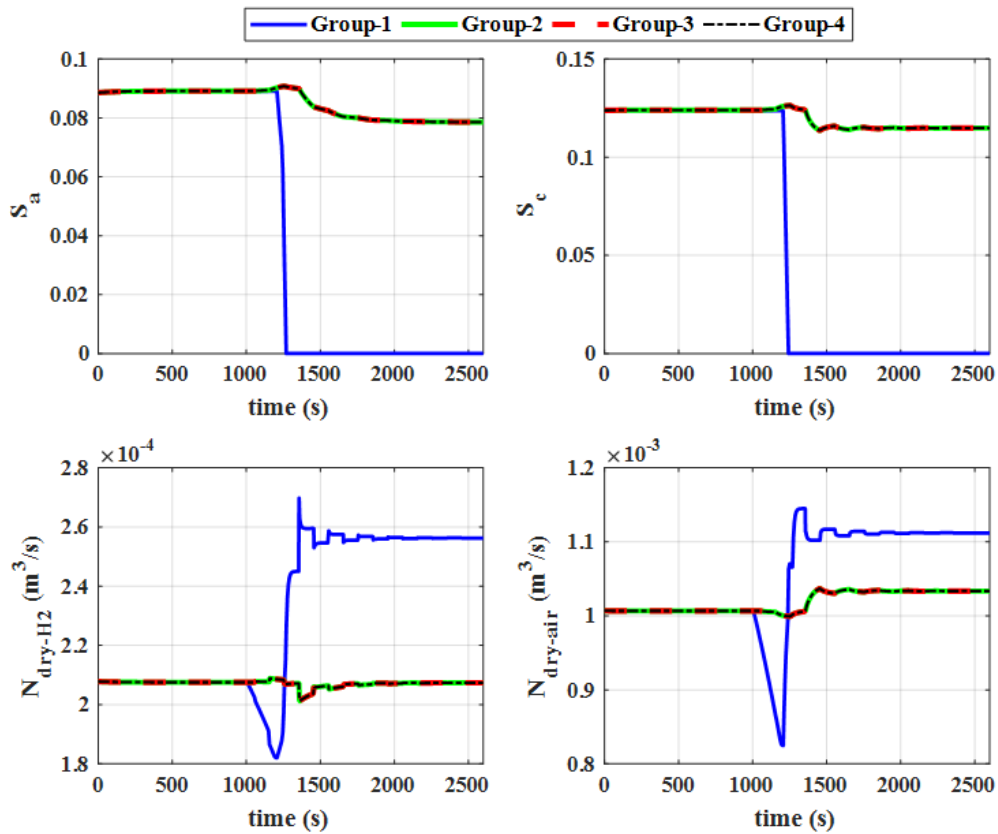


Figure 4-18. Simulation results of the saturation inside the channels and dry gas flow rates when the cooling fluid temperatures of the first group increased at 1000 s and when the FCMS controls the injected power of cell groups (The air and hydrogen pressure drops are applied).

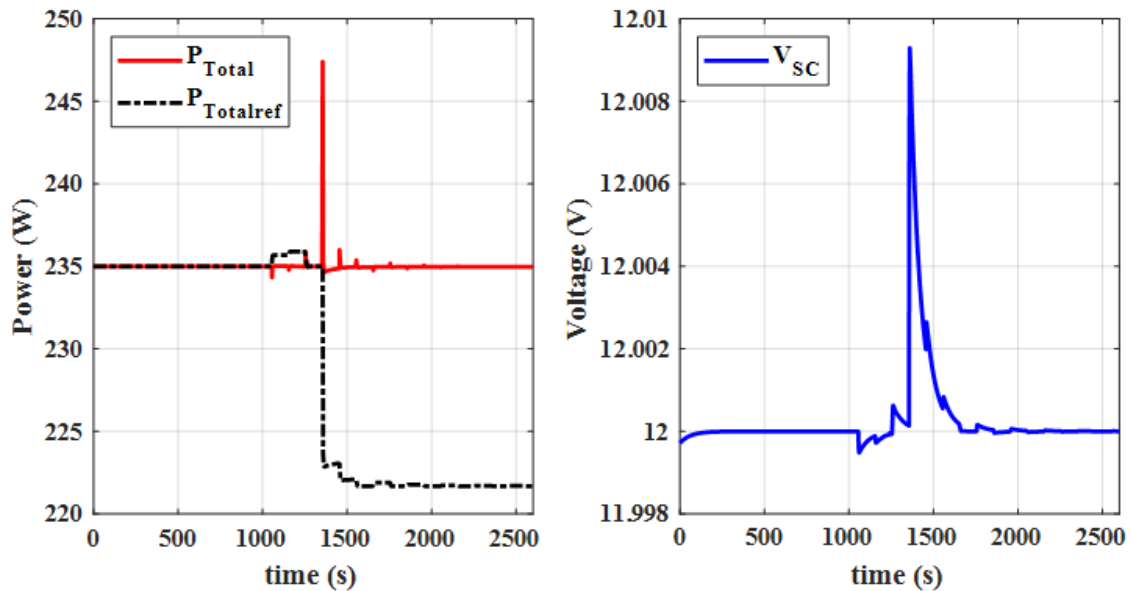


Figure 4-19. Simulation results of the SC voltage, the reference of total power, and the total power injected by cell groups when the cooling fluid temperatures of the first group increased at 1000 s and when the FCMS controls the injected power of cell groups (The air and hydrogen pressure drops are applied).

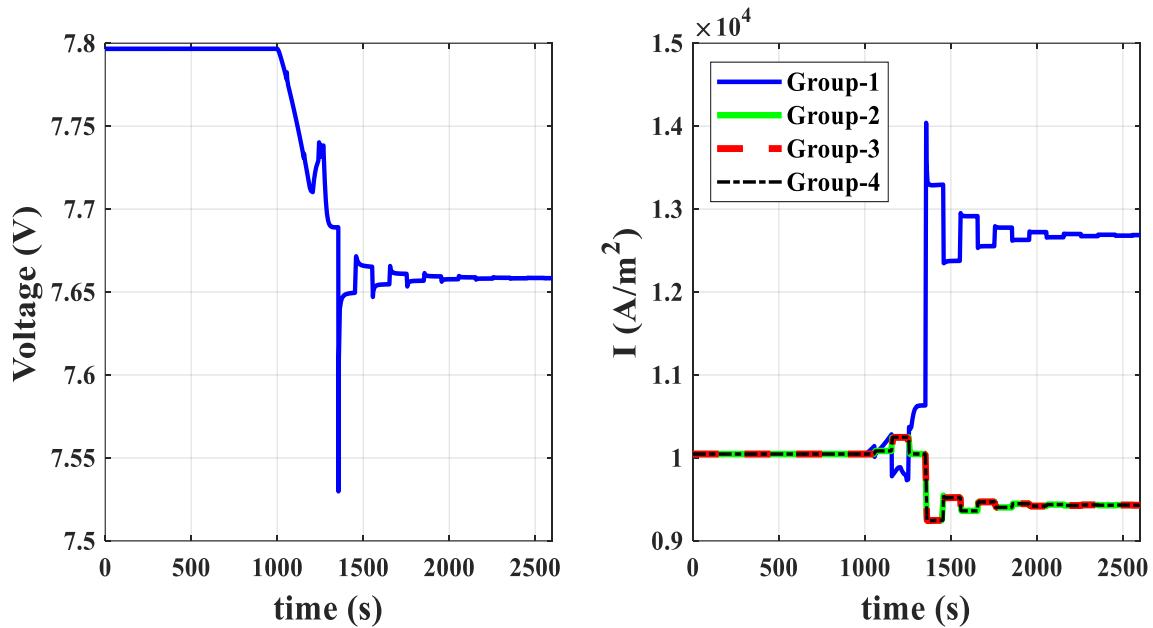


Figure 4-20. Simulation results of the stack voltage and the injected current by cell groups when the cooling fluid temperatures of the first group increased at 1000 s and when the FCMS controls the injected power of cell groups (The air and hydrogen pressure drops are applied).

In the next simulation, the temperature of the cooling fluid at the cathode sides of the first group is increased at 1000 s. The same load power is fixed to 238 W and the cells should equally supply this power. In this simulation, the applied pressure drop in the anode and cathode channels is equal to 11 *mbar* and 25 *mbar* respectively. The dew point temperature at the cathode and anode inlets are applied with bubblers at 30°C (anode side) and 50°C (cathode side). The model parameters are the same as in Table 2.1 except the parameters shown in Table 4.3. A slope of 0.08 from 60°C to 65°C increases the cathode side cooling fluid temperature of the first group. Therefore, the cathode side temperature of the first group increased as demonstrated in Figure 4-21. Due to the temperature gradient between the anode and cathode of the first group, more water accumulated in the colder side (anode). This leads to an increase in the water saturation level in the anodic compartment as shown in Figure 4-22. As seen in this figure, the hydrogen flow rate decreases due to an increase in the saturation level in the anode channel of the first group. However, as seen in Figure 4-22, the dry airflow rate of the first group increased a little bit due to the decrease of water vapor flow rate (Figure 4-21). The hydrogen stoichiometry of the first group decreased due to the hydrogen flow rate drop and the oxygen stoichiometry of the first group increased because of the airflow rate rise (Figure 4-23). The membrane water content and the single-cell voltage of groups are also depicted in Figure 4-23. The single-cell voltage of the first group increased due to the increase in the airflow rate. The normalized values of the membrane water content, oxygen stoichiometry, and hydrogen stoichiometry are shown in Figure 4-24 during this simulation. The supplied power by the cell groups is also shown in this figure.

Table 4.3. Model parameters for the flooding simulation.

Parameter	Unit	Value
e_{GDL}	m	3×10^{-4}
e_m	m	2.5×10^{-5}
λ_{GDL}	$W/(m \text{ } ^\circ K)$	0.45
R_f^{th}	$^\circ K/W$	$R_{GDL}^{th} / 10$
R_c^{th}	$^\circ K/W$	$3R_{GDL}^{th}$
ξ	-	0.4
D_{0m}		4×10^{-10}
$D_{H_2O}^{a,GDL}$		15×10^{-6}
$D_{H_2O}^{c,GDL}$		1.2×10^{-6}
$D_{O_2}^{0,GDL}$		3×10^{-6}

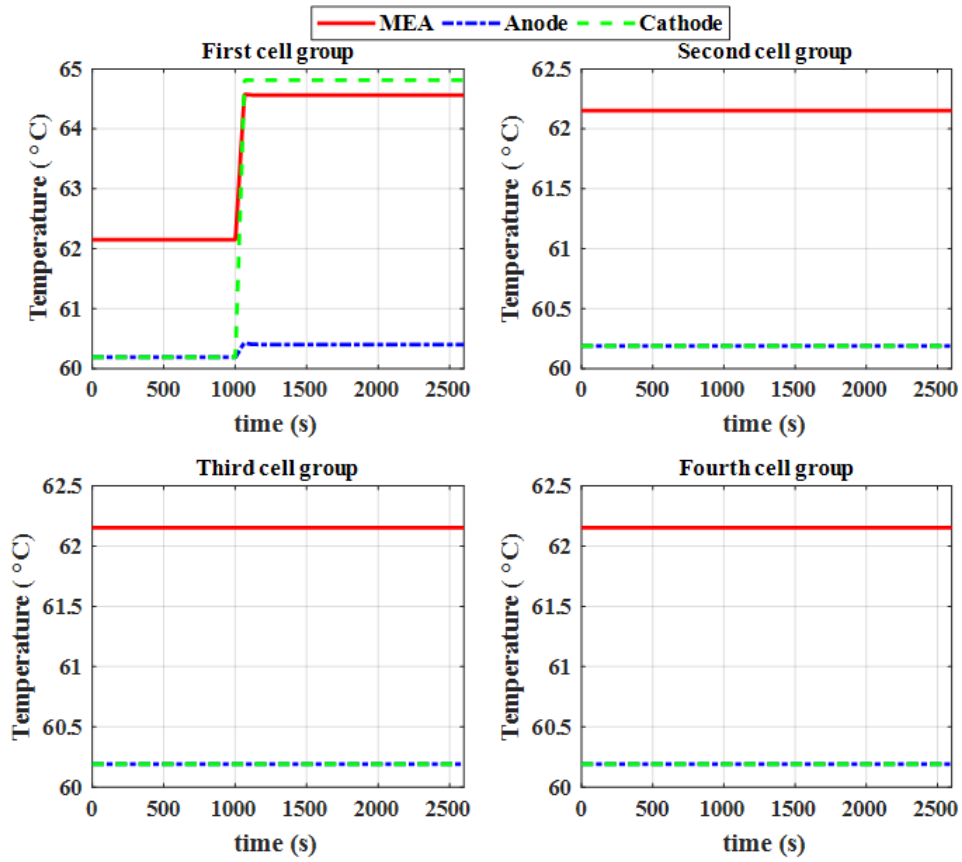


Figure 4-21. Simulation results of the cell temperatures when the cathode side cooling fluid temperature of the first group increased at 1000 s and when a constant current of 30A passing through the cells (The air and hydrogen pressure drops are applied).

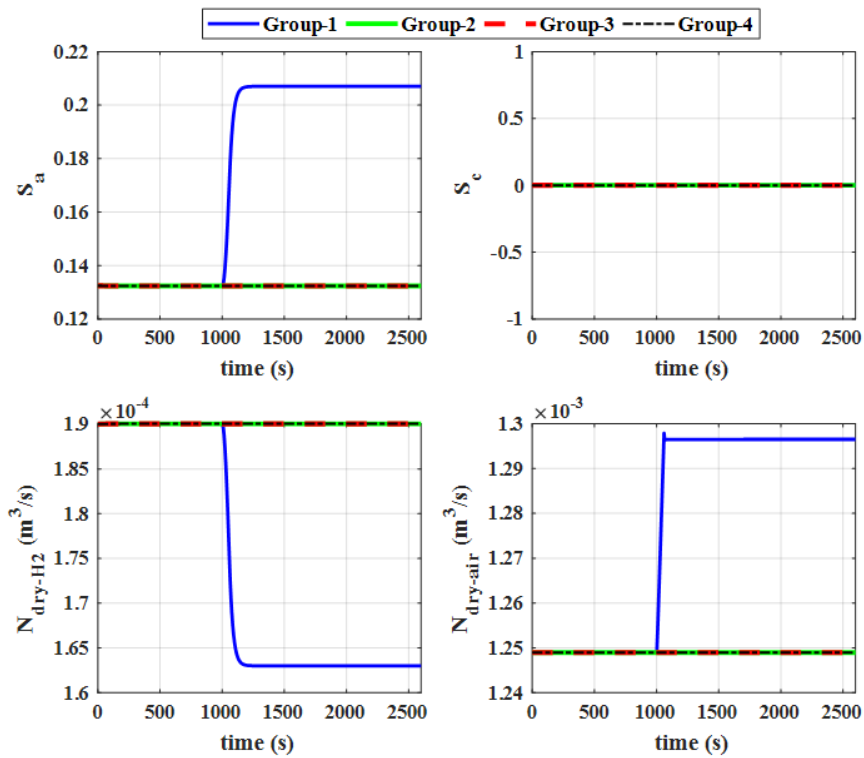


Figure 4-22. Simulation results of the saturation inside the channels and dry gas flow rates when the cathode side cooling fluid temperature of the first group increased at 1000 s and when a constant current of 30A passing through the cells (The air and hydrogen pressure drops are applied).

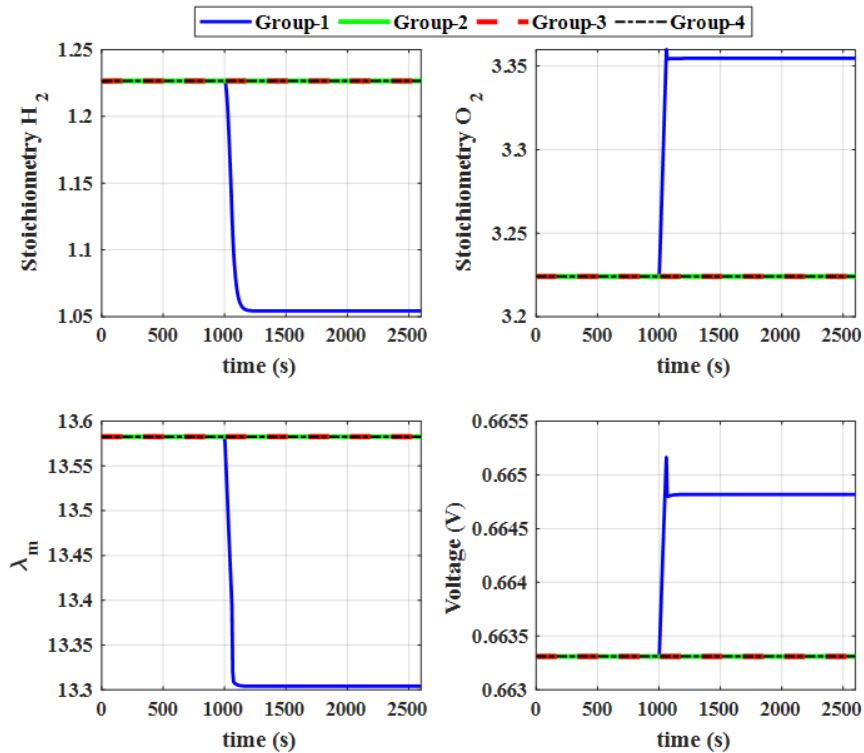


Figure 4-23. Simulation results of FLC inputs and the cell voltages when the cathode side cooling fluid temperature of the first group increased at 1000 s and when a constant current of 30A passing through the cells (The air and hydrogen pressure drops are applied).

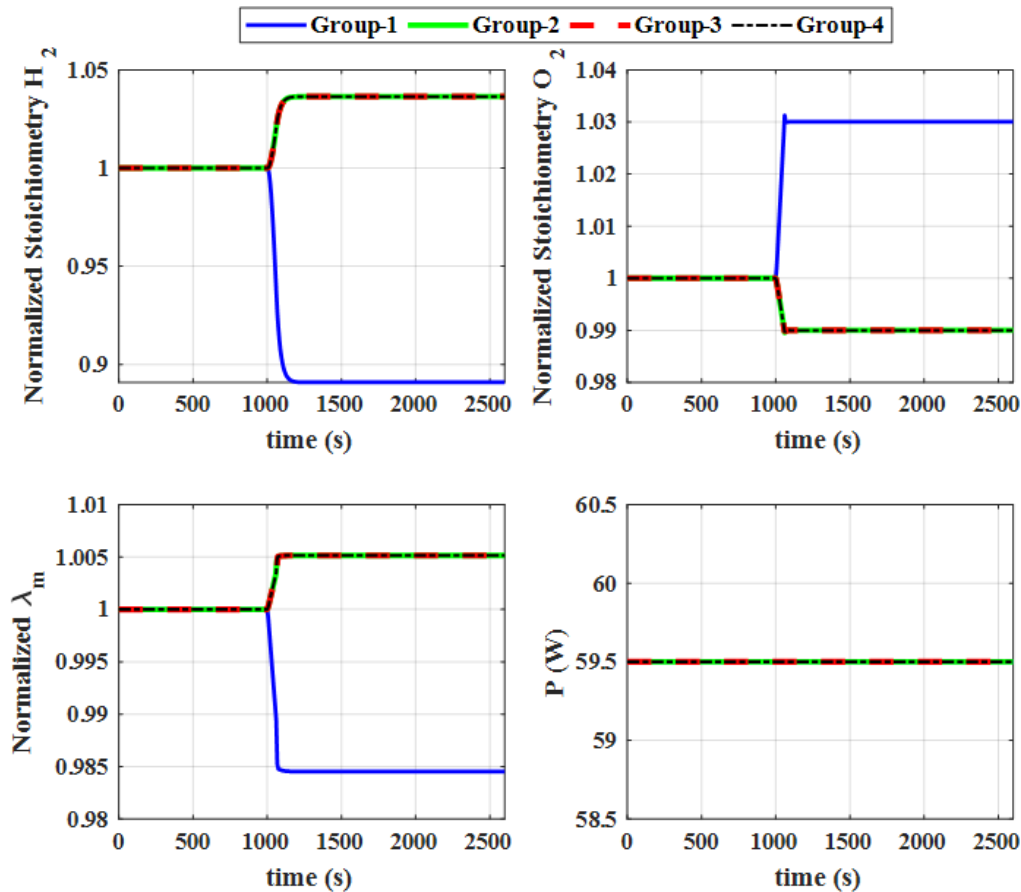


Figure 4-24. Simulation results of the normalized value of FLC inputs when the cathode side cooling fluid temperature of the first group increased at 1000 s and when a constant current of 30A passing through the cells (The air and hydrogen pressure drops are applied).

The fuel cell model parameters, the pressure drop inside the channels, and the dew point temperatures of the humidifier system are kept as same as the third simulation. However, the FCMS controls the injected power of different groups in the fourth simulation. The load power is fixed to 235 W. The injected power by different groups is shown in Figure 4-25. As seen in this figure, the management system decreases the injected power of the first group to struggle with the hydrogen stoichiometry reduction. However, the stoichiometry of oxygen is increased due to this power reduction. Regarding the intervals of the membership functions, which are adjusted for the FLC inputs, the power of cell groups is stabilized after a bit of oscillation. As depicted in these figures, the membrane water content of the first group slightly decreased. It should be noted that the hydrogen stoichiometry is about four percent improved by changing the injected power. For this optimization, the injected power of the different groups is changed by about seven percent. The absolute value of FLC inputs is depicted in Figure 4-26. The single-cell voltages are also shown in this figure.

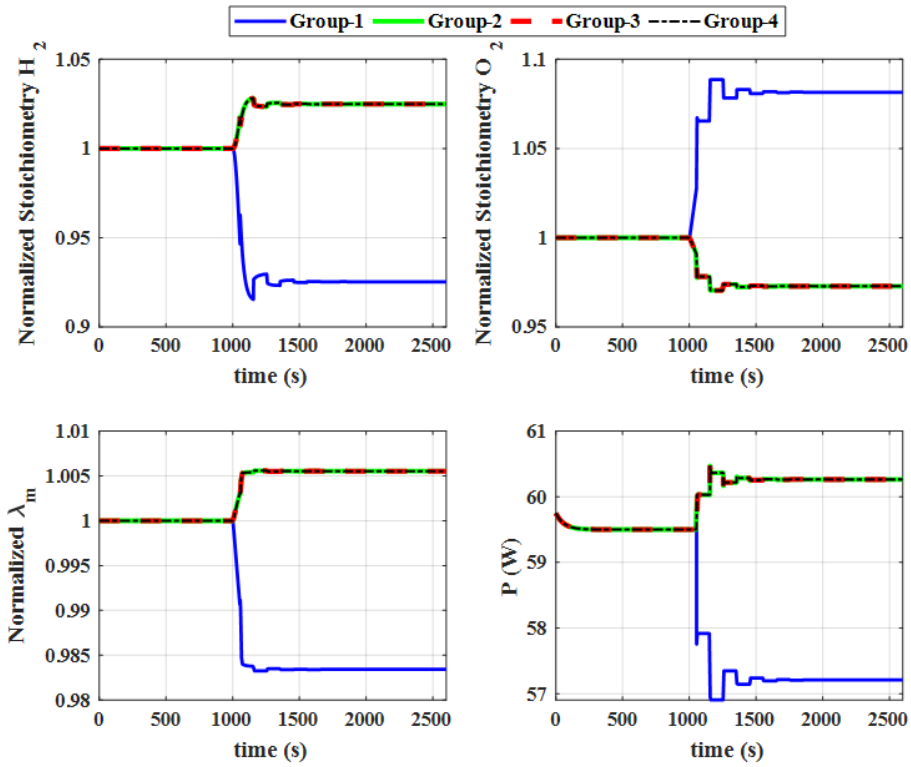


Figure 4-25. Simulation results of the normalized value of FLC inputs and the reference power that must be injected by the cell groups when the cathode side cooling fluid temperature of the first group increased at 1000 s and when the FCMS controls the injected power of cells groups (The air and hydrogen pressure drops are applied).

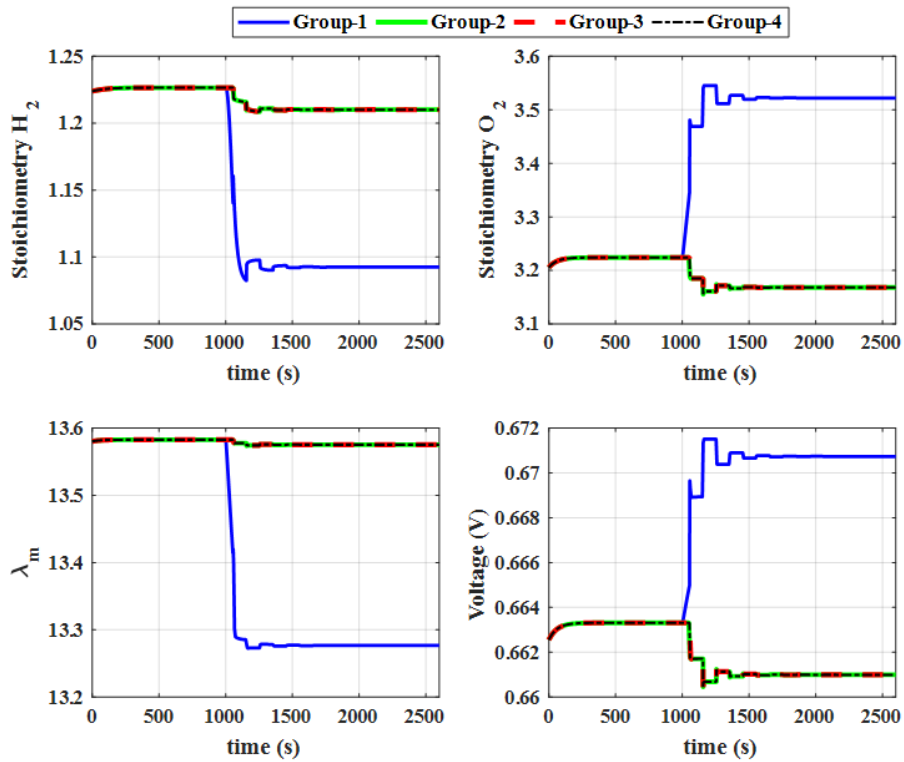


Figure 4-26. Simulation results of FLC inputs and the cell voltages when the cathode side cooling fluid temperature of the first group increased at 1000 s and when the FCMS controls the injected power of cells groups (The air and hydrogen pressure drops are applied).

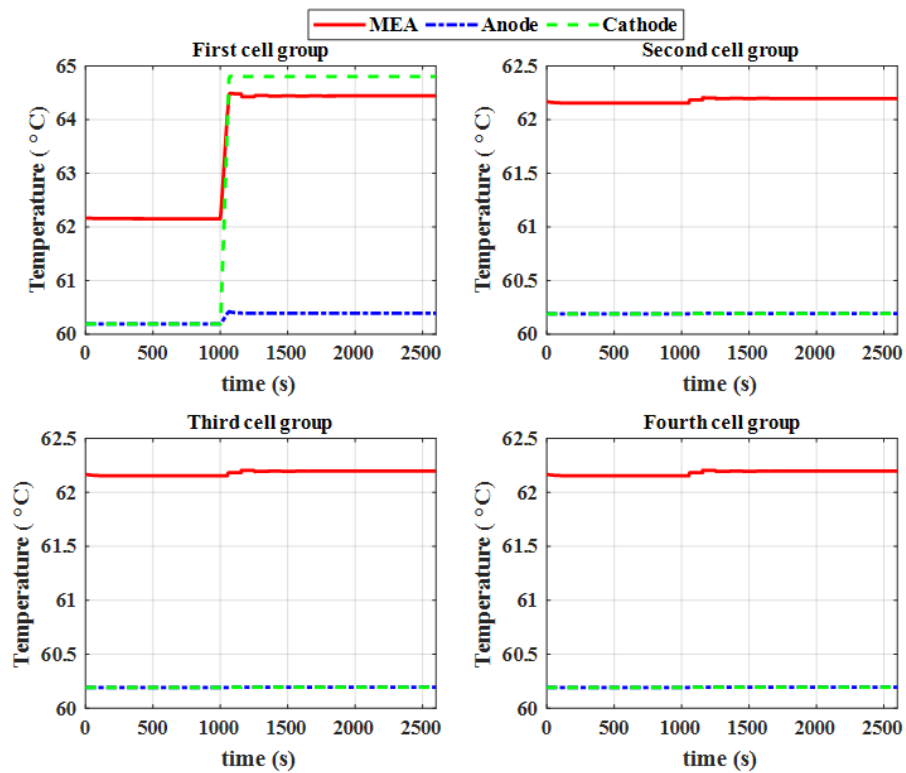


Figure 4-27. Simulation results of the cell temperatures when the cathode side cooling fluid temperature of the first group increased at 1000 s and when the FCMS controls the injected power of cells groups (The air and hydrogen pressure drops are applied).

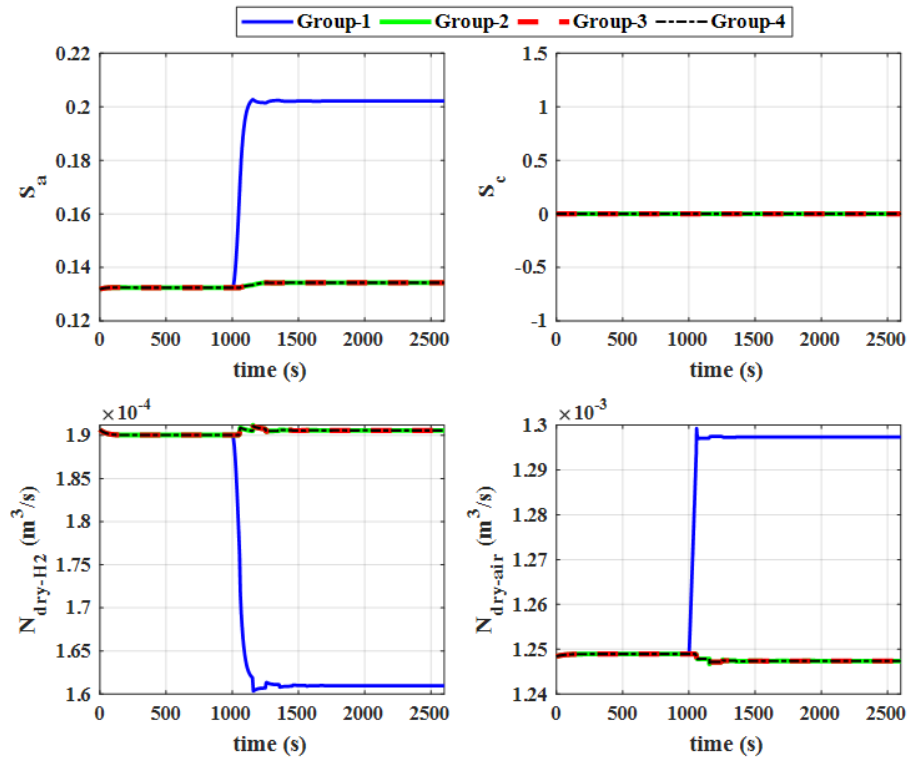


Figure 4-28. Simulation results of the dry gas flow rate and saturation inside the channels when the cathode side cooling fluid temperature of the first group increased at 1000 s and when the FCMS controls the injected power of cells groups (The air and hydrogen pressure drops are applied).

The cell temperatures are shown in Figure 4-27 during this simulation. As seen in Figure 4-28, the saturation level at the anode channel of the first group is the same as the third simulation. However, the saturation level in the anode channel of the other groups increased due to the increase of their supplied powers. Increasing the supplied power of the cell groups except the first group leads to an increase in their membrane temperature. As demonstrated in Figure 4-28, dry gas flow rates change concerning the amount of saturation and temperature changes.

The reference of the total power and the total injected power by cell groups are shown in Figure 4-29. As seen in this figure, the SC voltage changes to regulate the DC link voltage, and the SC voltage controller compensates for the power changes imposed by the FCMS. The sum of the cell group voltages during the second simulation is depicted in Figure 4-30. As seen in this figure, the stack voltage is slightly increased, despite the large change in the current injected by the first group. As seen in Figure 4-30, the current density of the cell groups is changed due to the change in the demanded power by the FCMS and the SC voltage controller.

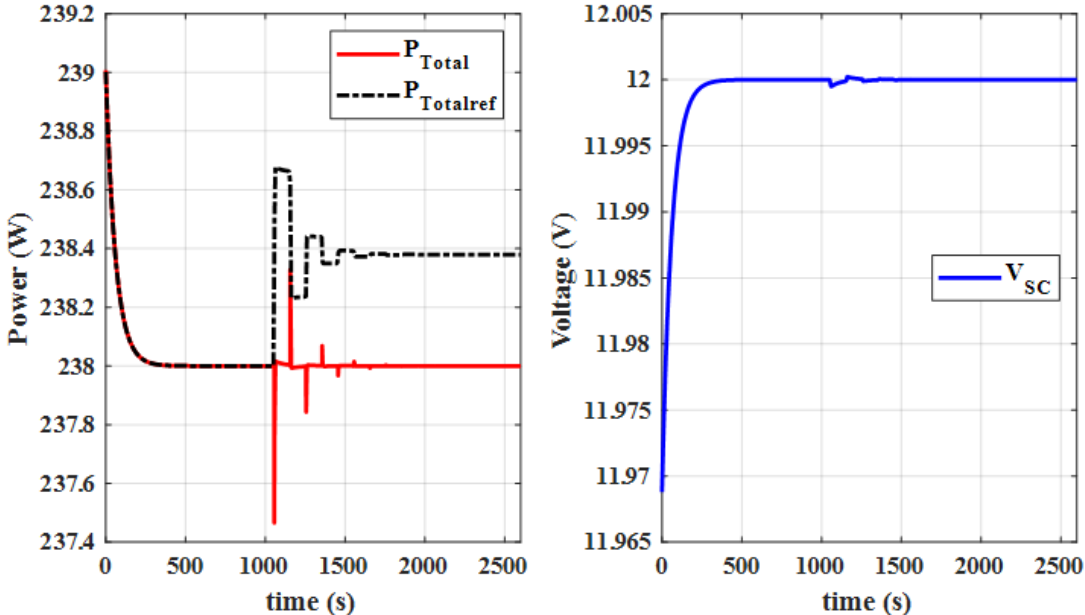


Figure 4-29. Simulation results of the SC voltage, the reference of total power and the total power injected by cell groups when the cathode side cooling fluid temperature of the first group increased at 1000 s and when the FCMS controls the injected power of cells groups (The air and hydrogen pressure drops are applied).

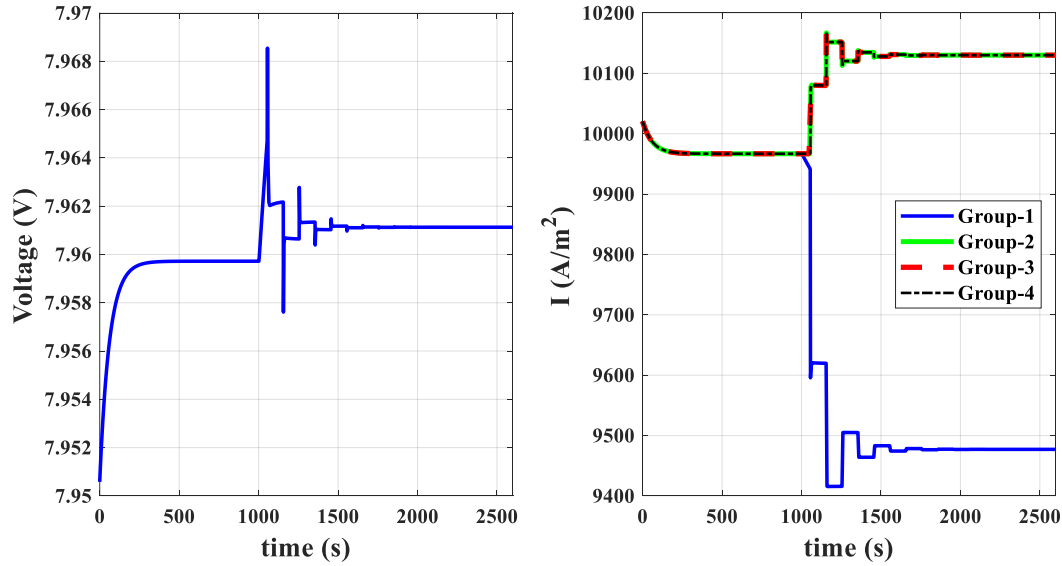


Figure 4-30. Simulation results of the stack voltage and the injected current by cell groups when the cathode side cooling fluid temperature of the first group increased at 1000 s and when the FCMS controls the injected power of cells groups (The air and hydrogen pressure drops are applied).

To further verify and validate the proposed management system, two other simulations are performed. In these simulations, all of the cell groups are in the normal condition until 1000 s. The boundary conditions of the first group are changed at 1000 s to simulate a fault. Then, the boundary condition of the first group is changed to normal at 4000 s. In these two simulations, the FCMS runs after 2500 s. The current passing through the cell groups is fixed to be close to 30 A in the normal condition of the cell groups by applying an appropriate load power.

In the fifth simulation, the drying condition of the first group is realized like the second simulation. A slope rate of 0.08 °C/s increases the cooling fluid temperatures from 60 °C to 75 °C at 1000 s and the same slope decreases their temperature from 75 °C to 60 °C at 4000 s. The model parameters and the other boundary conditions are kept as same as the second simulation. The normalized and absolute values of the FLC inputs are respectively shown in Figure 4-31 and Figure 4-32. As seen in these figures, the FCMS runs after 2500 s and can improve the state of the first group. The provided explanations of the second simulation can be applied to the interval of 1000 s to 4000 s. It should be noticed that the FCMS was controlling the power of the cell groups for the entire of the second simulation. The inputs of the FLC and the reference of powers in a steady state without utilizing the FCMS are compared to their values in steady-state with utilizing the FCMS in Table 4.4 based on Figure 4-32. In this table, the relative error for each parameter can be calculated by (4.5). This table shows that a 5% modification of water content dispersion is obtained at a cost of increasing the power dispersion 17%.

$$Re_x = \frac{abs(x_1 - x_{other\ groups})}{\max(x_1, x_{other\ groups})} \quad (4.5)$$

In this equation, Re_x is the relative error of the x (x can be the membrane water content, hydrogen stoichiometry, oxygen stoichiometry, or injected power) and the index of x indicates the cell group.

The temperature of the cell groups is shown in Figure 4-33. The temperature results in 1000 s to 4000 s are close to the second simulation. The appearance or disappearance of liquid water takes time. Therefore, the stoichiometry of hydrogen and oxygen has a transient state when the temperature of the cooling fluids is changed. The temperature rise influences gas viscosity and

water vapor flow rate before changing the amount of liquid water. As a result, the stoichiometry of the gases is primarily decreased due to the viscosity changes, and the increase of the water vapor flow rate. Then, it increased due to the disappearance of the liquid water from the channels. As shown in Figure 4-45, the dry gas flow and the saturation level inside the channels verify this theory. The same reason is behind the increase of stoichiometry when the cooling fluid temperatures return to their nominal value at 4000 s. As seen in Figure 4-34, the saturation levels increased from zero to their nominal value at 4000 s with a delay of about 200 s due to the slope applied for the cooling fluid temperature rises. As a result, the dry gas flow rates primarily increased due to the change of the viscosity and water vapor flow rate. Then, it decreased to its nominal value due to the saturation level change.

The reference of the total power and the total supplied power is shown in Figure 4-35 during the fifth simulation. Since the FCMS runs after 2500 s, the reference of total power is different from the total injected power by cell groups. The SC voltage is also changed during the transient conditions to regulate the DC link voltage. The stack voltage is shown in Figure 4-36. As seen in this figure, the stack voltage is decreased (7.69 V) due to the drying condition of the first group but it is increased (7.73 V) after 2500 s due to running the FCMS. This result verifies that the stack voltage has a lower value without the FCMS. This result further verifies the effectiveness of the proposed FCMS. The current density of cell groups is also shown in Figure 4-36 that is changed due to the FCMS and the SC voltage controller.

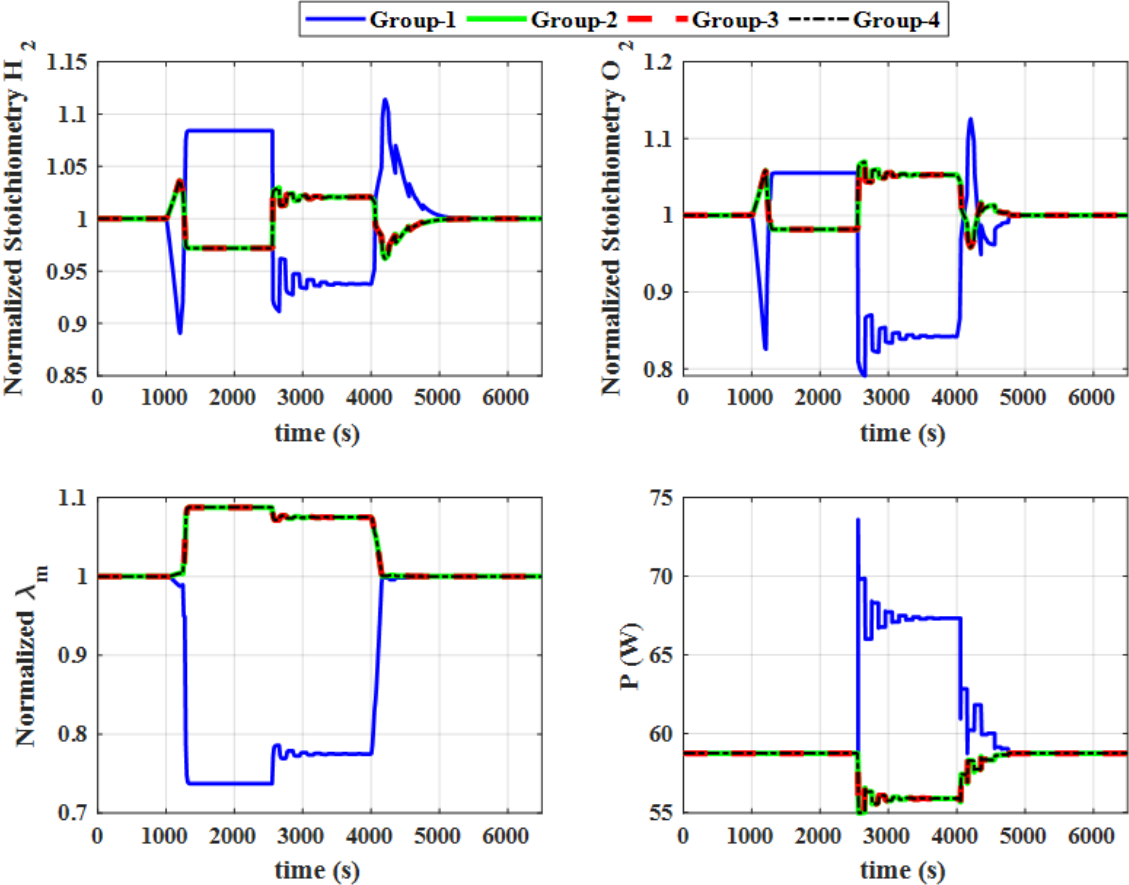


Figure 4-31. Simulation results of the normalized value of the FLC inputs and the reference power that should be injected by the cell groups when the cooling fluid temperatures of the first group increased from 60 °C to 75 °C at 1000 s and decreased to its nominal value of 60 °C at 4000 s (The air and hydrogen pressure drops are applied).

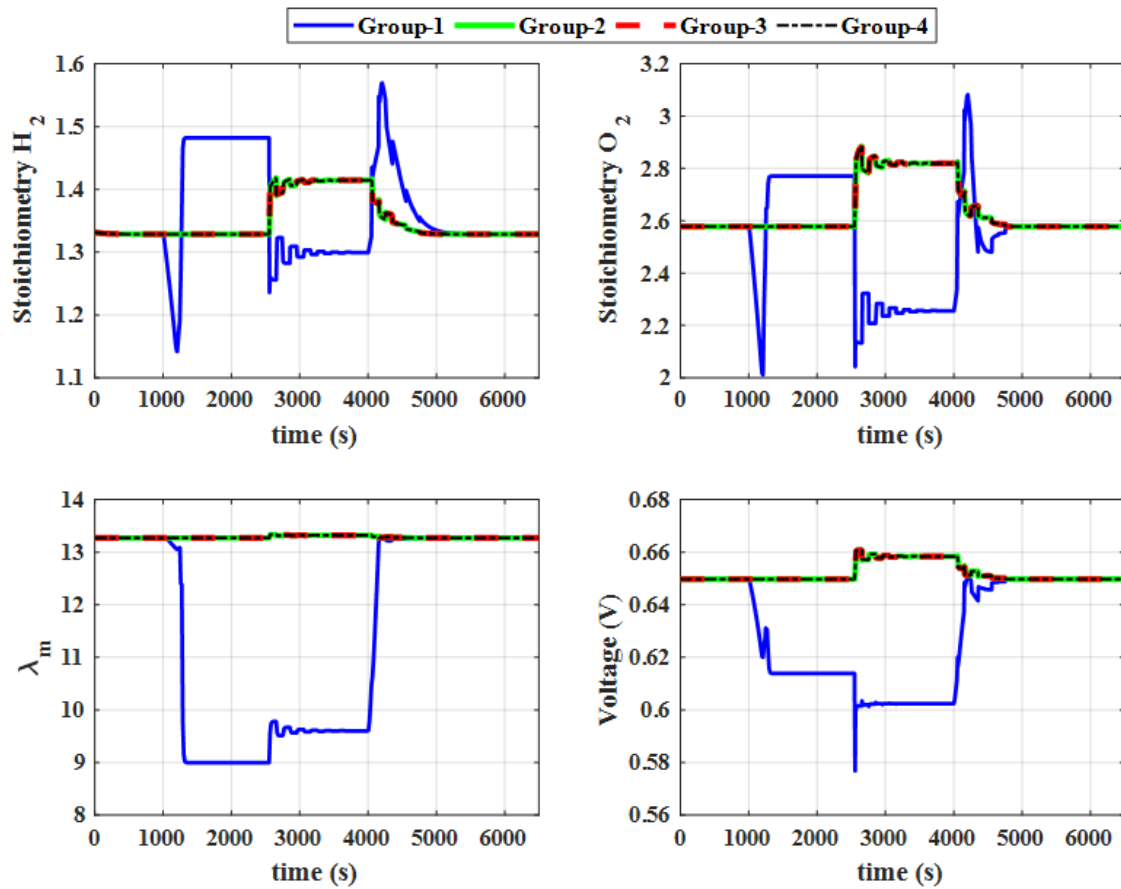


Figure 4-32. Simulation results of the FLC inputs and the cell voltages when the cooling fluid temperatures of the first group increased from 60 °C to 75 °C at 1000 s and decreased to 60 °C its nominal value at 4000s (The air and hydrogen pressure drops are applied).

Table 4.4. Inputs of the FLC and reference of powers in the steady-state during the drying condition of the first group

	λ_m	St_{H_2}	St_{O_2}	Power
First group- without the FCMS	9	1.48	2.77	58.75
The other groups – without the FCMS	13.27	1.33	2.58	58.75
Relative error- without the FCMS	0.32	0.1	0.07	0
First group- with the FCMS	9.6	1.3	2.26	67.33
The other groups – with the FCMS	13.32	1.41	2.82	55.88
Relative error- with the FCMS	0.28	0.07	0.20	0.17

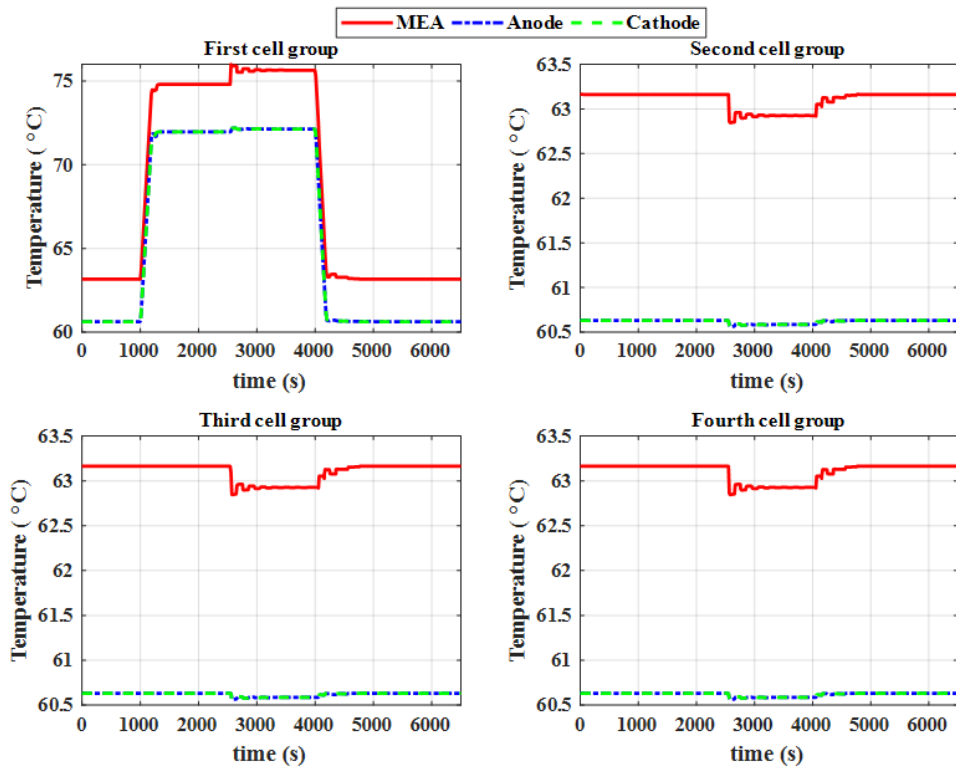


Figure 4-33. Simulation results of the cell temperatures when the cooling fluid temperatures of the first group increased from 60 °C to 75 °C at 1000 s and decreased to 60 °C its nominal value at 4000s (The air and hydrogen pressure drops are applied).

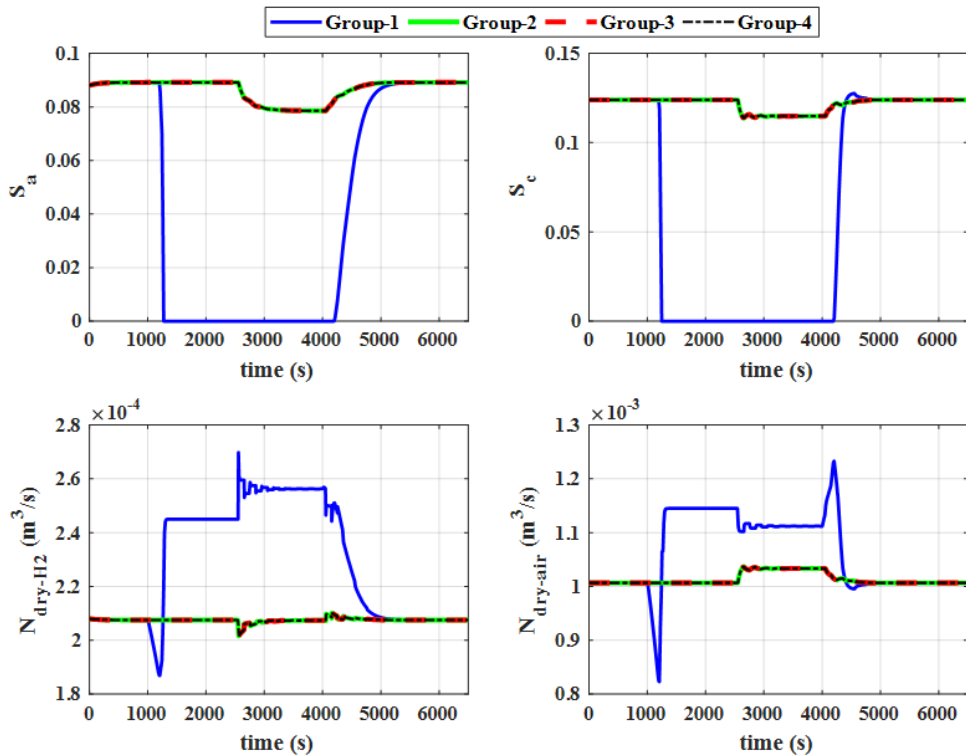


Figure 4-34. Simulation results of the saturation level inside the channels and dry gas flow rates when the cooling fluid temperatures of the first group increased from 60 °C to 75 °C at 1000 s and decreased to 60 °C its nominal value at 4000s (The air and hydrogen pressure drops are applied).

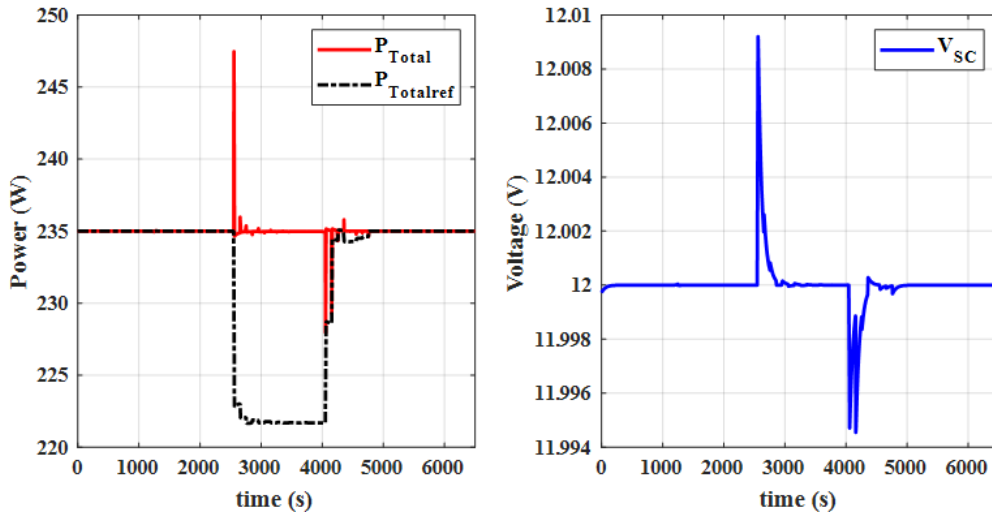


Figure 4-35. Simulation results of the SC voltage, the reference of total power and the total power injected by cell groups when the cooling fluid temperatures of the first group increased from 60 °C to 75 °C at 1000 s and decreased to 60 °C its nominal value at 4000s (The air and hydrogen pressure drops are applied).

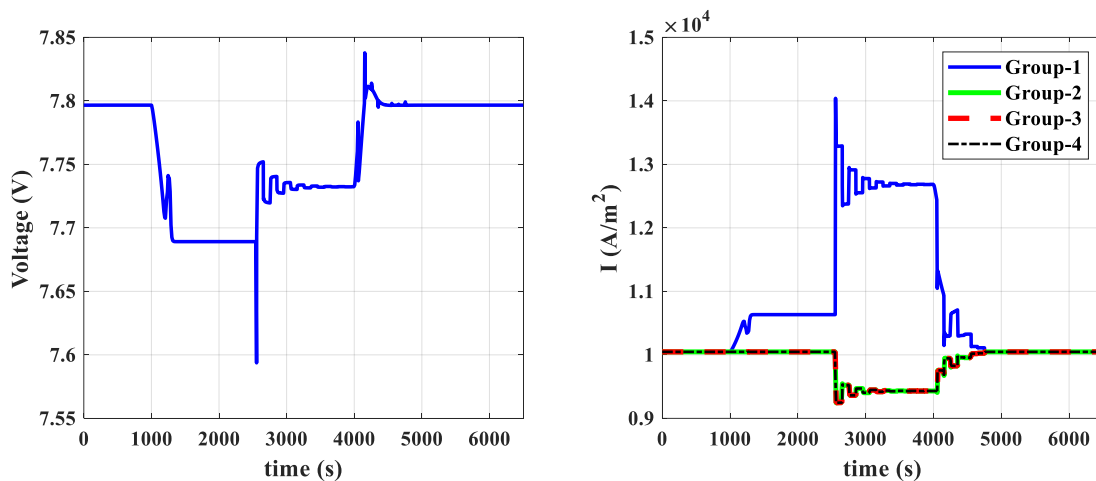


Figure 4-36. Simulation results of the stack voltage and the injected current by cell groups when the cooling fluid temperatures of the first group increased from 60 °C to 75 °C at 1000 s and decreased to 60 °C its nominal value at 4000s (The air and hydrogen pressure drops are applied).

The sixth simulation stands for simulating the flooding condition of the first group. A slope of 0.08 °C/s increases the cathode side cooling fluid temperature of the first group from 60 °C to 65 °C at 1000 s. The same slope is used to decrease it from 65 °C to 60 °C at 4000 s. The other model parameters and boundary conditions are as same as the fourth simulation. The normalized and absolute values of the FLC inputs are respectively shown in Figure 4-37 and Figure 4-38. As seen in these figures, the FCMS improves the state of the first group after it runs at 2500 s. The explanations of the fourth simulation can be applied to the interval of 1000 s to 4000 s. It should be noticed that the FCMS was controlling the power of the cell groups for the entire of the fourth simulation. The inputs of the FLC and the reference of powers in the steady-state without utilizing the FCMS are compared to their values in steady-state in the presence of the FCMS in Table 4.5 based on Figure 4-38. This table shows that a 6% modification of the hydrogen stoichiometry dispersion requires increasing the power dispersion of 5%.

The simulation results of the cell group temperatures are shown in Figure 4-39 for the sixth simulation. The temperature results for 1000 s to 4000 s are close to the fourth simulation. Due to the temperature gradient between the anode and cathode of the first group at 1000 s, more water is accumulated in the anode side of the first group and the level of saturation in its anode channel is increased (Figure 4-40). As a result, the hydrogen flow rate decreased and the hydrogen stoichiometry of the first group consequently decreased after applying the rise in the cathode side cooling fluid temperature of the first group at 1000 s. Due to the water transfer to the anode side, the water vapor flow rate at the cathode decreased and consequently, the oxygen stoichiometry increased (Figure 4-40).

The reference of the total power and the total supplied power is shown in Figure 4-41 during the sixth simulation. Since the FCMS runs after 2500 s, the reference of total power is different from the total injected power by cell groups due to the disturbance created by the FCMS. As depicted in Figure 4-41, the SC voltage is also changed during the transient conditions to regulate the DC link voltage. As seen in Figure 4-42, the stack voltage is increased a little bit (7.964 V) due to the increased oxygen stoichiometry of the first group without using the FCMS. However, the stack voltage is very slightly decreased (7.961 V) after running the FCMS at 2500 s. As seen in Figure 4-38, the most important objective, in this case, was to guarantee the hydrogen supply to avoid the hydrogen starvation. The current density of cell groups are also shown in Figure 4-42 that is changed due to the FCMS, the SC voltage controller, and the loop between the reference power and the output voltage of the cell.

These two last simulations (the five and six) validate the effectiveness of the proposed FCMS during the transient condition and verify that this system can return the electrical current to their nominal values once the fault was solved.

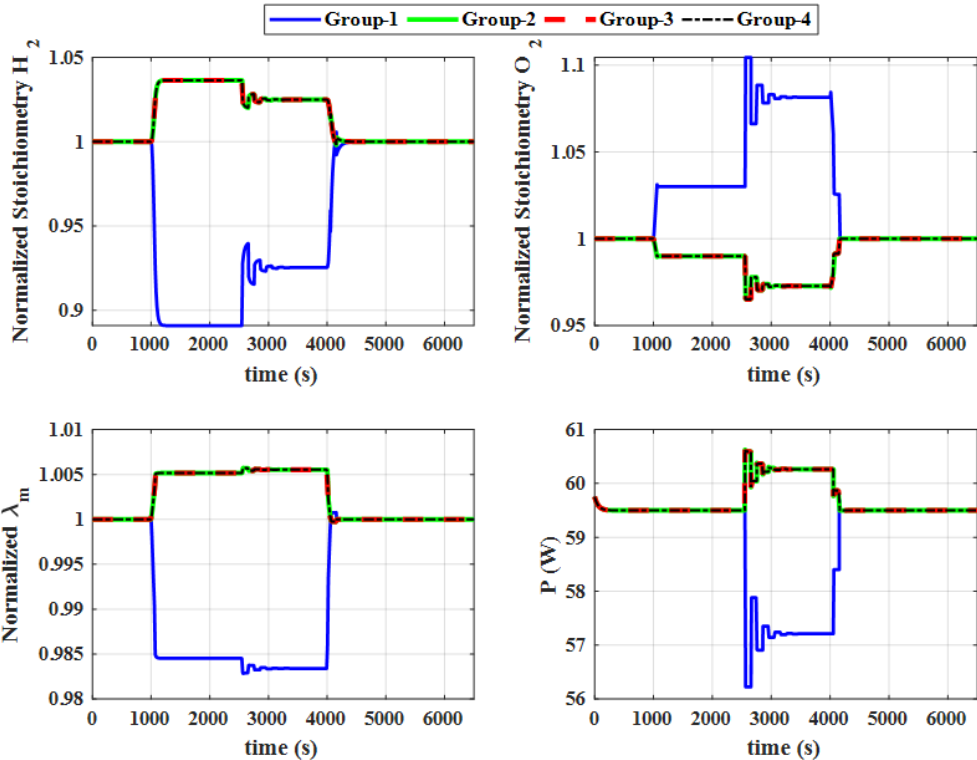


Figure 4-37. Simulation results of the normalized value of FLC inputs and the reference power that must be injected by the cell groups when the cathode side cooling fluid temperature of the first group increased from 60 °C to 65 °C at 1000 s and decreased to its nominal value of 60 °C at 4000 s (The air and hydrogen pressure drops are applied).

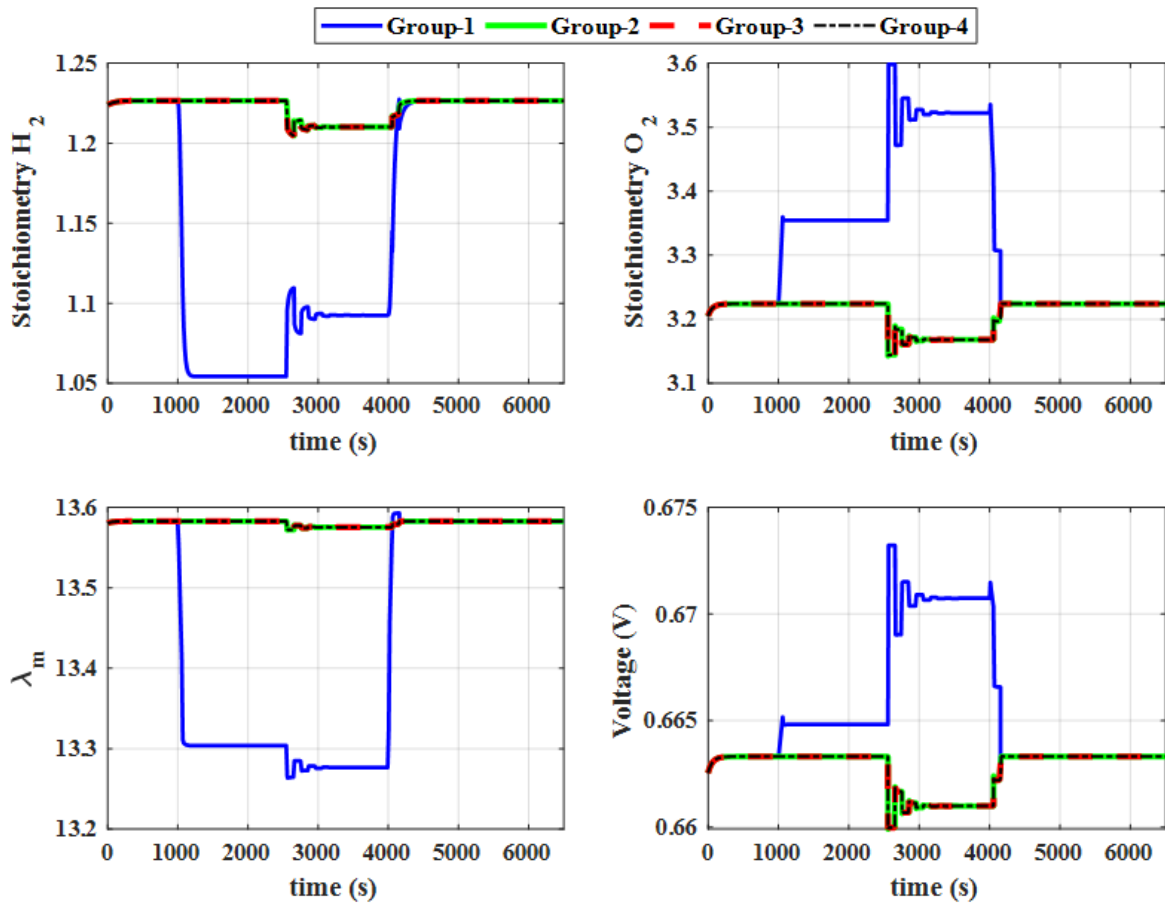


Figure 4-38. Simulation results of FLC inputs and the cell voltages when the cathode side cooling fluid temperature of the first group increased from 60 °C to 65 °C at 1000 s and decreased to its nominal value of 60 °C at 4000 s (The air and hydrogen pressure drops are applied).

Table 4.5. Inputs of the FLC and reference of powers in the steady-state during the flooding condition of the first group

	λ_m	St_{H_2}	St_{O_2}	Power
First group- without the FCMS	13.3	1.05	3.35	59.5
The other groups – without the FCMS	13.58	1.23	3.22	59.5
Relative error- without the FCMS	0.02	0.15	0.04	0
First group- with the FCMS	13.28	1.1	3.52	57.21
The other groups – with the FCMS	13.57	1.21	3.17	60.26
Relative error- with the FCMS	0.02	0.09	0.1	0.05

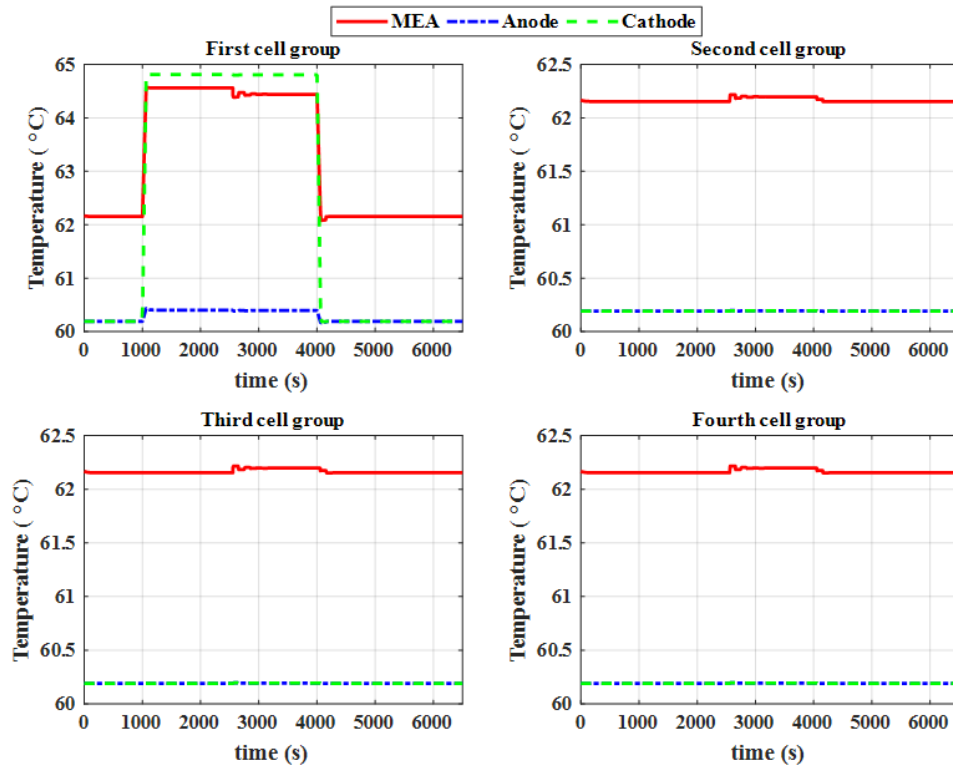


Figure 4-39. Simulation results of the cell temperatures when the cathode side cooling fluid temperature of the first group increased from 60 °C to 65 °C at 1000 s and decreased to its nominal value of 60 °C at 4000 s (The air and hydrogen pressure drops are applied).

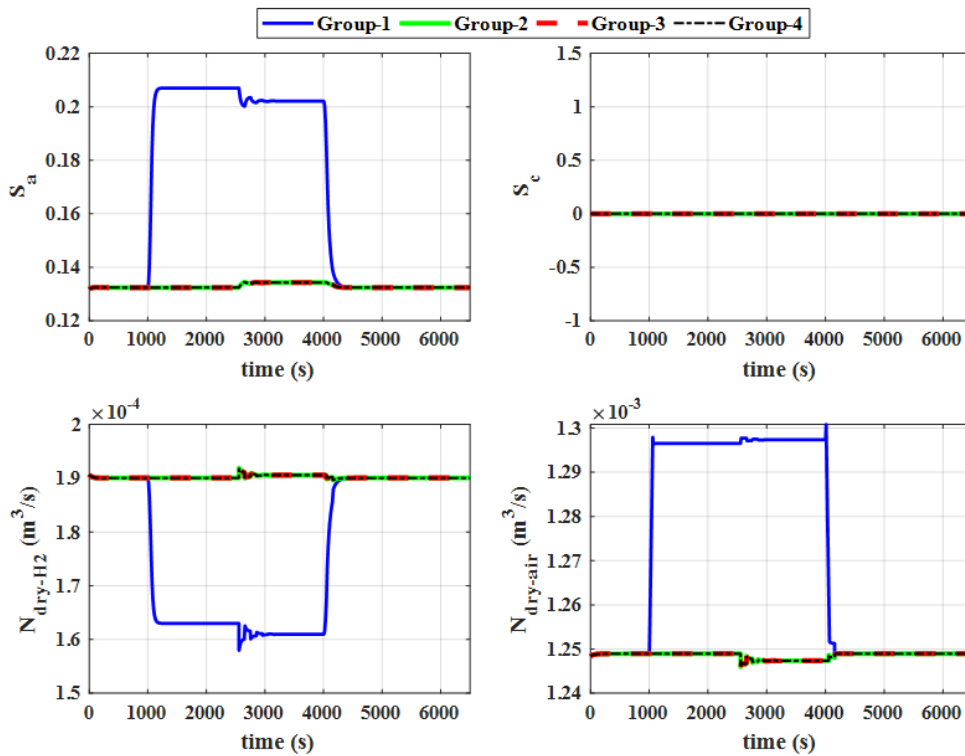


Figure 4-40. Simulation results of the dry gas flow rate and saturation inside the channels when the cathode side cooling fluid temperature of the first group increased from 60 °C to 65 °C at 1000 s and decreased to its nominal value of 60 °C at 4000 s (The air and hydrogen pressure drops are applied).

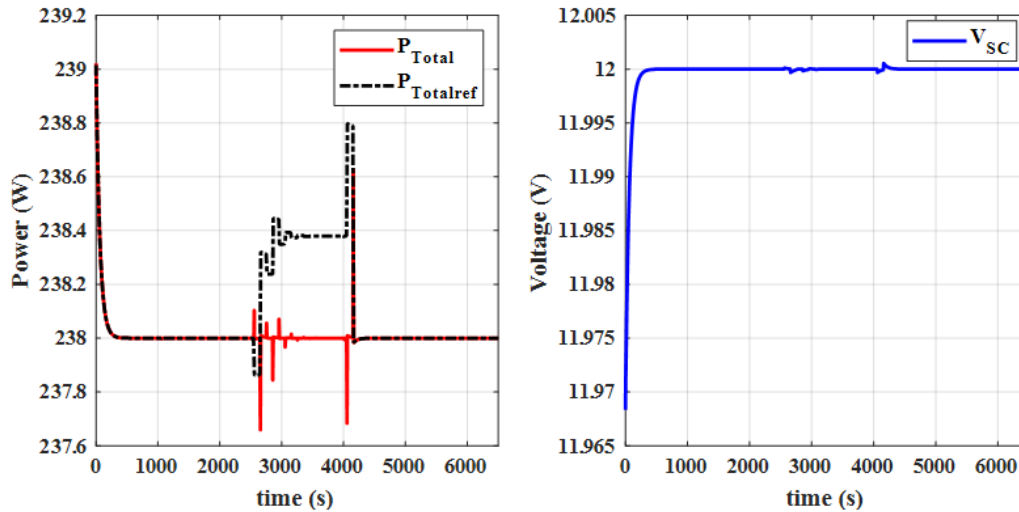


Figure 4-41. Simulation results of the SC voltage, the reference of total power and the total power injected by cell groups when the cathode side cooling fluid temperature of the first group increased from 60 °C to 65 °C at 1000 s and decreased to its nominal value of 60 °C at 4000 s (The air and hydrogen pressure drops are applied).

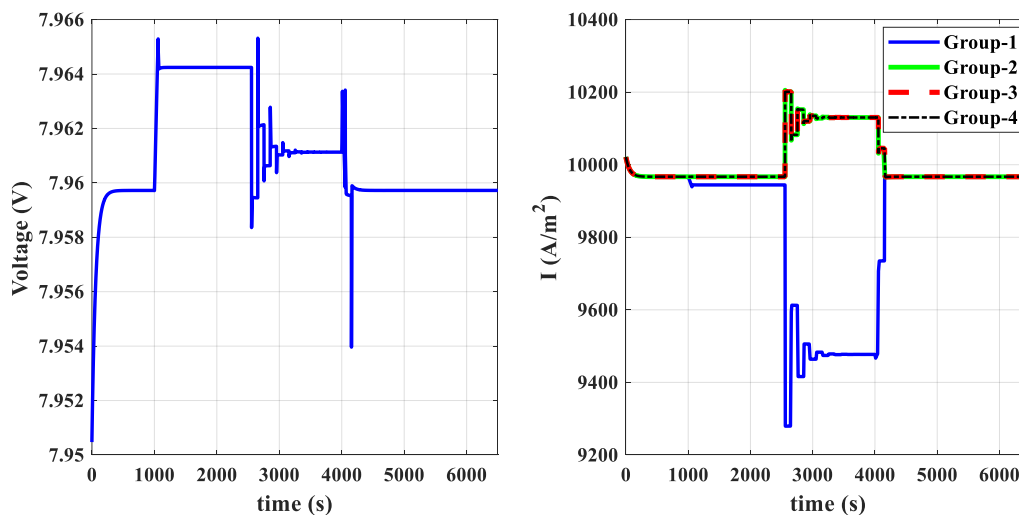


Figure 4-42. Simulation results of the stack voltage and the injected current by cell groups when the cathode side cooling fluid temperature of the first group increased from 60 °C to 65 °C at 1000 s and decreased to its nominal value of 60 °C at 4000 s (The air and hydrogen pressure drops are applied).

4.4. Energy management system

The ability to supply a load profile while curing a group of cells is the final step that approves the usefulness of the proposed system. Regarding the stability of the system, this topology can be used to manage the cells of a stack. To evaluate the effectiveness of the proposed topology in terms of energy management and dynamic performance, three different experiments are performed. A step of 400 W for eight seconds is applied to the baseload power in these three experiments. The four groups are in the normal condition for the first experiment. The load power and the injected power by the first and second groups of cells are shown in Figure 4-43 a-b. The behavior and magnitude of the injected power by two other groups is very close to the second group. As seen in this figure, the injected power by the SC is increased rapidly to control the DC link voltage. The injected power by the cell groups gradually increased to control the

voltage of the SC. Since the load step power is very high, the injected power increased to their maximum power. The difference between the load power and injected power by the cell groups is compensated by the SC. Because of the low dynamic of the fuel cells, the injected power by the cell groups is gradually decreased and the SC attracts the excess amount of power injected by the cell groups whereas the load power decreased to its nominal value. As seen in Figure 4-43a, the injected power by SC is equal to zero in steady-state. To provide a better view during the transient conditions of the first experiment, the load power and injected power by the cell groups and SC are shown in Figure 4-43 b with the time scale of 4 s/div. The DC link and SC voltages are shown in Figure 4-43 c during this experiment. As seen in this figure, the DC link voltage is well controlled and it has a constant value of 48 V. The SC voltage is gradually decreased due to its injected power but then it increased gradually due to the increase of the injected power by the cell groups and decrease of load power to its nominal value. To assess the behavior of the DC link voltage controller in transient condition, the SC injected power and the DC link and SC voltages are shown in Figure 4-43 d with the time scale of 4 ms/div. As seen in this figure, the DC link voltage decreases due to the step of load power but the fast increase in the injected power by the SC can compensate the required load power and regulate the DC link voltage. Furthermore, the SC voltage in this figure is in agreement with the SC constant voltage assumption over the transient conditions.

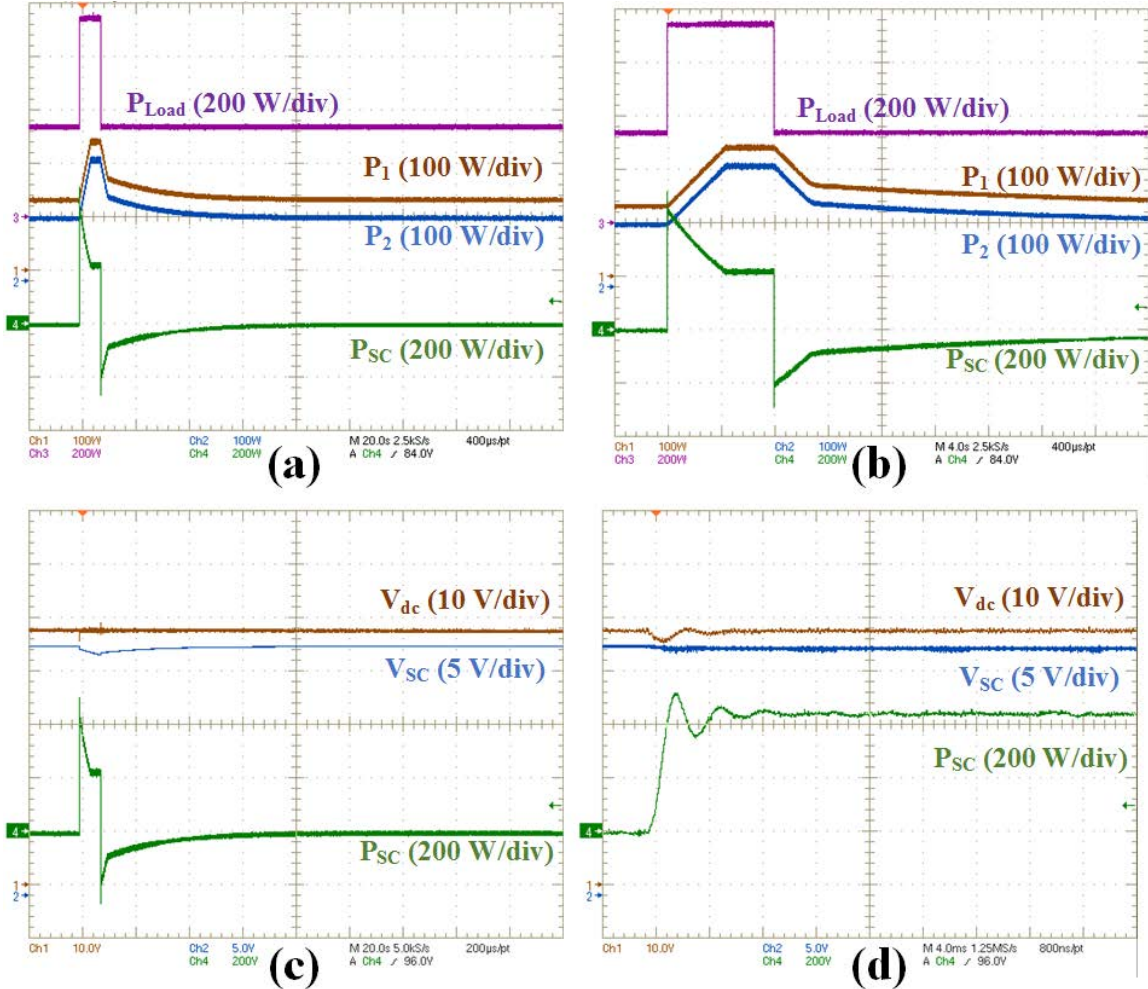


Figure 4-43. Experimental result of the energy management system when the cell groups are in the normal condition and overload occurs: a) Injected power and load power variations. b) Zoom on powers. c) DC link and SC voltage changes. d) zoom on part c.

In the second experiment, it is assumed that the first group of cells is in the drying condition whereas the other groups are in the normal condition. To produce more water in the first group of cells, its current should be controlled close to its maximum in the worst condition. As seen in Figure 4-44a, the injected power by the first group is controlled close to its maximum (240 W) during this experiment. A zoom is realized on the transient condition of the injected power by the SC and cell groups in Figure 4-44 b. As seen in Figure 4-44 c, the DC link voltage is well controlled and it has a constant value of 48 V. The SC voltage is reduced due to its injected power to supply the overload. The SC voltage gradually increased and approaches to its nominal value of 24 V by increasing the injected power of cell groups and decreasing the load power to its nominal value. The voltage of the output capacitors of the boost converters is shown in Figure 4-44 d. Since the step load leads to an increase in the injected power by the cell groups, the output capacitor voltages increase. The first group injects the maximum power during this experiment. Therefore, the first capacitor voltage decreases because of the DC link voltage stabilization by the SC. The output capacitors have an identical voltage when the injected power by the cell groups reach to their maximum power. The difference between the voltages at this point is originated from the losses difference in the boost converters. The injected power by the different groups except the first group is gradually decreased when the load power decreases to its nominal value. As a result, the difference between the first output capacitor and the other output capacitors increases. Notable that the voltage of the first group in the drying condition is kept in an acceptable range due to the improved equalizer controller.

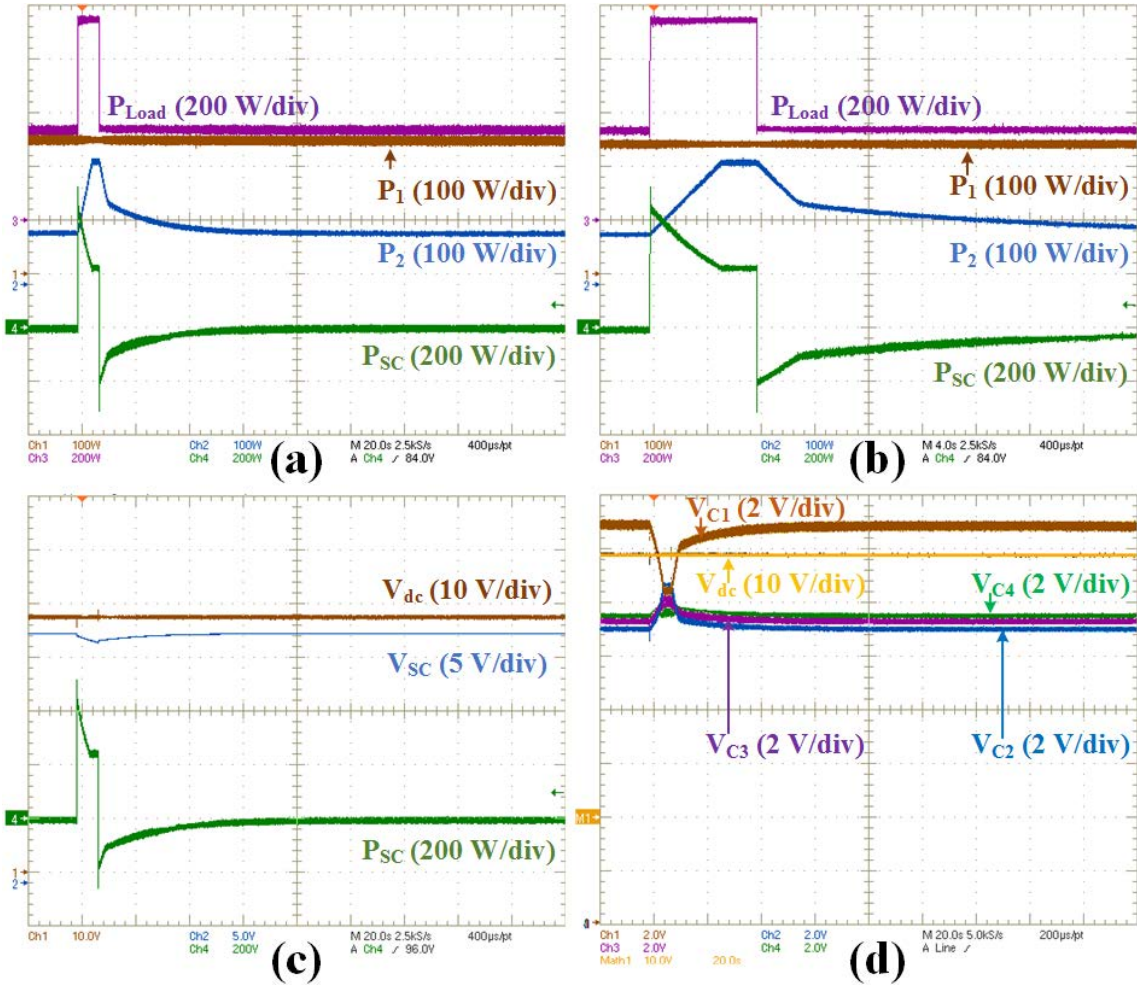


Figure 4-44. Experimental result of the energy management system when the cell groups are in the normal condition except the first group (drying condition) and overload occurs. a) Injected power and load power variations. b) Zoom on the power. c) DC link and SC voltage changes. d) Output capacitor voltage changes.

It is assumed that the first group of cells are in the flooding condition during the third experiment. The other groups are in normal condition. In this case, the water production inside the cells of the first group should be reduced. Therefore, the current or power injected by the first group should be controlled close to zero in the worst condition. The equalizer ensures the controllability of the boost converters in such conditions. As seen in Figure 4-45a, the injected power by the first group is controlled at zero Watt during this experiment. More details of the injected power by the SC and cell groups are demonstrated in Figure 4-45 b. Most of the overload is supplied by the SC due to the no injected power of the first group and limits in the maximum injected power by the cell groups. As a result, the SC voltage reduces more than the two previous experiments as shown in Figure 4-45 c. The DC link voltage is also shown in this figure and it is controlled at 48 V. The voltage of the output capacitors is shown in Figure 4-45 d during this experiment. Due to the use of the equalizer system, despite the lack of power injection by the first group in this experiment, the first capacitor has a voltage of 10 V. This experiment confirms the function of the used equalizer system to ensure the controllability of the boost converters.

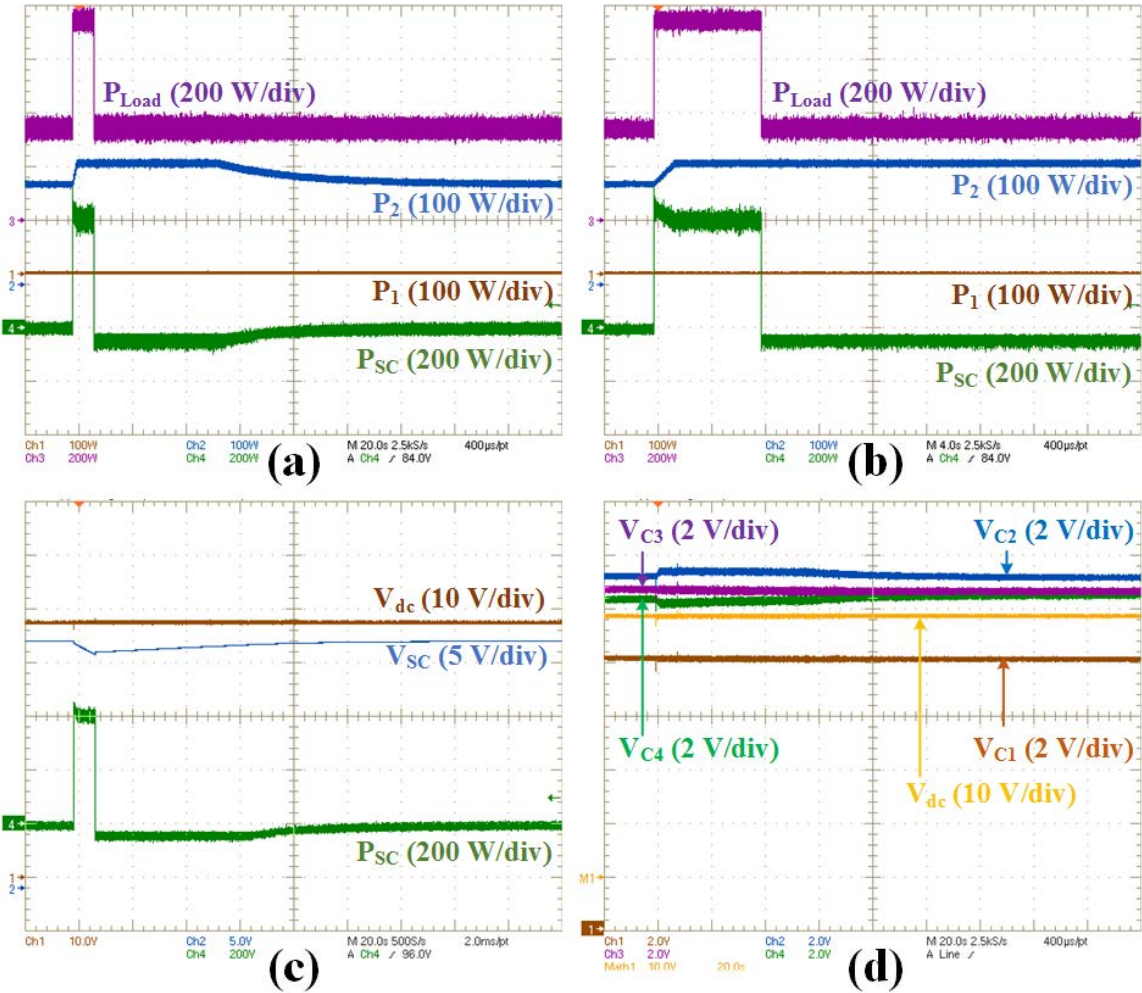


Figure 4-45. Experimental result of the energy management system when the cell groups are in the normal condition except the first group (flooding condition) and an overload occurred. a) Injected power and load power variations. b) Zoom on the part a. c) DC link and SC voltage changes. d) Output capacitor voltage changes.

4.5. Conclusions

A management system was developed in this chapter for PEMFCs. This management system can deal with the instabilities of cells inside a stack or instability of a stack in a multi-stack system. The simulation results, which were provided in this chapter, verify the capability of the system. However, better results in the future are conceivable by optimizing the management system. The experimental results, which show the behavior of the system in different operating conditions, validated the effectiveness of the proposed topology and its associated energy management functionalities. These results also confirmed that the controllability and the DC-link voltage regulation are always ensured even during drying or flooding conditions concerning one of the cell groups in which the power injected by each group of cells is modified to improve durability.

General conclusions

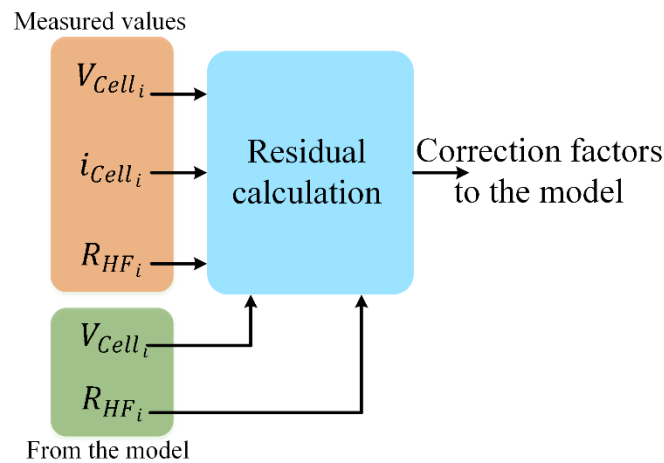
The basic interest of this thesis was to develop an FCMS. Based on the literature review conducted in the first chapter, a model-based approach was chosen to develop an FCMS. Hence, a mathematical one dimensional coupled method was proposed in the second chapter. Since the pressure drop inside the channels is the input of the proposed model, it could simulate a single cell in its stack environment. It was tried to make this model as simple as possible so that it could be simulated in real-time while maintaining accuracy. Some of the model parameters were experimentally identified whereas the identification of the other parameters will be the subject of a new thesis. The provided simulation results prove the possibility of a single cell simulation in a stack.

A power electronics architecture was proposed in the third chapter to implement the FCMS. Due to the low voltage of a single cell or a group with a small number of cells, its voltage must be increased by high voltage conversion ratio converters. Due to the efficiency of isolated converters, the classical boost converters were used for each group of cells. This connection allows managing the cell groups separately. For further increase in the output voltage, the output capacitors of the boost converters were connected in series. In such a connection, the same load current passes through all of the capacitors. As a result, a new voltage equalizer was proposed in this thesis to ensure the controllability of the boost converters. To regulate the DC link voltage and responding to the fast dynamic load profiles, the hybridization with the SC was used in this thesis. The SC is connected to the DC link through a bidirectional DC-DC boost converter. In this thesis, a hierarchical control was developed for this system. This control method consists of four basic parts: Control of the supplied power of the cell groups, Control of the H-bridge inverter, Control of the DC link voltage, and control of the SC voltage. The inner loops correspond to current or power loops. A sliding mode controller was used for the boost converters and the bidirectional converter to control the current of the cell groups and the SC. The fuel cell management system applies the reference power of each cell group. A classical control method was used based on two loops to regulate the DC link voltage and the SC voltage. given the different operation modes of the equalizer, a model was developed in Chapter 3. Furthermore, a dynamic average model was also developed for the system. the dynamical average model was used to analyze the stability of the system and to perform sizing. Regarding the presence of an H-bridge inverter in the equalizer topology, it was challenging to develop a dynamical average model. The simulation and experimental results verified the effectiveness of the system and the validity of the proposed model.

Finally, the management system was designed and evaluated in Chapter 4. The management strategy was developed based on the FLC in this chapter. The hydrogen stoichiometry, oxygen stoichiometry, and membrane water content are the input and the change in the output power is the output of the FLC. Mamdani's method was used to implement the FLC. The simulation results were provided in this chapter when one of the four groups is in the drying or flooding conditions. These results approved the validity of the proposed system. Finally, the ability of the system in supplying a load profile while curing a cell group was experimentally validated. Three different experiments were performed. Four cell groups were considered and the first group of cells was in the normal, drying, and flooding condition in each experiment while the other groups were in normal condition. The experimental results validated the effectiveness of the proposed topology and its associated energy management functionalities.

Following perspectives are conceivable:

- The mathematical model of the PEMFC, which was developed in Chapter 2, has many parameters. Some of these parameters were experimentally identified but many parameters remain to be identified. This model can be more comprehensive at the expense of more sophistication. For instance, all chemical reactions at the anode and cathode side can be taken into account in the charge transfer model to develop a more precise model. Regarding the experimental results, the liquid water transfer model also requires substantial modifications. These modifications are in progress.
- In Chapter 3, a hierarchical control method was used to control the power electronics architecture. A robust passivity based method is under investigation to control the whole system in one loop. The equalizer proposed in Chapter 3 was used for four cell groups. Increasing the number of groups leads to an increase in the number of secondary windings. As a result, a modular approach to increase the number of capacitors is under investigation.
- In Chapter 4, the power supplied by different cell groups was modified based on the FLC. The interval of membership functions was found by trial and error. A Neuro-fuzzy system can find the parameters of the FLC by exploiting approximation techniques from neural networks. As a result, the possibility of optimizing the management strategy is an open topic for future research.
- The FCMS were assessed by the simulation results. The experimental results of the whole system from the aspect of energy management were obtained for the worst condition of the first group of cells. Furthermore, the programmable power supplies were used to emulate the fuel cells. Therefore, the proposed power electronics structure, and the FCMS should be experimentally validated with a real PEMFC. The overestimation/underestimation of the PEMFC model parameters can lead to a disturbance in the detection of cell faults when an actual PEMFC is used.
- The parameters of the model can be modified over the lifespan of a PEMFC. To take into account the impact of aging, a method can be proposed to modify the parameters of the system based on the residual calculations. The block diagram of one possible method is shown in the figure below. As seen in this figure, the high-frequency resistance and cell output voltage are the essential parameters that are used to perform the model correction. The High-frequency resistance can be easily found by imposing a High-frequency sinusoidal signal on the reference current of each cell group.



Appendix A

French version of the introduction

Compte tenu des crises énergétique et environnementale dans le monde, les énergies renouvelables et propres sont amenées à être déployées en masse. La problématique majeure soulevée est la nature intermittente de leurs ressources [1], [2]. L'hydrogène comme un vecteur énergétique peut faire face à ce problème. Il est (sera) possible de produire de l'hydrogène à bas prix en utilisant l'énergie excédentaire générée par des sources d'énergie renouvelables et le stocker dans des réservoirs. Ce gaz peut être directement converti en électricité par une pile à combustible (PAC) lorsque le réseau a besoin de plus d'énergie électrique. Des piles à combustible à membrane d'échange de protons (PEMFC selon l'acronyme des expressions anglaises proton exchange membrane fuel cells ou polymer electrolyte membrane fuel cells) sont les PACs dont la maturité technologique est la plus avancée, notamment pour les applications embarquées. La tension nominale d'une cellule de PEMFC est autour de 0,7 V. Par conséquent, un certain nombre de cellules doivent être connectées en série à l'intérieur d'un stack pour augmenter la tension de sortie. L'inconvénient fondamental de ce type de connexion est le fait que la durée de vie d'un stack dépend de la durée de vie de chaque cellule. L'autre inconvénient de cette connexion est la possibilité de propagation d'un défaut entre une cellule et les cellules voisines en raison notamment du couplage thermique. La gestion individualisée des cellules ou de groupes de cellules permettrait de faire face à ces problèmes.

Les quatre obstacles majeurs à la pénétration des systèmes PACs sur le marché sont l'efficacité électrique, la fiabilité, la durabilité et le coût [3]. Actuellement, les performances des PACMEPs, en termes de densité de puissance (4 kW / L) et d'efficacité, sont suffisantes pour permettre leur diffusion à grande échelle [4]–[6]. D'autre part, la durabilité et le coût sont deux points qui nécessitent d'être améliorés [7]. Pour améliorer la durabilité, il est possible de développer de nouveaux matériaux plus robustes mais aussi de mieux contrôler les conditions de fonctionnement pour éviter les instabilités qui entraînent des dommages irréversibles [8]. En effet, un système de gestion comme les systèmes de gestion de batterie (BMS) peut contrôler l'équilibrage des cellules à l'intérieur d'un stack. Dans cette thèse, on s'intéressera à la mise en place d'un tel système adapté au contrôle des piles à combustible.

Ce doctorat est financé par le Laboratoire d'Energétique et de Mécanique Théorique et Appliquée (LEMETA) de l'Université de Lorraine, Nancy, France. L'objectif principal de ce projet est de développer un système de gestion des piles à combustible (SGPAC) pour améliorer la fiabilité et la durabilité des PEMFCs. Un convertisseur spécifique enrichira un brevet du LEMETA portant sur une nouvelle architecture de PEMFC.

Pour développer un tel système de gestion, il faut disposer d'une pile à combustible qui permet de modifier le courant produit par certaines cellules à l'intérieur du stack, et une structure électronique qui permet de contrôler la puissance des différentes cellules. Un nouveau brevet a résolu la première exigence et permet d'accéder au courant de n'importe quelle cellule [9]. Du fait de la basse tension d'une cellule ou d'un petit groupe de cellules, des convertisseurs à haut ratio d'élévation comme des convertisseurs isolés sont nécessaires mais leur efficacité est un défi fondamental à résoudre [10]–[12]. Le développement d'un tel système de gestion implique donc de faire face à de nombreux défis.

Énoncé du problème

Comme indiqué précédemment, l'un des obstacles les plus difficiles à surmonter pour permettre une utilisation de masse des PEMFCs est d'augmenter leur durée de vie. La durée de vie de la PAC peut être améliorée en utilisant de meilleurs matériaux. Cependant, il est également possible d'augmenter la durée de vie grâce à une gestion optimale des conditions de fonctionnement implémentée par une interface électrique, même dans un système avec des matériaux améliorés. À cet égard, certains efforts ont été réalisés par la communauté scientifique et les résultats ont été publiés dans la littérature, mais la PAC est chaque fois considérée comme un stack et un système fermé. Or, les instabilités de fonctionnement des cellules peuvent être contrôlées en gérant les cellules séparément. Il est également possible d'éviter la propagation de défauts en contrôlant séparément les cellules. Cependant, la gestion de la basse tension et du courant élevé est le principal défi de la structure d'électronique de puissance. Les défauts doivent tout d'abord être détectés. Le modèle physique mis en place dans cette thèse permet de détecter certains défauts. Il décrit le couplage entre transfert de matière, de chaleur et de charges mais est suffisamment simplifié pour être résolu en temps réel. Enfin, le système de gestion doit prendre des décisions sur la base des données du modèle et des grandeurs observables puis les mettre en œuvre par l'intermédiaire de la structure électronique.

Méthodologie

Les résultats présentés dans cette thèse découlent d'analyses bibliographiques, et de travaux de modélisation et de nature expérimentale. Après avoir examiné la littérature scientifique, le système a été modélisé et simulé à l'aide de l'outil MATLAB. Certains paramètres du modèle de PAC ont été identifiés grâce à des résultats expérimentaux originaux. Des expériences ont également servi à améliorer et à valider les modèles proposés : par exemple, le comportement de la structure d'électronique de puissance a été validé par comparaison à des résultats expérimentaux. Le premier chapitre est consacré à la première étape de la méthodologie proposée, c'est-à-dire l'étude bibliographique.

Piles à combustible à membrane électrolyte polymère

Une PEMFC est un dispositif électrochimique qui convertit directement l'énergie chimique du combustible en électricité par une réaction électrochimique. Comme le montre la Figure 1-1, une cellule élémentaire de ce dispositif se compose de deux électrodes (anode et cathode), de deux plaques bipolaires, de deux couches de diffusion gazeuse, et d'un électrolyte. L'électrolyte du type de pile étudié ici est un polymère conducteur de protons. Cette membrane est un diélectrique (les électrons ne peuvent pas la traverser) et ne permet qu'aux ions hydrogène (H⁺) et à l'eau de la traverser. Les couches de diffusion gazeuse et les plaques bipolaires permettent le transport des réactifs (hydrogène et oxygène) jusqu'aux sites catalytiques [13].

Une PEMFC utilise essentiellement du platine comme catalyseur dans ses électrodes, en quantité d'environ 0,3 gPt/kW. La membrane est placée entre deux électrodes. Le catalyseur, constitué de nanoparticules de platine est supporté par du carbone et le tout est lié par le même ionomère que celui de la membrane. Cet ensemble s'appelle l'ensemble membrane-électrode (MEA). L'hydrogène est dissocié en protons et électrons à l'anode. Le platine catalyse cette réaction. Les ions d'hydrogène peuvent traverser la membrane, mais les électrons passent par le circuit externe. Les électrons se déplacent dans le circuit externe du potentiel de la cathode au potentiel de l'anode, ce qui signifie la production d'énergie électrique. Un flux d'oxygène pur

ou d'air est délivré à la cathode où les molécules d'oxygène réagissent avec les électrons qui arrivent du circuit externe et les ions hydrogène qui passent à travers la membrane. Le produit de cette réaction est de l'eau. La chaleur est un sous-produit. En général, deux molécules d'hydrogène réagissent avec une molécule d'oxygène pour produire deux molécules d'eau [14].

Dégradation

Comme indiqué précédemment, de nombreuses cellules sont connectées en série dans un stack. La tension d'une cellule particulière dans un stack peut diminuer en raison d'un vieillissement spécifique ou d'un dysfonctionnement local comme un assèchement. De ce fait, une plus grande quantité de chaleur est générée dans cette cellule, ce qui entraîne une augmentation de sa température, une amplification de l'assèchement et donc une perte de tension supplémentaire. Ce phénomène boule de neige peut entraîner la défaillance de la cellule. Par conséquent, la durée de vie totale du système a été réduite par l'effet de cette cellule.

La dégradation des composants d'une PEMFC peut se diviser en trois catégories : la dégradation mécanique, chimique et thermique. Pratiquement, ces trois modes de dégradation sont couplés. La dégradation mécanique est provoquée par la différence de pression entre l'hydrogène et l'oxygène et par les contraintes qui se produisent en raison d'une pression de serrage non uniforme à l'échelle des canaux d'alimentation et du fait du cyclage en humidité. La dégradation chimique est liée aux différents composants de la cellule : variation de l'hydrophobicité de la couche de diffusion gazeuse, corrosion des plaques bipolaires, pollution du catalyseur et décomposition du polymère. Cette catégorie de dégradation a de nombreuses conséquences telles qu'une diminution de la conductivité, une perte d'activité du catalyseur, un amincissement de la membrane, etc. Une température excessive provoque une dégradation thermique. Les dégradations mécanique et thermique peuvent généralement être considérées comme des dégradations irréversibles. La dégradation des matériaux dans le temps est également irréversible et ne peut pas être évitée [17] mais elle peut être réduite grâce à une gestion du système adaptée.

Dégradation et effets boule de neige

En raison du procédé de fabrication d'une pile, on peut prévoir certaines hétérogénéités pendant la vie de la pile. L'hétérogénéité de la distribution du fluide de refroidissement est l'une de ces hétérogénéités qui peuvent avoir un impact irréversible sur la membrane. Par exemple, si l'une des cellules est moins refroidie en raison d'une hétérogénéité de débit du fluide de refroidissement, sa température commence à augmenter. En conséquence, sa membrane commence à s'assécher et elle devient plus résistive. Si le courant de cette cellule ne peut pas être modifié, la tension de cette cellule chute et une plus grande quantité de chaleur est dissipée par cette cellule. Plus la production de chaleur est élevée, plus la température des cellules augmente. Cette augmentation de température rend la membrane plus sèche encore et donc plus résistive. Ce phénomène boule de neige peut se poursuivre jusqu'à la rupture de la membrane. En raison des hétérogénéités de construction et d'assemblage des cellules et du procédé de fabrication, le niveau de dégradation de chaque cellule n'est pas le même. Cette hétérogénéité de dégradation des cellules entraîne la baisse du potentiel de certaines cellules. Si le courant produit par ces cellules ne peut pas être modifié, plus de chaleur est générée par ces cellules plus dégradées. Un effet boule de neige identique à celui mentionné pour l'hétérogénéité de l'écoulement du fluide de refroidissement peut alors se produire.

L'hétérogénéité de distributions des flux de gaz, en particulier au niveau du canal anodique peut avoir une autre conséquence. Comme le montre la figure 1.5, si plus de gouttes d'eau

apparaissent dans le canal anodique d'une cellule en particulier, le débit d'hydrogène correspondant diminue et la vapeur d'eau est donc moins évacuée, ce qui entraîne une production de liquide supplémentaire. Plus d'eau sous forme liquide à l'intérieur du canal fait baisser le débit de gaz. Cet effet boule de neige est illustré dans la figure 1.6. Comme le montre cette figure, une autre façon d'amorcer cette boucle est l'hétérogénéité des flux de fluide de refroidissement. Par exemple, si le canal côté anode d'une cellule refroidit plus que les autres canaux, la pression de vapeur d'équilibre de l'eau est réduite et, par conséquent, les gouttes d'eau peuvent être formées dans le canal qui rend le flux du gaz plus faible. La présence d'eau sous forme liquide côté anode peut avoir des effets destructeurs et irréversibles. Le manque de combustible localisé (Fuel Starvation) à l'anode est responsable de la dégradation de la cathode.

Les cellules à l'intérieur d'une pile sont couplées thermiquement. Par conséquent, une température trop élevée d'une cellule peut influencer les cellules voisines. Ce couplage est représenté schématiquement dans la Figure 1-7. Comme le montre cette figure, la deuxième cellule a un problème et sa température a augmenté. En raison du couplage, la température de l'anode de la troisième cellule et la température de la cathode de la première cellule augmentent. Ainsi, un gradient de température entre l'anode et la cathode apparaît pour les première et troisième cellules. Comme l'eau produite est évacuée du côté froid, des gouttes d'eau sont produites dans les endroits où la température est moins élevée [20], [28]. Par conséquent, les gouttes d'eau apparaissent sur le côté anode de la cellule précédente (la première cellule) et sur le côté cathode de la cellule suivante (la troisième cellule). Dans ces conditions, le manque d'hydrogène et le manque d'oxygène sont possibles pour la cellule précédente et la cellule suivante respectivement. Une fois que la température de la cellule voisine a augmenté en raison d'un manque de gaz, ces cellules elles-mêmes peuvent propager ce problème à leurs cellules voisines. Par conséquent, une cellule défectueuse peut influencer l'ensemble de la pile et un système de gestion de pile à combustible peut faire face à de tels défauts et, dans le cas le plus extrême, il peut séparer électriquement les cellules qui ne fonctionneraient plus pour assurer la continuité de la production d'énergie, en mode dégradé.

Durabilité

La durabilité de la pile à combustible pourrait être améliorée par un système de gestion individuelle des cellules ou groupes de cellules. L'instabilité des cellules doit d'abord être détectée par un outil de diagnostic. Il existe deux méthodes fondamentales de diagnostic: basé sur un modèle et non basé sur un modèle.

De nombreux phénomènes se produisent dans une cellule de pile à combustible, mais en raison de leurs corrélations, il est difficile de décrire qualitativement l'observation expérimentale sans utiliser de modèle. Les modèles physiques décrivant les phénomènes de transferts dans les piles à combustible peuvent être très utiles pour les études du vieillissement [17]. Une méthode basée sur un modèle prend en compte les phénomènes réels de vieillissement physique sur la base d'un modèle empirique ou physique. Une méthode basée sur un modèle permet de prévoir le vieillissement. De plus, cette méthode peut fournir des informations sur la dégradation des paramètres physiques internes pendant le fonctionnement [39]. Un modèle mathématique peut fournir la perception de l'interconnexion entre les paramètres électrochimiques et surtout les différents mécanismes du vieillissement. De plus, un modèle permet d'établir des règles de contrôle entraînant une durée de vie plus longue. Un modèle, qui prend en compte tous les phénomènes de dégradation et analyse leur impact global sur la durabilité de la pile à combustible, n'existe pas encore dans la littérature [17].

Dans cette thèse, un modèle de transferts est proposé. Ce modèle décrit le couplage entre les transferts de matière de chaleur et de charge en régime transitoire. Il est paramétré par un certain nombre de paramètres qui se veulent intrinsèques aux matériaux et à leur mise en forme. Ce

modèle doit fonctionner en parallèle avec le système réel. Par conséquent, ce modèle doit être simple et pouvoir être résolu en temps réel. Pour ces raisons, un modèle transitoire unidimensionnel est proposé dans cette thèse. Ce modèle est présenté dans le deuxième chapitre. Avec ce modèle, il est possible de détecter les défauts apparus dans les cellules d'une pile. Cependant, une topologie d'électronique de puissance est nécessaire pour gérer les cellules et alimenter la charge. Cette topologie doit permettre de gérer des cellules ou petits groupes de cellules de façon indépendante.

On peut considérer les systèmes multi-stacks comme une tentative d'augmenter la durée de vie au prix d'une perte de compacité. Quatre topologies de base sont utilisées pour les systèmes multi-stacks ou stacks segmentés : série, parallèle, cascade, série parallèle [3], [69], [70]. La topologie série nécessite un convertisseur basse tension. Dans une telle connexion, la défaillance d'une seule cellule entraîne la perte de l'ensemble du système. De plus, il n'y a pas de degré de liberté dans le contrôle séparé des cellules. La deuxième topologie, pour laquelle les cellules ou les piles sont connectées directement au bus DC par des convertisseurs indépendants, possède un degré de liberté pour contrôler les cellules [71]. Cette topologie nécessite un convertisseur à haut coefficient de conversion pour augmenter la tension de sortie, ce qui augmente les tensions sur les dispositifs semi-conducteurs. Cette architecture est la plus chère topologie en raison d'une grande exigence des composants de stockage passif de l'énergie. La topologie en cascade résout le problème de la topologie parallèle. Dans cette topologie, la tension du bus DC est répartie entre les cellules. Il en résulte une diminution de la tension sur les dispositifs semi-conducteurs. La topologie série-parallèle est la même que la topologie parallèle, sauf que plus de cellules sont connectées à chaque convertisseur. Cette topologie a les avantages et les inconvénients des topologies en série et parallèle. Dans une telle topologie, des convertisseurs avec un ratio de tension plus faible peuvent être utilisés. Compte tenu de la capacité de contrôler séparément les cellules ou les piles, la topologie en cascade peut être utilisée pour gérer les cellules. Cependant, il est difficile de connecter les cellules au bus DC tout en maintenant la contrôlabilité des convertisseurs.

Dans cette thèse, les conditions de fonctionnement sont contrôlées de telle sorte que les instabilités électrochimiques peuvent être évitées pour améliorer la durée de vie d'une pile. Le modèle proposé permet de détecter les différentes instabilités qui se produisent dans les cellules d'une pile. Toutefois, une structure est nécessaire pour modifier les conditions d'exploitation en fonction des données du modèle. La production d'eau à l'intérieur d'une cellule peut être contrôlée par son courant. Par conséquent, cette structure devrait être capable de modifier le courant d'un groupe de cellules en fonction des données du modèle. Par conséquent, cette structure se compose de deux parties de base : Architecture électronique et système de gestion. Les décisions sont prises par le système de gestion sur la base des données du modèle. La structure électronique exécute les décisions qui sont prises par le système de gestion.

Pour gérer les cellules séparément et en raison de la basse tension d'une cellule ou d'un petit nombre de cellules, des convertisseurs à haut ratio d'élévation comme les convertisseurs isolés peuvent être utilisés mais leur rendement est le plus grand défi [10]–[12]. Dans cette thèse, des convertisseurs DC-DC boost classiques sont utilisés tandis que leurs condensateurs de sortie sont connectés en série (topologie en cascade). L'utilisation de convertisseurs entrelacés multi-bras assurent la fiabilité ainsi que la diminution de l'ondulation du courant. Cette approche permet d'augmenter le degré de liberté dans la gestion et le contrôle des PEMFC. L'inconvénient de cette connexion série est la probabilité de perte de contrôlabilité. Dans une telle connexion, le même courant de charge traverse tous les condensateurs. Par conséquent, si la puissance d'entrée d'une cellule devient inférieure à la quantité requise, la tension du condensateur correspondant diminuera. Dans ce cas, la contrôlabilité sera perdue si la tension de sortie

devient inférieure à la tension d'entrée. Dans ce cas-là, un système d'équilibrage est requis pour assurer la contrôlabilité. Un nouveau système d'équilibrage est proposé dans cette thèse.

Une hybridation conventionnelle de la pile à combustible avec un pack de supercondensateurs est utilisée dans cette thèse pour assurer la fonction filtrage de puissance lorsque la PAC alimente des charges possédant des dynamiques de variations élevées. Un convertisseur DC-DC bidirectionnel en courant est utilisé comme convertisseur d'interface entre le pack de supercondensateurs et le bus DC. Pour simplifier la gestion d'énergie du système, une méthode fréquentielle utilisant un filtre passe-bas est utilisée pour partager la puissance demandée par la charge entre la PAC et le supercondensateur.

L'objectif principal de cette thèse est de proposer un système de gestion de pile à combustible afin d'améliorer sa durabilité. Comme expliqué dans cette introduction, le système proposé se compose de trois parties fondamentales. Le premier chapitre est axé sur la problématique et la bibliographie.

Le modèle proposé est bien expliqué dans le deuxième chapitre. La structure du système électronique de puissance est présentée dans le troisième chapitre et le quatrième chapitre concerne le système de gestion. Le système proposé examiné dans la thèse est illustré à la Figure 1-13.

Bibliography

- [1] M. Zandi *et al.*, “Evaluation and comparison of economic policies to increase distributed generation capacity in the Iranian household consumption sector using photovoltaic systems and RETScreen software,” *Renew. energy*, vol. 107, pp. 215–222, 2017.
- [2] M. Bahrami *et al.*, “Hybrid maximum power point tracking algorithm with improved dynamic performance,” *Renew. Energy*, vol. 130, pp. 982–991, 2019, doi: 10.1016/j.renene.2018.07.020.
- [3] N. Marx, L. Boulon, F. Gustin, D. Hissel, and K. Agbossou, “A review of multi-stack and modular fuel cell systems : Interests , application areas and on-going research activities,” *Int. J. Hydrogen Energy*, vol. 39, no. 23, pp. 12101–12111, 2014, doi: 10.1016/j.ijhydene.2014.05.187.
- [4] T. Yoshida and K. Kojima, “Toyota MIRAI Fuel Cell Vehicle and Progress Toward a Future Hydrogen Society,” *Interface Mag.*, vol. 24, no. 2, pp. 45–49, 2015, doi: 10.1149/2.F03152if.
- [5] Y. Wang, K. S. Chen, J. Mishler, S. C. Cho, and X. C. Adroher, “A review of polymer electrolyte membrane fuel cells: technology, applications, and needs on fundamental research,” *Appl. Energy*, vol. 88, pp. 981–1007, 2011, doi: 10.1016/j.apenergy.2010.09.030.
- [6] M. Matsunaga, T. Fukushima, and K. Ojima, “Powertrain system of Honda FCX Clarity fuel cell vehicle,” *World Electr. Veh. J.*, vol. 3, no. 1, pp. 820–829, 2009, doi: May 13-16.
- [7] J. Wang, “System integration, durability and reliability of fuel cells: Challenges and solutions,” *Appl. Energy*, vol. 189, pp. 460–479, 2017, doi: 10.1016/j.apenergy.2016.12.083.
- [8] H. Zhang, X. Li, X. Liu, and J. Yan, “Enhancing fuel cell durability for fuel cell plug-in hybrid electric vehicles through strategic power management,” *Appl. Energy*, vol. 241, no. February, pp. 483–490, 2019, doi: 10.1016/j.apenergy.2019.02.040.
- [9] G. Maranzana, S. Didierjean, J. Dillet, A. Thomas, and O. Lottin, “IMPROVED FUEL CELL. Patent n° : WO/2014/060198.,” 2014.
- [10] T. Arunkumari and V. Indragandhi, “An overview of high voltage conversion ratio DC-DC converter configurations used in DC micro-grid architectures,” *Renew. Sustain. Energy Rev.*, vol. 77, no. March, pp. 670–687, 2017, doi: 10.1016/j.rser.2017.04.036.
- [11] Q. Wu, S. Member, Q. Wang, and J. Xu, “A High Efficiency Step-Up Current-Fed Push-Pull Quasi-Resonant Converter with Fewer Components for Fuel Cell Application,” *IEEE Trans. Ind. Electron.*, vol. 0046, no. c, 2016, doi: 10.1109/TIE.2016.2638800.
- [12] S. Saravanan and N. Ramesh Babu, “Analysis and implementation of high step-up DC-DC converter for PV based grid application,” *Appl. Energy*, vol. 190, pp. 64–72, 2017, doi: 10.1016/j.apenergy.2016.12.094.
- [13] E. Laffly, M. Pera, and D. Hissel, “PEM fuel cell modeling with static-dynamic decomposition and voltage rebuilding,” *2008 IEEE Int. Symp. Ind. Electron.*, pp. 1519–

1524, 2008.

- [14] L. Xu, “Modeling and Simulation of PEM Fuel Cells Based on Electrochemical model,” no. 5, pp. 471–474, 2011.
- [15] C. Qin, J. Wang, D. Yang, B. Li, and C. Zhang, “Proton exchange membrane fuel cell reversal: a review,” *Catalysts*, vol. 6, no. 12, p. 197, 2016, doi: 10.3390/catal6120197.
- [16] J. Wu *et al.*, “A review of PEM fuel cell durability: Degradation mechanisms and mitigation strategies,” vol. 184, pp. 104–119, 2008, doi: 10.1016/j.jpowsour.2008.06.006.
- [17] E. Breaz, F. Gao, A. Miraoui, and R. Tirnovan, “A Short review Of Aging Mechanism Modeling Of Proton Exchange Membrane Fuel Cell In Transportation Applications,” *Ind. Electron. Soc. IECON 2014-40th Annu. Conf. IEEE*, pp. 3941--3947, 2014.
- [18] L. Zhang, M. Pan, and S. Quan, “Model predictive control of water management in PEMFC,” *J. Power Sources*, vol. 180, no. 1, pp. 322–329, 2008, doi: 10.1016/j.jpowsour.2008.01.088.
- [19] A. Thomas *et al.*, “Measurements of Electrode Temperatures , Heat and Water Fluxes in PEMFCs : Conclusions about Transfer Mechanisms service Measurements of Electrode Temperatures , Heat and Water Fluxes in PEMFCs: Conclusions about Transfer Mechanisms,” *J. Electrochem. Soc.*, vol. 160, no. 2, pp. 191–204, 2013, doi: 10.1149/2.006303jes.
- [20] A. Thomas, G. Maranzana, S. Didierjean, J. Dillet, and O. Lottin, “Thermal and water transfer in PEMFCs : Investigating the role of the microporous layer,” *Int. J. Hydrogen Energy*, vol. 39, no. 6, pp. 2649–2658, 2014, doi: 10.1016/j.ijhydene.2013.11.105.
- [21] S. Abbou, J. Dillet, G. Maranzana, S. Didierjean, and O. Lottin, “Local potential evolutions during proton exchange membrane fuel cell operation with dead-ended anode e Part I : Impact of water diffusion and nitrogen crossover,” *J. Power Sources*, vol. 340, pp. 337–346, 2017, doi: 10.1016/j.jpowsour.2016.11.079.
- [22] S. Abbou, J. Dillet, G. Maranzana, S. Didierjean, and O. Lottin, “Local potential evolutions during proton exchange membrane fuel cell operation with dead-ended anode e Part II : Aging mitigation strategies based on water management and nitrogen crossover,” *J. Power Sources*, vol. 340, pp. 419–427, 2017, doi: 10.1016/j.jpowsour.2016.10.045.
- [23] J. Dillet, D. Spornjak, A. Lamibrac, G. Maranzana, R. Mukundan, and J. Fairweather, “Impact of fl ow rates and electrode speci fi cations on degradations during repeated startups and shutdowns in polymer-electrolyte membrane fuel cells,” *J. Power Sources*, vol. 250, pp. 68–79, 2014, doi: 10.1016/j.jpowsour.2013.10.141.
- [24] J. Durst *et al.*, “Degradation heterogeneities induced by repetitive start / stop events in proton exchange membrane fuel cell : Inlet vs . outlet and channel vs . land,” *Applied Catal. B, Environ.*, vol. 138–139, pp. 416–426, 2013, doi: 10.1016/j.apcatb.2013.03.021.
- [25] A. Lamibrac *et al.*, “Experimental characterization of internal currents during the start-up of a proton exchange membrane fuel cell,” *J. Power Sources*, vol. 196, no. 22, pp. 9451–9458, 2011, doi: 10.1016/j.jpowsour.2011.07.013.
- [26] C. M. Rangel, R. A. Silva, M. A. Travassos, T. I. Paiva, and V. R. Fernandes, “Fuel Starvation : Irreversible Degradation Mechanisms in PEM Fuel Cells Fuel Starvation : Irreversible Degradation Mechanisms in PEM Fuel Cells,” *WHEC-World Hydrog. Energy Conv. Ess. Ger. May 2010*, 2010.

- [27] M. Jouin, R. Gouriveau, D. Hissel, and N. Zerhouni, “Degradations analysis and aging modeling for health assessment and prognostics of PEMFC,” *Reliab. Eng. Syst. Saf.*, vol. 148, pp. 78–95, 2016.
- [28] A. Thomas, “Water and heat transfers in a membrane fuel cell: experimental demonstration of coupling and analysis of mechanisms,” 2012.
- [29] Z. Zheng *et al.*, “A review on non-model based diagnosis methodologies for PEM fuel cell stacks and systems,” *Int. J. Hydrogen Energy*, vol. 38, no. 21, pp. 8914–8926, 2013, doi: 10.1016/j.ijhydene.2013.04.007.
- [30] J. Kim, I. Lee, Y. Tak, and B. H. Cho, “State-of-health diagnosis based on hamming neural network using output voltage pattern recognition for a PEM fuel cell,” *Int. J. Hydrogen Energy*, vol. 37, no. 5, pp. 4280–4289, 2011, doi: 10.1016/j.ijhydene.2011.11.092.
- [31] D. Hissel, S. Member, D. Candusso, and F. Harel, “Fuzzy-Clustering Durability Diagnosis of Polymer Electrolyte Fuel Cells Dedicated to Transportation Applications,” *IEEE Trans. Veh. Technol.*, vol. 56, no. 5, pp. 2414–2420, 2007.
- [32] S. Becker and V. Karri, “Predictive models for PEM-electrolyzer performance using adaptive neuro-fuzzy inference systems,” *Int. J. Hydrogen Energy*, vol. 35, no. 18, pp. 9963–9972, 2010, doi: 10.1016/j.ijhydene.2009.11.060.
- [33] J. Hua, J. Li, M. Ouyang, L. Lu, and L. Xu, “Proton exchange membrane fuel cell system diagnosis based on the multivariate statistical method,” *Int. J. Hydrogen Energy*, vol. 36, no. 16, pp. 9896–9905, 2011, doi: 10.1016/j.ijhydene.2011.05.075.
- [34] L. A. M. Riascos, M. G. Simoes, and P. E. Miyagi, “On-line fault diagnostic system for proton exchange membrane fuel cells,” *J. Power Sources*, vol. 175, no. 1, pp. 419–429, 2008, doi: 10.1016/j.jpowsour.2007.09.010.
- [35] J. Chen and B. Zhou, “Diagnosis of PEM fuel cell stack dynamic behaviors,” *J. Power Sources*, vol. 177, no. 1, pp. 83–95, 2008, doi: 10.1016/j.jpowsour.2007.11.038.
- [36] K. Polat and S. Gu, “Automatic determination of diseases related to lymph system from lymphography data using principles component analysis (PCA), fuzzy weighting pre-processing and ANFIS,” *Expert Syst. Appl.*, vol. 33, no. 1, pp. 636–641, 2007, doi: 10.1016/j.eswa.2006.06.004.
- [37] N. Y. Steiner, D. Hissel, P. Mocoteguy, and D. Candusso, “Non intrusive diagnosis of polymer electrolyte fuel cells by wavelet packet transform,” *Int. J. Hydrogen Energy*, vol. 6, no. 1, pp. 740–746, 2010, doi: 10.1016/j.ijhydene.2010.10.033.
- [38] F. Akbaryan and P. R. Bishnoi, “Fault diagnosis of multivariate systems using pattern recognition and multisensor data analysis technique,” *Comput. Chem. Eng.*, vol. 25, no. 9–10, pp. 1313–1339, 2001.
- [39] D. Zhou *et al.*, “Degradation Prediction of PEM Fuel Cell Stack Based on Multiphysical Aging Model With Particle Filter Approach,” *IEEE Trans. Ind. Appl.*, vol. 53, no. 4, pp. 4041–4052, 2016.
- [40] M. Andersson, S. B. Beale, M. Espinoza, Z. Wu, and W. Lehnert, “A review of cell-scale multiphase flow modeling , including water management , in polymer electrolyte fuel cells,” *Appl. Energy*, vol. 180, pp. 757–778, 2016, doi: 10.1016/j.apenergy.2016.08.010.
- [41] C. Alegre, L. Alvarez-manuel, R. Mustata, L. Vali, and A. Lozano, “Assessment of the durability of low-cost Al bipolar plates for High Temperature PEM fuel cells,” *Int. J.*

- Hydrogen Energy*, vol. 44, no. 25, pp. 12748–12759, 2019, doi: 10.1016/j.ijhydene.2018.07.070.
- [42] G. Zhang and K. Jiao, “Multi-phase models for water and thermal management of proton exchange membrane fuel cell : A review,” *J. Power Sources*, vol. 391, no. February, pp. 120–133, 2018, doi: 10.1016/j.jpowsour.2018.04.071.
- [43] F. J. Asensio, J. I. S. Martín, I. Zamora, G. Saldaña, and O. Oñederra, “Analysis of electrochemical and thermal models and modeling techniques for polymer electrolyte membrane fuel cells,” *Renew. Sustain. Energy Rev.*, vol. 113, no. July, p. 109283, 2019, doi: 10.1016/j.rser.2019.109283.
- [44] Y. Qi, M. Espinoza-andaluz, M. Thern, and M. Andersson, “Polymer electrolyte fuel cell system level modelling and simulation of transient behavior,” *eTransportation*, vol. 2, p. 100030, 2019, doi: 10.1016/j.etrans.2019.100030.
- [45] R. Petrone *et al.*, “A review on model-based diagnosis methodologies for PEMFCs,” *Int. J. Hydrogen Energy*, vol. 38, no. 17, pp. 7077–7091, 2013, doi: 10.1016/j.ijhydene.2013.03.106.
- [46] Y. Li *et al.*, “Characteristic analysis in lowering current density based on pressure drop for avoiding flooding in proton exchange membrane fuel cell,” *Appl. Energy*, vol. 248, no. March, pp. 321–329, 2019, doi: 10.1016/j.apenergy.2019.04.140.
- [47] Y. Li, P. Pei, Z. Wu, P. Ren, X. Jia, and D. Chen, “Approaches to avoid flooding in association with pressure drop in proton exchange membrane fuel cells,” *Appl. Energy*, vol. 224, no. April, pp. 42–51, 2018, doi: 10.1016/j.apenergy.2018.04.071.
- [48] X. Xue, J. Tang, A. Smirnova, R. England, and N. Sammes, “System level lumped-parameter dynamic modeling of PEM fuel cell,” *J. Power Sources*, vol. 133, no. 2, pp. 188–204, 2004, doi: 10.1016/j.jpowsour.2003.12.064.
- [49] M. Whiteley, S. Dunnett, and L. Jackson, “Simulation of polymer electrolyte membrane fuel cell degradation using an integrated Petri Net and 0D model,” *Reliab. Eng. Syst. Saf.*, vol. 196, no. October 2019, p. 106741, 2020, doi: 10.1016/j.res.2019.106741.
- [50] K. Sankar and A. K. Jana, “Nonlinear multivariable sliding mode control of a reversible PEM fuel cell integrated system,” *Energy Convers. Manag.*, vol. 171, no. February, pp. 541–565, 2018, doi: 10.1016/j.enconman.2018.05.079.
- [51] K. Sankar, K. Aguan, and A. K. Jana, “A proton exchange membrane fuel cell with an air flow cooling system : Dynamics , validation and nonlinear control,” *Energy Convers. Manag.*, vol. 183, no. July 2018, pp. 230–240, 2019, doi: 10.1016/j.enconman.2018.12.072.
- [52] Y. Mu, P. He, J. Ding, and W. Tao, “Modeling of the operation conditions on the gas purging performance of polymer electrolyte membrane fuel cells,” *Int. J. Hydrogen Energy*, vol. 42, no. 16, pp. 11788–11802, 2017, doi: 10.1016/j.ijhydene.2017.02.108.
- [53] J. Chen, L. Huang, C. Yan, and Z. Liu, “A dynamic scalable segmented model of PEM fuel cell systems with two-phase water flow,” *Math. Comput. Simul.*, vol. 167, pp. 48–64, 2020, doi: 10.1016/j.matcom.2018.05.006.
- [54] M. W. Fowler, R. F. Mann, J. C. Amphlett, B. A. Peppley, and P. R. Roberge, “Incorporation of voltage degradation into a generalised steady state electrochemical model for a PEM fuel cell,” *J. Power Sources*, vol. 106, no. 1–2, pp. 274–283, 2002.
- [55] M. Bressel, M. Hilairet, D. Hissel, and B. O. Bouamama, “Fuel Cells Remaining Useful

Life estimation using an Extended Kalman Filter.”

- [56] M. Bressel, M. Hilairet, D. Hissel, and S. Member, “Remaining Useful Life Prediction and Uncertainty Quantification of Proton Exchange Membrane Fuel Cell Under Variable Load,” vol. 63, no. 4, pp. 2569–2577, 2016.
- [57] G. Tian, I. Endichi, D. Candusso, F. Harel, D. Hissel, and J. Kauffmann, “Diagnosis methods dedicated to the localisation of failed cells within PEMFC stacks,” vol. 182, pp. 449–461, 2008, doi: 10.1016/j.jpowsour.2007.12.038.
- [58] G. Tian, S. Wasterlain, D. Candusso, F. Harel, D. Hissel, and X. François, “Identification of failed cells inside PEMFC stacks in two cases : Anode / cathode crossover and anode / cooling compartment leak,” *Int. J. Hydrogen Energy*, vol. 35, no. 7, pp. 2772–2776, 2010, doi: 10.1016/j.ijhydene.2009.05.015.
- [59] A. Narjiss, D. Depernet, D. Candusso, F. Gustin, and D. Hissel, “Online Diagnosis of PEM Fuel Cell,” *13th Int. Power Electron. Motion Control Conf.*, pp. 734–739, 2008.
- [60] M. Jouin, R. Gouriveau, D. Hissel, C. Marie, and A. Savary, “PEMFC aging modeling for prognostics and health assessment,” *IFAC-PapersOnLine*, vol. 48, no. 21, pp. 790–795, 2015.
- [61] P. Ren, P. Pei, Y. Li, Z. Wu, D. Chen, and S. Huang, “Diagnosis of water failures in proton exchange membrane fuel cell with zero-phase ohmic resistance and fixed-low-frequency impedance,” *Appl. Energy*, vol. 239, no. November 2018, pp. 785–792, 2019, doi: 10.1016/j.apenergy.2019.01.235.
- [62] S. Rodat, S. Sailler, F. Druart, P.-X. Thivel, Y. Bultel, and P. Ozil, “EIS measurements in the diagnosis of the environment within a PEMFC stack,” *J. Appl. Electrochem.*, vol. 40, no. 5, pp. 911–920, 2010, doi: 10.1007/s10800-009-9969-0.
- [63] S. M. R. Niya, R. Niya, R. K. Phillips, and M. Hoorfar, “Process modeling of the impedance characteristics of proton exchange membrane fuel cells,” *Electrochim. Acta*, vol. 191, pp. 594–605, 2016, doi: 10.1016/j.electacta.2016.01.128.
- [64] I. Pivac, B. Simic, and F. Barbir, “Experimental diagnostics and modeling of inductive phenomena at low frequencies in impedance spectra of proton exchange membrane fuel cells,” *J. Power Sources*, vol. 365, pp. 240–248, 2017, doi: 10.1016/j.jpowsour.2017.08.087.
- [65] W. Merida, D. A. Harrington, J. M. Le Canut, and G. Mclean, “Characterisation of proton exchange membrane fuel cell (PEMFC) failures via electrochemical impedance spectroscopy,” *J. Power Sources*, vol. 161, no. 1, pp. 264–274, 2006, doi: 10.1016/j.jpowsour.2006.03.067.
- [66] J.-M. Le Canut, R. Latham, W. Merida, and D. A. Harrington, “Impedance study of membrane dehydration and compression in proton exchange membrane fuel cells,” *J. Power Sources*, vol. 192, no. 2, pp. 457–466, 2009, doi: 10.1016/j.jpowsour.2009.03.027.
- [67] G. Dotelli, R. Ferrero, P. G. Stampino, S. Latorrata, and S. Toscani, “Combining Electrical and Pressure Measurements for Early Flooding Detection in a PEM Fuel Cell,” *IEEE Trans. Instrum. Meas.*, vol. 65, no. 5, pp. 1007–1014, 2015.
- [68] F. Barbir, H. Gorgun, and X. Wang, “Relationship between pressure drop and cell resistance as a diagnostic tool for PEM fuel cells,” *J. Power Sources*, vol. 141, no. 1, pp. 96–101, 2005, doi: 10.1016/j.jpowsour.2004.08.055.

- [69] D. Candusso *et al.*, “Fuel cell operation under degraded working modes and study of diode by-pass circuit dedicated to multi-stack association,” *Energy Convers. Manag.*, vol. 49, no. 4, pp. 880–895, 2008, doi: 10.1016/j.enconman.2007.10.007.
- [70] A. De Bernardinis, M.-C. Pera, J. Garnier, D. Hissel, G. Coquery, and J.-M. Kauffmann, “Fuel cells multi-stack power architectures and experimental validation of 1 kW parallel twin stack PEFC generator based on high frequency magnetic coupling dedicated to on board power unit,” *Energy Convers. Manag.*, vol. 49, no. 8, pp. 2367–2383, 2008, doi: 10.1016/j.enconman.2008.01.022.
- [71] N. Marx, D. C. T. Cardenas, L. Boulon, F. Gustin, and D. Hissel, “Degraded mode operation of multi-stack fuel cell systems,” *IET Electr. Syst. Transp.*, vol. 6, no. 1, pp. 3–11, 2016, doi: 10.1049/iet-est.2015.0012.
- [72] A. M. Imtiaz, S. Member, and F. H. Khan, “‘ Time Shared Flyback Converter ’ Based Regenerative Cell Balancing Technique for Series Connected Li-Ion Battery Strings,” *IEEE Trans. power Electron.*, vol. 28, no. 12, pp. 5960–5975, 2013.
- [73] A. Hijazi, A. Sari, X. Lin-shi, and P. Venet, “Balancing Circuit New Control for Supercapacitor Storage System Lifetime Maximization,” *IEEE Trans. Power Electron.*, vol. 32, no. 6, pp. 4939–4948, 2017.
- [74] Y. Shang, B. Xia, J. Yang, C. Zhang, N. Cui, and C. Mi, “A delta-Structured switched-Capacitor equalizer for series-Connected battery strings,” *2017 IEEE Energy Convers. Congr. Expo. ECCE 2017*, vol. 2017-Janua, no. 61633015, pp. 4493–4496, 2017, doi: 10.1109/ECCE.2017.8096771.
- [75] Y. Ye *et al.*, “Topology , Modeling , and Design of Switched-Capacitor-Based Cell Balancing Systems and Their Balancing Exploration,” *IEEE Trans. Power Electron.*, vol. 32, no. 6, pp. 4444–4454, 2017.
- [76] Y. Shang *et al.*, “A Switched-Coupling-Capacitor Equalizer for Series-Connected Battery Strings,” *IEEE Trans. Power Electron.*, vol. 32, no. 10, pp. 7694–7706, 2017.
- [77] M. Uno and A. Kukita, “PWM Converter Integrating Switched Capacitor Converter and Series-Resonant Voltage Multiplier as Equalizers for Photovoltaic Modules and Series-Connected Energy Storage Cells for Exploration Rovers,” *IEEE Trans. Power Electron.*, vol. 32, no. 11, pp. 8500–8513, 2017, doi: 10.1109/TPEL.2016.2645705.
- [78] Z. Shu, X. He, Z. Wang, D. Qiu, and Y. Jing, “Voltage balancing approaches for diode-clamped multilevel converters using auxiliary capacitor-based circuits,” *IEEE Trans. Power Electron.*, vol. 28, no. 5, pp. 2111–2124, 2013, doi: 10.1109/TPEL.2012.2215966.
- [79] X. Liu, J. Lv, C. Gao, and Z. Chen, “A Novel Diode-Clamped Modular Multilevel Converter With Simplified Capacitor Voltage-Balancing Control,” *IEEE Trans. Ind. Electron.*, vol. 64, no. 11, pp. 8843–8854, 2017.
- [80] Y. Ye and K. W. E. Cheng, “Analysis and Design of Zero-Current Switching Switched-Capacitor Cell Balancing Circuit for Series-Connected Battery/Supercapacitor,” *IEEE Trans. Veh. Technol.*, vol. 67, no. 2, pp. 948–955, 2018, doi: 10.1109/TVT.2017.2749238.
- [81] M. Uno and A. Kukita, “Single-Switch Single-Transformer Cell Voltage Equalizer Based on Forward – Flyback Resonant Inverter and Voltage Multiplier for,” *IEEE Trans. Veh. Technol.*, vol. 63, no. 9, pp. 4232–4247, 2014.
- [82] Y. Chen, X. Liu, Y. Cui, J. Zou, and S. Yang, “A MultiWinding Transformer Cell-to-

- Cell Active Equalization Method for Lithium-Ion Batteries With Reduced Number of Driving Circuits,” *IEEE Trans. Power Electron.*, vol. 31, no. 7, pp. 4916–4929, 2016.
- [83] Y. Shang, S. Member, B. Xia, S. Member, and C. Zhang, “An Automatic Equalizer Based on Forward- Flyback Converter for Series-Connected Battery Strings,” *IEEE Trans. Ind. Electron.*, vol. 64, no. 7, pp. 5380–5391, 2017, doi: 10.1109/TIE.2017.2674617.
- [84] V. Yuhimenko *et al.*, “Average Modeling and Performance Analysis of Voltage Sensorless Active Supercapacitor Balancer With Peak Current Protection,” *IEEE Trans. Power Electron.*, vol. 32, no. 2, pp. 1570–1578, 2017.
- [85] K. Lee, S. Lee, Y. Choi, and B. Kang, “Active Balancing of Li-Ion Battery Cells Using Transformer as Energy Carrier,” *IEEE Trans. Ind. Electron.*, vol. 64, no. 2, pp. 1251–1257, 2017.
- [86] Y. Lee and G. Cheng, “Quasi-Resonant Zero-Current-Switching Bidirectional Converter for Battery Equalization Applications,” *IEEE Trans. Power Electron.*, vol. 21, no. 5, pp. 1213–1224, 2006.
- [87] L. Li, Z. Huang, H. Li, and H. Lu, “A high-efficiency voltage equalization scheme for supercapacitor energy storage system in renewable generation applications,” *Sustain.*, vol. 8, no. 6, 2016, doi: 10.3390/su8060548.
- [88] M. Uno and A. Kukita, “Single-Switch Single-Magnetic PWM Converter Integrating Voltage Equalizer for Partially Shaded Photovoltaic Modules in Standalone Applications,” *IEEE Trans. Power Electron.*, vol. 33, no. 2, pp. 1259–1270, 2018, doi: 10.1109/TPEL.2017.2678526.
- [89] K. Yashiro and M. Uno, “Transformer-Less Bidirectional PWM Converter Integrating Voltage Multiplier-Based Cell Voltage Equalizer for Series-Connected Electric Double-Layer Capacitors,” *IEEE Trans. Power Electron.*, vol. 8993, no. c, 2018, doi: 10.1109/TPEL.2018.2859343.
- [90] L. Li, Z. Huang, H. Li, and J. Peng, “A rapid cell voltage balancing scheme for supercapacitor based energy storage systems for urban rail vehicles,” *Electr. Power Syst. Res.*, vol. 142, pp. 329–340, 2017, doi: 10.1016/j.epsr.2016.09.021.
- [91] Z. Zhang, S. Member, H. Gui, S. Member, D. Gu, and Y. Yang, “A Hierarchical Active Balancing Architecture for Lithium-Ion Batteries,” *IEEE Trans. Power Electron.*, vol. 32, no. 4, pp. 2757–2768, 2017.
- [92] M. Uno and A. Kukita, “String-to-Battery Voltage Equalizer Based on Half-Bridge Converter with Multi-Stacked Current Doublers for Series-Connected Batteries,” *IEEE Trans. Power Electron.*, 2018, doi: 10.1109/IPEC.2014.6869775.
- [93] T. Mizuno, T. Inoue, K. Iwasawa, and H. Koizumi, “A Voltage Equalizer Using Flyback Converter With Active Clamp,” *Circuits Syst. (APCCAS), 2012 IEEE Asia Pacific Conf.*, pp. 340–343, 2012.
- [94] T. Anno and H. Koizumi, “Double-input bidirectional DC/DC converter using cell-voltage equalizer with flyback transformer,” *IEEE Trans. Power Electron.*, vol. 30, no. 6, pp. 2923–2934, 2015, doi: 10.1109/TPEL.2014.2316201.
- [95] J. Liu, J. Yang, J. Zhang, N. Zhao, and T. Q. Zheng, “Voltage Balance Control Based on Dual Active Bridge DC/DC Converters in a Power Electronic Traction Transformer,” *IEEE Trans. Power Electron.*, vol. 33, no. 2, pp. 1–1, 2017, doi: 10.1109/TPEL.2017.2679489.

- [96] H. Kang and H. Cha, “A New Nonisolated High-Voltage-Gain Boost Converter With Inherent Output Voltage Balancing,” *IEEE Trans. Ind. Electron.*, vol. 65, no. 3, pp. 2189–2198, 2018.
- [97] N. Sulaiman, M. A. Hannan, A. Mohamed, E. H. Majlan, and W. R. Wan Daud, “A review on energy management system for fuel cell hybrid electric vehicle: Issues and challenges,” *Renew. Sustain. Energy Rev.*, vol. 52, pp. 802–814, 2015, doi: 10.1016/j.rser.2015.07.132.
- [98] N. Sulaiman, M. A. Hannan, A. Mohamed, P. J. Ker, E. H. Majlan, and W. R. Wan Daud, “Optimization of energy management system for fuel-cell hybrid electric vehicles: Issues and recommendations,” *Appl. Energy*, vol. 228, no. July, pp. 2061–2079, 2018, doi: 10.1016/j.apenergy.2018.07.087.
- [99] A. R. Miller, K. S. Hess, D. L. Barnes, and T. L. Erickson, “System design of a large fuel cell hybrid locomotive,” *J. Power Sources*, vol. 173, no. 2, pp. 935–942, 2007.
- [100] X. Lü *et al.*, “Energy management of hybrid electric vehicles : A review of energy optimization of fuel cell hybrid power system based on genetic algorithm,” *Energy Convers. Manag.*, vol. 205, no. January, p. 112474, 2020, doi: 10.1016/j.enconman.2020.112474.
- [101] H. Marzougui, A. Kadri, J. Martin, M. Amari, and S. Pierfederici, “Implementation of energy management strategy of hybrid power source for electrical vehicle,” *Energy Convers. Manag.*, vol. 195, no. May, pp. 830–843, 2019, doi: 10.1016/j.enconman.2019.05.037.
- [102] P. Thounthong and B. Davat, “Study of a multiphase interleaved step-up converter for fuel cell high power applications,” *Energy Convers. Manag.*, vol. 51, no. 4, pp. 826–832, 2010, doi: 10.1016/j.enconman.2009.11.018.
- [103] X. Lü, Y. Qu, Y. Wang, C. Qin, and G. Liu, “A comprehensive review on hybrid power system for PEMFC-HEV : Issues and strategies,” *Energy Convers. Manag.*, vol. 171, no. April, pp. 1273–1291, 2018, doi: 10.1016/j.enconman.2018.06.065.
- [104] Z. Zhang, R. Pittini, M. A. E. Andersen, and O. C. Thomsena, “A review and design of power electronics converters for fuel cell hybrid system applications,” *Energy Procedia*, vol. 20, pp. 301–310, 2012, doi: 10.1016/j.egypro.2012.03.030.
- [105] P. Pany, R. K. Singh, and R. K. Tripathi, “Active load current sharing in fuel cell and battery fed DC motor drive for electric vehicle application,” *Energy Convers. Manag.*, vol. 122, pp. 195–206, 2016, doi: 10.1016/j.enconman.2016.05.062.
- [106] N. Marx, D. Hissel, F. Gustin, L. Boulon, and K. Agbossou, “On the sizing and energy management of an hybrid multistack fuel cell e Battery system for automotive applications,” *Int. J. Hydrogen Energy*, vol. 42, no. 2, pp. 1518–1526, 2016, doi: 10.1016/j.ijhydene.2016.06.111.
- [107] X. Lü, P. Wang, L. Meng, and C. Chen, “Energy optimization of logistics transport vehicle driven by fuel cell hybrid power system,” *Energy Convers. Manag.*, vol. 199, no. July, p. 111887, 2019, doi: 10.1016/j.enconman.2019.111887.
- [108] H. Fathabadi, “Fuel cell hybrid electric vehicle (FCHEV): Novel fuel cell / SC hybrid power generation system,” *Energy Convers. Manag.*, vol. 156, no. May 2017, pp. 192–201, 2018, doi: 10.1016/j.enconman.2017.11.001.
- [109] T. Li, H. Liu, and D. Ding, “Predictive energy management of fuel cell supercapacitor hybrid construction equipment,” *Energy*, vol. 149, pp. 718–729, 2018, doi:

- 10.1016/j.energy.2018.02.101.
- [110] D. Zhou, A. Al-durra, F. Gao, A. Ravey, I. Matraji, and M. Godoy, “Online energy management strategy of fuel cell hybrid electric vehicles based on data fusion approach,” *J. Power Sources*, vol. 366, pp. 278–291, 2017, doi: 10.1016/j.jpowsour.2017.08.107.
- [111] F. Odeim, J. Roes, and A. Heinzl, “Power Management Optimization of a Fuel Cell/Battery/Supercapacitor Hybrid System for Transit Bus Applications,” *IEEE Trans. Veh. Technol.*, vol. 65, no. 7, pp. 5783–5788, 2015.
- [112] Q. Li, H. Yang, Y. Han, M. Li, and W. Chen, “A state machine strategy based on droop control for an energy management system of PEMFC-battery- supercapacitor hybrid tramway,” *Int. J. Hydrogen Energy*, vol. 41, no. 36, pp. 16148–16159, 2016, doi: 10.1016/j.ijhydene.2016.04.254.
- [113] N. Bizon *et al.*, “Hydrogen economy of the fuel cell hybrid power system optimized by air flow control to mitigate the effect of the uncertainty about available renewable power and load dynamics,” *Energy Convers. Manag.*, vol. 179, no. October 2018, pp. 152–165, 2019, doi: 10.1016/j.enconman.2018.10.058.
- [114] N. Bizon and I. Cristian, “Hydrogen saving through optimized control of both fueling flows of the Fuel Cell Hybrid Power System under a variable load demand and an unknown renewable power profile,” *Energy Convers. Manag.*, vol. 184, no. January, pp. 1–14, 2019, doi: 10.1016/j.enconman.2019.01.024.
- [115] S. Ahmadi, S. M. T. Bathaee, and A. H. Hosseinpour, “Improving fuel economy and performance of a fuel-cell hybrid electric vehicle (fuel-cell , battery , and ultra-capacitor) using optimized energy management strategy,” *Energy Convers. Manag.*, vol. 160, no. December 2017, pp. 74–84, 2018, doi: 10.1016/j.enconman.2018.01.020.
- [116] G. Maranzana, O. Lottin, T. Colinart, S. Chupin, and S. Didierjean, “A multi-instrumented polymer exchange membrane fuel cell : Observation of the in-plane non-homogeneities,” *J. Power Sources*, vol. 180, no. 2, pp. 748–754, 2008, doi: 10.1016/j.jpowsour.2008.03.002.
- [117] T. Gaumont, G. Maranzana, O. Lottin, J. Dillet, L. Guetaz, and J. Pauchet, “In Operando and Local Estimation of the Effective Humidity of PEMFC Electrodes and Membranes,” *J. Electrochem. Soc.*, vol. 164, no. 14, pp. 1535–1542, 2017, doi: 10.1149/2.0161714jes.
- [118] S. Abbou, J. Dillet, D. Spornjak, R. Mukundan, R. L. Borup, and G. Maranzana, “High Potential Excursions during PEM Fuel Cell Operation with Dead-Ended Anode,” *J. Electrochem. Soc.*, vol. 162, no. 10, pp. 1212–1220, 2015, doi: 10.1149/2.0511510jes.
- [119] G. Maranzana, A. Lamibrac, J. Dillet, S. Abbou, S. Didierjean, and O. Lottin, “Startup (and shutdown) model for polymer electrolyte membrane fuel cells,” *J. Electrochem. Soc.*, vol. 162, no. 7, pp. F694–F706, 2015, doi: 10.1149/2.0451507jes.
- [120] L. Dubau *et al.*, “Carbon corrosion induced by membrane failure : The weak link of PEMFC long-term performance er o,” *Int. J. Hydrogen Energy*, vol. 39, no. 36, pp. 21902–21914, 2014, doi: 10.1016/j.ijhydene.2014.07.099.
- [121] J. Durst *et al.*, “Degradation heterogeneities induced by repetitive start/stop events in proton exchange membrane fuel cell: Inlet vs. outlet and channel vs. land,” *Applied Catal. B, Environ.*, vol. 138, pp. 416–426, 2013, doi: 10.1016/j.apcatb.2013.03.021.
- [122] T. Gaumont *et al.*, “Measurement of protonic resistance of catalyst layers as a tool for degradation monitoring,” *Int. J. Hydrogen Energy*, vol. 42, no. 3, pp. 1800–1812, 2017, doi: 10.1016/j.ijhydene.2016.10.035.

- [123] S. K. Babu *et al.*, “Spatially resolved degradation during startup and shutdown in polymer electrolyte membrane fuel cell operation,” *Appl. Energy*, vol. 254, no. August, p. 113659, 2019, doi: 10.1016/j.apenergy.2019.113659.
- [124] R. Mustata, L. Valino, F. Barreras, M. I. Gil, and A. Lozano, “Study of the distribution of air flow in a proton exchange membrane fuel cell stack,” *J. Power Sources*, vol. 192, no. 1, pp. 185–189, 2009, doi: 10.1016/j.jpowsour.2008.12.083.
- [125] J. Koh, H. Seo, C. G. Lee, Y. Yoo, and H. C. Lim, “Pressure and flow distribution in internal gas manifolds of a fuel-cell stack,” *J. Power Sources*, vol. 115, no. 1, pp. 54–65, 2003.
- [126] C. Chen, S. Jung, and S. Yen, “Flow distribution in the manifold of PEM fuel cell stack,” *J. Power Sources*, vol. 173, no. 1, pp. 249–263, 2007, doi: 10.1016/j.jpowsour.2007.05.007.
- [127] A. Datta and A. Majumdar, “A calculation procedure for two phase flow distribution in manifolds with and without heat transfer,” *Int. J. Heat Mass Transf.*, vol. 26, no. 9, pp. 1321–1328, 1983, doi: 10.1016/S0017-9310(83)80063-5.
- [128] S. Basu, J. Li, and C. Wang, “Two-phase flow and maldistribution in gas channels of a polymer electrolyte fuel cell,” *J. Power Sources*, vol. 187, no. 2, pp. 431–443, 2009, doi: 10.1016/j.jpowsour.2008.11.039.
- [129] L. Zhang, W. Du, H. T. Bi, D. P. Wilkinson, J. Stumper, and H. Wang, “Gas – liquid two-phase flow distributions in parallel channels for fuel cells,” *J. Power Sources*, vol. 189, no. 2, pp. 1023–1031, 2009, doi: 10.1016/j.jpowsour.2009.01.010.
- [130] Y. Ding, “Numerical Simulations of Gas-Liquid Two-Phase Flow in Polymer Electrolyte Membrane Fuel Cells,” 2012.
- [131] J. Park and X. Li, “Effect of flow and temperature distribution on the performance of a PEM fuel cell stack,” *J. Power Sources*, vol. 162, no. 1, pp. 444–459, 2006, doi: 10.1016/j.jpowsour.2006.07.030.
- [132] V. Oeuriot, J. Dillet, G. Maranzana, O. Lottin, and S. Didierjean, “An ex-situ experiment to study the two-phase flow induced by water condensation into the channels of proton exchange membrane fuel cells (PEMFC) er o,” *Int. J. Hydrogen Energy*, vol. 40, no. 22, pp. 7192–7203, 2015, doi: 10.1016/j.ijhydene.2015.04.008.
- [133] J. Dillet, O. Lottin, G. Maranzana, S. Didierjean, D. Conneau, and C. Bonnet, “Direct observation of the two-phase flow in the air channel of a proton exchange membrane fuel cell and of the effects of a clogging / unclogging sequence on the current density distribution,” *J. Power Sources*, vol. 195, no. 9, pp. 2795–2799, 2010, doi: 10.1016/j.jpowsour.2009.10.103.
- [134] R. Anderson, L. Zhang, Y. Ding, M. Blanco, X. Bi, and D. P. Wilkinson, “A critical review of two-phase flow in gas flow channels of proton exchange membrane fuel cells,” *J. Power Sources*, vol. 195, no. 15, pp. 4531–4553, 2010, doi: 10.1016/j.jpowsour.2009.12.123.
- [135] M. Mortazavi and K. Tajiri, “Two-phase flow pressure drop in flow channels of proton exchange membrane fuel cells : Review of experimental approaches,” *Renew. Sustain. Energy Rev.*, vol. 45, pp. 296–317, 2015, doi: 10.1016/j.rser.2015.01.044.
- [136] M. Bahrami *et al.*, “Design and modeling of an equalizer for fuel cell energy management systems,” *IEEE Trans. Power Electron.*, p. 1, 2019, doi: 10.1109/TPEL.2019.2899150.

- [137] F. A. L. Dullien, *Porous media: fluid transport and pore structure*. Academic press, 2012.
- [138] S. Chupin, “Local behaviour and electrical performance of a membrane fuel cell: towards a diagnostic tool,” 2009.
- [139] T. Colinard, “Water management and electrical performance of a fuel cell: from the pores of the membrane to the cell,” 2008.
- [140] C. R. Wilke, “A viscosity equation for gas mixtures,” *J. Chem. Phys.*, vol. 18, no. 4, pp. 517–519, 1950.
- [141] R. C. Sellin, K. Mozet, J. Dillet, S. Didierjean, and G. Maranzana, “Measuring electro-osmotic drag coefficients in PFSA membranes without any diffusion assumption,” *Int. J. Hydrogen Energy*, vol. 44, no. 45, pp. 24905–24912, 2019, doi: 10.1016/j.ijhydene.2019.07.076.
- [142] M. Phattanasak, J. Martin, S. Pierfederici, and B. Davat, “Predicting the onset of bifurcation and stability study of a hybrid current controller for a boost converter,” *Math. Comput. Simul.*, vol. 91, pp. 262–273, 2013, doi: 10.1016/j.matcom.2013.03.009.
- [143] R. Gavagsaz-ghoachani *et al.*, “Estimation of the bifurcation point of a modulated-hysteresis current-controlled DC--DC boost converter: stability analysis and experimental verification,” *IET Power Electron.*, vol. 8, no. 11, pp. 2195–2203, 2015, doi: 10.1049/iet-pel.2015.0078.
- [144] L. Saublet, R. Gavagsaz-ghoachani, J. Martin, B. Nahid-mobarakeh, S. Member, and S. Pierfederici, “Bifurcation Analysis and Stabilization of DC Power Systems for Electrified Transportation Systems,” *IEEE Trans. Transp. Electrif.*, vol. 2, no. 1, pp. 86–95, 2016, doi: 10.1109/TTE.2016.2519351.
- [145] M. C. Mira, Z. Zhang, A. Knott, and M. A. Andersen, “Analysis , Design , Modeling , and Control of an Interleaved-Boost Full-Bridge Three-Port Converter for Hybrid Renewable Energy Systems Publication date : Analysis , Design , Modelling and Control of an Interleaved-Boost Full-Bridge Three-Port Converter f,” *IEEE Trans. Power Electron.*, vol. 32, no. 2, pp. 1138--1155, 2017, doi: 10.1109/TPEL.2016.2549015.
- [146] L. Wang, S. Member, Q. Vo, and A. V Prokhorov, “Dynamic Stability Analysis of a Hybrid Wave and Photovoltaic Power Generation System Integrated Into a Distribution Power Grid,” *IEEE Trans. Sustain. Energy*, vol. 8, no. 1, pp. 404–413, 2017.
- [147] J. W. Qin, Hengsi and Kimball, “Generalized Average Modeling of Dual Active,” *IEEE Trans. Power Electron.*, vol. 27, no. 4, pp. 2078–2084, 2012.
- [148] H. Renaudineau, J. Martin, B. Nahid-mobarakeh, S. Member, and S. Pierfederici, “DC – DC Converters Dynamic Modeling With State Observer-Based Parameter Estimation,” *IEEE Trans. Power Electron.*, vol. 30, no. 6, pp. 3356–3363, 2015.
- [149] H. Renaudineau, “Hybrid renewable energy sourced system energy management & self-diagnosis,” 2013.
- [150] A. Payman, S. Pierfederici, F. Meibody-Tabar, and B. Davat, “An Adapted Control Strategy to Minimize DC-Bus Capacitors of a Parallel Fuel Cell/Ultracapacitor Hybrid System,” *IEEE Trans. Power Electron.*, vol. 26, no. 12, pp. 3843–3852, 2011, doi: 10.1109/TPEL.2009.2030683.
- [151] A. Payman, S. Pierfederici, and F. Meibody-Tabar, “Energy control of supercapacitor/fuel cell hybrid power source,” *Energy Convers. Manag.*, vol. 49, no. 6,

- pp. 1637–1644, 2008, doi: 10.1016/j.enconman.2007.11.012.
- [152] P. Thounthong, S. Pierfederici, and B. Davat, “Analysis of Differential Flatness-Based Control for a Fuel Cell Hybrid Power Source,” *IEEE Trans. Energy Convers.*, vol. 25, no. 3, pp. 909–920, 2010.
- [153] Q. Tabart, I. Vechiu, A. Etxeberria, and S. Bacha, “Hybrid Energy Storage System MicroGrids Integration For Power Quality Improvement Using Four Leg Three Level NPC Inverter and Second Order Sliding Mode Control,” *IEEE Trans. Ind. Electron.*, vol. 65, no. 1, pp. 424–435, 2018, doi: 10.1109/TIE.2017.2723863.
- [154] D. El Kony and S. A. Saafan, “Study of the temperature dependence of both permeability and selectivity of Mg Zn hexaferrites,” *J. Magn. Magn. Mater.*, vol. 267, no. 1, pp. 46–52, 2003, doi: 10.1016/S0304-8853(03)00303-2.
- [155] B. N. Alajmi, K. H. Ahmed, S. J. Finney, and B. W. Williams, “Fuzzy-Logic-Control Approach of a Modified Hill-Climbing Method for Maximum Power Point in Microgrid Standalone Photovoltaic System,” *IEEE Trans. Power Electron.*, vol. 26, no. 4, pp. 1022–1030, 2011, doi: 10.1109/TPEL.2010.2090903.
- [156] P. Takun, S. Kaitwanidvilai, and C. Jettanasen, “Maximum power point tracking using fuzzy logic control for photovoltaic systems,” in *Proceedings of International MultiConference of Engineers and Computer Scientists. Hongkong*, 2011.
- [157] C. Wang, “A Study of Membership Functions on Mamdani- Type Fuzzy Inference System for Industrial,” 2015.
- [158] T. J. Ross, *Fuzzy logic with engineering applications*, vol. Second edi. 2005.
- [159] R. R. Yager and L. A. Zadeh, *An introduction to fuzzy logic applications in intelligent systems*. 1992.
- [160] J. M. Mendel, “Fuzzy Logic Systems for Engineering : A Tutorial,” *Proceeding IEEE*, vol. 83, no. 3, pp. 345–377, 1995.

Abstract

Contribution to the development of a fuel cell management system

The essential challenge in using renewable energy-based electricity generation is the intermittency of resources. Therefore, new ways to store electricity is inevitable. Hydrogen as an energy carrier can deal with this issue. Hydrogen can be produced by using the excess energy of renewable energy sources. Therefore, a Polymer Electrolyte Membrane Fuel Cell (PEMFC) as a device that can directly convert hydrogen energy to electricity is an important part of this solution. The cost and durability are the major challenges to enable the diffusion of this technology in the mass market. In the frame of a multi-vectors microgrid, a Fuel Cell Management System (FCMS) is proposed and designed in this thesis that allows optimizing the reliability and life of PEMFCs through controlling the operating condition of cells to avoid electrochemical instabilities. A proposed diagnostic method along with a new hybrid power electronics architecture is the core of this FCMS. The diagnostic method can detect most of the FCMS instabilities by a new comprehensive real-time model. This model can simulate a cell in its stack environment. A hybrid power electronics architecture is developed for this FCMS that guarantees better aging of the system by separately manipulating the supplied power of cells. The proposed power electronics architecture is hybridized by a Supercapacitor (SC) that can compensate for the low dynamic of PEMFCs in supplying the fast dynamic load profiles. A Fuzzy Logic Control (FLC) method is developed as a part of the FCMS to change the reference power of the cell groups based on the model data. The proposed system and its different parts are validated through the simulation and experimental results.

Keywords: *Fuel cell, Aging, Power electronic, Equalizer system, Energy management*

Résumé

Contribution à l'élaboration d'un système de gestion des piles à combustible

L'intermittence des ressources constitue le principal défi de l'utilisation de la production d'électricité à partir d'énergies renouvelables. Par conséquent, de nouveaux moyens de stockage de l'électricité sont inévitables. L'hydrogène, en tant que vecteur énergétique, peut résoudre ce problème. L'hydrogène peut être produit en utilisant l'énergie excédentaire des sources d'énergie renouvelables. C'est pourquoi une pile à combustible à membrane électrolytique polymère (PEMFC), en tant que dispositif capable de convertir directement l'énergie de l'hydrogène en électricité, est un élément important de cette solution. Le coût et la durabilité sont les principaux défis à relever pour permettre la diffusion de cette technologie sur le marché de masse. Dans le cadre d'un micro-réseau multi-vecteurs, un système de gestion des piles à combustible (FCMS) est proposé et conçu dans cette thèse. Il permet d'optimiser la fiabilité et la durée de vie des PEMFC en contrôlant l'état de fonctionnement des cellules pour éviter les instabilités électrochimiques. Une méthode de diagnostic ainsi qu'une nouvelle architecture d'électronique de puissance hybride sont le cœur de ce FCMS. La méthode de diagnostic peut détecter la plupart des instabilités du FCMS grâce à un nouveau modèle en temps réel. Ce modèle peut simuler une cellule dans son environnement de pile. Une architecture d'électronique de puissance hybride est développée pour ce FCMS qui garantit un meilleur vieillissement du système en contrôlant séparément la puissance fournie par les cellules. L'architecture d'électronique de puissance proposée est hybridée par un supercondensateur (SC) qui peut compenser la faible dynamique des PEMFC en fournissant les profils de charge dynamiques rapides. Une méthode de contrôle en logique floue (FLC) est développée dans le cadre du FCMS pour modifier la puissance de référence des groupes de cellules sur la base des données du modèle. Le système proposé et ses différentes parties sont validés par les résultats de la simulation et de l'expérimentation.

Mots clés : *Pile à Combustible, Vieillessement, Electronique de puissance, système d'équilibrage, Gestion d'énergie*